# How does mineralogy control the technical properties of paper kaolins and ceramic clays?

Zur Erlangung des akademischen Grades eines
Doktors der Naturwissenschaften von der Fakultät für
Bauingenieur-, Geo- und Umweltwissenschaften des
Karlsruher Instituts für Technologie (KIT)
genehmigte

DISSERTATION

von
Dipl.-Min. Kerstin Petrick
aus Baden-Baden

Tag der mündlichen Prüfung: 23.11.2011
Referentin: PD Dr. K. Emmerich
Korreferent: Prof. Dr. H.-G. Stosch

Karlsruhe 2011

# Eidesstattliche Erklärung

Hiermit versichere ich, die Arbeit selbständig angefertigt und keine anderen als die angegebenen Quellen und Hilfsmittel benutzt sowie die wörtlich oder inhaltlich übernommenen Stellen als solche kenntlich gemacht und die Satzung der Universität Karlsruhe (TH) zur Sicherung guter wissenschaftlicher Praxis in der jeweils gültigen Fassung beachtet zu haben.
Die vorliegende Dissertation wurde weder anderweitig als Prüfungsarbeit verwendet, noch an einer anderen Fakultät als Dissertation vorgelegt.
Ich versichere, bisher keine erfolglosen Promotionsversuche unternommen zu haben.

Kerstin Petrick
Karlsruhe, 2011

# Table of contents

# Acknowledgment

I would like to express my deep and sincere gratitude to my supervisor, PD Dr. Katja Emmerich, for the continuous support of my Ph.D. study and research, for her patience, motivation, enthusiasm, and wide knowledge.

I am deeply grateful to my thesis committee Prof. Dr. Heinz-Günter Stosch, Prof. Dr. Frank Schilling, Prof. Dr. Werner Smykatz-Kloss, Prof. Dr. Helge Stanjek, Prof. Dr. Thomas Neumann, and PD Dr. Jörg-Detlef Eckhardt for their insightful and precious comments.

I want to thank all the members of the Bioton project: Peter Krolla-Sidenstein, Dr. René Kaden, Eve Menger-Krug, Dr. Andreas Zehntsdorf, Kati Görsch, Daniel Beyer, Dr. Heike Fischer, Dr. Stefan Huber, Paul Wilhem Kuch, Matthias Dieterle, Dr. Ralf Diedel, and Miriam Peuker. The good collaboration and cordial working atmosphere have been of very great value for this study.

Particular thanks and gratitude go to Dr. Douglas McCarty and Dr. Edwin Zeelmakers for providing the XRD pattern fitting software SYBILLA.

For the performance of analytical measurements and advices, I owe my most sincere gratitude to Marita Heinle (ICP-OES), Stefan Heissler (IR spectroscopy), Nora Groschopf (XRF), Dr. Frank Friedrich (ESEM), and Dr. Peter Weidler (XRD). In this context, I specially thank Prof. Dr. Friedrich Wagner and Dr. Ursula Wagner for performing Mössbauer spectroscopy and for their keen interest in the subject of my studies.

For the opportunity to perform a part of the CEC measurements and to get an insight to the clay lab of the IGT, ETH Zurich, I am grateful to Dr. Michael Plötze, Beat Hornung, and Annette Röthlisberger.

I am very grateful to the DTTG for the grant, which allowed me to participate in the AIPEA summer school (ASYS) at Bari, Italy.

In the name of Dr. Rainer Schuhmann and Franz Königer, I enormously thank all my colleagues from the CMM, especially Dr. Annett Steudel, Eduard Stefanescu, and Heike Kaden for their kind willingness to spontaneously taking charge of measurements, which allowed me to save a considerable amount of time.

I gratefully thank my student co-workers Andrea Buer, Stina Wiechel, and Christoph Weick for their important help in the laboratory and their vivid curiosity in clay mineralogy.

Big thanks to Mike Füssler for technical support as well as to Christian Biedermann together with all system administrators of the IFG.

I express my gratitude to the secretaries Astrid Biedermann, Stefanie Sellheim-Ret, and Rosemarie Bender for always having been efficient and reliable in their support and assistance.

I would like to thank the Library staff of the KIT for making quality information and relevant literature easily accessible.

For the warm atmosphere and conversation during coffee breaks, I am heartily thankful to my friends and Ph.D. fellow campaigners Julia Scheiber, Maria Kesting, Tatjana Ladnorg, and Anne Lebhardt. Many thanks also to Thomas Sollich for realizing numerous pleasurable “container cooking events”.

Enormous thanks to my friends Dr. Eike-Marie Nolte, Dr. Nina Köhler, Leila El Gasmi, Maren Hochschild, Sabine Stabenow, and Susanne Westermann for their encouragement and support throughout my studies.

My loving thanks are due to my parents Monika and Kristof Petrick for giving me the strong feeling of emotional security.

I owe my deepest loving thanks and gratitude to Enrico Magnani. *Sei tu!*

# Abstract

The clay processing industry requires tailored solutions to enhance the workability and performance of clays. A new interdisciplinary approach is the development of processing technologies for clay raw material driven by microbial reactions. The clay supplying and processing industry envisions the implementation of microbially driven processes as a forward-looking concept, since biotechnology may provide a cost-effective, environmentally sound, and sustainable exploration of natural resources.

However, the implementation of biotechnology in raw clay processing requires an overall understanding of microorganism-clay interactions. The key to access such a highly complex system is given by an interdisciplinary approach. For this purpose, the Bioton project (BMBF, grant 01FR0626B) was initiated, combining biotechnological know-how, monitoring of clay processing parameters as well as microbiological and mineralogical characterization during diverse processing stages. The Bioton project targets two main goals: The enhancement of brightness of paper kaolins and the enhancement of plasticity of ceramic clays.

Within this context, the present study is dedicated to the mineralogical characterization of kaolin and clay samples from the Bioton project. A comprehensive mineralogical characterization is the basis for understanding and predicting the processing behavior of complex mineral admixtures as well as for the development and application of biotechnological methods to improve the properties of clay materials.

This issue is very challenging due to the large variation in mineralogical composition and the complexity of factors, which influence clay properties. For that reason, conventional industrial clay assessment is solely based on the deduction of mineralogical parameters from chemical composition and grain-size distribution, which is often not sufficient for the evaluation of processing properties.

In order to overcome this complexity, the bulk material of three kaolin samples and two ceramic clays as well as several of their respective grain-size fractions were comprehensively investigated by a multi-method approach, comprising various physical-chemical and mineralogical methods, as described in Chapter 4.

A particular analytical challenge within this approach is given by the identification of minor constituents with respect to bulk composition, which, despite their marginal quantities, exert a strong influence on material properties. As described in Chapter 1, numerous studies evidenced that kaolin brightness is adversely affected by small amounts of staining Fe phases. The workability of ceramic clays is known to be influenced by the presence of swellable minerals.

Therefore, special attention was paid to the identification of Fe-bearing phases and their distribution characteristics in form of oxides and silicates as well as to the quantification of swellable 2:1 layer silicates, presented as smectite and I-S mixed-layer minerals. In order to detect even small amounts of swellable components, one-dimensional fitting of XRD patterns was included in the multi-method approach, which was applied for the first time to industrially used clays.

Regarding the paper kaolins (Chapter 5), the various samples showed differences in the character and abundance of I-S mixed layer minerals, which were found to correlate positively with the extent of Fe reduction caused by the removal of $Fe^{3+}$ impurities using a Fe-reducing culture of *Shewanella putrefaciens*. The determination of the Fe distribution prior to and after bioleaching by means of Mössbauer spectroscopy indicated that this microorganism is capable to reduce both, the oxide-bound and the silicate-bound Fe. The enhancement of brightness was found to be a function of the location of Fe depletion, since brightness increased mainly by the reduction of oxide-bound Fe and was less affected by the reduction of silicate-bound Fe. The microbiologically induced removal of the silicate-bound Fe was shown to occur mainly in the structure of the 2:1 layer silicates, as no evidence of structural changes was observed for kaolinite by means of STA and ESEM investigations. Moreover, differences in the grain-size distribution characteristics of the three kaolin samples after bioleaching indicated changes in rheology, ascribable to the composition of the reducing medium.

The comprehensive investigation of the ceramic clays (Chapter 6) revealed that the processing properties of ceramic clays are influenced by the interaction of various material parameters, which were found to be different for the two investigated ceramic clays in terms of effective grain-size distribution, soluble salt concentration, particle agglomeration by Fe coatings, occurrence of discrete smectite, amount and degree of ordering of I-S mixed-layer minerals.

From the structural information, a qualitative delamination model was deduced, which gives an indication of how the swellable components may influence the processing properties of ceramic clays. With increasing amounts of swellable layers, the number of “predetermined breaking-points” increases, and so too, does the number of water-accessible surfaces. As a consequence, microstructural modifications seem to be facilitated for clay systems containing larger amounts of swellable components, which may in turn result in greater plasticity.

The combination of various analytical methods revealed that both, the Fe distribution in terms of oxide-bound Fe and silicate-bound Fe and the swellable components found in I-S mixed-layer silicates or in form of smectites have a strong impact on brightness as well as on the plasticity of clays. Therefore, future quality assessment of raw clay properties' should take into account these two key parameters.

However, further studies are required to quantify the contribution of each parameter to clay performance, with special attention paid to the swellable components, as challenges remain in terms of quantitative determination of all material parameters due to the small concentrations of components and/or inappropriate structural models for Rietveld quantification of mixed-layer minerals in complex mineral admixtures.

# Kurzfassung

Die tonproduzierende und -verarbeitende Industrie benötigt maßgeschneiderte Lösungen zur Verbesserung der Verarbeitbarkeit und Anwendbarkeit tonhaltiger Rohstoffe. Ein neuartiger interdisziplinärer Ansatz ist hierbei die Entwicklung mikrobiell gesteuerter Aufbereitungstechnologien. Die tonproduzierende und -verarbeitende Industrie sieht in der Einbeziehung mikrobiologischer Prozesse ein zukunftweisendes Konzept, durch dessen Anwendung eine kostengünstige, umweltfreundliche und nachhaltige Nutzung von Lagerstätten gewährleistet werden soll.

Die Einbeziehung biotechnologischer Aufbereitungstechnologien erfordert jedoch ein umfassendes Prozessverständnis bezüglich der Interaktion von Mikroorganismen und Tonen, dessen Zugang nur auf Basis interdisziplinärer Zusammenarbeit erworben werden kann. Zu diesem Zweck wurde das Bioton-Projekt mit Vertretern aus Industrie, Biotechnologie, Keramtechnologie, Mikrobiologie und Mineralogie initiiert (BMBF-Födernummer 01FR0626B), das der Erforschung der Verarbeitungseigenschaften tonhaltiger Rohstoffe zu verschiedenen Prozesszeitpunkten gewidmet ist. Das Bioton-Projekt verfolgt zwei Hauptziele: die Verbesserung des Weißgrades von Papierkaolinen sowie die Verbesserung der Plastizität keramischer Tone.

In diesem Zusammenhang wurden in der vorliegenden Studie ausgewählte Kaoline und Tone des Bioton-Projektes mineralogisch charakterisiert. Eine umfassende mineralogische Untersuchung stellt die wissenschaftliche Basis zum Prozessverständnis und zur Verhaltensvorhersage komplexer Mineralgemische dar und ist unabingbarer Bestandteil für die Entwicklung und Anwendung biotechnologischer Methoden in Hinblick auf die Eigenschaftsverbesserung von Tonen.

Die komplexe Zusammensetzung und Vielfalt der Einflussfaktoren machen das System Ton zu einer analytischen Herausforderung. Aufgrund der Komplexizität erfolgt die industrielle Rohstoffbewertung oftmals lediglich anhand analytisch einfach zugänglicher Daten, wie der chemischen Zusammensetzung und der Korngrößenverteilung, was sich allerdings meist als unzureichend zur Ableitung von Prozesseigenschaften erweist.

Zur Überwindung der Komplexizität wurden drei Kaoline und zwei keramische Tone sowie ihre jeweiligen Kornfraktionen mittels eines Multi-Methodenansatzes umfassend untersucht. Der gewählte Multi-Methodenansatz beinhaltet eine Kombination verschiedener physiko-chemischer sowie mineralogischer Methoden, die ausführlich in Kapitel 4 beschrieben sind.

Eine besondere Herausforderung an die Analytik stellt dabei die Identifizierung quantitativ geringfügiger Bestandteile dar, die trotz ihrer geringen

Gehalte einen großen Einfluss auf die Materialeigenschaften ausüben. Wie in Kapitel 1 erläutert, hat eine Vielzahl vorausgegangener Studien den färbenden Einfluss bereits geringer Fe-Mengen auf den Weißgrad von Kaolinen dargelegt. Ebenso ist bekannt, dass die Verarbeitungseigenschaften keramischer Tone durch das Vorhandensein quellfähiger Tonminerale beeinflusst werden.

Deshalb wurde der Identifizierung Fe-haltiger Phasen und ihrer Verteilung in oxidisch-gebundener als auch silicatisch-gebundener Form, sowie der Quantifizierung quellfähiger 2:1 Schichtsilicate, vorhanden als Smectit und/oder I-S Wechsellagerungsmineralen, besondere Beachtung beigemessen. Zur Detektion selbst geringer Gehalte quellfähiger Tonmineralanteile wurde als Methodik die eindimensionale Modellierung von Röntgendiffraktogrammen, hier zum ersten Mal zur Charakterisierung industriell eingesetzter Tone, angewandt.

Die Untersuchung der Papierkaoline (Kapitel 5) zeigte Unterschiede im strukturellen Charakter sowie dem Gehalt quellfähiger Anteile in den I-S Wechsellagerungsmineralen zwischen den einzelnen Proben auf. Ein Zusammenhang zwischen Abnahme des Fe-Gehaltes – hervorgerufen durch den Einsatz reduzierend wirkender *Shewanella putrefaciens* Kulturen – und Wechsellagerungsanteil wurde beobachtet. Die Bestimmung der Fe-Verteilung mittels Mößbauer-Spektroskopie vor und nach der Behandlung mit *Shewanella putrefaciens* zeigte, dass der Mikroorganismus die Fähigkeit besitzt, sowohl oxidisch- als auch silicatisch-gebundenes Fe zu reduzieren. Anhand der stärkeren Weißgraderhöhung durch die Reduzierung oxidisch-gebundenen Fe, konnte gezeigt werden, dass die Erhöhung des Weißgrades mit dem Ort der Fe-Verarmung korreliert. Strukturelle Untersuchungen mittels STA und ESEM lassen den Schluss zu, dass innerhalb der Gruppe Fe-haltiger Silicate, die Fe-Reduzierung vornehmlich in der Struktur der 2:1 Silicate stattfindet, da keine Veränderungen der Kaolinitstruktur durch die mikrobielle Behandlung beobachtet wurden. Unterschiede in der Korngrößenverteilung aller Kaolinproben vor und nach der mikrobiellen Behandlung weisen auf eine veränderte Rheologie der Kaolinsuspension hin, welche auf die Zusammensetzung des zugegebenen Kulturmediums zurückzuführen ist.

Die umfassende Charakterisierung der keramischen Tone (Kapitel 6) zeigte, dass die Verarbeitungseigenschaften durch die Interaktion verschiedener Materialparameter bedingt sind. Für folgende Parameter wurden Unterschiede zwischen den zwei untersuchten Proben detektiert: effektive Korngrößenverteilung, Konzentration löslicher Salze, Partikelagglomeration unterschiedlichen Ausmaßes hervorgerufen durch Fe-Überzüge, Anwesenheit von Smectit sowie im Anteil und Ordnungsgrad der I-S Wechsellagerungsminerale.

Anhand der strukturellen Informationen wurde ein qualitatives Delaminationsmodel abgeleitet, das eine Vorstellung von der Einflussnahme quellfähiger Anteile auf die Verarbeitungseigenschaften keramischer Tone geben soll. Mit größer werdendem Anteil an quellfähigen Silicatschichten steigt der Anteil an „Sollbruchstellen“, und somit auch die Anzahl an wasserzugänglichen Oberflächen. Daraus ergibt sich, dass mikrostrukturelle Veränderungen für Tone mit einem größeren Gehalt an quellfähigen Anteilen erleichtert scheinen, was wiederum in einer höheren Plastizität resultiert.

Die Anwendung einer Kombination unterschiedlicher analytischer Methoden zur mineralogischen Charakterisierung toniger Rohstoffe hat gezeigt, dass sowohl die Fe-Verteilung als auch die Anwesenheit quellfähiger Silicatschichten einen starken Einfluss auf den Weißgrad von Papierkaolinen als auch auf die Plastizität von keramischen Tonen haben. Daher sollten diesen beiden Parameter in die industrielle Rohstoffbewertung einbezogen werden.

Allerdings sind noch weitere Studien zur Quantifizierung der Einflussnahme eines jeden Parameters auf die Verarbeitungseigenschaften von tonigen Rohstoffen nötig. Die Quantifizierung quellfähiger Schichtanteile stellt nach wie vor eine besondere analytische Herausforderung dar, da diese aufgrund der meist geringen Gehalte in komplexen Mineralgemischen und durch das Fehlen geeigneter Strukturmodelle innerhalb der Rietveld-Methodik schwer zu erfassen sind.

# List of abbreviations

| | |
|---|---|
| AEM | analytical electron microscopy |
| AIPEA | Association Internationale pour l’Étude des Argiles |
| AKW | Amberger Kaolinwerke Kick Co. KG, Germany |
| AQDS | anthraquinone-2,6-disulfonate |
| BMBF | German Ministry of Education and Research |
| CBD | citrate-bicarbonate-dithionite method |
| CEC | cation exchange capacity |
| CSD | coherent scattering domain |
| CV | coefficient of variation |
| DIN | German Institute for Standardization |
| DRIFT | Diffuse reflectance infrared Fourier-transform spectroscopy |
| EDTA | ethylene diamine tetraacetic acid |
| EG | ethylene glycol |
| ESEM | environmental scanning electron microscopy |
| ESR | electron spin resonance spectroscopy |
| ISO | International Organization for Standardization |
| MAS NMR | magic angle spinning nuclear magnetic resonance spectroscopy |
| ODPF | one-dimensional XRD pattern fitting |
| QPA | quantitative phase analysis |
| RT | room temperature |
| SC-HGMS | superconducting high gradient magnetic separation |
| STA | Simultaneous Thermal Analysis |
| TEM | transmission electron microscopy |
| UFZ | Umweltforschungszentrum, Leipzig |
| XANES | X-ray absorption spectroscopy |

| | |
|---|---|
| XRF | X-ray fluorescence spectroscopy |
| XRD | X-ray diffraction |

# 1 Introduction

The present study is a contribution to describe the phase content and predict the processing behavior of raw clay materials with respect to the development of tailored solutions, which aims to enhance the workability and performance of industrially used clays. This issue is very challenging, as raw clay materials are complex multi-component systems, consisting of clay minerals, non-clay minerals, and organic compounds in different aggregate states. The processing behavior of a given raw clay material may be described as the sum of properties imparted by each constituting phase or component and, additionally, as interaction between them. Therefore, the key for the understanding of bulk material properties is given by the identification and quantification of each constituent.

Many studies carried out to elucidate clay properties use well-defined monomineralic systems in order to minimize as much as possible the influences of interaction deriving from other phases or components. If complex mineral admixtures are the object of investigations, often solely one influencing factor is modified to illustrate property changes. These approaches are helpful in understanding single influencing factors, but represent just one step on the way of further understanding complex polymineralic systems like kaolins or common clays, as properties derived from interaction between clay constituting phases and compounds are not reflected.

Due to their compositional complexity, the industrial evaluation of clays consists of deducing mineralogy merely from chemical composition.

The present study aims to demonstrate that a careful mineralogical characterization of technically used clays by independent methods provides valuable information for further understanding the complex mineral admixtures.

The inclusion of mineralogy offers a powerful tool for the evaluation of processing properties of clays and should be – together with common industrial clay assessment methods – the basis of decision-making for clay grade classification.

Moreover, a comprehensive mineralogical characterization of clays is needed to detect possible changes taking place in the context of modification of properties, as the following study was carried out with regard to microbial-induced clay processing.

Therefore, the following Chapters give an introduction into geomicrobiological clay processing with respect to paper kaolins and ceramic clays and their processing-related properties, followed by a presentation of an analytical strategy designed for the mineralogical characterization of these clays.

## 1.1 The Bioton project

The following study was carried out in the framework of the "Bioton project", financed by the German Ministry of Education and Research (BMBF), grant 01FR0626B. The denomination "Bioton" derives from "Bio" for biological and "Ton", the German word for clay.

Aim of the Bioton project is the application and further development of biotechnological methods to enhance workability and performance of raw clay materials. The clay supplying and processing industry envisions the implementation of microbially driven processes as a forward-looking concept, since biotechnology may provide a cost-effective, environmentally sound, and sustainable exploration of natural resources.

The implementation of biotechnology in raw clay processing requires an overall understanding of microorganism-clay interactions. The key to access such a highly complex system is given by a multi-disciplinary approach. For this purpose, the Bioton project was initiated, combining biotechnological know-how, monitoring of clay processing parameters, microbiological and mineralogical characterization during diverse processing stages. The Bioton project targets two main goals: The enhancement of brightness of paper kaolins as well as the enhancement of plasticity of ceramic clays.

In this context, main research topics of the Bioton project were related to the characterization and cultivation of autochthonous microorganisms (Menger-Krug et al., 2008; Krolla-Sidenstein et al., 2009) and their effects on processing properties (Peuker et al., 2009). Furthermore, the influence of metabolic products and their biotechnological production by appropriate microorganisms for clay modification was investigated (Beyer et al., 2011).

Aim of the present study is the comprehensive and consistent mineralogical characterization of kaolin and clay samples from the Bioton project. A comprehensive mineralogical characterization is the basis for understanding and predicting the processing behavior of complex mineral admixtures as well as for the development and application of biotechnological methods to improve the properties of clay materials.

The material characterization was based on a multi-method approach, presented in Chapter 1.5, comprising various physical-chemical and mineralogical methods, which are described in Chapter 3. A particular analytical challenge was the identification of minor constituents with respect to bulk composition, which, despite their marginal quantities, exert a strong influence on material properties.

In the context of the investigated samples, one challenge was represented by the identification of Fe-bearing phases and their distribution, in oxides and silicates. Fe-distribution was detected after different bioleaching stages by Mössbauer spectroscopy.

A further analytical challenge was the quantification of swellable 2:1 layer silicates, present as smectite and mixed-layer minerals, due to their complex structural features and low abundances.

A new phase-quantification approach to paper kaolins and ceramic clays was applied by means of one-dimensional XRD-pattern fitting (ODPF). The combination of ODPF with other mineralogical methods enabled the detection of even small amounts of swellable components.

One the basis of the mineralogical results, the long-term objective to establish a comprehensive quality-assessment scheme for clays used in paper and ceramic applications comes closer.

## 1.2 Biotechnology and geomicrobiology in mineral processing

The benefit of commercially applied biotechnology was demonstrated by different sectors of mineral industry and environmental protection due to favorable process economics and reduced environmental problems compared to conventional hydrometallurgical processes (Olson et al., 2003). Hydrometallurgy is part of the field of extractive metallurgy involving the use of aqueous chemistry for the recovery of metals from ores, concentrates, and recycled or residual material.

Until the late 1940s, the nature of metal mobilization was thought to be a purely abiotic process. Colmer and Hinkle (1947) predicted a role for biological influence on Fe oxidation in the formation of acid mine drainage, proved in 1950 by Colmer and co-workers by isolating acidophilic bacteria from such drainage. An early documented commercial application of a biohydrometallurgical process was copper extraction from mine waste (Zimmerley et al., 1958). Since then, the potential of microorganisms to dissolve metals from solid material is applied to different purposes, reviewed for instance by Burgstaller and Schinner (1993), Bosecker (1997), and Brombacher et al. (1997). The review articles of Ehrlich (1996; 1998) and Olson et al. (2003) are also suggested for further reading.

Numerous studies are dedicated to the recovery of industrially valuable metals using bioleaching technologies, e.g., zinc (Müller et al., 1995), nickel (Sukla et al., 1993), and copper (Pradhan et al., 2008). Other examples for the application of microorganisms for industrial purposes are the recovery of metallurgy wastes (Krasnodebska-Ostrega et al., 2009) as well as the quality improvement of industrial minerals, such as kaolins (Toro et al., 1992; Cameselle et al. 1995; 2003; Zegeye et al., 2008), clays and sands (Groudev, 1987; Arslan and Bayat, 2009).

However, biotechnological methods in mineral processing have only been applied on a commercial scale to ore leaching (Groudev, 2001) and waste recovery (Liu and Lipták, 1997). Until now, there exists no comparable industrial plant for biotechnologically based beneficiation of raw clay materials.

Previous studies considered mainly individual influencing factors of microbiological treatment on processing relevant properties like rheological behavior, brightness or mineralogical phase content (e.g., Friedrich et al., 1991; Kämpfer, 1991; Mörtel and Heimstädt, 1996; Berthelin et al., 2004).

Microorganisms naturally occur in clays. As stated by Shelobolina et al. (2005), clay formations represent a unique subsurface microbial habitat. Due to their fine particle size, clays have a low hydraulic conductivity and consequently the rate of microbial metabolism is extremely slow. Microorganisms are generally larger than clay mineral particles and it has been suggested that microbial populations present in clays were trapped there during deposition. If this is the case, these bacteria may have survived from the time of original clay sedimentation tens of millions of years ago (Chapelle and Lovley, 1990; Frederickson et al., 1995).

## 1.3 Paper kaolins

### 1.3.1 Properties and applications of kaolins

Kaolins are raw clay materials predominantly composed of 1:1 layer silicates of the kaolinite group, which comprises the minerals kaolinite, the polytypes dickite, nacrite, and the hydrated form halloysite (Jasmund and Lagaly, 1993). The percentage of kaolin group minerals in crude kaolins ranges widely, from 85-95% in the Coastal Plain kaolins of the southeastern United States and the Rio Jari kaolins of Brazil to less than 20% in Cornwall, England, and Hirschau, Germany (Hurst and Pickering, 1997).

Kaolin is one of the most important industrial raw clay materials, due to the multitude of favorable properties. It is chemically inert over a relatively wide range of pH values (4-9), white in color, and shows good covering power when used as pigment or extender. Kaolin is soft and non-abrasive when degritted and has a low conductivity for heat and electricity (Prasad et al., 1991). Kaolin is used in a variety of products, such as paper, ceramics, plastics, paint, medicine, food, and cosmetics (Murray, 1988). This functional versatility reflects the natural variability in deposit quality, which is controlled by mineralogy and processing.

Poorer quality kaolins contain relatively large quantities of impurity minerals and are sold often unprocessed for local use in cement, brick or refractory application.

For technically more demanding applications such as paper coating and as fillers, the kaolins must be beneficiated by either dry or wet processing, in order to remove or reduce impurities (Murray, 1980). Common impurities in kaolins are quartz, mica, illite, smectite, feldspar, goethite, hematite, pyrite, anatase, rutile, ilmenite, and trace quantities of tourmaline, zircon, kyanite, and a few other heavy minerals (Murray, 2007). The presence of quartz or cristobalite generally introduces abrasion problems and is intolerable if the kaolin is to be used to coat paper. Kaolin deposits containing only coarse-grained quartz are of great value, because such quartz can be easily removed, where the separation of fine-grained quartz from kaolins is technically not possible (Murray, 1988).

The largest use of kaolin is in the production of paper. Paper production alone uses approximately 80% of high-grade kaolin sold each year (Harvey and Lagaly, 2006). The application of kaolin as coating or filler for paper requires very rigid specifications including particle size, color, brightness, and viscosity. These parameters are mainly affected by the mineralogical composition.

Brightness of the paper is largely a function of the brightness of the kaolin employed, which in turn depends on the kind and amount of dyeing impurities. Gloss increases with decreasing particle size. Opacity is controlled by light scatter, which is dependent on the difference in the refractive index of the kaolinite and of air-filled voids. A large range of particle size distribution with a maximum of about 80% smaller than 2 µm are the grades used to give rise to an adequate opacity for paper coating (Murray, 2007).

As paper coating, kaolin is applied to the surface of paper to ensure gloss, smoothness, brightness, opacity, and printability of the paper sheet (Bundy, 1993). A typical paper-coating formulation consists of water, pigment, binder, and small quantities of other additives such as dispersants, lubricants, and biocides. This mixture contains up to 65% solids. Pigments most commonly used for coating include kaolin, calcium carbonate, titanium dioxide, and talc. Because the coating is applied to the paper surface at speeds of 1500 to 2000 meters per minute (90-120 km/h), rheological behavior presents a critical parameter. If the shear viscosity is too high, the coating blade may drag across the surface and cause streaks, gaps or rips (Kogel et al., 2002).

As paper filler, kaolin is added to the pulp to fill voids between the wood fibers to improve the paper’s strength as well as the appearance and printing characteristics. Filler also serves to reduce cost by substituting relatively inexpensive kaolin (40 to 60 $/ton) for significantly more expensive pulp (630 $/ton) (Kogel et al., 2002). The upper limit for the amount of filler added to the paper is 20-30%. Particle size is critical because kaolin that is too fine will not be retained in the sheet.

Table 1.1 shows the main characteristics required for processed kaolin in paper applications, reported from Galán et al. (1996) and Kogel et al. (2002). Generally, paper-coating kaolins possess good flow properties, are relatively white and bright, and have minimal grit content. Filler grades are coarser, more viscous, and are not as bright as coating-grade kaolins.

Table 1.1: Industry required specifications of processed kaolin for the utilization as paper coating or filler (Galán et al., 1996; Kogel et al., 2002).

| Specification | Paper coating | Paper filler |
|---|---|---|
| amount of kaolinite [%] | >93 | >85 |
| particle size <2 µm [%] | 80-95 | 50-70 |
| brightness [%]* | 85-92 | 80-85 |
| Brookfield viscosity [cP]** | <500 | <4000 |

*reflectance measured at 457 nm; **at 70% of solids content

### 1.3.2 Industrial material screening for paper applications

Industrial material screening of kaolins is carried out to determine their end use as coatings or filler. Common industrial analyses for the evaluation of kaolin samples comprise determination of particle size, brightness, chemical composition, and viscosity, both of the raw material and the material after different processing steps (Kogel et al., 2002).

The amount of particle size <2 µm is determined to specify kaolins to coating-grade or filler-grade applications according to the classification reported in Table 1.1. Brightness is determined by the percentage of reflectance at 457 nm (Section 4.1.1).

In order to estimate the process-relevant clay mineral content of a kaolin sample, the amount of process-irrelevant feldspars is calculated by means of the chemical composition, assuming that the whole contents of $Na_2O$ and $K_2O$ originate from feldspars. This method is questionable, as kaolins may contain considerable amounts of K-bearing micas. The amount of $Fe_2O_3$ serves as parameter for the estimation of brightness. These rough industrial screening methods are common techniques to bypass the more demanding determination of mineralogy by X-ray diffraction (Salmang and Scholze, 2007).

However, the survey of mineralogical parameters would provide valuable information on further understanding kaolin processing. For instance, kaolins show often different values of brightness, although having nearly the same amount of $Fe_2O_3$, which are not explicable by industrial screening methods. In this context, Mössbauer spectroscopy provides a powerful analytical tool for the detection of the Fe-species distribution in order to distinguish between dyeing and non-dyeing species. The identification and quantification of clay minerals would also permit a more precise prediction of rheological properties of kaolin slurries.

In this study, several kaolin samples from the mining area of Hirschau-Schnaittenbach, Germany, with different Fe content and brightness were investigated with a variety of analytical methods to elucidate the influence of Fe-distribution on optical properties of kaolins.

### 1.3.3 Dyeing impurities of kaolins

Kaolins are often associated with Fe and Ti impurities, which impair whiteness and reduce brightness, leading to a diminished economic value and hinder their application (Ryu et al., 1995; Lee et al., 2002). The concentration of Fe, tolerable for commercial application, varies considerably. Schroeder et al. (1998) reported Fe contents of commercial-grade kaolin from diverse origins from 0.34 to 1.33%, but also larger contents up to 11% have been reported (Jepson, 1988; Bahranowski et al., 1993). Mandal and Banerjee (2004) considered values <0.8% as reasonable for the production of high quality products. In addition to Fe impurities, the presence of micas, smectite and feldspar in kaolins influence rheology, optical and abrasion characteristics (Prasad et al., 1991).

High brightness and whiteness are the most critical properties required for paper coating. Presence of dyeing impurities like ferruginous and titanoferrous minerals adversely affects the optical properties of kaolin.

Möbius (1977) investigated a set of kaolin samples from various origins and found a linear correlation between the total $Fe_2O_3$ content and brightness for kaolins from Cornwall, whereas other samples did not show such a correlation. However, all samples showed a correlation of the Fe oxide content (determined in terms of dithionite and HCl dissolution cycles) and brightness. Furthermore, a stronger linear correlation was found for kaolin samples, containing additionally more than 0.5% of $TiO_2$. Möbius (1977) inferred that there is no general relationship between Fe content and brightness, but that the dyeing capacity of Fe solely depends on Fe distribution in different phases. Similar results were reported by Chandrasekhar and Raghavan (2004).

Extensive research on the nature of Fe in kaolin showed that Fe may be present in two forms (1) in the tetrahedral or octahedral sites of the layer silicate sheets, in this study referred to as “Fe-silicate” or “silicate-bound” and (2) as discrete Fe phases present as oxides, hydroxides, oxy-hydroxides (here referred to as “Fe (oxy-hydr)oxides or “oxide-bound”), as well as sulphides and carbonates (Jepson, 1988; Shelobolina et al., 2005).

Reddish hematite and yellowish goethite are the most common Fe phases found in kaolins (Malengreau et al., 1996). In natural soils, Fe (oxy-hydr)oxides are present both as discrete phases or as poorly crystallized X-ray amorphous particles with short range order. They exist in form of admixtures or as coatings and cements, commonly precipitated or adsorbed on the surfaces or interspaces of the soil constituting minerals (Murad, 1987; 1988; Schwertmann, 1988).

Jepson (1988) and Chandrasekhar and Raghavan (2004) pointed out that oxide-bound Fe influences the kaolin brightness more adversely than silicate-bound Fe, irrespective of the total analytical Fe content.

The effects of silicate-bound Fe on clay mineral properties have been reviewed by Stucki (1988), Stucki and Lear (1989), and by recent publications of Stucki (2006; 2011).

Fe may occur in both, octahedral and tetrahedral sheets of 1:1 and 2:1 clay minerals, and in the gibbsite/brucite sheet of 2:1:1 minerals. Fe also exists as a charge-balancing cation on clay mineral exchange complexes (Coyne and Banin, 1986; Ebitani et al., 2002) or in form of Fe oxides as pillars between the 2:1 layers obtained from artificial synthesis (Bachir, 2009; Naguib, 2010).

Evidence of silicate-bound Fe was gathered by means of various analytical techniques. Electron paramagnetic resonance (EPR) spectroscopy (Brindley et al., 1986; Gaite et al., 1997; Balan et al., 2000) and Fourier transform infrared (FTIR) spectroscopy (Petit et al., 1999) revealed Fe substitution in the octahedral site of kaolinite. Bahranowski et al. (1993) deduced from bulk chemistry analysis that Fe in kaolins may exist as oxide-coatings as well as an isomorphous ion in the kaolinite structure. The ambivalent occurrence of Fe has also been observed by Malengreau et al. (1994) based on infrared diffuse reflectance spectroscopy (DRIFT) and by Schroeder and Pruett (1996) and Schroeder et al. (1998) by means of magic angle spinning nuclear magnetic resonance spectroscopy (MAS NMR). These authors reported values for Fe octahedral site occupancy in kaolinites of less than 3%.

Gualtieri et al. (2000) studied the local environment of Fe in kaolinites with different degree of structural disorder by X-ray absorption spectroscopy (XANES) and found that all investigated kaolinites contained $Fe^{3+}$ in 6-fold coordination. The disordered kaolinite sample showed additionally some Fe in 4-fold coordination. Herbillon et al. (1976) and Mestdagh et al. (1980) ascribed the reduction of kaolinite crystallinity (i.e., an increased degree of structural disorder according to Guggenheim et al., 2002; 2006) to the presence of silicate-bound Fe. Amouric et al. (1986) confirmed the presence of silicate Fe in disordered kaolinites by TEM studies. Based on XRD analyses, several empirical methods of determining the crystallinity of kaolinite have been proposed (Hinckley, 1963; Hughes and Brown, 1979). A more recent theoretical method is based on crystal structure defects (Plancon and Zacharie, 1990).

Johnston and Cardile (1987) investigated the nature of Fe in illites by Mössbauer spectroscopy and showed $Fe^{3+}$ to occupy both, tetrahedral and octahedral sites.

As pointed out by Stucki (2006), the presence of Fe in the structure of smectites is clearly the rule rather than the exception. By means of Mössbauer spectroscopy, Goodman et al. (1976), Cardile (1989), and Luca and Cardile (1989) found Fe to substitute tetrahedral sites of smectites. Evidence for the presence of octahedral Fe was gathered by infrared spectroscopy (Stubican and Roy, 1961; Farmer and Russell, 1964), and is still the subject of recent research as reviewed by Madejová (2003).

A discussion about how Fe is distributed between octahedral sites in 2:1 dioctahedral smectites has been going on for many years. A rule that continues to be generally accepted is that nontronite and ferruginous smectites are largely or completely trans-vacant, whereas cis-vacant montmorillonites contain only little $Fe^{3+}$ (Stucki, 2006). These conclusions are mainly based on X-ray diffraction, selected area diffraction, Mössbauer and infrared spectroscopy (Bookin et al., 1978; Besson et al., 1983; Tsipursky and Drits, 1984; Madejová et al., 1994; Wolters, 2005).

A further source of Fe is given by its incorporation into the $TiO_2$ structure in the form of “iron stained titania”. The effect of titania on kaolin brightness has been studied and reviewed by Weaver (1976). Pure $TiO_2$ strongly absorbs light in the UV region due to metal-oxygen charge transfer. When Fe is present in the $TiO_2$ structure, a Fe(II)-Ti(IV) transition is possible. This charge transfer process has an absorption centered at 350 nm in the near UV region tailing into the visible at the blue end of the spectrum. The intensity of the charge transfer band is 100-1000 times stronger in terms of extinction coefficient than other transitions. Thus, the amount of Fe in $TiO_2$ may be small, but this impurity significantly imparts color to the kaolin. Schwertmann et al. (1995) confirmed the isomorphous replacement of Ti by Fe in the $TiO_2$ structure by XRD, Mössbauer and EPR studies. Chandrasekhar and Raghavan (1999) considered the titania effect responsible for a poor kaolin brightness improvement, although reducing the $Fe_2O_3$ content of about 50% by high gradient magnetic separation and chemical leaching (CBD treatment).

The identification of Fe-bearing phases in kaolins is a difficult task due to the distribution of Fe between various phases, which occur often as intimate mixtures and in small amounts (Schroeder and Pruett, 1996). Additional complication arises from the low silicate-bound Fe concentrations, the detection of which is analytically challenging.

Ti in kaolin samples may be present as discrete Ti-minerals such as anatase or rutile, as a surface-adsorbed form (Weaver, 1976) or as isomorphous substitution for Si and possibly Al in kaolinite (Dolcater et al., 1970; Malengreau et al., 1995). For standard kaolins used in industry, Ti contents of up to 2% have been reported (Jepson, 1988).

### 1.3.4 Conventional kaolin processing

In kaolin beneficiation, removal of Fe and Ti minerals is generally carried out by a combination of physical, physico-chemical, and chemical methods in terms of magnetic separation, froth flotation, and dissolution using mineral acids, inorganic or organic ligands with or without reducing agents.

Since the 1970s, magnetic separation has been employed to improve the brightness of kaolin (Iannicelli, 1976). The development of superconducting high gradient magnetic separators (SC-HGMS) in the 1980s led to an enormous increase in commercially usable kaolin reserves (Watson, 1994). The process of magnetic separation is based on the differences among the magnetic susceptibilities of the constituent minerals (Norrgran and Orlich, 1988). The minerals that are removed are dominantly hematite, Fe-enriched titanoferrous minerals along with some ilmenite, magnetite, and biotite (Murray, 2007).

Froth flotation is more selective for the removal of Fe-Ti-containing impurities. Only oxide-bound Fe can be removed by dissolution, whereas minerals with silicate-bound Fe can also be removed to some extent by magnetic separation and froth flotation. Mineral acid-leaching cannot remove all oxide-bound Fe from kaolin in spite of being the most efficient and aggressive method (Bahranowski et al., 1993).

The concept of chemical as well as biological Fe removal is based on Fe-reduction reactions, transforming the generally insoluble oxidized form of Fe (ferric iron, $Fe^{3+}$) in its more soluble reduced form (ferrous iron, $Fe^{2+}$) (Nealson and Saffarini, 1994).

Other reagents used for Fe removal from clays are pyrophosphate, oxalate, ethylene diamine tetraacetic acid (EDTA) or the citrate-bicarbonate-dithionite method (CBD) established by Mehra and Jackson (1960). For the improvement of kaolin brightness on the industrial scale, the most commonly used chemical reducing agent is dithionite (Stucki, 2006). Due to the better solubility of $Fe^{2+}$ compounds compared to those of $Fe^{3+}$, especially the oxides, even the most insoluble Fe species like goethite and hematite may be dissolved if the redox potential of the extractant is low enough (Borggaard, 1988).

As ultra-fine Fe-bearing particles are difficult to treat by conventional mineral processing methods like magnetic separation (Raghavan et al., 1997), biochemical leaching appears to be a good alternative for their effective removal as shown by Styriaková and Lovás (2007). The authors reported a total Fe removal of 93% from quartz sands, combining bioleaching and magnetic separation processes.

### 1.3.5 Microbial refinement of kaolin

Microbial metabolism primarily controls Fe-redox chemistry in most environments. Numerous studies demonstrated that microorganisms exploit the favorable redox potential between the $Fe^{2+}/Fe^{3+}$ couple and various electron donors and acceptors for their metabolism (e.g., Konhauser, 1998). In this way, $Fe^{2+}$ is used as an electron donor to provide reducing equivalents for the assimilation of carbon into biomass by lithotrophic $Fe^{2+}$-oxidizing microorganisms under both, oxic and anoxic conditions, and $Fe^{3+}$ can be used as a terminal electron acceptor for lithotrophic and heterotrophic $Fe^{3+}$-reducing microorganisms (Weber et al., 2006).

At pH values at or above circumneutral, Fe exists primarily as insoluble, solid-phase minerals in the divalent ferrous ($Fe^{2+}$) or trivalent ferric ($Fe^{3+}$) oxidation state (Cornell and Schwertmann, 2003). When lowering the pH, the solubility of both Fe species increases (Stumm and Morgan, 1996).

Fe-bearing minerals readily function as electron acceptors for ferric iron reducing microorganisms (Luu and Ramsay, 2003). Metal-reducing microorganisms have been shown to be capable of reducing $Fe^{3+}$ in kaolin constituent minerals, both in Fe oxide species like goethite (Roden and Zachara, 1996; Zachara et al., 1998; Liu et al., 2001) and magnetite (Kostka and Nealson, 1995; Dong et al., 2000), as well as in phyllosilicates (Kostka et al., 1999a; 1999b; Dong et al., 2003a).

However, the intimate association of Fe-bearing phases in kaolins makes it often not straightforward to separately determine their respective effects on physical and chemical properties (Schroeder and Pruett, 1986; Lee et al., 2002).

In the following, a short overview is given on the current status of research on interaction between microorganisms and Fe (oxy-hydr)oxides as well as Fe-bearing clay minerals, which is mainly based on recently published reviews by Luu and Ramsay (2003), Stucki (2006), Stucki and Kostka (2006), Weber et al. (2006), and Dong et al. (2009a). Subsequently, results of studies conducted in the context of bioleaching of kaolins are summarized.

Microorganisms used for bioreducing are usually facultatively or obligately anaerobic and widely occur in soils (Wu et al., 1988; Gates et al., 1993; 1998), sediments (Kostka et al., 1996; Cervini-Silva et al., 2003), sedimentary rocks (Dong et al., 2003a; 2003b; Shelobolina et al., 2003), and hydrothermal environments (Kashefi et al., 2008).

The microbial Fe reduction process of both Fe (oxy-hydr)oxides and silicate-bound Fe was shown to be coupled to carbon oxidation and electron transport in $Fe^{3+}$-reducing bacteria (Lovley and Philips, 1988; Kostka and Nealson, 1995; Kostka et al., 1999a). Common redox-active organic compounds identified in soils and sediments are plant exudates (Nevin and Lovley, 2000), humic acids (Lovley et al., 1996), and antibiotics (Hernandez et al., 2004).

Given the relative thermodynamic favorability of Fe reduction, crystalline $Fe^{3+}$ oxide mineral reduction (goethite, hematite, and magnetite) is decreased compared with amorphous or poorly crystalline ferric oxides, such as ferrihydrite (Thamdrup, 2000). Previous studies have shown that Fe-reducing microorganisms are capable of “living on the energetic edge”, making crystalline solid-phase $Fe^{3+}$ (Frederickson et al., 1995; Kukkadapu et al., 2001) and silicate-bound Fe bioavailable (Kostka et al., 1996). A study of Stanjek and Marchel (2008) indicated that the (microbially induced) redox cycles of Fe oxides and Fe-rich clay minerals are intrinsically linked to each other.

Roden and Zachara (1996) examined quantitative aspects of microbial reduction of synthetic goethite using *Shewanella species* and found a linear correlation between initial reduction rate and oxide surface area. Their results suggested that the formation of $Fe^{2+}$-bearing phases limited the extent of $Fe^{3+}$ oxide reduction.

As stated by Weber et al. (2006), there has been considerable debate regarding the direct relevance of laboratory studies that have examined the reduction of crystalline Fe minerals under artificial organic and nutrient-rich conditions to optimize microbial growth. Glasauer et al. (2003) did not observe reduction of goethite and hematite by *Shewanella putrefaciens*, in direct contrast to previous reduction studies conducted with this microorganism in nutrient-rich media (Frederickson et al., 1995; Kukkadapu et al., 2001).

Various mechanisms have been proposed how microorganisms might transfer electrons to extracellular Fe-bearing minerals. Comparing the microbial reduction mechanisms described both for Fe (oxy-hydr)oxides (Weber et al., 2006) and for silicate-bound Fe (Dong et al., 2009a), no difference can be ascertained as the respective reduction mechanism depends primarily on the type of microorganism. The two primary strategies are pictured below for the case of Fe reduction in silicates (Figure 1.1).

Regarding the reduction of $Fe^{3+}$ in silicates, the amount and the crystal-chemical environment of $Fe^{3+}$ as well as the layer charge of clay minerals are important factors that control the extent of reduction, as a low layer charge favors the accessibility of clay minerals to microbial interactions (Jaisi et al., 2007a). The correlation between relative reducibility and layer expandability is strengthened by recent data from Dong et al. (2009b), which shows that the rate and extent of mixed-layer illite-smectite and rectorite are between those for the discrete end-members.

Among the minerals studied, expandable layer silicates are the easiest reducible by microorganisms with the fastest rate and the highest extent of biological reduction, whereas illite is the least reducible (Dong et al., 2003a; 2009a).

The extent of microbial reduction of $Fe^{3+}$ in clay minerals and Fe (oxy-hydr)oxides depend both on experimental conditions (type of microorganisms and mineral, their concentration ratio, presence or absence of electron shuttle components and organic compounds, temperature, solution chemistry in terms of pH and aqueous chemical composition) as well as specific mineral characteristics (Fe content, particle size, surface area, layer charge, interlayer composition).

The following relative tendencies have been observed: The extent of bioreduction (1) increases with increasing microorganism/mineral ratio (Kostka et al., 1999a; Jaisi et al., 2007b); (2) increases with increasing total Fe content (Ernstsen et al., 1998; Gates et al., 1998); (3) increases with decreasing particles size, thus, increasing surface area (Ernstsen et al., 1998; Bosch et al., 2007; Jaisi et al., 2007c); (4) is favored by a lower layer charge (Seabaugh et al., 2006; Dong et al., 2009b); (5) is enhanced by the presence of electron shuttle components (Seabaugh et al., 2006; Komlos et al., 2007); (6) appears to be reduced by the presence of organic compounds in the interlayer of clay minerals (Zhang et al., 2007a); (7) is influenced in different ways by temperature (Zhang et al., 2007b; Kashefi et al., 2008) and pH (Kostka et al., 1999a; Zhang et al., 2007b).

Up to now, the mechanisms of microbial reduction of ferric Fe in silicates described in literature have mainly been inferred from study of montmorillonite and nontronite (Fe-rich smectites), as smectites are by far the most frequently studied systems in this context. Recently, studies have been expanded to illite and chlorite, mixed-layer illite-smectite and rectorite (Dong et al., 2009b), palygorskite (Dong et al., 2009c), vermiculite (Komlos et al., 2007), natural soils and sediments (Favre et al., 2002; 2006; Komlos et al., 2007; Stucki et al., 2007), but knowledge about reduction mechanisms is still limited (Dong et al., 2009a).

Two mechanisms have been proposed for microbial reduction of $Fe^{3+}$ in smectites: solid-state and dissolution-precipitation. Solid-state transformation means a reduction mechanism without any significant structural changes, which are reversible upon reoxidation. In contrast, dissolution-precipitation transformation denotes a reduction mechanism, leading to (partially) irreversible structural dissolution under release of ions and the formation of biogenic products, such as silica (Furukawa and O'Reilly, 2007), smectite (Zhang et al., 2007b), and illite (Kim et al., 2004).

Evidence for a solid-state mechanism was reported by Lee et al. (2006), Stucki and Kostka (2006), Kashefi et al. (2008), and recently by Stucki (2009), based on studies of smectites and ferruginous smectite samples, whereas the dissolution mechanism was favoured by authors investigating nontronite samples (Dong et al., 2003b; Kim et al., 2004; Li et al., 2004; Jaisi et al., 2005; Zhang et al., 2007a; 2007b). These observations led to the conclusion that the mechanism of $Fe^{3+}$ reduction may be mineral specific, mainly driven by the total Fe content as well as layer charge. However, extending this concept to illite (low Fe content and high layer charge with respect to smectite), there is some evidence for both reduction mechanisms. Dong et al. (2003b) reported that illite dissolution may have occurred as a result of bioreduction, whereas other studies have shown that the illite structure largely remains intact (Kukkudapu et al., 2006; Seabaugh et al., 2006).

The solid-state and the dissolution-precipitation bioreduction mechanism represent two extreme cases and reality might lie somewhere between these mechanisms. For instance, Kukkudapu et al. (2006) observed that biogenic $Fe^{2+}$ largely remained in the illite structure, but the illite became more soluble in weak acid than the original material, suggesting some change of the illite structure.

Moreover, the concentration and type of microorganism play a key role in determining the mechanism of $Fe^{3+}$ reduction (Dong et al., 2009a). The effects of different microorganisms on possible pathways of electron transfer from the bacteria into the clay mineral structure were studied by comparing *Geobacter* and *Shewanella* species (Figure 1.1).

In contrast to *Shewanella* species, the species of *Geobacter* cannot produce any electron-shuttling compounds (Nevin and Lovley, 2002) and thus requires the direct contact between bacterium and clay mineral surface for bioreduction to take place. The electron pathway may be parallel to (001), where the transfer of electrons to the $Fe^{3+}$ centers near the clay mineral edges may be readily accomplished, but it may be difficult to transfer electrons to the $Fe^{3+}$ centers in the middle of the layers. As a consequence, the extent of bioreduction may be limited and the clay mineral largely remains in solid-state.

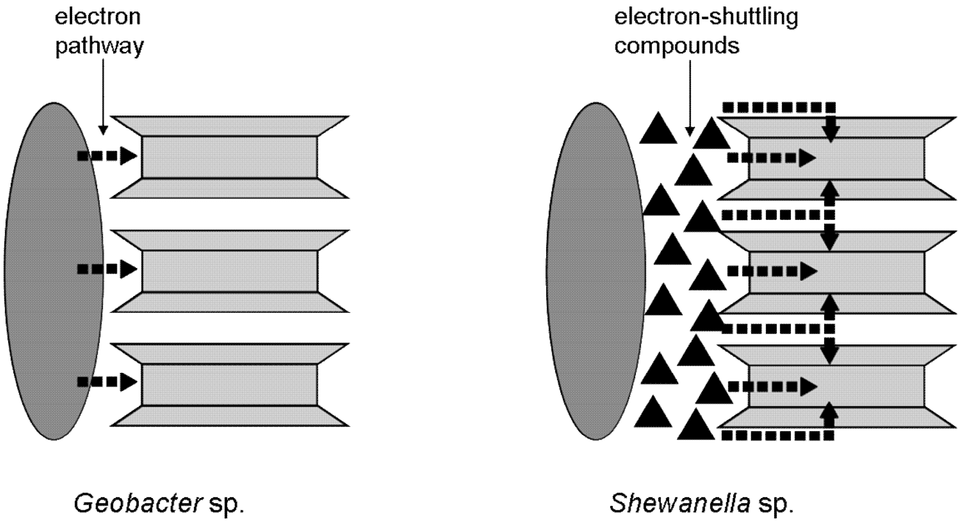

Figure 1.1: Two possible pathways of electron transfer from bacteria to the $Fe^{3+}$ centers in the clay mineral structure, without (Geobacter species) and with (Shewanella species) electron-shuttling compounds (black triangles). Modified after Dong et al. (2009a).

Shelobolina et al. (2003) showed that the extent of silicate $Fe^{3+}$ reduction in smectites by *Geobacter* species is generally lower than that achieved by other microorganisms. *Shewanella* species produce electron-shuttling compounds themselves. Thus, a direct contact between bacteria and clay mineral surface for electron transfer is not required. This facilitates the electron transfer to the $Fe^{3+}$ centers both parallel and perpendicular to (001), resulting in a larger extent of bioreduction (Kostka et al., 1999b), under partial dissolution of the clay mineral structure (Dong et al., 2009a). The further addition of electron-shuttling compounds, like anthraquinone-2,6-disulfonate (AQDS), which is a functional surrogate of humic substances, significantly enhances Fe reduction (Dong et al, 2003b; Jaisi et al., 2005), suggesting that bioreduction may be limited by the availability of such shuttling compounds.

Groudev (1987) and Cameselle et al. (1995; 2003) have studied efficiency enhancement of bioleaching of kaolins by a two-stage process. In the first stage, the microorganism is grown in an adequate medium under appropriate culture conditions in order to improve the production of active metabolites for the leaching process. In the second stage, the culture medium is used as a leaching agent for the kaolin. The absence of a growing microorganism permits the use of more aggressive leaching conditions, such as low pH and higher temperatures, and leads therefore to a higher dissolution rate and extent of Fe removal.

Employment of $Fe^{3+}$-reducing microorganisms has been suggested as an alternative refinement method to remove Fe impurities from kaolin (Lee at al., 2002). Styriaková and Styriak (2000) demonstrated the efficiency of bacterial Fe removal from kaolins. After one month of bioleaching, 43% of the Fe occurring as amorphous oxyhydroxides and of 15% of silicate Fe in micas was extracted. Styriakovà et al. (2003) found that bioleaching of kaolins caused structural and compositional transformation of the constituting micas. Metabolic activities of *Bacillus cereus* led to the extraction of silicate-bound Fe in the octahedral sheet of micas under formation of illite. The mica destruction was also reflected by a shift of grain-size distribution toward smaller fractions.

Mineral transformation reactions were already reported in the context of abiotic Fe reduction, using dithionite as reducing agent. The dithionite-treatment of smectites caused a decreased interlayer spacing, turning a fraction of the interlayer cations less exchangeable. This phenomenon has been confirmed for $Na^+$, $K^+$, $Ca^{2+}$, $Cu^{2+}$, and $Zn^{2+}$ (Lear and Stucki, 1989; Khaled and Stucki, 1991). Shen and Stucki (1994) further suggested the decrease of interlayer spacing as a possible mechanism for the in situ conversion of smectite to illite. Similar results were obtained for bacteria-reduced smectites, and may be the explanation for the presence of illite (Kim et al., 2004).

Phillips et al. (1993) related the degree of crystallinity of Fe (oxy-hydr)oxides to microbial reduction activity. The highest reduction activity was found for goethite followed by ferric hydroxide. Hematite was nearly unreduceable. The authors concluded that the lower the degree of crystallinity, the higher is the probability of reduction. The influence of crystallinity of a high- and low-defect kaolinite on bioleaching efficiency was also investigated by Mockovciaková et al. (2008), who reported a higher Fe extraction rate for disordered kaolinites. By means of nitrogen absorption studies the authors found an elevated percentage of meso- and macropores of untreated disordered kaolinite samples, which are thought to facilitate the bioleaching process.

## 1.4 Ceramic clays

### 1.4.1 Properties and applications of ceramic clays

The term ceramic clay refers to common clay, which is intended for a wide variety of ceramic applications, like high quality tableware, sanitaryware, electrical porcelain, glazes, or tiles. Common clays are fine grained and typically exhibit plastic behavior when wet. The plastic clay material can be formed into many desired shapes, dried and fired to give products with rock-like hardness. Their uses are governed by several factors including the geological and geochemical conditions under which the clays were formed and transformed, resulting in mineralogical composition of the deposit, as well as physical and chemical properties (Murray and Keller, 1993; Murray, 2000).

The latest innovation in tilemaking is the production of large-size tiles, double pressing, pressing without mould, cutting of green tiles (Dondi et al., 2003). New classes of clay materials produced by adequate blending as well as the advancement of processing technologies, able to couple high plasticity and suitable rheological behavior, are required to realize these inventions. Dondi et al. (2008) stated that the desired set of technological properties presents difficulties for mineral processing, even by selective clay exploitation and blending, because of two main reasons: First, prediction of clay processing behavior will always entail uncertainty due to the complex interaction of mineralogical and physical-chemical parameters, and second, many parameters are not adequately monitored by routine analyses with conventional industrial screening techniques (Worrall, 1986; Powell, 1996).

### 1.4.2 Industrial material screening for ceramic applications

It is well-accepted that the mineralogical composition controls ceramic processing related properties (Schmidt, 1981), but relations between components in mineralogical systems and properties taking into account the main components only (Schüller, 1980). As summarized by Kaufhold and Penner (2006), especially the amount and nature of swelling clay minerals (smectite and smectitic components in illite-smectite mixed-layer minerals) exert a strong influence on workability, such as viscosity (Störr, 1983, Lagaly, 1989), making moisture content (Hofmann, 1962), plasticity (Kromer and Rose, 1994), dry bending strength (Wiegmann et al., 1978; Schüller, 1980), and shrinkage (Kromer and Schüller, 1973; Wiegmann et al., 1978; Störr and Schwerdtner, 1979).

Despite the known influence of mineral composition, the quality of raw clays for industrial application is often still evaluated merely by their chemical composition (Schejbal, 1978) and grain-size distribution (Winkler, 1954).

The mineralogical composition of ceramic clays is characterized by varying amounts of finely dispersed quartz, feldspars (mostly K-feldspars, albite/oligoclase), micas (often referred to as sericite[*], muscovite and biotite), illites, kaolinite, Fe-(oxy-hydr)oxides, and occasionally varying portions of mixed-layer minerals, as illite-smectite. In addition, several clays contain very fine organic matter and also lignite, which sometimes contains marcasite (Kromer, 1979; 1980).

Westerwald ceramic clays, which are investigated in this study, have a complex composition due to the coexistence of different clay minerals, mainly illite, illite-smectite mixed-layer minerals (I-S), smectites and kaolinite with varying degree of disorder (Kaufhold and Penner, 2006).

Despite the known variations in properties due to the variability of mineralogical composition, even ceramic clays similar in composition show different processing properties. Those differences can only be elucidated with a comprehensive mineralogical characterization by the advanced methods described above.

In this context, two ceramic clays (W1 and W2), from the Westerwald area (Germany), with different processing properties, but apparently nearly identical chemical and mineralogical composition, were investigated comprehensively. The different processing properties in terms of extrusion behavior and making moisture content could not be explained on the basis of the bulk material composition. As minor constituents exert a strong effect on processing properties (Schüller, 1980), a detailed characterization of the smectite layer content is required to understand and predict the behavior of ceramic masses in a forming process.

Aim of this study is a consistent mineralogical characterization by a multi-method approach that is able to detect processing-related differences between two similar ceramic clays according to industrial assessment.

---

[*] sericite: according to Rieder et al. (1998) the use of the name for fine-grained aggregates of mica-like phases is discouraged.

### 1.4.3 Plasticity of ceramic clays

Plasticity is defined by Grim (1968) as a property where material deforms under applied pressure, with the deformed shape remaining when the deforming force is removed.

According to the recommendations of the AIPEA nomenclature (Guggenheim et al., 2006), the definition of clay and clay mineral implies plasticity as one essential characteristic. Citing these authors, "the term clay refers to a naturally occurring material composed primarily of fine-grained minerals, which is generally plastic at appropriate water contents and will harden when dried or fired. Although clay usually contains phyllosilicates, it may contain other materials that impart plasticity and harden when dried or fired. Associated phases in clay may include materials that do not impart plasticity and organic matter […]. The term clay mineral refers to phyllosilicates minerals and to minerals, which impart plasticity to clay and which harden upon drying or firing. This definition expands the previous definition of Brindley and Pedro (1972) by relating clay minerals to the properties of clays. However, clay minerals are not defined a priori as fine-grained because clays are fine-grained, but rather they may be of any crystallite size so that the term clay mineral is consistent with the definition of mineral, which is unrelated to crystallite size. Clearly, although the small particle size and high surface area of clays contribute to their unique properties and are very important (Guggenheim and Martin, 1995), the particle-size issue has been separated from the clay mineral definition."

Besides the small particle size, several other parameters determine the rheological properties of clays: bulk mineralogy (type and quantity of clay minerals and non-clay minerals), particle size and distribution, particle shape, layer charge, structure of the particle edges and edge charge density, exchangeability of cations, as well as soluble salts and organic matter (Lagaly, 1989; 2006; Murray, 2007).

Generally, clays develop plasticity when they are mixed with a defined amount of water (Grim, 1968). A measure of this clay-specific water requirement (in technical terms also referred to as making moisture content) is the plasticity index according to Atterberg (1912). The plasticity index is the difference between the liquid limit, i.e., the lowest water content at which the mass can be rolled into threads without breaking, and the plastic limit, i.e., the water content at which the mass begins to flow. Both values are expressed in weight percentage of the clay dried at 120 °C (Jasmund and Lagaly, 1993). Müller-Vonmoos et al. (1985) compared the plasticity indices of $Na^+$- and $Ca^{2+}$-dispersed kaolinite, illite and montmorillonite and showed that the plasticity index increased in the sequence kaolinite-illite-montmorillonite, whereas the $Ca^{2+}$-form of the non-swellable clay minerals kaolinite and illite, and the $Na^+$-form of swellable montmorillonite showed higher values, respectively.

Hofmann (1961, 1962) as well as Weiss and Frank (1961) explained the cause of plasticity in terms of card-house and band-like aggregation models. Card-house structures are formed by edge-to-face contact of the clay particles to a three-dimensional network, whereas band-like structures are formed by face-to-face contact. In the true sense of the definition, card-house structures as such only occur in the acid pH range, built up from direct edge-to-face contact, whereas edge-to-face contacts established by counter ions are referred to as card-house-like structures (Jasmund and Lagaly, 1993).

When a mechanical force is applied to the clay body, the card-house-like contacts between two particles may be broken and the particles can shift into neighboring contact positions. The cohesion between the particles is never lost since the water content will not exceed the liquid limit. In the case of band-like structures, the particles may not only change positions, the network can also be deformed by rotation of the particles. The formation and destruction of card-house and band-like structures, as well as their transformation from one form to another, are responsible for the complex flow behavior of clay masses and dispersions (Lagaly, 1989; 2006).

The aggregation form depends primarily on the potential of attractive forces between the particles, which are strongly influenced by the exchangeable cations and the electrolyte concentration of the pore solution (Jasmund and Lagaly, 1993). Concerning the ion exchange capacity of clay minerals, principally two cases have to be distinguished: Non-swellable clay minerals (e.g., kaolinite and illite) exhibit exchangeable cations only on their edges (Weiss and Russow, 1963), whereas swellable clay minerals (e.g., smectites) additionally have exchangeable cations in the interlayer and at basal surfaces. Correspondingly, the cation exchange capacity (CEC) of kaolinite and illite is low compared to swellable clay minerals. Weiss (1958) reported CEC values of 1-10 meq/100 g for kaolinite and 35 meq/100 g for illite. Smectites have CEC values of 70-120 meq/100 g depending on their chemical composition (Jasmund and Lagaly, 1993). With increasing pH also the clay mineral edges become negatively charged due to desorption of protons and ionization of silanol groups, resulting in a higher cation exchange capacity (Lagaly, 1989).

Dispersions of kaolinite or illite tend to form voluminous card-house-like structures in the presence of $Ca^{2+}$-counter ions, able to incorporate water molecules. This arrangement results in a high plasticity. In the presence of $Na^{+}$-ions, the particles are oriented in face-to-face band-like structures. The parallel arrangement of the particles hinders the incorporation of water molecules, resulting in a low plasticity. Generally, the plasticity of non-swelling clay minerals increases with increasing valence and radius of the exchangeable cations (Bain, 1971; Grim, 1968; Müller-Vonmoos et al., 1985).

In the $Ca^{2+}$-form, the interlayer space of swellable clay minerals is smaller compared to that of the $Na^{+}$-form, which leads to a lower plasticity of $Ca^{2+}$-saturated smectites (Jasmund and Lagaly, 1993).

The effects of grain size on plasticity were already described by Whittaker (1939) and White (1949). Bain (1971) correlated grain size and crystallinity of kaolinite to chart plasticity and stated that fine-grained, poorly crystallized kaolinites showed higher plasticity indices in contrast to coarse-grained, well-crystallized kaolinites.

According to Müller-Vonmoos and Loken (1989), the shearing behavior of clays depends primarily on particle anisotropy and the negative charge of the layer surfaces. Particle diameters are 0.1-5 µm for kaolinite and illite, and 0.03-3 µm for smectite; layer thicknesses of kaolinite (25-80 layers) and illite (5-80 layers) are between 175 and 560 Å for kaolinite, 50 and 800 Å for illite, and between 300 and 3000 Å for smectite (5-12 layers) (Weiss, 1989). Thus, kaolinite has the largest grain size and the smallest diameter-to-thickness ratio among the examined minerals. Müller-Vonmoos and Loken (1989) concluded that the relatively high shear strength of kaolinite arises principally from intergranular friction, whereas the shear behavior of illite is mainly influenced by the counter ions present in the pore water. Due to the small particle size and inferior bonding force in the interlayer, smectite particles respond to shear stress by disintegration into their component layers, thus giving rise to highly anisotropic particles.

The phenomenon of particle disintegration was also investigated by Nadeau (1984a; 1984b; 1984c; 1987), who demonstrated that I-S mixed-layer particles break up into fundamental particles of ~10 Å along the smectitic interlayer when dispersed. The delamination of I-S mixed-layer particles occurs at the low-charged interlayer space. The type of fundamental particles obtained depends on the charge distribution, i.e., the variation of the cation density from interlayer space to interlayer space. The particles break up only at interlayer spaces with cation densities typical of smectite (Lagaly, 2006), which act as kind of “predetermined breaking points”. More information on the nature of fundamental particles is given in Chapter 2.4.

The implementation of predetermined breaking points to clay systems is exploited to prepare stable dispersions of ultra-fine kaolinite particles. The intercalation of organic molecules facilitates the separation into thinner particles when a mechanical force is applied. This process is known as delamination (Lahav, 1990; Hauser-Fuhlberg, 2005). Already in the 1960s, Weiss (1963) inferred that the intercalation of kaolinite with ammonium ions leads to delamination, which may be responsible for plasticity improvement, presumably already applied in traditional Chinese pottery.

### 1.4.4 Conventional plasticity-enhancing methods

The purpose of plasticity enhancement is the improvement of workability in terms of molding with application of limited extrusion force and to achieve adequate molding properties by lowering the making moisture content.

Plasticity of clays may be improved by various methods like extrusion or by addition of plasticity-enhancing substances using mineralogical additives like bentonite or pure smectite or chemical additives, which may be inorganic (e.g., soda, sodium phosphate species, water glass) or organic (e.g., carboxymethylcellulose, polymeric alcohols).

Besides the shaping of clay bodies, extrusion also leads to the modification of plasticity by introduction of shear energy as the effect of extrusion relies mainly on the activation and homogenization of inner gliding surfaces. The influence of textural changes on plasticity of clay masses during extrusion were summarized by Bartusch and Händle (2007). Various scenarios of extrusion to impart plasticity were described by Lutz (2007).

The addition of small portions of swellable components in form of pure smectite or present in bentonite is a common plasticity-enhancing method in ceramic processing (Odom, 1984). Tomita et al. (2008) compared the extrusion behavior of ceramic masses mixed both with organic binders and smectite, respectively, and stated that the smectite-enhanced masses showed extrusion properties similar to that of the masses containing organic binder. Furthermore, the properties of ceramic masses can be influenced by ion-exchange, as Ca-smectite shows a higher green strength, lower dry strength, and a better flowability than Na-smectite (Grim and Güven, 1978).

Dispersing agents like soda, monomeric and oligomeric phosphates, and water glass solutions are well-known to decrease the yield stress of kaolin dispersions (Lagaly, 1989; Jasmund and Lagaly, 1993). Phosphate compounds, like Na-pyrophosphate, are very efficient deflocculants for clay suspensions, acting by mainly two mechanisms: (1) by electrostatic stabilization increasing the overall negative surface charge, as the anionic part of the molecule is being adsorbed especially at the edges of the clay mineral particles; (2) by complexing the dissolved bivalent cations and replacing them by $Na^+$ cations, which leads to an increase of the electrical double layer thickness (Andreola et al., 2004; 2006). Manfredini et al. (1990) investigated the flocculation capacity of some phosphate species and found that hexametaphosphate provides the highest colloidal protective effect, while tripolyphosphate showed the highest complexing action towards flocculating cations, followed by pyrophosphate.

Plasticizing effects can also be brought about by addition of organic thickening agents, lubricants, molding aids, wetting agents, temporary binders, and release agents (Hölzgen and Quirmbach, 2007). The plasticity-enhancing effect of organic additives is primarily based on particle modification, which directs to a more easy slip by overcoming of interlocking or mechanical bonds between adjacent particles. The mechanisms involved in this process are charge balancing, particle coating in terms of morphology masking, as well as increasing of the swelling effect by addition of polymers with high molecular weight.

Another industrially used process to improve plasticity is the storage of clay masses under different temperature or humidity conditions. This process is referred to as clay maturation or clay ageing ("Mauken" in German).

The enhancement of plasticity by clay maturation is seen as the underlying key process for the manufacturing of traditional Chinese eggshell porcelain. Weiss (1963) reported clay maturation to be due to in delamination of kaolinite particles, which were previously intercalated by ammonium ions. Regarding the traditional clay maturation process, the author supposed that the ammonium ions originated from urinary excretion of bovines, employed to plow up the kaolin pit under storage. In this context, Weiss (1963) referred already to the formation of possible microbial metabolic products, which were thought to influence plasticity.

Up to now, the role of microorganisms in the process of clay maturation is not fully understood, but subject of several investigations (Menger-Krug et al., 2008; Petrick et al., 2008; Gaidzinski et al., 2009).

The term clay maturation is also applied in the context of clay suspension storage with different saline solutions (Sánchez et al., 2002). The authors observed an increase of plasticity with increasing maturation time and inferred that changes in plasticity were the result of structural modifications caused by degradation of the clay minerals. Sánchez et al. (2002) expressed this degradation in terms of "crystallinity", which dropped down in the course of maturation. These results are in accordance with Grim (1968), who observed an inverse relationship between crystallinity and plasticity.

### 1.4.5 Microbial plasticity-enhancing methods

The incorporation of microbially produced additives to adjust rheology of clays is a common practice in ceramic processing (Sarikaya and Staley, 1994). Mainly applied are biological additives in terms of metabolic products of microorganisms like polysaccharides, acids of the citric acid cycle (gluconic acid, citric acid, oxalic acid), or enzymes.

Bischoff (2004) investigated the influence of microbially produced polysaccharides (dextran, xanthane, and alginate) on the rheological properties of clay suspensions of low concentration (15% w/v), made up of clays from the Westerwald area, and reported a strong increase in viscosity with increasing molecular weight of the added polysaccharides.

The effect of biological treatment is based on the formation of a biofilm, consisting of microorganisms, extracellular polymeric substances (ESP), and water (Wingender et al., 1999). The gel-like EPS network is the metabolic product of microorganisms and consists of different types of polysaccharides. The EPS matrix can be considered as a physical gel, which imparts plasticity. Physical forces, such as entanglement, van der Waals interactions, or hydrogen bonds, generally lead to the formation of fluctuating junction points, which give rise to transient network structures (Wloka et al., 2004).

## 1.5 Multi-method approach

As discussed in Chapter 1.3 and 1.4, properties of industrially used clays are strongly related to their mineralogical constituents, which in turn are related to their respective structural features (Moore and Reynolds, 1997).

In the following chapter, a summary of mineralogical characterization methods is given with focus on the clay minerals present in the investigated paper kaolins and ceramic clays, thus, kaolinite, I-S mixed layer minerals and their discrete end-members illite and smectite.

### 1.5.1 General considerations on quantitative phase analysis

The selection of an adequate analysis strategy has to be made on the basis of several (often mutually dependent) considerations, such as target of the study, time requirement, accessibility to analytical instruments, available sample amount, as well as feasibility in terms of manpower and financial budget.

However, in every case quantification of complex mineral admixtures should be carried out involving various analytical methods. This is for two main reasons: The combination of different analytical methods contributes (1) to enhancing the knowledge on mineralogy of a given sample as every method provides special information and (2) to constraining methodology-dependent uncertainties. The application of such a multi-method approach aims at achieving consistent results by crosschecking the respective results gathered with different (independent) methods. Figure 1.2 depicts the multi-method approach applied in this study, which was extended if required (e.g. by the addition of Mössbauer spectroscopy for the detection of Fe-species).

The term “consistent result” refers to a result, which is the most probable after crosschecking single results. For example, in order to verify the quantification results from Rietveld analysis, the mineralogical phase content may be converted to chemical composition in terms of element oxides. Afterwards, the amount of element oxides is compared with the chemical composition from XRF measurements. Eventually arising deviations between these two data sets indicate that one or more structural models chosen for Rietveld analysis were not adequate or not available, which is the case for I-S mixed-layer minerals. Another option is that not all phases were correctly identified.

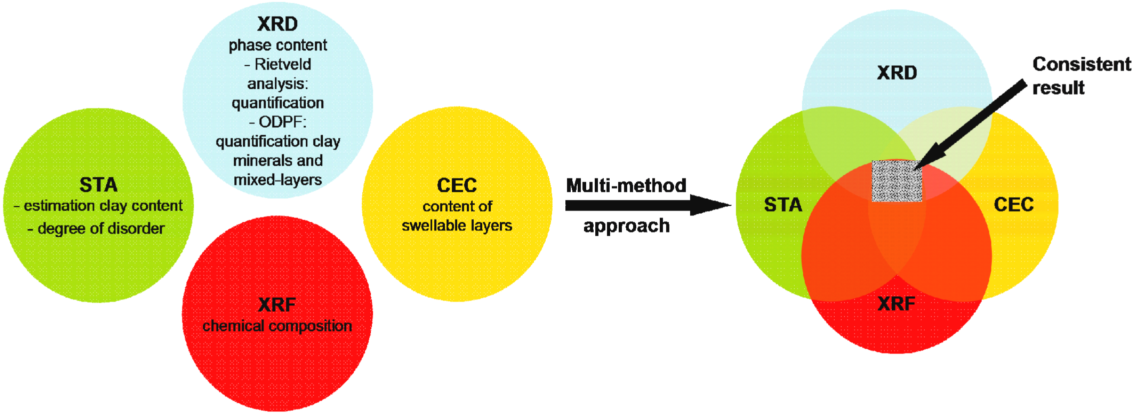

Figure 1.2: Combination of various analytical techniques for the quantification of clay minerals in complex mineral admixtures.

Generally, quantification results have to be critically evaluated, as every analytical method yields results, which are obtained under certain assumptions. Thus, results gathered from a single method present merely an iterative approximation on the way to the accurate value.

The characterization of complex clay mixtures like kaolins or common clays is still a specific task (Omotoso et al., 2006; Kleeberg, 2009a). Quantitative XRD analysis of the smectite content with the Rietveld method has been possible with commercial software like AutoQuan since 2006, based on smectite structural models developed by Ufer et al. (2004). Until now, no appropriated structural model for illite-smectite mixed-layer minerals within the Rietveld method is available, but is under development (Ufer et al., 2009).

The combination of different analytical methods, such as X-ray fluorescence (XRF), Simultaneous Thermal Analysis (STA), and determination of the cation exchange capacity (CEC) in addition to Rietveld analysis of XRD patterns allows an approximation of the mineralogical phase content. In such a multi-method approach, a new analytical tool applied to industrially used clays is offered by one-dimensional XRD profile fitting (ODPF), previously mainly used to oil exploration-related identification of mixed-layer minerals and clay mineral paragenesis (e.g., Środoń, 1981; Drits et al., 1997a; Lindgreen et al., 2000; McCarty et al., 2008; Lanson et al., 2009). ODPF enables the characterization of complex samples consisting of discrete clay minerals and mixed-layer phases.

However, also the application of one-dimensional modeling not always provides an unambiguous determination of the actual structure as several structural models may fit the experimental data equally well (Drits, 1987; Sakharov et al., 1999; McCarty et al., 2004). Fitting results have to be critically evaluated by comparing them with chemical and mineralogical analyses in order to achieve a consistent characterization.

Figure 1.3 illustrates the flow chart of analytics applied in this study. In order to quantify the mineralogical phase content, results obtained by Rietveld analysis were crosschecked with the chemical composition from XRF analysis. The amount of clay minerals determined after this crosscheck is compared with the mass loss from STA measurements (Δm DHX), which indicates the maximum possible clay content in a given sample. An estimation of the amount of swellable components is gathered by CEC measurements. For validation of the CEC measurements, the exchanged cations are quantified by ICP-OES. The amount of swellable components is crosschecked with the results from ODPF, which gives information on the clay content in terms of quantification and eventual mixed-layering. Then, all crosschecked results are compared with each other, leading ideally to a consistent quantification result of the sample under investigation.

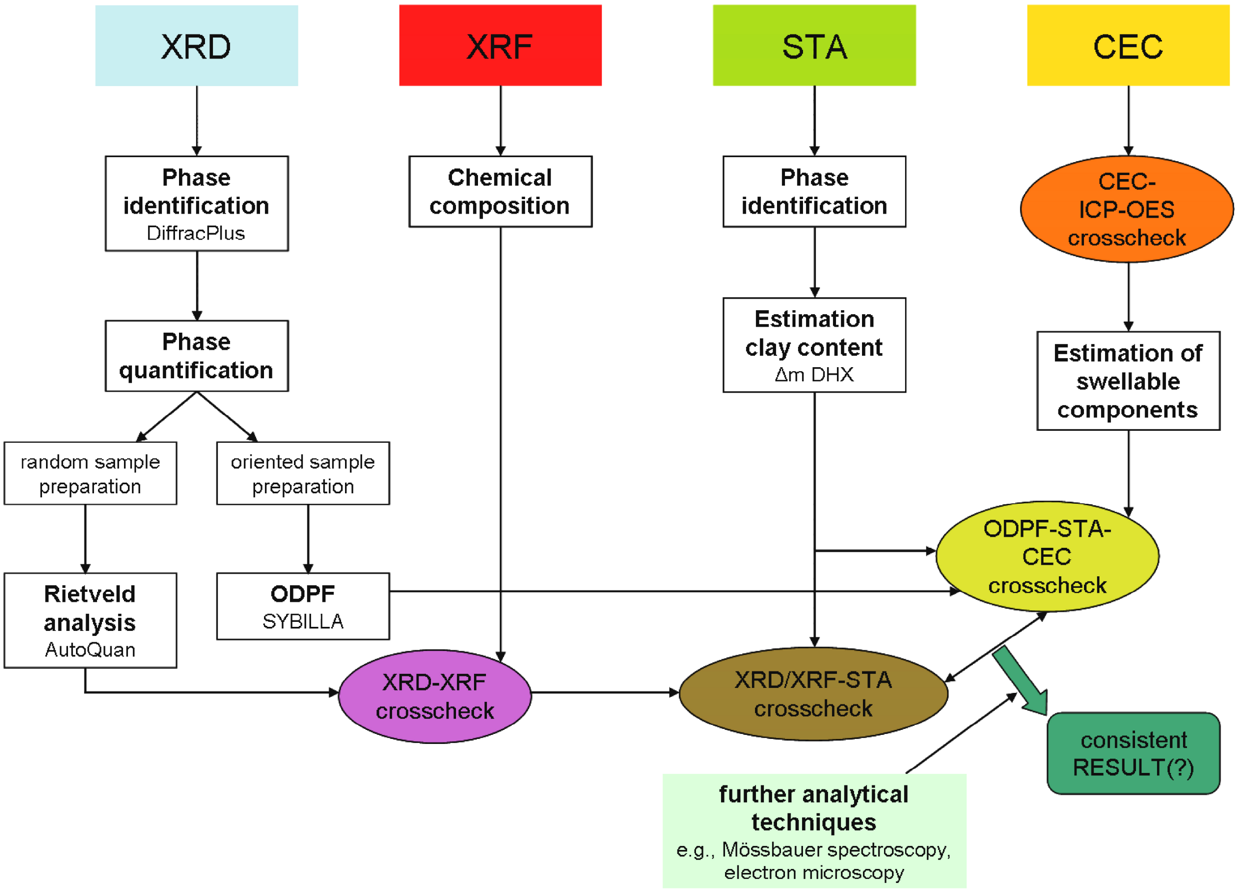

Figure 1.3: Flow chart of the multi-method approach applied in this study for the quantification of clay containing samples.

The flow chart presented here should not be misunderstood as a rigid scheme as further analytical methods, such as Mössbauer spectroscopy or microscopic techniques, may be inserted. Furthermore, possible deviations arising after the respective crosschecks of single methods requires an iterative approach, which consists in modifying equivocal results and comparing them again with the results from other methods. For instance, the crosschecked results from Rietveld analysis and XRF analysis (referred to as XRD-XRF crosscheck in Figure 1.3) often lead to deviations confronting them with the results from STA measurements. An overestimated clay content according to STA measurements may be balanced, e.g., by increasing slightly the illite content and lowering the K-feldspar content. If this modified result is also consistent with those from XRF measurements, this modification is considered as reasonable.

### 1.5.2 The role of powder X-ray diffraction for the determination of clay minerals

Powder X-ray diffraction (XRD) is the common standard technique of mineral identification and quantification (e.g., Chung and Smith, 2000). Clay minerals are very difficult to quantify, because of their variable chemical composition and structures. Due to their platy habit, clay mineral particles have a strong tendency for orientation, enhancing the (00*l*)-reflections and weakening the (*hk*)-reflections as compared with a sample of fully random orientation (Środoń, 2006).

Information on the magnitude of analytical errors is available from recent worldwide contests and round-robins (e.g., the Reynolds Cup) in quantitative analysis of artificial rocks containing clay minerals. Outcomings of these contests indicate that some XRD techniques are capable of providing very accurate results of below 10% of cumulative error from actual values (McCarty, 2002; Kleeberg, 2005).

Numerous strategies of XRD data processing are in use. They all rely upon measuring the diffraction intensity of a given mineral in the sample under investigation and comparing it with the intensity of a pure standard or – in the case of Rietveld analysis – a structural model of the concerning mineral.

Three main techniques are currently in use for clay mineral quantification:

(1) single peak/natural standard technique, which relies upon a selected individual peak as a measure of mineral abundance, and upon natural specimens as standards (e.g., Hillier, 2000; Środoń et al., 2001);

(2) whole pattern/natural standard technique, which obtains intensities of the phase in a mixture by fitting the entire XRD pattern with patterns of pure standards (e.g., Smith et al., 1987; Batchelder and Cressy, 1998; Chipera and Bish, 2002);

(3) whole pattern/computed standard techniques, which fit the experimental pattern with the patterns of pure phases calculated from crystallographic data (e.g., Bish and Howard, 1988).

The latter method is also referred to as Rietveld analysis. Main advantages of the Rietveld technique are the calculation of standards and the correction for instrumental errors, which makes this technique easily transferable from one instrument to another, less dependent on the quality of sample preparation, and independent on the availability of pure standards.

The main drawback of the Rietveld method in clay mineral quantification is due to their complex structures in terms of mixed-layering, polytypism, as well as tri-dimensional defects (Środoń, 2006). In order to overcome this problem, numerous studies are dedicated to the development of computed crystallographic models, which describe various types of structural disorder (Bergmann and Kleeberg, 1998; Ufer, 2004; Ufer et al., 2008). Until now, no structural model is available to describe mixed-layering by Rietveld analysis, but is under development (Ufer et al., 2009).

Further information on analytical techniques for the identification and quantification of clay minerals in complex mineral admixtures is provided in Chapter 4. 2.

# 2 Structure and occurrence of clay minerals

## 2.1 General structural features of clay minerals and mixed-layer minerals

The correlation between structure and properties of clay minerals is a well-known phenomenon and is referred to as structure–functionality principle (Emmerich, 2009).

The versatility of the properties of clay minerals is caused by their structural variety and their deviations from a given ideal structure. Deviations from the ideal crystal structure lead to real clay mineral structures and occur in two interacting ways: (1) by deviation from the ideal chemical composition caused by cation substitution, both in the tetrahedral and/or octahedral sheet and by mixed-layering; (2) by deviation of the ideal symmetry from distortion within, both, the tetrahedral and/or octahedral sheet, distortion between the tetrahedral and octahedral sheet, as well as translation and rotation of layers (Moore and Reynolds, 1997).

Detailed information on structural features of clay minerals and mixed-layer minerals can be found in the textbooks of Brindley and Brown (1980), Jasmund and Lagaly (1993), Moore and Reynolds (1997), Meunier (2005), Bergaya et al. (2006), Velde and Meunier (2008), and the review by Środoń (1999).

### 2.1.1 Clay minerals

Clay minerals are hydrous aluminosilicates and are classified according to crystal chemical aspects as phyllosilicates, or layer silicates (Strunz, 1941). Their layers are composed either of one octahedral and one tetrahedral sheet (1:1 layer silicates) or of one octahedral sheet sandwiched between two tetrahedral sheets (2:1 layer silicates).

The tetrahedral sheet is composed of corner-linked [$SiO_4$]-tetrahedra. A fraction (<50%) of the central $Si^{4+}$ can be substituted by $Al^{3+}$, and also by $Fe^{3+}$ in lower quantities (Goodman et al., 1976; Luca and Cardile, 1989).

The octahedral sheet is constituted of edge-linked [$M(O,OH)_6$]-octahedra, with M as octahedral site cation, usually $Al^{3+}$, $Mg^{2+}$, $Fe^{2+}$, or $Fe^{3+}$, but also nearly all other transition elements and $Li^+$ have been identified. Due to the valence of the octahedral site cation, the octahedral sheet is either dioctahedral or trioctahedral. Dioctahedral means the occupation of two out of three possible positions in the octahedral sheet with trivalent cations; trioctahedral denotes the occupation of all available positions with divalent cations.

Joining the sheets to layers, the layers in one particle spread over tens to thousands of nanometers in a* and b* direction. In c* direction, the layers are stacked on top of each other, forming clay mineral particles with a thickness of a few to tens of layers. The layers are either electrically neutral or have a negative charge as a consequence of isomorphous substitutions within the tetrahedral and/or octahedral sheet. The negatively charged layers are bound by interlayer cations or sheets of interlayer hydroxides. The chemical bonds within the layers are much stronger than between the layers, which results in the plate or lath habit of clay crystals and their perfect cleavage along (001).

A classification of clay minerals according to their layer type and layer charge is given by the AIPEA Nomenclature Committee (Guggenheim et al., 2006).

A discrete (also referred to as pure or end-member) clay mineral is characterized by identical layers and possibly interlayers within a crystal, preserving the strict periodicity of the structure in c* direction. Thus, Bragg's law (Chap. 4.2.3) is obeyed and XRD patterns show integral or rational series of (00*l*)-peaks, which means that all peaks produced from one mineral are equidistant: $d(001)=d(002)/2=d(003)/3=d(00l)/l$, with *l* being the integral order.

### 2.1.2 Mixed-layer minerals

If one crystal contains different layer types or interlayer composition, the strict periodicity is interrupted, giving rise to the phenomenon of mixed layering or interstratification.

Mixed-layer minerals are formed by two or more kinds of intergrown layers. Thus, they are discrete phases, not physical mixtures. The component layers are arranged along a line perpendicular to (001) or parallel to c*, either in random, partially regular, or regular sequences.

Interstratification is very frequent within dioctahedral or trioctahedral species as the respective a* and b* dimensions of the layers involved vary only slightly between each other (Reynolds, 1992), but not between dioctahedral and trioctahedral species. This is the reason why mixed-layer minerals formed by stacking of dioctahedral and trioctahedral layers were hitherto not found in nature, but are the subject of synthesis (Venugopal et al., 2008).

The most commonly described two-component mixed-layer minerals are illite-smectite (I-S) and kaolinite-smectite (K-S) within the dioctahedral species, as well as biotite-vermiculite and chlorite-vermiculite, or chlorite-smectite within the trioctahedral species.

More recent studies showed the existence of three interstratified components, such as illite-smectite-vermiculite (Drits et al., 1997b; Placon and Drits, 2000) or serpentine-nontronite-vermiculite (Huggett et al., 2006).

*Ordering principles and nomenclature of mixed-layer minerals*

Mixed-layer minerals either have ordered (regular) structures, if different layers A and B alternate periodically along the c* direction (e.g., ABABAB…, AABAABAAB…, ABBBABBB…) or disordered (irregular) structures, if the layer stacking is random (e.g., AABABABBA…).

The ordering type of a mixed-layer mineral is defined by the term Reichweite *R*, the German word for “reach back”. The concept of Reichweite was suggested by Jadgozinski (1949) and expresses the probability of a two-component system to find a given layer A to be next to layer B.

*R0* describes a random sequence. The junction probability of A and B layers depends only on their relative proportions $P_A$ and $P_B$.

*R1* indicates short-distance order. According to the relative proportions of A and B layers, two cases have to be distinguished: maximum degree of order and partial ordering.

The maximum degree of order occurs if $P_A=P_B$. Then, the layers are regularly stacked (ABABAB…), giving rise to a 1:1 interstratified material, which is not a mixed-layer mineral in its true sense, but a new clay mineral with a cell that can be defined as AB, thus, maintaining the strict periodicity in c* direction. As the definition for a clay mineral is fulfilled, regular *R1* sequences are identified by special names, recognized by the AIPEA Nomenclature Committee. For example, rectorite is a regular interstratification of dioctahedral mica and dioctahedral smectite, or corrensite, which exists in two varieties: a regular interstratification of trioctahedral chlorite and trioctahedral smectite or trioctahedral vermiculite, respectively. The committee’s criterion for a regular sequence is that the diffraction pattern shows at least ten rational (00*l*)-reflections, all of the same width (Bailey, 1982).

*R1* partial ordering occurs if the proportions of layers A and B differ from each other, if $P_A \neq P_B$. An example may illustrate this ordering condition. Considering the case of 30% A and 70% B, *R1* ordering means that all A layers are separated by at least one B layer, and 40% of the B layers are still available to be randomly distributed. This condition implies ordering with respect to one component (here A) but random with respect to the other (here B).

*R3* indicates long distance order, which will occur when $P_A$ and $P_B$ are sufficiently different from each other. Taking into account the case of 10% A and 90% B arranged in a stacking sequence, means that 80% of B are still available to be distributed. In this case, the distribution has to be done in such a manner that each A layer is surrounded by at least three B layers, because the first B has influence that reaches three positions to the last B. This ordering type leads to segregation of one component (B in this case).

The existence of *R2* ordering is discussed controversially. Bethke and Altaner (1986) and Bethke et al. (1986) proposed a layer-by-layer mechanism of smectite illitization via *R2* ordering from calculated and experimental XRD patterns. Środoń and Eberl (1984) stated that *R2* ordering is not a probable arrangement, and that XRD patterns may be interpreted as a mixture of *R1* and *R3* ordering.

Mixed-layer minerals take their names of the respective components, whereas the component with the smaller d(001)-spacing appears first by convention. A complete description requires additionally the proportion of each layer and the type of ordering. For instance, a mixed-layer mineral of 70% illite and 30% smectite is represented by the expression *R1* I(0.7)/S.

### *Identification of mixed-layer minerals*

The main analytical tool for the identification and quantification of mixed-layer minerals is XRD. Since the 1980s also transmission electron microscopy (TEM) and analytical electron microscopy (AEM) are applied for the characterization of mixed-layering (e.g., Schreyer et al., 1982; Ahn and Peacor, 1986a; 1986b; Guthrie and Veblen, 1989; Shau et al., 1990; Środoń et al., 1990; 1992; Elsass, 2006). In contrast to XRD, which averages billions of crystals, TEM allows the observation of individual particles. Thus, the major problem is gathering statistically valid numbers.

The interpretation of XRD patterns of mixed-layer minerals often poses problems, particularly if the mixed-layer minerals are present in physical mixtures with other clay minerals. For identification, multiple analyses of carefully prepared samples have to be carried out. Such a multi-specimen method comprises XRD analyses of the samples from oriented preparation in air-dried state, solvation with ethylene glycol (EG) or glycerol, and heat-treatment at different temperatures (Bish and Reynolds, 1989; Drits et al., 1997b; Sakharov et al., 1999).

Oriented sample preparation leads to an enhancement of the (00*l*)-reflections. (*hk*)-reflections are not very diagnostic, as the structures of most clay minerals are very similar in a* and b* directions.

In order to eliminate the influences of different cation saturations in the interlayer of the swellable components, the cations are exchanged by $Ca^{2+}$. According to Eberl et al. (1987), $Ca^{2+}$-saturation seems preferable if smectites or mixed-layer minerals containing smectite are investigated, because of the lower sensitivity against climatic influences compared to $Na^{+}$-saturated samples. At low humidity, some $Na^{+}$-smectites tend to display characteristics of vermiculite.

Identification of swellable components is more reliable from EG- or glycerol-treated samples, as air-dried smectite-containing samples stored under undefined humidity conditions always represent interstratified smectite of 0, 1, and 2 water layers depending on layer charge and charge distribution (Ferrage et al., 2005; 2007). Further instruction for XRD sample preparation is given in Section 4.2.3.

Information from XRD patterns are provided by the position, intensity, width, and symmetry of the (00*l*)-diffraction peaks. Mixed-layer minerals contain two or more types of layers, thus different unit cells, giving rise to non-integral or irrational series of (00*l*)-peaks, d(001)≠d(002)/2≠d(003)/3≠d(00*l*)/*l*, with *l* being the integral order. Therefore, Bragg's law does not apply. Deviation arises from the variation of the basal periodicity along c* and are a fair criterion to identify the presence of mixed-layer structures (Drits and Tchoubar, 1990).

Méring (1949) observed that the peak positions of mixed-layer minerals are intermediate between those of the discrete end-members, and that peak positions and intensities correlate with the proportions of the end-members in the interstratification (Méring's principle). As a consequence, peaks show highly variable broadening, depending on the distance between the corresponding end-member peaks. Fig 2.1 illustrates Méring's principle.

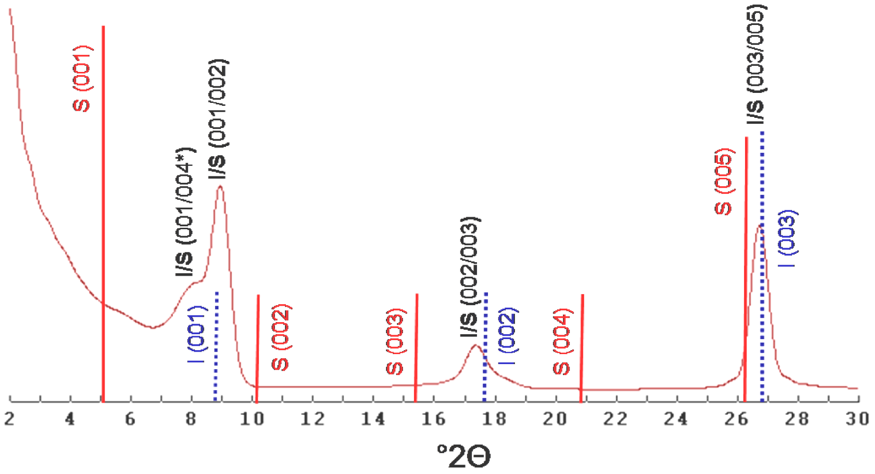

Figure 2.1: Calculated XRD pattern of an *R3* I(0.9)/S mixed-layer mineral to illustrate Méring's principle. The solid lines represent peak positions of smectite, the dashed lines the peak positions of illite. The calculated peaks of the mixed-layer minerals are on intermediate positions as a result of the respective proportions of the end-members.

A numerical test for rationality or the degree of irrationality of a given (00*l*) diffraction series is provided by the coefficient of variation (CV) and the Q-value.

The CV is defined as the ratio of the standard deviation σ to the mean µ (equation 2.1).

$$cv = \frac{\sigma}{\mu} \qquad \text{(eq. 2.1)}$$

To determine the CV for (00*l*)-diffraction patterns, each observed d(00*l*)-value is multiplied by the respective integral order *l*, giving rise to a set of d(00*l*)-values, from which the mean value and the standard deviation are calculated. Rational interstratification is assigned by CV-values <0.75%; CV-values >0.75% indicate mixed-layering (Bailey, 1982).

The comparison of an EG-corrensite and of a randomly interstratified chlorite/EG-smectite containing 70% of chlorite shall illustrate the procedure (Table 2.1). The examples were taken from Moore and Reynolds (1997).

Table 2.1: Coefficient of variation for (00*l*) diffraction patterns of EG-corrensite and randomly interstratified chlorite/EG-smectite.

| | Corrensite | | Chlorite/EG-smectite | |
|---|---|---|---|---|
| *l* | *d* | *l·d(001*)* | *d* | *l·d(001)* |
| 1 | 31.31 | 31.31 | 15.29 | 15.29 |
| 2 | 15.73 | 31.46 | 7.41 | 14.82 |
| 3 | | | 4.74 | 14.22 |
| 4 | 7.78 | 31.12 | 3.49 | 13.96 |
| 5 | 6.23 | 31.15 | 2.83 | 14.15 |
| 6 | 5.19 | 31.14 | | |
| 7 | 4.46 | 31.22 | 2.05 | 14.35 |
| 8 | 3.89 | 31.12 | | |
| 9 | 3.46 | 31.14 | 1.59 | 14.04 |
| 10 | 3.11 | 31.10 | | |
| Mean | | 31.20 | | 14.40 |
| CV | | 0.38% | | 3.34% |

The Q-value predicts the different peak widths and is a quantitative expression of Méring’s principle, as irrational mixed-layering results in peak broadening. With the Q-value, slight peak broadenings are detectable and, therefore, even small amounts of interstratification. The Q-value is calculated taking the ratio of the d(001)-values of the suspected end-members, and multiplying this ratio by the *l* value of the high-proportion end-member. Q is the positive deviation from the nearest integer.

The application of the Q-value is demonstrated by an example taken from Moore and Reynolds (1997), in which a few percent of mica are suspected in a chlorite. To calculate the Q-value, the ratio of the d(001)-values of mica and chlorite (10/14.2=0.704) is taken and multiplied by the respective *l* values for the chlorite reflections (Table 2.2). The respective deviations of these numbers from their nearest integers are called Q-values. The Q-value predicts the different line widths. In this example, the broadest reflections will be the (002)- and (005)-reflections.

Table 2.2: Calculation of the broadening descriptor Q.

| *l* | *l*·0.704 | Q |
|---|---|---|
| 1 | 0.704 | 0.296 |
| 2 | 1.408 | 0.408 |
| 3 | 2.113 | 0.113 |
| 4 | 2.817 | 0.183 |
| 5 | 3.521 | 0.479 |
| 6 | 4.225 | 0.225 |
| 7 | 4.930 | 0.070 |
| 8 | 5.634 | 0.366 |
| 9 | 6.338 | 0.338 |
| 10 | 7.042 | 0.042 |

The values for Q can only vary between 0 and 0.5. Q=0 designates a reflection unaffected of mixed-layer broadening. In this case, the peak’s width is produced only by the crystallite thickness and instrumental effects. Q=0.5 marks the maximum peak width possible for the respective mixed-layer mineral. A series of different Q-values indicates irregular interstratification.

A relation between Q and peak width can be established by means of known standards or from calculated X-ray patterns, e.g., by the profile-fitting program NEWMOD (Reynolds, 1985).

A further approach to the identification of mixed-layer minerals is given by direct modeling of (00*l*)-XRD patterns. This technique is referred to as one-dimensional XRD-pattern fitting (ODPF) and gathers information from peak position, morphology, intensity and broadening (Drits and Tchoubar, 1990). The trial-and-error procedure used for modeling is usually very time-consuming as input data are adjusted manually, until a satisfactory fit of the entire XRD profile is reached.

Input variables are preferred orientation and crystallite thickness as well as changes of lattice parameters due to isomorphous substitutions and variations in interlayer spacing.

The use of preferred orientation probabilities (Moore and Reynolds, 1997; Dohrmann et al., 2009) and of log-normal shape of crystallite thickness distribution restrains modeling parameters (Dudek and Środoń, 1996; Drits et al., 1997a). Nevertheless, the large number of input variables generates non-unique solutions to the effect that different combinations of input variables may fit a given XRD pattern equally well (Sakharov et al., 1999; McCarty et al., 2008).

Unfortunately, no convention about the term "satisfactory fit" exists. Often, the least-squares sum is used as criterion to describe the deviation between measured and fitted XRD patterns. According to Środoń (2006), the least squares criterion is appropriate, if quantitative analysis of a physical mixture of clay minerals is the target of modeling. If the determination of the layer ratio within a given mixed-layer mineral is the focus of investigation, the criterion of fit should be based on peak positions, as they are usually most sensitive to the layer ratio. For instance, a 0.1° 2θ deviation in peak position changes the evaluation of illite layers in randomly interstratified I-S by a value of about 15%.

The modeling procedure can be automated using available optimization techniques. At least two of such approaches are in use, which both are proprietary of oil companies. At Exxon, Pevear and Schuette (1993) applied genetic algorithms and the program NEWMOD to model XRD patterns of mixed-layered containing clay minerals admixtures. The SYBILLA program, developed by Chevron applies evolutionary programming and is based on the modeling program of Drits and Sakharov (1976). Furthermore, SYBILLA can handle multi-component mixed-layering, and automatically models all operator-identified clay mineral phases of a given sample.

## 2.2 Structure and occurrence of individual clay minerals

In the following, a short overview is given of the clay minerals presented in the investigated paper kaolins and ceramic clays.

### 2.2.1 Kaolinite

Kaolinite is a dioctahedral 1:1 layer silicate with the ideal structural formula $Al_2Si_2O_5(OH)_4$ and a theoretical chemical composition of 46.54% $SiO_2$, 39.50% $Al_2O_3$, and 13.96% $H_2O$.

Kaolinite forms as a residual weathering product or by hydrothermal alteration of aluminosilicates, especially of feldspars (Oberlin and Couty, 1970). Kaolinite occurs in soils and sedimentary rocks like kaolin, which contains minable amounts of kaolinite.

The thickness of the unit layer is 7.15 Å. The charges in the ideal kaolinite structure are balanced. Thus, kaolinite has no layer charge. Talibudeen and Goulding (1983) reported kaolinite samples to have low percentages (0.1 to 10%) of vermiculitic, micaceous, or smectitic layers, which is probably the explanation for the negative layer charge of some kaolinites, resulting in a low shrink-swell capacity and a low cation exchange capacity (<15 meq/100 g).

Kaolinite, in contrast to the kaolin group member halloysite, has not been observed to swell in water, but treatment with organic solutions, e.g., formamide, hydrazine or dimethyl sulfoxide, cause it to swell. The swelling reaction is used for the identification of kaolinite besides chlorite as well as for its distinction from halloysite (Theng et al., 1984). As chlorite and kaolinite have diagnostic d(00*l*)-reflections in common, also thermal treatment at 550 °C of the sample under investigation may serve to distinguish between those two clay minerals. In contrast to chlorite, kaolinite undergoes phase transformation by dehydroxylation and the characteristic (00*l*)-reflections of kaolinite disappear (Jasmund and Lagaly, 1993).

The dehydroxylation temperature of kaolinite depends on its structural degree of disorder. With increasing degree of disorder, the dehydroxylation temperature decreases (Smykatz-Kloss, 1974). The structural defects of kaolinite are very complex. Plancon and Tchoubar (1977) described different types of structural defects, like random shifts between adjacent 1:1 layers by ±nb/3, irregular rotational shifts between adjacent layers, and irregular cation distribution site vacancies in the octahedral sheet. These imperfections have influence on many properties exploited industrially, such as the firing temperature (Placon et al., 1988).

A method for estimating the structural disorder of kaolinites is the Hinckley index (Hinckley, 1963), also referred to as “crystallinity index”. This index is the ratio of the sum of the heights of the reflections $(1\bar{1}0)$ and $(11\bar{1})$ measured from the inter-peak background, and the height of the $(1\bar{1}0)$-reflection measured from the general background. The justification for this rather arbitrary procedure was that as the crystallinity decreased, the proportion of random shifts between adjacent layers by ±nb/3 increased, resulting in a decrease in resolution of neighbouring peaks and an increase in the inter-peak diffraction intensity (Plancon et al., 1988).

### 2.2.2 Illite

Illite is a dioctahedral 2:1 layer silicate of common occurrence in soils and sedimentary rocks and was first described by Grim et al. (1937), who named the mineral according to a type site in Illinois.

Due to the wide variety of chemical composition, Rieder et al. (1998) suggested to use the term “illite” as a series name. The composition of illite differs from dioctahedral mica muscovite in having different degrees of heterovalent ($Al^{3+}$ for $Si^{4+}$ in the tetrahedral sheet as well as $Mg^{2+}$ and $Fe^{2+}$ for $Al^{3+}$ in the octahedral sheet) and homovalent ($Fe^{3+}$ for $Al^{3+}$) substitutions. The different chemical compositions were found to reflect diverse geogenetic environments, such as hydrothermally altered igneous rocks (Środoń et al., 1992), shales and mudstones (Lindgreen et al., 1991).

A high-quality structure refinement of illite is still missing, but the most common polytype seems to be $2M_1$ (Brigatti et al., 2006).

According to Köster (1982), general formulae of illite and muscovite are $K_{0.7}M^{+}_{0.1}(Al, Fe^{3+})_{1.7}(Mg, Fe^{2+})_{0.3}[Si_{3.5}Al_{0.5}O_{10}(OH)_2]$ (illite) and

$KAl_2[AlSi_3O_{10}(OH, F)_2]$ (muscovite).

The layer charge of illite due to tetrahedral and octahedral substitutions is between 0.6 and 0.9 (Bailey et al., 1986), charge-balanced by $K^+$ as interlayer cation. The size, charge, and coordination number enables potassium to fit tightly into the hexagonal ring of oxygens of the adjacent tetrahedral sheets. This arrangement gives rise to a strong interlocking ionic bond, which holds the individual layers together and prevents hydration of the interlayer cation, imparting non-swellability of the structure.

Illite is identified by its characteristic XRD rational basis reflections series, with d(001) at 10 Å as main peak (Brindley and Brown, 1980). The FWHM value of this reflection is known as “Kübler index” (Kübler, 1964) and serves as indicator of diagenesis and low-temperature metamorphism in different geological environments (Guggenheim et al., 2002).

For the distinction of cis-vacant and trans-vacant illite, Bailey (1984) and Drits et al. (1984) have established a relationship between the intralayer shift (i.e., the displacement along a* between two adjacent 2:1 layers and octahedral site size (Bailey, 1984). This intralayer shift is larger than the theoretical value (1/3a*) for trans-vacant illite, allowing the trans- or cis-vacant structures to be identified by XRD. Also the higher dehydroxylation temperature of cis-vacant illites gathered by thermal analysis is employed to distinguish cis-vacant from trans-vacant illite varieties (Drits et al., 1995).

### 2.2.3 Smectite

Smectite is a group name comprising dioctahedral and trioctahedral 2:1 layer silicates with a layer charge between 0.2 and 0.6 per formula unit (FU) or half unit cell and which contain hydrated exchangeable cations (Martin et al., 1991; Guggenheim et al., 2006).

Smectites are of widespread occurrence in diverse geological settings, formed mainly by hydrothermal alteration or by weathering of volcanic tuffs and ashes. Sedimentary rocks with minable smectite contents are known as bentonites (Jasmund and Lagaly, 1993).

Smectites are usually characterized by a complex chemical composition due to various isomorphous substitutions within the tetrahedral and octahedral sheet (Grim, 1968; Drits, 2003). The most common smectite-group mineral is montmorillonite, which is dioctahedral. The crystal structure and swelling behavior of montmorillonite was first described by Hofmann et al. (1933). Montmorillonite shows distinct differences in chemistry, octahedral sheet structure, Fe-content, layer charge and charge location. The chemical variety is expressed by the general chemical formula $M^{+}_{x}(Si_{4-y}Al_{y})[(Al, Fe^{3+})_{2-z}(Mg, Fe^{2+})_{z}]O_{10}(OH)_{2}$, with x being the layer charge, which ranges from 0.2 to 0.6; x=y+z and y<<z. $M^{+}$ represents the common interlayer cations $Na^{+}$, $Ca^{2+}$, or $Mg^{2+}$.

Emmerich et al. (2009) and Wolters et al. (2009) proposed a classification for the unambiguous description of smectites based on five structural features: (1) identification as dioctahedral or trioctahedral; (2) layer charge; (3) charge distribution between tetrahedral and octahedral sheets; (4) cation ordering within the octahedral sheet; and (5) Fe content.

Most of the technological uses of smectite are related to reactions that take place in the interlayer space. $Na^{+}$, $Ca^{2+}$, and $Mg^{2+}$, which balance the negative charge arising from isomorphous substitutions in the tetrahedral and octahedral sheet, are commonly hydrated and exchangeable. Hydration properties of the interlayer cations depend mainly on vapor pressure and electrolyte concentration of the surrounding solution. Increasing pressure or decreasing electrolyte concentration leads to the formation of hydration shells with 0, 1, 2, or 4 water layers, which influence the basal spacing of the silicate layers. Reported d(00*l*)-values ranges from 10-10.5 Å for the dehydrated state, 11.8-12.4 Å for 1 water layer, 14.5-15.5 for 2 water layers, and 19-20 Å for 4 water layers. The specific d(00*l*)-values of a given interlayer cation depend furthermore on layer charge and charge distribution (Jasmund and Lagaly, 1993).

Smectites are identified by their characteristic XRD rational basis reflection series, which depend primarily on the interlayer properties in the above-mentioned way. Different treatments of samples from oriented preparation lead to diagnostic changes of the (00*l*)-peaks, as further described in Section 4.2.3. The position of the (060)-peak enables the distinction between the dioctahedral and trioctahedral types, as dioctahedral smectites have (060)-reflections in the range of 1.49-1.52 Å, whereas trioctahedral smectites show somewhat higher values between 1.52-1.55 Å (Hofmann and Weiss, 1968).

Due to turbostratic disorder, XRD measurements of smectites are not sensitive to gather information on cation distribution. Drits et al. (1995) provided structural insights of the octahedral sheet of dioctahedral smectites by investigating the thermal stability of cis-vacant and trans-vacant varieties. A further valuable tool to obtain insight of the cation distribution is provided by infrared spectroscopy (Petrick, 2007; Gates, 2008).

### 2.2.4 Illite-smectite mixed-layer minerals

As described in Section 2.1.2, illite-smectite is a mixed-layer mineral, the crystals of which consist of interstratified illite and smectite layers.

The origin of I-S via transition of smectite to illite is taken for granted within the discipline of clay mineralogy, but the transition mechanisms are still under debate (Cuadros and Altaner, 1998; Stixrude and Peacor, 2002; Lanson et al., 2009).

Two main mechanisms are discussed for the smectite to illite transition: solid-state transformation and dissolution-precipitation. The first mechanism (Shutov et al., 1969; Hower et al., 1976) involves illitization in the solid state, with a gradual layer-by-layer replacement of smectite by illite. The second mechanism involves complete dissolution of smectite followed by precipitation of I-S or illite under major changes in structure and texture. Regarding the precipitation-dissolution mechanism, two versions have been described: The progressive dissolution of smectite in a reaction front on a very small scale with in-situ precipitation of the phase (Ahn and Peacor, 1986a) as well as the initial dissolution of smectite followed by progressive coarsening of illite governed by an Ostwald ripening process (Eberl and Środoń, 1988; Eberl et al., 1990).

Cuadros and Altaner (1998) have pointed out that in many studies the solid-state transformation mechanism was proposed for materials with low permeability such as bentonites (Altaner et al., 1984; Środoń et al., 1986; Inoue et al., 1990), shales (Bell, 1986), and mudstone (Lindgreen et al., 1991). Conversely, the dissolution-precipitation mechanism was proposed for environments of higher permeability, such as hydrothermal systems (Yau et al., 1987; Inoue and Kitagawa, 1994).

However, there is consensus that I-S mixed-layer minerals represent an intermediate stage, a transition of smectite to illite occurring in different geological environments (e.g., shales, heated by dike intrusion, during burial diagenesis with increasing depth, or in hydrothermally altered zones around ore bodies) in which metastable, highly imperfect, and disordered layered components transforming to more homogeneous, well-ordered, defect-free phases (Moore and Reynolds, 1997). These changes are driven by time, increasing temperature and pressure, fluid movements, as well as shearing stress associated with tectonism and are most clearly expressed in the transition from argillaceous sediments to metamorphosed pelitic rocks (e.g., Lee et al., 1985; Grizelj et al., 2011).

Attempts to explain the transition mechanisms are inextricably linked with the crystallographic nature of illite and smectite in I-S, mainly described at present by two competing models: The MacEwan crystallite model and the fundamental particle model, as illustrated in Fig. 2.2.

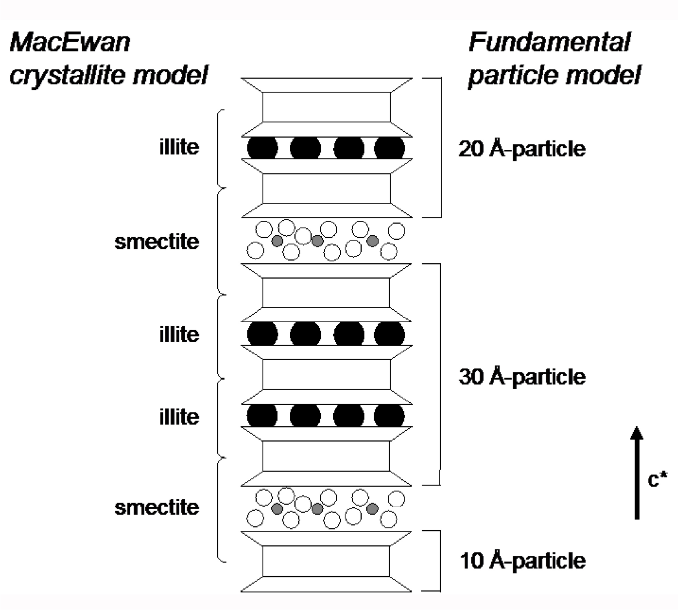

Figure 2.2: Comparison of the MacEwan crystallite model and the fundamental particle model. Modified after Altaner and Bethke (1988).

The MacEwan crystallite model is deduced from Markov theory (Hendricks and Teller, 1942; MacEwan, 1956; 1958) and envisions layers of illite and smectite as intimately interlayered, stacked either randomly or regularly, into a fixed sequence, which acts as a coherent scattering unit for X-rays. The MacEwan crystallite model regards I-S as relatively large crystallites comprising both illite and smectite of 5 to 15 layers as determined from XRD studies of dispersed samples (Reynolds and Hower, 1970; Reynolds, 1980). The division between layers is through the center of the octahedral sheet. The transition from a smectite to an illite layer is thought to be a solid-state transformation under preservation of morphology by in-situ chemical and structural modifications (Moore and Reynolds, 1997).

Nadeau et al. (1984a; 1984b; 1984c) and Nadeau (1985) proposed a new hypothesis regarding the nature of mixed-layer minerals based on XRD and TEM studies, which is the fundamental particle model. The authors showed that dispersion of sodium-saturated I-S caused the separation of I-S crystallites into exceedingly thin “fundamental particles” whose thickness along c* was 10 Å or small integer multiples. Hence, the particles are considerably thinner than the crystallite sizes of about 100 to 200 Å commonly inferred from XRD studies.

Nadeau and co-workers proposed that the interfaces between fundamental particles can hydrate so that random aggregation of fundamental particles occurs during sample preparation for XRD analysis, which then behave like MacEwan crystallites (Altaner and Bethke, 1988). According to this model, interlayers internal to the fundamental particles act as illite, and the hydrous basal surfaces between those particles form smectite interlayers. The authors assumed that there are no smectite interlayers in a fundamental particle, but that its basal surfaces are smectitic, i.e., there is one smectite interlayer per fundamental particle as each surface counts as one half of the smectite interlayer (Środoń et al., 1992). Nadeau et al. (1984b; 1984c) inferred that the fundamental particles are themselves independent, primary crystals, not fragments from larger crystals. This model suggests that the particles are not grown together epitactically. They are simply stacked together into a group of particles, but in close enough physical contact to act as coherent scattering units, giving rise to yield "MacEwan-like" (averaged over $10^6$ to $10^9$ crystallites) XRD patterns by the process of "interparticle diffraction".

On the other hand, many TEM studies have shown that I-S occurs as large, extended "megacrystals" (Ahn and Peacor, 1986a). The term "megacrystal" was used by the authors to describe a continuous crystalline array, forming a matrix for non-phyllosilicates in shales. Grinding such crystals in order to prepare samples for XRD may therefore cause cleavage along interlayers, giving rise to small particles, which may be as small as "fundamental particles" (Ahn and Peacor, 1986b). Reynolds (1992) reported two types of artifacts that could be produced from XRD sample preparation: The first is the modification of the stacking sequences that control ordering in the organization of unit cells or unit layers along the c* direction. The second could change the order of the stacks with respect to each other, introducing or increasing the incidence of turbostratic defects.

If fundamental particles occur in nature and are not merely an artifact of sample preparation, the I-S transition mechanism of direct precipitation is more consistent with the formation of fundamental particles as primary crystallization products rather than a rearrangement of the structure of precursor minerals. Indications of the dissolution-precipitation model are changes in morphology and polytypism as the proportion of illite increases (Moore and Reynolds, 1997).

Thus, individual fundamental particles are taken as primary crystallization products rather than secondary particles disaggregated from larger crystals during sample preparation

Nadeau (1998) stated that "the new paradigm causes confusion because a coherent one-dimensional arrangement of layers is no longer a mixed-layer mineral."

# 3 Materials

Clay is an abundant raw material, which has an enormous variety of applications and properties that are largely dependent on their mineral structure and composition, but also on other additional factors: The non-clay mineralogical composition, the presence of organic material, the type and amount of exchangeable ions and soluble salts, as well as the texture (Grim, 1950).

The uniqueness of raw clay composition, which imparts the specific material properties, is the result of geological processes, leading to the formation of the deposit.

This Chapter gives a brief overview of the samples chosen for this study, their geological settings as well as the procedure of sampling and preparation.

## 3.1 Paper kaolins

As starting material, three sedimentary kaolin samples with various degrees of brightness were chosen. The determination of brightness required materials with particles sizes <25 µm, which were obtained by wet sieving.

In order to elucidate the influence of Fe on kaolin brightness, two kaolins (LA540 and B4915) with nearly the same brightness, but different $Fe_2O_3$ contents, were selected. A third kaolin (B4914) was chosen for its different brightness at similar $Fe_2O_3$ content, compared to sample B4915. Table 3.1 lists the phenomenological description of the three kaolins and their processing properties-related parameters in terms of brightness and Fe content.

All kaolins were supplied by AKW Amberger Kaolinwerke Eduard Kick GmbH & Co. KG, Hirschau, Germany.

Table 3.1: Phenomenogical description and processing properties-related parameters of the paper kaolins.

| Sample | LA540 | B4914 | B4915 |
|---|---|---|---|
| Color | cream white | light cream white | cream white |
| Average aggregate size [µm] | <25 µm | <25 µm | <25 µm |
| Brightness R457 [%] | 68.2 | 76.5 | 67.9 |
| $Fe_2O_3$ [%] | 1.46 | 0.78 | 0.95 |

### 3.1.1 Geological setting

The kaolins investigated in this study originate from sedimentary kaolin deposits of the region of Hirschau-Schnaittenbach in the South-East of Germany. The kaolins occur as Mid Bunter age beds (Figure 3.1), which have been kaolinized in situ from arkosic sandstones, formed from Variscan Orogeny granite and gneiss parent rocks (Bauberger and Haunschild, 1960).

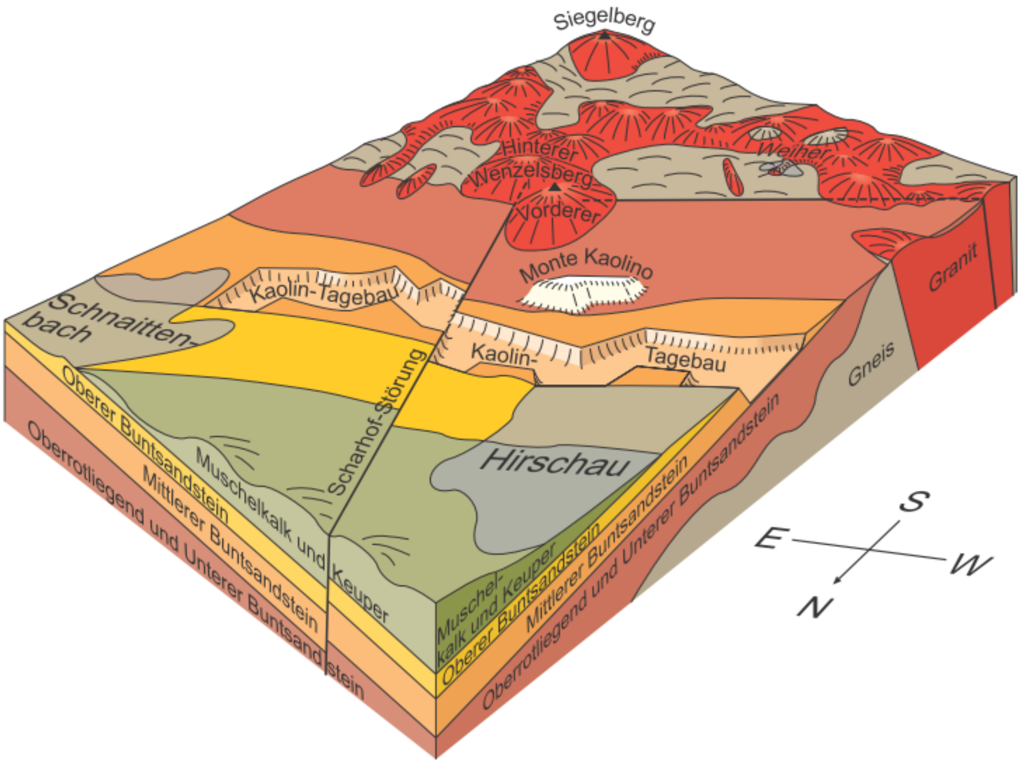

Figure 3.1: Block diagram illustrating the vicinity of the deposition area in the Mid Bunter age beds to the source area (granite and gneiss). The distance between Hirschau and Schnaittenbach is about 4 km. www.geotope.bayern.de.

The kaolinization had not occurred quantitatively, which means that kaolinite and quartz coexist with largely unaltered feldspar (mainly microcline), micas and illite. The feldspar content increases from Schnaittenbach to Hirschau, whereas the kaolinite content decreases (Köster, 1974).

A change in mineralogy was also observed for the East-West strike direction. Kroll and Borchert (1969) reported an increase of the kaolinite content for samples <63 µm for the western part of the deposits from 69% up to 86% in the eastern part, with decreasing quartz and feldspar content. The kaolinite content of the raw material varies from 10% (western part) to 25% (eastern part) with a simultaneous shift of grain-size distribution toward finer fractions (Henseleit and Huber, 2002). The Hirschau-Schnaittenbach dip shows an inhomogeneous distribution profile of kaolinization, having its maximum of about 60 m near the northern zone of the middle of the dip (Köster and Tillmann, 1975). Currently, about 700,000 tons per year of kaolin are mined (Haus, 2002).

### 3.1.2 Sampling technique and sample preparation

The kaolin mining district of Hirschau-Schnaittenbach is characterized by significant quality differences, so selective mining and segregation are necessary.

The usual practice is to mine a particular quality of kaolin and transport it to a stockpile, which is made up of similar brightness-based qualities. Afterwards, the kaolin is subject to wet processing. The main processing steps will be reported briefly in the following. A more comprehensive flow sheet for kaolin wet processing is given, e.g., by Murray (2007).

In the first step of wet processing, the kaolin is blunged and dispersed into a slurry by mixing it with water and a small percentage of a chemical dispersant. The solids fraction in the blunger is about 0.4. The chemical dispersant (0.2-0.6% of sodium polyacrylate based on the dry weight of the kaolin) is necessary in order to prevent flocculation of the dispersed particles.

The next step is to remove the grit with the help of hydrocyclones. Grit refers to the fraction coarser than 25 µm and usually comprises quartz, feldspar, and a suite of heavy minerals (Murray, 2007). After degritting, the kaolin slurry is separated into a coarse and a fine fraction, again by hydrocyclones. The coarse fraction may be delaminated or is filtered and dried to produce filler clays. The fine fraction is passed through a high intensity magnetic separator (SC-HGMS), which removes discrete Fe and Ti minerals.

The following floc and leach step consists of acidifying and flocculating the slurry at a pH between 2.5 and 3 under addition of sulfuric acid and sodium thiosulfate, which dissolves some of the kaolin-staining Fe compounds by reducing ferric iron to ferrous iron. The ferrous iron then combines with the sulfate anion to form soluble Fe sulfate.

In the following filtration step, the slurry is pumped to frame pressure filters to remove water and the soluble $FeSO_4$. After filtration, the filter cake is redispersed and pumped to a drier where it is dried for bulk or bag shipment.

After wet processing, the kaolins investigated in this study were subdivided into two parts: One part was investigated in the current state after wet processing, whereas the second part was subject to microbiological refinement.

The microbiological refinement of the kaolin samples with *Shewanella putrefaciens* was carried out at the Helmholtz Center for Environmental Research (UFZ, Leipzig, Germany). A detailed description of the various treatment steps is given by Beyer et al. (2011), briefly reported here.

*Shewanella putrefaciens* (formerly *Pseudomonas putrefaciens*) is a Gram-negative bacterium, which is ubiquitous in marine and freshwater environments (Lee et al., 1977) and sediments (Myers and Nealson, 1990). *Shewanella* species have been shown to play an important role in the turnover of organic matter coupled to facultative anaerobic respiration, using, i.a., Fe- and Mn-bearing species as terminal electron acceptors (see Section 1.3.5 and the citations therein). As *Shewanella putrefaciens* is capable to reduce both, oxide-bound Fe as well as silicate-bound Fe (Kostka et al., 1999b; Dong et al., 2003a), the microorganism is believed to be a promising candidate for the bioleaching of the kaolins chosen for this study.

The bacterial strain of *Shewanella putrefaciens* was taken from the cultured collection of the UFZ, internally referenced as B622/T. For biomass production, the microorganism was cultivated in a growing medium under aerobic conditions, containing lactate as electron donor (Table 3.2). For each batch, 100 mL of the growing medium were transferred to a shaking flask and cultures were shaken (135 rpm) and incubated at 30 °C at a pH of 7.2. The bacteria were harvested and washed with 10 mM NaCl solution just before being used in the experiments.

Table 3.2: Composition of the microbiological culture medium for the strain maintenance and biomass production of *Shewanella putrefaciens*.

| Substance | concentration [g/L] |
|---|---|
| Meat extract * | 1 |
| Yeast extract ** | 2 |
| Peptone (pancreatic) | 5 |
| NaCl | 5 |
| Mg-L-lactate | 10 |
| Agar-Agar | 15 |

* BioChemika for microbiology (Sigma-Aldrich, product no. 70164, Charge 0001442576)

** Fermtech (Fa. Merck, product no. 111926, Charge VM 135126 002)

The composition of the reducing medium (Table 3.3) was chosen according to Bonneville et al. (2006). In order to enhance the bioreduction potential, the electron-shuttling compound AQDS (anthraquinone-2,6-disulfonate) was added as suggested by Royer et al. (2002a). All substances were suspended in tap water to simulate the local conditions of the processing plant. A water chemistry analysis can be found in the Appendix (Chapter 9, Table 9.1). Then, 35 g of each kaolin sample (three batches per sample) were dispersed in 200 mL of the reducing medium under constant stirring. Samples were taken after seven days, centrifuging the suspensions for 120 min at 3100xG. The supernatants were removed and the respective kaolin pellets were resuspended in 100 mL tap water. Afterwards, the suspensions were shaken for 24 h. The washed suspensions were again centrifuged (10 min at 9500xG) and the supernatants were discarded. The kaolin deposits were dried at 60 °C for 24 h and afterwards ground in a ball mill for 1.5 min with a frequency of 30 rpm.

The control sample (B4915 K) was treated identically, except that the reducing medium was free of *Shewanella putrefaciens*.

Table 3.3: Composition of the $Fe^{3+}$-reducing medium for the microbial refinement of kaolins with *Shewanella putrefaciens*.

| Substance | concentration [g/L] |
|---|---|
| Mg-L-lactate | 1.28 |
| KCl | 0.42 |
| $Na_2SO_4$ | 1.99 |
| $NH_4Cl$ | 1.07 |
| $CaCl_2 \times 2\ H_2O$ | 0.18 |
| $MgSO_4 \times 7\ H_2O$ | 0.24 |
| AQDS | 0.02 |

## 3.2 Ceramic clays

Two sedimentary clays (W1 and W2) from the Westerwald area (Germany) were investigated. The clays were supplied by Sibelco Deutschland GmbH.

According to industrial assessment standards, W1 and W2 are characterized by an identical chemical composition and particle size distribution, but show different working properties in terms of extruding behavior (generally also referred as “plasticity” according to Göhlert and Uebel, 2007) and making moisture content. A phenomenogical description of the two samples and their processing properties is given in Table 3.4.

Table 3.4: Phenomenogical description and processing properties-related parameters of the ceramic clays.

| Sample | W1 | W2 |
|---|---|---|
| Color | gray | cream colored |
| Average aggregate size of the starting material in pit-moist state | 1-1.5 cm | ≈0.5 cm |
| Dispersibility in water | easy to disperse | more difficult to disperse under formation of a “sticky” sediment |
| Processing behavior | plastic | less plastic |
| - extrusion | 37 bar | 23 bar |
| - making moisture content | 28.0% | 26.5% |

### 3.1.3 Geological setting

Clays (W1 and W2) from the Westerwald area were taken from adjacent deposits, about 10 km north of Montabaur: W1 from the clay deposit “Geigenflur” and W2 from the clay deposit “Petschmorgen” (Figure 3.2). Both deposits have formed by decomposition and weathering during the Tertiary (Eocene/Oligocene) on Devonian slates (Rhenish Massif). During the Miocene, the area experienced volcanic activity. The warm volcanic waters ascending along the zones of weakness caused the alteration of volcanites and probably led to the formation of smectites (Kromer, 1980).

The largest quantity of the Westerwald clays is exported to Italy for use in ceramic tile. They are also used in manufacture of heavy clay products including brick and tile. About 4.5 million tons are processed annually (Saller, 1999).

### 3.1.4 Sampling technique and sample preparation

Five tons of each of the freshly-mined clays W1 and W2 were homogenized in a processing plant. The water content after mining and homogenization was about 12% for both clays. Water (tap water from the community of Wirges, Westerwald) was added to increase the moisture content to 15% with respect to the final bulk mass. Thereafter, the clays were homogenized again. This large amount of sample was taken to ensure representative sampling from the quarry and to realize a clay maturation experiment, discussed by Menger-Krug et al. (2008) and Petrick et al. (2008). For the experiment, a part of the batch was prorated to 15 buckets of 20 kg each. For the mineralogical characterization, each sample was reduced to 500 g by subsampling in terms of coning and quartering, and then using a rotating sample divider (Crosby and Patel, 1995).

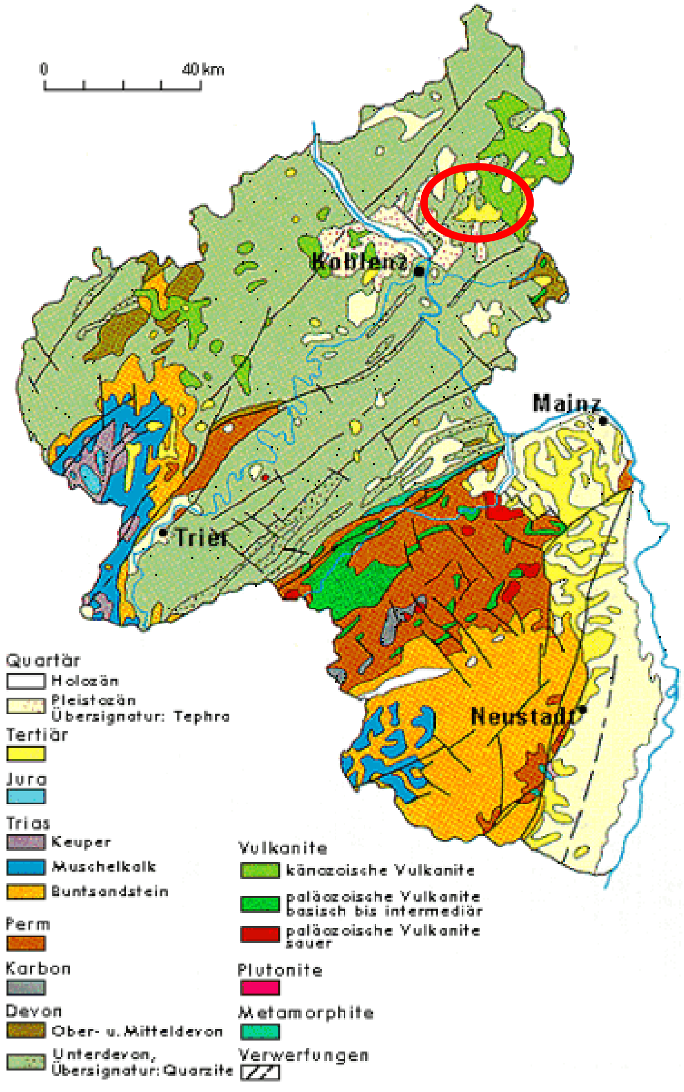

© Geologisches Landesamt Rheinland-Pfalz, Mainz 1993

Figure 3.2: Geological setting of the deposits “Geigenflur” (W1) and “Petschmorgen” (W2). The distance between the deposits is about 5 km. www.lgb-rlp.de.

## 3.3 Sample overview

Table 3.5 shows the samples employed in this study: Three kaolin samples, with various Fe contents and brightness values (LA540, B4914, and B4915), supplied by AKW- Amberger Kaolinwerke Eduard Kick und Co., as well as two samples of ceramic clays, W1 and W2, with different plasticity, supplied by Sibelco Deutschland, formerly WBB Fuchs.

For all samples, several grain-size fractions were gathered and comprehensively investigated by different analytical methods, as described in the next Chapter.

Table 3.5: List of samples: starting material and the respective material after different treatment steps.

| Sample | Specification |
|---|---|
| LA540 | paper kaolin |
| LA540 MO | paper kaolin after microbial treatment |
| B4914 | paper kaolin |
| B4914 MO | paper kaolin after microbial treatment |
| B4915 | paper kaolin |
| B4915 MO | paper kaolin after microbial treatment |
| B4915 K | paper kaolin, control |
| W1 | ceramic clay, plastic |
| W2 | ceramic clay, less plastic |

# 4 Methods

This chapter summarizes the analytical methods applied to elucidate the processing properties of paper kaolins and ceramic clays. The chapter is subdivided in two parts. The first part deals with physical-chemical methods, on which the industrial standard testing procedures primarily rely. The second part is dedicated to mineralogical methods with focus on XRD profile fitting.

## 4.1 Physical-chemical methods

### 4.1.1 Brightness

Determination of brightness is widely used in paper industry as an indicator of whiteness (Bajpai, 2005) and provides a convenient way of evaluating optical properties of pulps during bleaching operations (Erb and Krystek, 1996).

In literature, the terms brightness and whiteness are often used synonymously in order to describe the phenomenon of remission of light scattered from a material (Bristow, 1994). Both terms rely on the same measuring principle by means of spectrophotometry, but with different measuring geometries (Gysau, 2006).

Brightness indicates a measure of percentage of reflectivity at an effective wavelength of 457 nm and a width of 44 nm compared to a standard, which is assigned 100% brightness. Whiteness or color is a value measured over the visible spectrum (400-700 nm). The preferred whiteness of kaolins for paper coating is blue-white rather than cream-white. However, most kaolins are cream-white and this is referred to as the yellowness factor or b-value in *Lab* color values (Chandrasekhar and Ramaswamy, 2006; Murray, 2007).

The most common method in paper industry is the determination of brightness according to ISO 2469 and ISO 2470.

ISO 2469 details the equipment and procedure for brightness measurements. ISO 2470 is the current international standard for measuring the brightness of white or nearly white pulp, paper, and board.

In the present study, brightness was determined by means of spectrophotometry according to ISO 2470. This measuring method is called brightness R457 or ISO brightness R457 (Bristow, 1994), whereas the remission value R stands for the determination of brightness without UV radiation, prompting the fluorescence of optical brighteners. The advantage of narrowing the spectral observation region is that changes in remission during bleaching are more pronounced in the short-wavelength “blue-colored” range (Anonymous, 2001).

Spectrophotometry is an appropriate tool to numerically objectivize subjective human’s color perception in that it deals with wavelengths mainly in the visible range, extending somewhat into adjacent ranges of near-ultraviolet and near-infrared. The light is dispersed into its component wavelengths by a grating, and only a discrete wavelength is focused on the sample (Harris, 1991). Common application of spectrophotometers is the measurement of light absorption, but they can be designed to measure diffuse or specular reflectance, like for the purpose of whiteness measurements.

A spectrophotometer measures the intensity of light as a function of wavelength and compares the intensity of light interacting with a sample (I) to the intensity of light interacting with a reference sample ($I_0$). The absorbance A is the ratio $I_0/I$ and expresses the amount of absorbed light according to Lambert-Beer’s law:

$$A = \frac{I_0}{I} \qquad \text{(eq. 4.1)}$$

**Equipment**

Analytical balance, stopwatch, brush, PE-shovel, mill (IKA A 10), thermostatically controlled drying oven, pressing mold, pelleting press (Effbe Type MH-F-100), double-beam spectrophotometer from Datacolor (Elrepho 450x), data processing software PP 81

**Chemicals**

$BaSO_4$ (Merck)

**Brief description**

Pellet preparation: 10 g of the oven-dried sample (60 °C for kaolin slurries and 105 °C for powdered samples brought to constant mass) were milled for 3 min at 25000 rpm. The powdered sample is filled in a pressing mold and a pressure of 0.12 N/mm$^2$ is applied for 10 s to obtain a pellet of 5-7 mm thickness.

Spectroscopic measurements: Illuminating conditions were chosen to be diffuse with a 0° viewing geometry (d/0 in geometric designation). Light source is pulsed xenon, filtered to an effective wavelength of 457 nm. Color coordinates in terms of hue, degree of saturation, and shadow (e.g., Lins and Blatzek, 1980) were measured according to DIN 6164 with the standard illuminant D65 against the pre-calibrated barium sulfate standard (DIN 5033-9). The determined color coordinates were plotted in the color chart system defined according to DIN 6164 with help of the data processing software, giving rise to brightness values.

**Error**

Due to orientation effects of anisometric clay mineral particles, the pressure during pellet manufacturing has to be strictly abided. Higher pressure leads to glossier surfaces, which, in turn, leads to greater brightness values.

### 4.1.2 pH and electrical conductivity

Working properties are closely coupled to pH and electrical conductivity of clay suspensions (Penner and Lagaly, 2001), as pH and soluble salt concentration influence the aggregation behavior of clay mineral particles. Besides pH, the rheological behavior of clay suspensions is influenced by a multitude of factors, such as phase content, e.g., presence of Fe (oxy-hydr)oxides, particle morphology, crystallinity, or solid content (Jasmund and Lagaly, 1993).

Despite the multitude of influences, the following general tendencies have been observed concerning the borderline cases of kaolinite and bentonite dispersions: Up to pH 7, kaolin suspensions show an increasing yield point with increasing pH due to the formation of face(-)-to edge(+)-contacts. Above pH 7, the yield point drops and kaolin suspensions maintain a low viscosity even with increasing solid content. Bentonite dispersions have different flow behavior in dependency of the predominant ion species. Due to the destruction of the card-house structure, Na-bentonites show a strong decrease in viscosity between pH 5 and 7, whereas Ca-bentonites decrease strongly already between pH 3 and 5. Above pH 8, Ca-bentonites show a strong increase of the yield point, leading to increased viscosity (Jasmund and Lagaly, 1993).

Aside from working properties, the survey of pH of the clay suspensions is indispensable for pH-dependent characterization methods, such as CEC measurements, whose values increase with increasing pH (Lagaly, 1989; Steudel, 2008).

**Equipment**

Analytical balance, spatula, 1 L PE-bottles, centrifuge (Multifuge 3S-R Heraeus/Kendro), graduated centrifuge flasks, stopwatch, magnetic stirrer, KCl electrode (WTW SenTix 81), electrode for electrical conductivity measurement (WTW TetraCon 325)

**Chemicals**

Calcium chloride ($CaCl_2$), deionized water

**Brief description**

The pH was determined on the basis of DIN 19261 and DIN 38414-4 for six replicates. 40 ml of a 0.01 M $CaCl_2$ solution was mixed with 4 g of the respective bulk clay material, dried at 40 °C for 24 h. The suspensions were shaken in PE-bottles for 24 h. Centrifugation was carried out at 4350*g, T=20 °C for 25 min. Afterwards, pH was determined with a KCl electrode (WTW SenTix 81) in the removed supernatant under stirring. Electrical conductivity was measured simultaneously (WTW TetraCon 325). The values were read out after 10 min.

**Error**

Reproducibility is affected by several parameters. Preliminary tests showed that pH decreased with time until the system reached equilibrium in dependency of $p_{CO2}$ (Henry's law). Read out times <10 min led to larger pH values up to 1.5 log $[H^+]$. In order to avoid matrix effects, pH was measured in the supernatant.

### 4.1.3 Soluble salt concentration

The term "soluble salts" covers a range of anions and cations present in clays and soils in either crystallized solid form or in dissolved form in the pore solution (Pansu and Gautheyrou, 2006). The concentration of water-soluble salts by means of anions ($Cl^-$, $SO_4^{2-}$) was determined from six replicates by ion chromatography. This analytical method provides simultaneously the separation of mixtures in a single-step process into its individual components and the quantitative estimate of each constituent (Scott, 1995). The separation technique is based on electrostatic forces between solute ions in the mobile phase, which are attracted to opposite-charged species in the stationary phase, usually a resin.

**Equipment**

Analytical balance, disc mill or mortar, thermostatically controlled drying oven, 1 L beaker, laboratory stirrer (Ika RW 28 W), folded filters, vacuum filtration equipment (Schleicher and Schuell MV050), ion chromatograph (Dionex DX-120)

**Chemicals**

Single-element standards (Merck), deionized water

**Brief description**

Preparation of the eluate was carried out according to DIN 38414-4. 200 g of the representative mass constant sample (dried for 24 h at 60 °C) was extracted with 400 ml deionized water by stirring the suspension for 30 min at 500 rpm. Afterwards, the suspension was centrifuged for 1 h at 4200*g. The supernatant was filtrated passing it through a vacuum filtration device with a pore size of 0.45 µm. Then, the filtrate (mobile phase) was analyzed by means of ion chromatography with a dilution factor of .5.

**Error**

Sample aggregation can lead to an incomplete dissolution of soluble salts. Masking of peaks due to large concentrations of one species.

### 4.1.4 Plasticity

As stated by Göhlert and Uebel (2007), there is neither a reliable definition nor a reliable method in ceramics to determine the plasticity. The term plasticity is also referred to as extrudability, ductility, consistency or workability. Hence, there is no generally acknowledged method or measuring device to specify the plasticity of ceramic masses. Among the numerous specific methods, a measuring strategy has to be established based on the material under investigation.

In terms of rheology, ceramic clays hold a special position between ideal elastic and ideal plastic masses, as they exhibit elastic as well as plastic behavior.

Main factors accounting for plasticity of clays are the moisture content, soluble salt concentration, pH, grain-size distribution, mineralogical composition, and fabric (Section 1.4.3).

In the present study, two indicators of plasticity were gathered by determining the making moisture content and the extrusion behavior.

*Making moisture content*

The making moisture content, also referred to as mixing water content, was measured according to Pfefferkorn (1924) with a deformation ratio of 2.0 (Vogt and Vogt, 2004). The Pfefferkorn method is based on the determination of the water content, which is required to cause a definite deformation of a cylinder-shaped test body on the falling of a mass-standardized plate. Depending on the molding of the test body (e.g., extrusion, pultrusion or punching), common deformation ratios are 3.3, 2.5, and 2.0, which means a compression to 70%, 60%, and 50% of the original height, respectively (Schmidt, 1979).

The making moisture content was determined according to equation 4.2:

$$p = \frac{(m_1 - m_2)}{m_2} \cdot 100 \qquad \text{(eq. 4.2)}$$

where p is the making moisture content [%], $m_1$ [g] the mass of test body in moisture state, $m_2$ [g] the mass of test body after drying at 110 °C for 24 h.

**Equipment**

Plasticimeter M-1192 (Feinwerktechnik Andreas Saal), forming tool (Carl Jäger Tonindustriebedarf), analytical balance, drying oven, weighing bottles with cap, crucible tong, spatula, desiccator

**Chemicals**

none

**Brief description**

Three cylinder-shaped samples were taken from a part of an extruded clay body (240x140x140 mm). Then, each sample was placed on the plasticimeter to measure the deformation ratio after the impact from a falling plate (mass of 1.2 kg, height = 1.85 m). Afterwards, the making moisture content was determined gravimetrically by drying the sample at 110 °C for 24 h.

**Error**

Storage and sampling technique have a strong influence on results, as the extruded clay masses should be prevented from humidity loss and deformation during transport from the processing plant to the laboratory. In order to avoid anisotropy effects, samples should be taken either parallel or perpendicular to the extrusion direction.

### *Extrusion behavior*

The extruding behavior was determined measuring the radial pressure in a trapezoidal die with a laboratory extruder (Göhlert and Uebel, 2007). The applied pressure needed for extrusion is indirectly related to the swellable clay content, as these components impart plasticity to the clay body. The greater the amount of swellable components, the greater is the pressure required for extrusion.

In order to be considered in the test series, the extruded clay mass must be, at its surface, free from irregularities, such as small-scale fractures ("shark skin") or large scale fractures ("dragon teeth") (Ramamurthy, 1986; Kulikov and Hornung, 2001).

**Equipment**

Balance, laboratory extruder (VAR 50A/50 ECT Händle) with trapezoidal die (22 x 20 x 15 mm), counterflow intensive mixer (Eirich R02), moisture analyzer (Sartorius NA50XX20A)

**Chemicals**

Deionized water

**Brief description**

In order to obtain a plastic clay mass, deionized water was added according to the making moisture content determined by the Pfefferkorn method, under simultaneous homogenization of the material with the help of a counterflow intensive mixer. The water content was controlled gravimetrically with a moisture analyzer. Afterwards, 2 kg of each plastic clay mass was given to the extruder, measuring the pressure in a trapezoidal die during the material shaping process.

**Error**

Values have to be critically evaluated, as the amount of water, added to gain a plastic clay body, exerts a strong impact on extrusion behavior.

## 4.2 Mineralogical methods

### 4.2.1 Water content

As samples interact with the atmospheric conditions of the surrounding, determination of the water content enables calculation of dry sample mass as reproducible reference value for all related properties like grain-size distribution and cation exchange capacity.

The determination of the mineralogical water content ($w_{min}$) was carried out gravimetrically, drying the samples at temperature of 105 °C. The temperature is sufficiently high to eliminate adsorbed water molecules and sufficiently low not to cause loss of organic matter and structurally bound water in layer silicates (Pansu and Gautheyrou, 2006).

The water content $w_{min}$ [%] was calculated according to equation 4.3:

$$w_{\min} = \frac{m_1 - m_2}{m_1 - m_0} \cdot 100 \qquad \text{(eq. 4.3)}$$

$m_0$ [g]: mass of the empty weighing bottle with cap ajar heated for a minimum of 2 h at 105 °C and allowed to cool down in a desiccator for 1 h

$m_1$ [g]: mass of the weighing bottle with cap ajar containing the air-dried sample

$m_2$ [g]: mass of the weighing bottle with cap closed and sample after 24 h of heat-treatment at 105 °C cooled in a desiccator for 1 h

**Equipment**

Analytical balance, thermostatically controlled drying oven, weighing bottles with cap, crucible tong, spatula, desiccator containing silica gel

**Brief description**

The determination of the water content was carried out gravimetrically drying 2 g of the disaggregated sample (<2 mm) at 105 °C for 24 h. Sample disaggregation was performed with help of a spatula.

**Error**

After heat-treatment, the weighing bottles should be closed by a cap to avoid moisture intake. Unevenly disaggregated samples can lead to an incomplete loss of moisture. Cooling and weighing times should be perfectly respected in order to keep the temperature-dependent mass error as small as possible. Weighing bottles should not be touched with hands, since fingerprints may change their mass.

### 4.2.2 Grain-size distribution

As stated in Section 1.4.2, grain-size distribution is a very important characteristic for the assessment of raw clay materials. In the present study, grain-size distribution was determined by sedimentation analysis via Sedigraph method (exclusively done for the ceramic clays) and by pipette method. With the latter, various grain-size fractions were gathered for mineralogical investigations. Fractionation of the bulk material is the only way to enrich the clay phases, as the amount of clay minerals increases with decreasing particle size (Jepson, 1984).

The classification of particles was done on the basis of DIN 4022, which relies on the scale proposed by Atterberg (1912). The fractionation classes were defined due to preliminary tests, revealing different grain-size distribution characteristics among the paper kaolins and the ceramic clays. The paper kaolins were subdivided into the following fractions: >20 µm, 2-20 µm, 0.6-2 µm, 0.2-0.6 µm, and <0.2 µm. Fractions obtained from the ceramic clays were: >63 µm, 20-63 µm, 2-20 µm, 0.6-2 µm, and <0.6 µm. For some samples, additional fractions <0.2 µm and <0.1 µm were separated.

Stokes' law for a viscous drag on a sphere (1845) governs every sedimentation analysis and is central to the derivation of settling equations, which relate settling time to particle size (Lagaly, 2006). For sedimentation in a gravity field, the gravity force is included in the calculation (equation 4.4). For sedimentation in a centrifugation field, the centrifugal acceleration is counted in (equation 4.5). In order to consider the non-spherical morphology of clay minerals, the particle size is expressed in terms of equivalent diameter. It is numerically equal to the diameter of a spherical particle having the same density and velocity of fall (e.g., Müller, 2008).

The settling time of a particle in the gravity field is

$$t = \frac{18\eta_0}{(\rho - \rho_0) \cdot g} \cdot \frac{h}{d^2} \qquad \text{(eq. 4.4)}$$

The settling time of a particle in a centrifugation field is given by

$$t = \frac{18\eta_0}{(\rho - \rho_0) \cdot 4r\pi^2 \cdot (R/60)^2} \cdot \frac{h}{d^2} \qquad \text{(eq. 4.5)}$$

with $\eta_0$ being the viscosity of water, ρ the density of the mineral (here, the density of 2.65 g/cm$^3$ of quartz serves as an average value commonly used for clays (Henningsen, 1981)), $\rho_0$ the temperature-dependent density of water, h the settling distance of the particles, and d the equivalent particle diameter. In equation 4.4, g is the gravity force and in equation 4.5, the term $4r\pi^2(R/60)^2$ describes the centrifugal acceleration with r being the radius of the centrifuge rotator and R/60 as rotation per minute. The centrifugation time was calculated according to Tributh and Lagaly (1986b).

In the present study, the paper kaolins were investigated by the pipette technique. As processing properties of ceramic clays depend strongly on grain-size distribution (Winkler, 1954), sedimentation analyses were carried out by means of the pipette technique, and additionally the Sedigraph method.

The Sedigraph method is based on a combination of two physical phenomena: gravitational sedimentation and low energy X-ray absorption (Webb, 2004). A beam of X-rays is collimated into a thin horizontal band to measure the particle mass concentration in a liquid medium. This is done first by measuring the intensity $I_{max}$ of a reference transmitted X-ray beam that has been projected through the liquid medium prior to the introduction of the sample. More X-rays are absorbed by the solid than the liquid. Therefore, the transmitted X-ray beam is attenuated. During sedimentation, as more and more of the larger particles settle below the measurement zone, attenuation diminishes and the intensity of the transmitted X-ray beam increases from $I_{min}$ (starting value of the homogeneous suspension) to $I_{max}$. Calculation of the mass fraction of particles in the measuring zone at time t ($M_t$) is carried out by measuring the transmitted intensities between the two extremes ($I_t$) according to equation 4.6:

$$I_t = I_{\max} \cdot 10^{-kM_t} \qquad \text{(eq. 4.6)}$$

k is the attenuation/extinction coefficient, incorporating variables, as density, thickness, and refractive index of the material. For non-absorbing, i.e., transparent, materials k=0, thus, no attenuation occurs (Lindberg et al., 1994).

By the pipette method samples are directly removed from the suspension using glass pipette, which is U-shaped at the bottom. The amount of solids is determined by drying the pipetted samples, which are weighed out in order to obtain the grain-size distribution (Skopp, 2002). The method applied in this study is strictly speaking a combination of the pipette method according to Andreasen (DIN 66115) and the Atterberg method (not regulated by DIN, Hiltmann and Stribrny, 1998).

For the “combined pipette method”, the sample is withdrawn by a pipette (characteristic of the Andreasen method), but the removal is repeated until the supernatant is apparently clear (characteristic for the Atterberg method). The Andreasen method, in contrast, implies the removal of a defined sample volume, usually 10 ml of the suspension. The use of Atterberg cylinders in the “classical” Atterberg method may be disadvantageous in that coarser particles often plug the outlet valve, leading to their carry over to a finer fraction. This drawback can be overcome using a pipette for the suspension withdrawal.

Standard procedures in clay processing for evaluation of raw clay qualities and grain-size distribution require the use of chemical dispersants (DIN 19683-2), like phosphates or acrylates. The following mineralogical studies were done with regard to microbial processing (Krolla-Sidenstein et al., 2009). For that reason, chemical dispersants were not used in order to avoid affection of metabolic activities of the microorganisms (Liu et al., 1982). In order to gain comparability among grain-size distribution according to industrial standards with those respecting microbial processing, different pathways of sample preparation were followed. Deviations of parameters determined with and without chemical dispersant will be discussed in Section 6.3.1.

**Equipment**

Sedigraph method: X-ray attenuation device (Sedigraph) from Micrometrics (MasterTech 52 Sedigraph III), drying oven, stirrer, ultrasound bath

Pipette method: PE-bottles (2 L), end-over-end shaker, ultrasonic bath, graduated cylinders (500 mL) or beaker (5 L), sieve (63 µm), timer, thermometer, U-shaped glass pipette, peleus ball, buckets, plastic pots, agate mill or agate mortar, centrifuge (Multifuge 3S-R Heraeus/Kendro), centrifuge beakers, shaking table, drying oven, analytical balance, spatula, brush

**Chemicals**

Sodium pyrophosphate ($Na_4P_2O_7 \cdot 10\ H_2O$), deionized water

**Brief description**

Particle size distribution of the ceramic clays was determined via three different pathways: For pathway 1, the determination of the particle size distribution was carried out according to industrial standards by the X-ray attenuation method (Micrometrics MasterTech 52 Sedigraph III), applying a dispersant. 20 g of the oven-dried samples (110 °C) were suspended in 100 mL of 0.002 M Na-pyrophosphate by stirring (500 rpm) and ultrasonication (ELMA T460/H, 70 W, 35 kHz).

For pathway 2, 50 g of the ceramic clay samples and 100 g of the kaolin samples, each with inherent moisture, were suspended in 2 L deionized water. PE-bottles containing the suspensions were sonicated for 30 min in an ultrasound bath (Sonorex Bandelin RK 514 BH, 215 W, 35 kHz) and then placed on an end-over-end shaker for 24 h. Afterwards, the samples were grain-size fractionated. The fraction >63 µm was separated by wet-sieving. The fractions 20-63 µm, 2-20 µm, and <2 µm were obtained by gravitational sedimentation. Settling times were calculated according to equations 4.3 and 4.4. The fraction <0.6 µm was extracted by centrifugational sedimentation from the <2 µm fraction (solid content <0.3%). This separation resulted in the additional fraction 0.6-2 µm.

The determination of the particle size distribution of the paper kaolins was also carried out according to pathway 2, extracting the fractions >20 µm, 2-20 µm, 0.6-2 µm, 0.2-0.6 µm, and <0.2 µm. For some samples an additional fraction <0.1 µm was separated. The fractionation conditions are reported in Table 4.1.

Pathway 3 was analogue to pathway 2, using a 0.01 M solution of Na-pyrophosphate as dispersant. Then, grain-size distribution was determined by weighing the mass of each fraction.

Table 4.1: Conditions of grain-size fractions collected by sedimentation with the pipette method according to pathway 2.

| Fraction [µm] | Separation method | Gravitational force [G] | Settling time* [min] |
|---|---|---|---|
| >63 | sieve | 1 | - |
| <20 | Sedimentation in | 1 | 10 |
| <2 | the gravity field | 1 | 930 |
| <0.6 | Sedimentation in | 1240 | 10 |
| <0.2 | the centrifugation | 4350 | 25 |
| <0.1 | field | 4350 | 100 |

*referred to T=20 °C and settling distance $h_1$=20 cm in the gravity field and $h_2$=6 cm in the centrifugation field, respectively.

**Error**

For particle sizes <0.2 µm, acceleration and deceleration time of the centrifuge leads to deviations of <2% from the needed equivalent diameter (Wolters, 2005). Problems exist with the pipette method due to convection currents near the tip of the pipette and greater potential for operator error (Skopp, 2002). The settling equation according to Stokes' law is based on a number of assumptions, such as the rounded shape of the particles, an average particle density or the constant density and temperature of the liquid, which are less fulfilled in the case of clay-containing suspensions (platy-shaped clay particles, density variations of clay mineral particles due to differences in chemical composition and hydration state, dynamic of the settling process), resulting in a carry-over of particles to a smaller or larger fraction.

### 4.2.3 X-ray diffraction

The wide use of X-ray diffraction (XRD) in all fields of science and technology is due to the fact that powder XRD provides a powerful testing method to determine a range of physical and chemical material characteristics. The applications include phase analysis, i.e., the identification and quantification of phases present in a sample, as well as acquisition of crystallographic structural data, like crystallographic unit cell size, crystal structure, crystallographic texture, crystalline size, macro-stress and micro-strain, and also electron radial distribution functions (Will, 2006).

As pointed out by Moore and Reynolds (1997), powder XRD is the instrumentation most commonly used to study clay-sized minerals, not only for the reason that clay minerals are usually <2 µm and therefore too small to be studied by optical methods or single crystal X-ray methods, but also because XRD of powdered samples provides information about bulk properties, thus information averaged over an enormous number of unit cells and crystals.

X-ray diffraction results from the scattering of X-rays by lattice points. Depending on the Bravais lattice, interferences between scattered rays are constructive when they are in phase, thus, the path difference of the diffracted rays differs from each other by an integer number of wavelength. This selective condition is described by Bragg's law (equation 4.7)

$$n\lambda = 2d\sin\theta \qquad \text{(eq. 4.7)}$$

where n is an integer number, λ the wavelength, d the spacing between the lattice planes, and θ the Bragg angle, which is half the angle between incident and reflected beam.

If the analysis is one-dimensional, like in the case of XRD analysis from oriented samples, n is substituted by *l*, and Bragg's law rearranged is

$$l\lambda / 2d = \sin\theta \qquad \text{(eq. 4.8)}$$

with d=d(001)/*l*, where *l* is the integral order.

*Rietveld analysis*

Rietveld analysis is a crystal structure refinement method developed by H.M. Rietveld in the late 1960s. In order to understand the properties of clays and to improve them, the atomic structure of the clay minerals has to be known. The single crystal diffraction technique, using relatively large crystals of the material, gives a set of (*hkl*)-reflections from which the crystalline lattice and the unit cell in real space can be obtained by Fourier transformation. However, most materials of technical interest, like clays minerals, cannot develop large crystals, so one has to resort to the powder diffraction technique using material in the form of small crystallites (Taylor, 1985).

The general drawback of the powder diffraction technique for crystal structural analysis is the loss of structural information in that the three dimensional information of the reciprocal lattice gathered with single-crystal diffraction is superposed into one dimension. The work of Rietveld (1967, 1969) overcame this problem, recognizing that the powder pattern profile is the sum of all the individual (*hkl*)-peaks and every point in the step scan is an observation, which allows the extraction of crystal structural information from power diffraction data, despite of partially overlapping individual Bragg reflections.

Rietveld refinement is a least-squares optimization procedure to fit a model of the examined sample to a measured diffraction pattern. Hereby, the least-squares sum is minimized as follows

$$\sum_{i=1}^{M} w_i (y_i - y_{ic})^2 = p \qquad \text{(eq. 4.9)}$$

with p becoming as low as possible, $w_i$ being the weight of an individual measuring point, commonly $T_i y_i$, whereby $T_i$ is the measuring time of measuring point I and $y_i$ the measured counts of the i$^{th}$ point, $y_{ic}$ the calculated counts of the i$^{th}$ point, and M the total number of measuring points.

A key feature of the Rietveld method is the feedback during refinement between improving knowledge of the structure and improving allocation of observed intensity. These characteristics mark the difference to the pattern decomposition method, which has no reference to a crystal structural model (Young, 1995).

Equation 4.10 is the basic equation of the Rietveld method and describes that every point of the diffraction pattern contains contributions of intensity from neighboring peaks of one or more phase(s) as well as from background scattering:

$$y_i = \sum_p \left[ S_p \sum_k \left[ APL\Psi M_k \left| F_k \right|^2 G(\Delta\Theta_{ik}) po_k \right] \right] + y_{bi} \qquad \text{(eq.4.10)}$$

with $y_i$ being the intensity of the angular position i in the powder pattern, $S_p$ the scale factor of the phase p, which relates the phase intensities to the pattern, APL for absorption, polarization and the Lorentz factor, Ψ geometrical factor (for the k line), M plane multiplicity factor, F the structure factor, G the profile shape function (“smears” the intensity around the Bragg position), po the preferred orientation correction factor, and $y_{bi}$ the background intensity.

Figure 4.1 clarifies the single expressions.

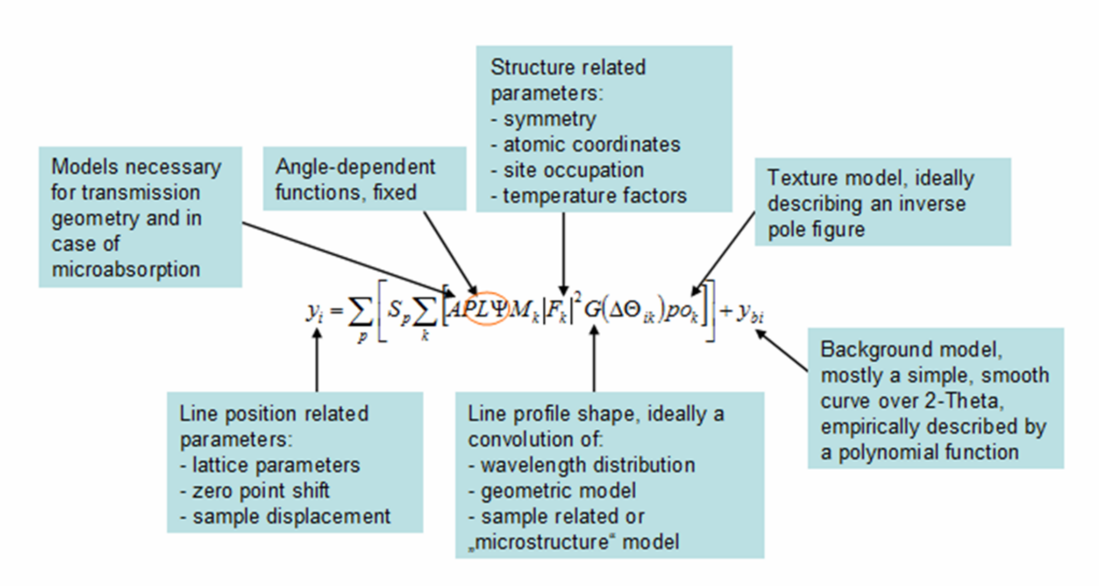

Figure 4.1: Models and parameters used in the Rietveld method. Modified after Kleeberg (2009b).

In the present study, Rietveld analysis was carried out with AutoQuan software (Seifert Analytical X-ray), including a ready-to-use structure database of minerals, which is based on BGMN structure files (Bergmann et al., 1998). BGMN uses a profile shape model folding the parameters' wavelength distribution, geometry function, and sample function.

The wavelength distribution is modeled by a set of Lorentzian functions describing both, the $K\alpha_1$ and the $K\alpha_2$ lines. Other device-specific parameters such as distances, slits, and angles are characterized by the geometry function, which is the sum of 2θ-dependent specific geometry functions. Mathematical modeling of each 2θ-position of the geometry function is performed by squared Lorentzian functions, allowing even asymmetric profiles to be modeled with sufficient accuracy.

The device-dependent functions in terms of wavelength distribution and geometry function are determined before fitting and remain constant during calculation (Figure 4.2). Thus, the Rietveld calculation only deals with determining the sample-dependent profile parameters described by the sample function.

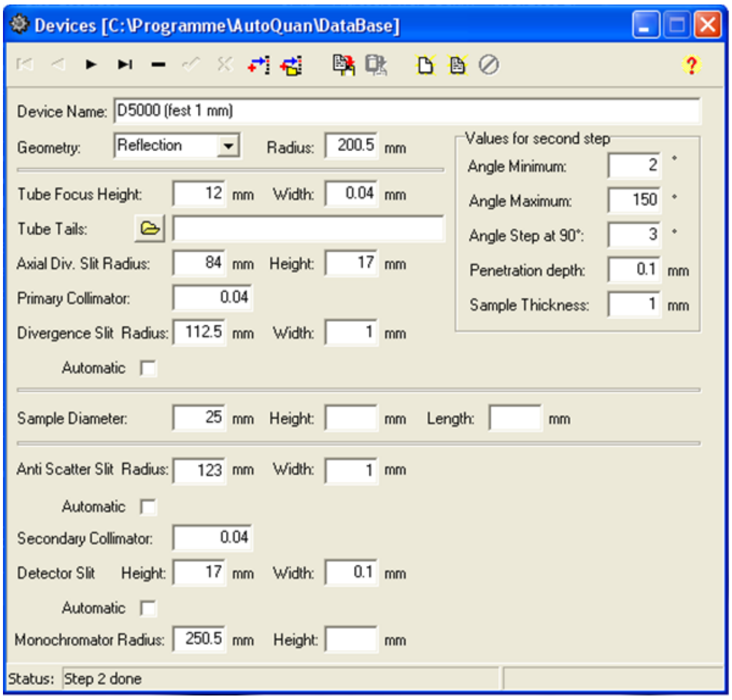

Device Name: D5000 (fest 1 mm)
Geometry: Reflection
Radius: 200.5 mm
Tube Focus Height: 12 mm Width: 0.04 mm
Tube Tails:
Axial Div. Slit Radius: 84 mm Height: 17 mm
Primary Collimator: 0.04
Divergence Slit Radius: 112.5 mm Width: 1 mm
Automatic ☐
Values for second step
Angle Minimum: 2 °
Angle Maximum: 150 °
Angle Step at 90°: 3 °
Penetration depth: 0.1 mm
Sample Thickness: 1 mm
Sample Diameter: 25 mm Height: mm Length: mm
Anti Scatter Slit Radius: 123 mm Width: 1 mm
Automatic ☐
Secondary Collimator: 0.04
Detector Slit Height: 17 mm Width: 0.1 mm
Automatic ☐
Monochromator Radius: 250.5 mm Height: mm
Status: Step 2 done

Figure 4.2: Input mask for the calculation of the device function in the Rietveld program AutoQuan with ray geometry values adjusted for the applied X-ray diffraction device Bruker D5000.

The sample function implies the contribution of diffraction by the sample to the measured profile. The occurrence of peak broadening due to real structure parameters like crystallite size, preferred orientation and micro-strain is described by a set of different Lorentzian functions.

On basis of the Rietveld method, quantitative phase analysis (QPA) of multicomponent mixtures using X-ray powder diffraction data has been carried out by Wiles and Young (1981). To perform QPA, no calibration data or internal standard is required. Knowledge on the approximate crystal structure of each phase of interest is necessary. Errors achieved for synthetic mixtures are generally less than 1 wt% absolute (Bish and Howard, 1988). Kleeberg (2009a) reported absolute errors of up to 5 wt% for samples containing clay mineral amounts of 10-20 wt%, and an estimated general accuracy within 3 wt% at the 95% confidence level for routine analysis of geo-materials.

The success of a fitting procedure is assessed by the difference between measured and calculated profiles and expressed by R values (Jansen et al., 1994). The $R_{wp}$ value, which was applied in the present study, is given by equation 4.11:

$$R_{wp} = \left[ \frac{\sum_{i=1}^{M} w_i (y_i - y_{ic})^2}{\sum_{i=1}^{M} w_i {y_i}^2} \right]^{\frac{1}{2}} \qquad \text{(eq. 4.11)}$$

with $R_{wp}$ being the weighted residual square sum and the other quantities being the same as in equation 4.9. A small $R_{wp}$ value stands for a better fit. As emphasized by Bergmann et al. (1998), the $R_{wp}$ value is only a mathematical criterion. A small $R_{wp}$ value may also be obtained from fitting a profile with a continuously high background with a relatively poor crystallographic model. This effect results from the fact that the background fitting is also part of the calculation. For that reason, $R_{wp}$ values can only be compared with each other, if they refer to the same profile.

*One-dimensional pattern fitting*

As mentioned in Sections 1.5 and 2.1.2, one-dimensional fitting of XRD patterns (ODPF) provides a powerful tool for the characterization of complex clay samples consisting of clay minerals and mixed-layer minerals.

One-dimensional XRD patterns are gathered from oriented sample preparation, resulting in “simplified” XRD patterns, which display ideally only the (00*l*)-reflections. These reflections are not sensitive to the translations of the layers parallel to their own planes, but solely depend on the distribution of the atoms in the direction perpendicular to the layers, which is the primary topic of interest in the study of lamellar structures, such as phyllosilicates (Plancon, 2010).

The method itself consists of a trial-and-error procedure by directly comparing experimental XRD profiles to those calculated from a structure model, which is derived from the calculation of one-dimensional structure factors of a layer type based on one-dimensional atomic coordinates. The summation of the respective structure factors is obtained by generation of a matrix, describing the probability and arrangement of the layers in the stack ("MacEwan crystallite").

The structure models of mixed-layer minerals comprise the number, nature, chemistry, and proportion of the different layer types, as well as a statistical description of their stacking sequences in terms of Reichweite parameter and junction probabilities (Lanson, 2005).

Determination of the phase content deduced from ODPF has to be considered as semi-quantitative as the relative intensities are extremely sensitive to a number of parameters, such as the chemical composition of the interlayer and the distribution of the ions and molecules therein, the thickness of coherent scattering domains as well as the heterogeneity in constitution of these domains (Drits and Tchoubar, 1990). Thus, for many studies a good agreement for the peak positions and a semi-quantitative agreement for the profiles and relative intensities may be regarded as sufficient.

In this study, XRD patterns were modeled with the SYBILLA software developed by Chevron. This program was employed, e.g., in studies by Sakharov et al. (1999), McCarty et al. (2008), and Hubert et al. (2009).

SYBILLA is very similar to NEWMOD, but is equipped with additional features, such as modeling of 2- and 3-component mixed-layer minerals, fitting of multi-phase samples, automatic scaling to a diffraction pattern in the manual mode, and automatic fitting by genetic algorithms in the "server mode".

SYBILLA provides a graphic user interface to the algorithm initially developed by Drits and Sakharov (1976), which allows the direct comparison between experimental and calculated XRD profiles. The quality of agreement between the experimental and the calculated XRD patterns was evaluated by the profile factor $R_p$ (Howard and Preston, 1989, equation 4.12), which is the unweighted version of the $R_{wp}$ parameter reported in equation 4.11:

$$R_p = \left[ \frac{\sum_{i=1}^{M} (y_i - y_{ic})^2}{\sum_{i=1}^{M} {y_i}^2} \right]^{\frac{1}{2}} \qquad \text{(eq. 4.12)}$$

Instrumental and experimental parameters, such as horizontal and vertical beam divergence, goniometer radius and slide length were introduced without further adjustment. Sigmastar σ* (standard deviation of a Gaussian orientation function for the crystals in the powder aggregate) was set to 12, the mass absorption coefficient μ* to 45, and the number of unit cells in a crystallite (T mean) was mainly kept between 3 and 14, as recommended by Moore and Reynolds (1997). Higher T-mean values are often required for kaolinite. The thickness of the coherent scattering domains (CSDs) was assumed to be lognormally distributed and characterized by their mean value (Drits et al., 1997b).

As variable parameters ("genes") for the fitting process the position and amount of interlayer species ($H_2O$ and EG molecules), the octahedral Fe content, the interlayer cation content, as well as the number, nature, proportion, and stacking sequences of the mixed-layer phases were introduced.

The parameters were systematically varied in two steps. In the first step, "SYBILLA Server" was employed to do the complete modeling automatically. In this mode, genetic algorithms (e.g., Mitchell, 1998) are used to optimize the structural and probability parameters. In the second step, "SYBILLA Manual" was used to model experimental X-ray patterns by manually changing the structural and probability parameters of the chosen phases until a satisfactory fit is achieved. During these manual operations, the program continuously changes the content of the different phases.

However, the application of one-dimensional modeling is not always successful in unambiguously determining the real structure as several structural models may fit the experimental data equally well (Drits, 1987; Sakharov et al., 1999; McCarty et al., 2004). Fitting results have to be critically evaluated by comparing them with chemical and mineralogical analyses in order to obtain a consistent characterization. To conclude in the words of Howard and Preston (1989), "the subtleties involved in profile fitting commonly relegate the technique to the realm of art rather than science".

**Equipment**

Agate mortar, spatula, sample holder, glass plate, and additional equipment for oriented sample preparation: round glass slides, research pipette with 10 mL tips (Eppendorf), 10 mL screw cap centrifugation tubes, thermostatically controlled drying oven (60 °C), XRD device Bruker D5000, equipped with a graphite secondary monochromator and scintillation detector, using CuKα radiation. Sizes of the divergence slit and the antiscatter slit were 1 mm, and 0.1 mm for the detector slit.

Data processing software: mineral identification was carried out with the DiffracPlus Evaluation program, Version 10.0, by Bruker. The quantitative mineral content was determined by Rietveld method applying AutoQuan software (Bergmann et al., 1998) by Seifert Analytical X-ray, version 2.7.0.

Characterization of the clay minerals and the mixed-layer phases were performed by one-dimensional XRD profile fitting of the EG-solvated samples of the coarse clay fraction (0.6-2 μm) and the middle to fine clay fraction (<0.6 μm) using SYBILLA software developed for Chevron Energy Technology.

**Chemicals**

Calcium chloride ($CaCl_2$), ethylene glycol, deionized water

**Brief description**

Top-loaded powdered samples (≈2 g) were gently pressed with the glass plate in the sample holder (Ø 2.5 cm) and measured in reflection geometry (Bragg-Brentano) at 0.02° 2θ step intervals from 2-80° with 3 s per step.

For XRD measurements of the textured samples, a part of the fraction <0.6 µm of the ceramic clays and a part of the fraction <0.2 µm of the paper kaolins was Ca-saturated adding a $CaCl_2$ solution (excess of 20 times the CEC) to the suspensions of 2.5% solid content. The suspensions were shaken for 24 h. After centrifugation, the supernatant was removed and the bottom was saturated again. The saturation step was repeated three times. Then, the suspensions were washed with deionized water until chloride free (conductivity of the supernatant <4 µS/cm). The Ca-saturated suspensions were oven-dried at 60 °C.

Oriented samples were produced for the Ca-saturated samples by pipetteting 1.5 mL of the respective suspension on a glass slide and dried overnight under atmospheric conditions at room temperature. Air-dried samples (AD) were prepared with a thickness of 15 mg/cm$^2$ to prevent peak-intensity loss (Moore and Reynolds, 1997). Ethylene glycol (EG) solvation was achieved by exposing the slides to EG vapor at 60 °C for 24 h (Whitney and Northrop, 1987). Heat-treated samples were obtained by heating the slides at 375 °C for 3 h (Moore and Reynolds, 1997). Oriented samples were measured at 0.02° 2θ step intervals from 2-30° with 6 s per step.

**Error**

Sample preparation accounts for the largest systematic error in powder XRD (Klug and Alexander, 1974), resulting from insufficient sample statistics due to grain-size effects, preferred orientation, microabsorption, sample roughness, and sample displacement errors in terms of sample position, thickness, and height (Bergmann et al, 1998).

The number of crystallites (10$^4$ as lowest statistical limit) can be increased by grain-size reduction via gentle grinding. The counting statistics is also improved by an enlarged divergence of the primary beam and spinning the sample. Preferred orientation of crystallites enhances specific crystallographic directions (00*l* for clay minerals), leading to inflated intensities (Dohrmann et al., 2009). Microabsorption occurs in multi-phase samples from different linear attenuation coefficients and grain sizes of the constituent phases. Principally, the amount of microabsorption may be approximated (Brindley, 1945), if the linear attenuation coefficients and the mean crystallite size of all phases are known. Grain-size-induced microabsorption can be diminished by reducing the grain size, as smaller particles absorb less radiation. The problem of microabsorption derived from linear attenuation coefficients may be addressed by changing the anode material, e.g., using Co-radiation in the presence of large amounts of Fe. However, one has to keep in mind that the content of the phase with the greater linear attenuation coefficient is generally determined to be too low. Sample roughness may have an impact on intensity, particularly in the low 2θ-region in that crystallites can be shielded by protruding grains, lowering the counting statistics. Sample displacement errors lead to intensity loss (sample thickness) or peak shift (sample position and sample height).

Another issue regarding the preparation of textured samples by pipetting a suspension on a glass slide is the segregation of particles, which may occur during drying. According to Tricky (1973) and Blanc et al. (2007), the segregation leads to an over-estimation at low-angle domains. Due to the low penetration depth of the X-rays at low 2θ-diffraction angles, the information does not originate from the whole sample volume, but only from the clay minerals-enriched sample surface.

### 4.2.4 X-ray fluorescence

The chemical composition of the bulk material and the grain-size fractionated samples was determined by X-ray fluorescence (XRF) analysis. The knowledge of the chemical composition is important for two reasons. First, to cross-check the quantification results from Rietveld analysis and, therefore, the mineralogical phase content determined by Rietveld analysis was converted to chemical composition in terms of element oxides. Afterwards, the amount of element oxides was compared with the chemical composition from XRF measurements. The second reason is the assessment of raw material qualities for industrial applications by estimation of the clay content (Schejbal, 1978).

The measuring principle of X-ray fluorescence is based on the photoelectric effect. By irradiating a sample with X-rays of sufficient energy, electrons are ejected from the inner shells, creating vacancies. As vacancies present an unstable condition, electrons from the outer shells are transferred to the inner shells, releasing energy in form of element characteristic X-ray fluorescence. In wavelength-dispersive X-ray fluorescence spectrometry (WDXRF), the fluorescence radiation is collimated onto a diffraction crystal and its intensity is detected at selected positions of the energy spectra. Selection of usable element-specific lines is done on basis of intensity, spectra accessibility of the instrument, and the lack of line overlapping.

For WDXRF measurements, the powdered samples were transformed to molten pellets by mixing them with flux material and heating them up. Then, the molten pellets were analyzed. Simultaneously, the loss on ignition was determined.

**Equipment**

XRF analyses were performed on a MagiXPRO spectrometer from Philips with a 3.2 kW rhodium X-ray tube. For pellets preparation were needed an analytical balance, spatula, Pt crucible, smelting apparatus (Vulcan 4MA, HD Electronic).

**Chemicals**

Lithium tetraborate ($Li_2B_4O_7$) from Merck (Spectromelt A10, supra pure)

**Brief description**

0.8 g of the powdered samples was mixed with lithium tetraborate in a ratio of 1:7. The material was molten stepwise in Pt crucibles in a smelting apparatus. The melt was poured into a platinum jacket for cooling. Loss on ignition was determined by storing 0.2 g of each sample at 1000 °C for 2 h.

**Error**

Wolters (2005) reported the relative error (variance) for each element measured by internal standards.

### 4.2.5 Simultaneous Thermal Analysis

Supplementary information on mineral identification and characterization was gathered by Thermal Analysis (TA).

TA comprises static and dynamic procedures. For static procedures, the sample is dried at constant temperature until mass constancy is reached, e.g. to measure the water content or loss on ignition. Within dynamic procedures, the sample is submitted to a temperature–time program with a defined heating rate, in order to pursue constantly mass variations, heat-flow changes or mechanical properties. Dynamic methods are often much less time-consuming and more informative (Emmerich, 2009).

According to DIN 51005, Simultaneous Thermal Analysis (STA) means coupling of at least two TA methods. Common STA devices usually combine Thermogravimetry (TG) and Differential Thermal Analysis (DTA) or Differential Scanning Calorimetry (DSC).

TG measures the change of sample weight during a given temperature–time program in a defined atmosphere (Hemminger and Cammenga, 1989). Weight changes as a result of thermal decomposition (e.g., water release) or reaction of the sample with the gas phase (e.g., oxidation).

Both DTA and DSC detect temperature-dependent changes of enthalpy (Hemminger and Cammenga, 1989). The reactions occurring are either energy-consuming (endothermic reaction) or energy-releasing (exothermic reaction). Thermal decomposition (e.g., dehydration, dehydroxylation, structural decomposition) and phase transformations (modification changes) are generally endothermic. Reactions as oxidation, formation of new phases, including recrystallization, are exothermic. Conventionally, an endothermic reaction is graphed sloping down whereas an exothermic reaction is graphed sloping up (Lombardi, 1980).

DTA and DSC curves resemble each other. For both techniques, the measurement signal is a thermally induced electric voltage caused by a temperature difference between the sample and an inert reference. In contrast to DTA, the DSC measurement signal may be calibrated to reaction heat-flows by power compensation, which measures the amount of energy required to compensate temperature differences due to thermal reactions of the sample.

Evolved Gas Analysis (EGA) enhances the information content by coupling the TA to a gas detection system (Kaisersberger, 1979). Gases evolved during thermal reactions are directed to a mass spectrometer (MS) or an infrared spectrometer (IR) and detected there.

Pulse TA (PTA) enlarges the range of applications, since coupling of STA-MS offers the possibility to quantify the $CO_2$ release from a sample during thermal reactions by injection of a specific amount of $CO_2$ into the carrier gas flow (Maciejewski et al., 1997). The mean amount of evolved $CO_2$ during a given reaction is calculated according to equations 4.13 and 4.14

$$V_{CO_2} = V_{pulse} \cdot \frac{A_{CO_2}}{A_{pulse}} \qquad \text{(eq. 4.13)}$$

$$m_{CO_2} = \rho_{CO_2} \cdot V_{CO_2} \qquad \text{(eq. 4.14)}$$

with $V_{CO2}$ being the volume of evolved $CO_2$ [mL], $V_{pulse}$ the volume of injected $CO_2$ [mL], $A_{CO2}$ the peak area of evolved $CO_2$ [a.u.], $A_{pulse}$ the peak area of injected $CO_2$ [a.u.], $m_{CO2}$ the mass of evolved $CO_2$ [mg], $\rho_{CO2}$ the density of $CO_2$ at injection temperature [$gL^{-1}$] ,e.g., 1.7988 $gL^{-1}$ at 23 °C; 1.7730 $gL^{-1}$ at 27 °C; 1.7562 $gL^{-1}$ at 30 °C (Lide, 2009). The PTA-data for this study were gathered at room temperature.

As peak shape and peak temperature of minerals strongly depend on experimental conditions (e.g., Smykatz-Kloss, 1974; Ortega, 1997; Rouquerol et al., 2006), a detailed overview of the experimental parameters is given in Table 4.2.

Table 4.2: Experimental parameters for STA measurements.

| Parameter | TG/DSC/MS |
|---|---|
| Sample amount | 100 mg |
| Grain size | powder |
| Packing density | loosely packed, no pressing |
| Reference material | empty crucible with lid |
| Furnace atmosphere | 50 ml/min air + 20 ml/min $N_2$ |
| Crucibles | Pt/Rh with lid |
| Thermocouples | $Pt/Pt_{90}Rh_{10}$ |
| Heating rate | 10 K/min |
| Temperature range | 35-1100 °C |

A comprehensive description of the measuring principle and applications in clay mineralogy are available in textbooks and journal reviews, e.g., by Smykatz-

Kloss (1974); Paterson and Swaffield (1987); Hemminger and Cammenga (1989); Niederbudde et al. (2002), and Emmerich (2009).

In this study, a variety of information was obtained by STA measurements: On the basis of the mass loss during the dehydroxylation reaction, the maximum possible clay content was estimated by comparing the measured mass loss from TG curves with the calculated mass loss based on the quantification results from Rietveld analysis.

Further information on kaolinite structure was gathered by PA curves (Smykatz-Kloss, 1974). PA curves display the dependency of the peak temperature of a decomposition reaction (e.g., dehydroxylation) from the applied sample mass during thermal analysis and differ for minerals with different degrees of structural disorder. The dehydroxylation temperature of kaolinite depends strongly on the degree of structural disorder. PA curves were recorded and compared with well characterized samples of known degrees of structural disorder.

PTA measurements were used to determine the amount of organic compounds.

From STA measurements, the maximum clay content was estimated by comparing the measured mass loss during dehydroxylation reaction ($\Delta m\ T_{DHXmeas}$) between 400 and 900 °C from TG curves with a calculated mass loss ($\Delta m\ T_{DHXcalc}$) based on the quantification results from Rietveld analysis.

The calculated mass loss is given by

$$\Delta m T_{DHXcalc} = x\frac{2M_{H_2O}}{M_{Kao}} + y\frac{M_{H_2O}}{M_{Smectite}} + z\frac{M_{H_2O}}{M_{Illite}} \qquad \text{(eq. 4.15)}$$

where x, y and z are the coefficients of the respective mass fractions of kaolinite, the smectitic components, and illite as obtained from Rietveld analysis. M is the respective molar mass, assuming 18 g/mol for water, 258 g/mol for kaolinite, 375 g/mol for smectite, and 390 g/mol for illite.

The estimation process was carried out for a range of coefficients (x, y, z), which comprised the mean values of each mass fraction, as well as their standard deviations (+s, -s). The success of estimation was proved by a Δ-value, subtracting $\Delta m\ T_{DHXcalc}$ from $\Delta m\ T_{DHX}$. An overestimation of the clay content by Rietveld analysis led to a negative delta value. As $\Delta m\ T_{DHX}$ marks the upper limit, negative delta values were discarded.

**Equipment**

Netzsch STA 449C Jupiter, QMS 430C Aeolos, purge gas $N_2$, Pulse box (Netzsch), Software Proteus Netzsch, PeakFit (Jandel Scientific), dessicator, analytical balance, spatula, Pt crucibles with lid

**Chemicals**

$Mg(NO_3)_2 \cdot 6H_2O$, synthetic air (20.5% $O_2$ in $N_2$) and $N_2$ (quality 4.8), $CO_2$

**Brief description**

In order to ensure reproducibility in weighing, samples were stored at 53% r.h. over a saturated solution of $Mg(NO_3)_2 \cdot 6H_2O$ (Koster van Groos and Guggenheim, 1984). Sample amounts of 50 or 100 mg were measured at a constant heating rate. The measuring conditions are summarized in Table 4.2 and were chosen according to Niederbudde et al. (2002) and Wolters (2005).

For PTA experiments, an isothermal segment at 1100 °C (30') was attached to the conventional t-T-program for several injections of 250 µL and 500 µL $CO_2$. The pulse box was operated at room temperature.

**Errors**

Factors influencing the measurement are due to the equipment (e.g., size, shape and material of crucibles, use of lids), experiment (e.g., sample amount, particle size and packing density, heating rate) and sample characteristics (e.g., sample composition, particle size, crystallinity). A comprehensive description is given by Niederbudde et al. (2002), Petrick (2007), and Emmerich (2009).

### 4.2.6 Cation exchange capacity and exchangeable cations

The cation exchange capacity (CEC) is an important characteristic of clay minerals and describes their ability to adsorb cations. There are two possibilities where adsorption takes place: in the interlayer space as well as on the clay mineral edges and surfaces. The total CEC is the sum of these two contributions, whereas the amount of exchangeable interlayer cations depends on layer charge and the amount of edge-located cations is pH-dependent. The interpretation of CEC values is not straightforward due to the influence of sample components on pH.

For smectites, the edge-located amount can reach up to 20% at pH 7 (Lagaly, 1981). Kaufhold et al. (2002) showed that edge-located cations comprise an average value of 10%. pH dependency of CEC can be eliminated by lowering the pH in the acid range (pH 4-5). The difference between the total CEC at pH 7 and the exchange capacity in the acid range gives the contribution of the edge-located cations (Kaufhold, 2001; Steudel, 2008).

The positive correlation between layer charge and CEC is not fulfilled for highly charged layer silicates (micas, illite, highly charged vermiculites) as only edge-adsorbed cations are exchangeable due to $K^+$-fixation in the interlayer space (Norrish, 1954; Sawhney, 1972).

To determine the CEC, the exchangeable cations were replaced by copper triethylenetetramine (Cu-trien) cations (Meier and Kahr, 1999; Ammann et al., 2005). Afterwards, the consumption of Cu-trien was measured photometrically in the clear supernatant.

The CEC is calculated according to the following expressions:

$$CEC = \frac{2 \cdot \lfloor (c_{Cu-Trien} \cdot V_{Cu-Trien} - c \cdot (V_{Cu-Trien} + V_{H_2O}) / 1000) \cdot 100 \rfloor}{m} \quad \text{(eq. 4.16)}$$

$$m = m_1 \cdot \frac{(100 - w_{\min})}{100} \quad \text{(eq 4.17)}$$

$$c = \frac{A}{a} \quad \text{(eq. 4.18)}$$

with $c_{Cu\text{-}Trien}$ [mmol/L] being the concentration of the Cu-Trien, V [mL] the respective volume of Cu-Trien or deionized water, c the concentration of the supernatant [mmol/L], m [mg] the mass of the dried sample at 105 °C, $m_1$ [mg] the air-dried sample mass, $w_{min}$ [%] the water content (equation 4.3 in Section 4.2.1), A the measured absorbance of the supernatant, and a the slope of the calibration curve.

In order to balance the sum of exchangeable cations to the measured CEC, the amount of exchanged cations ($Na^+$, $Mg^{2+}$, $K^+$, $Ca^{2+}$, $Al^{3+}$, $Fe^{3+}$) in the supernatant was determined by Inductively Coupled Plasma Optical Emission Spectroscopy (ICP-OES). This type of emission spectroscopy uses an inductively coupled plasma (argon gas ionized in an intense electromagnetic field) to produce excited atoms and ions that emit electromagnetic radiation at wavelengths characteristic of a particular element. The registration of emission signals is carried out by means of UV and visible spectrometry. The intensity of this emission is indicative of the element concentration within the sample (Mermet and Poussel, 1995).

The content of swellable components (sum of smectite and smectitic layers in I-S) was calculated according to Lagaly (1993), assuming an average molar mass M of 375 g/mol for smectites (Wolters, 2005), 10% of variable charge, and a mean layer charge density (χ) of 0.30 eq/formula unit (Kaufhold et al., 2002). In addition, kaolinite and illite were assumed to have a CEC of 5 meq/100g (Kaufhold and Penner, 2006), giving rise to the expression

$$w_{sc} = \frac{CEC_{corr} M}{1000\chi} \quad \text{(eq. 4.19)}$$

where $w_{sc}$ is the content of swellable components [%] and $CEC_{corr}$ is the cation exchange capacity after subtraction of 10% of variable charge and the kaolinite and illite contents determined from quantitative phase analysis. The amount of exchanged cations in the exchanging solution was compared with the CEC values.

**Equipment**

CEC: Desiccator, UV-vis spectrometer (Genesys 10 UV), disposable cuvettes and pipettes, centrifuge (Multifuge 3S-R Heraeus/Kendro), graduated centrifuge flasks, equipment for determining the water content (Section 3.2.1)

ICP-OES: Vials (20 mL), research pipette with 5 mL tips (Eppendorf), centrifuge (Multifuge 3S-R Heraeus/Kendro), ICP-OES spectrometer (Horiba Jobin Yvon JY 38 S)

**Chemicals**

0.01 M Cu-triethylentetramine, magnesium nitrate ($Mg(NO_3)_2$), deionized water, nitric acid supra pure ($HNO_3$, 65%)

**Brief description**

The samples were stored over magnesium nitrate (53% r.h.) for at least 24 h. 100 mg of each sample was weighed in a 50 mL centrifuge flask. 5 mL of the 0.01 M Cu-Trien and 10 mL of deionized water were added. The samples were shaken for three hours on a shaking table to guarantee the complete exchange of the Cu-complex with the interlayer cations. The suspensions were centrifuged at 4500 rpm for 10 min and the blue clear supernatants were measured photometrically at a wavelength of 580 nm. All measurements were performed as duplicates. As in-house standards, two well-characterized bentonites (Calcigel and Volclay) were inserted in the batch to check the precision of measurements. Before starting the measurements, a calibration curve was recorded, adding defined volumes (0, 0.5, 1, 2, 3, 4, and 5 mL) of 0.01 M Cu-Trien to 10 mL deionized water, respectively. The slope of this calibration curve enters in the calculation of the CEC (equations 4.15 and 4.17).

To determine the amount of exchanged cations by ICP-OES, 5 mL of each supernatant was diluted 1:10 with deionized water and acidified with one drop (≈1 µL) of $HNO_3$ suprapure.

**Errors**

The precision of the method was tested for the in-house standard bentonites (Calcigel with an average CEC of 63 meq/100 g and Volclay with an average CEC of 85 meq/100 g), which showed a deviation of ±3 meq/100 g for a sample size >75 (Steudel, 2008).

### 4.2.7 Mössbauer spectroscopy

Mössbauer spectroscopy was applied to identify the valence state and site occupancy of Fe in the individual minerals. It is a suitable method for the examination of clays due to the fact that practically all clays contain enough Fe to yield $^{57}$Fe Mössbauer spectra (Weaver et al., 1967; Taylor et al., 1968). In kaolins, for instance, ancillary Fe (oxy-hydr)oxides can readily be distinguished from silicate-bound Fe using Mössbauer spectroscopy (Stucki, 2006). Such a distinction, however, requires measurements at cryogenic temperatures, preferably at the temperature of liquid helium (4.2 K), because only then all Fe (oxy-hydr)oxides exhibits magnetic hyperfine patterns that are well-distinguishable from the silicate-bound Fe. Examination of the Mössbauer hyperfine parameters (isomer shift, electric quadrupole splitting and magnetic hyperfine field) gives additional information on Fe oxide phases (Murad, 1987; 1988; 1999; Rancourt, 1999).

Mössbauer spectroscopy is based on the recoil-free emission and absorption of nuclear γ-rays in solids (Mößbauer, 1958). These γ-rays are used to measure the hyperfine splittings of nuclear energy levels, which in turn are sensitive to the local electron configuration and the magnetic properties of the solid.

For Mössbauer absorption spectroscopy, the sample is exposed to γ-radiation and a detector measures the intensity of the beam transmitted through the sample. The γ-rays are emitted by a source in which a radioactive isotope decays to the same isotope as that present in the absorbing sample. In the case of $^{57}$Fe Mössbauer spectroscopy, $^{57}$Co in the source decays to $^{57}$Fe, a stable isotope of Fe with a natural abundance of about 2%. The 14.4 keV γ-rays of $^{57}$Fe can be resonantly absorbed by $^{57}$Fe nuclei in the absorber, since they have just the right energy. When the energy of the emitted γ-rays is varied very slightly via the Doppler effect, i.e., by moving the source at velocities of the order of a few mm/s, the hyperfine splittings and shifts of the nuclear levels in the absorber nuclei can be scanned.

In the Mössbauer spectra, the γ-ray intensity transmitted through the absorber is plotted as a function of source velocity. At Doppler velocities for which the energy of the incident γ-rays corresponds to the resonant energy of the hyperfine levels of the sample, γ-rays are absorbed, resulting in a drop of the measured intensity. The number, positions, and intensities of peaks provide information about the chemical environment of the absorbing nuclei.

Three types of nuclear interactions contribute to Mössbauer spectra: The isomer shift (or chemical shift, CS), the electric quadrupole splitting (QS) and the magnetic hyperfine splitting (or Zeeman splitting). CS is the shift of the peak minimum away from zero velocity and arises form the difference in s electron density between source and absorber. QS occurs by interaction of the nuclear quadrupole moment with the electric field gradient produced by the electronic environment of the Mössbauer nuclei, which leads to a splitting of the Mössbauer line into a quadrupole doublet. A magnetic hyperfine splitting takes only place when a magnetic field is present at the nucleus, which is usually the case in magnetically ordered Fe compounds.

The combination of isomer shift and quadrupole splitting parameters is usually sufficient to identify the valence state and site occupancy of Fe. $Fe^{3+}$ occurs primarily in 4- or 6-fold coordination with oxygen, while $Fe^{2+}$ may be rarely 4- or 5-fold coordinated, commonly 6-fold coordinated and occasionally 8-fold coordinated with oxygen (Dyar et al., 2006). As the Mössbauer parameters are often temperature dependent, the hyperfine splitting at cryogenic temperatures down to liquid helium temperature can be used to distinguish between superparamagnetic Fe (oxy-hydr)oxides and paramagnetic silicate Fe-bound in silicates.

The following description of single Mössbauer spectra features of Fe-bearing minerals is based on a personal communication in 2011 with F. Wagner, Technical University of Munich, who kindly performed the Mössbauer spectroscopy measurements of this study.

Fe (oxy-hydr)oxides are practically all ordered already at RT (room temperature), exceptions being akaganeite, which orders at about 260 K, and lepidocrocite, which orders at about 75 K. However, when the particles become very small (below about 10 nm), they will consist of only a single magnetic domain and exhibit superparamagnetism at RT. This means that the magnetization of the particle as a whole flips so rapidly that Mössbauer spectroscopy sees only a time-averaged hyperfine field, which is zero. Upon cooling such specimens, the superparamagnetism becomes blocked and the magnetic splitting appears.

Hematite is less prone to show superparamagnetism than goethite. Hematite in soils rarely seems to have particle sizes below 10 nm, which is about the limit for showing superparamagnetism at RT. So usually, hematite at RT has a magnetically split spectrum with a hyperfine field of about 51 T.

Goethite with sizes of about 10 nm already exhibits superparamagnetism at RT and such goethites are quite frequent in soils. They exhibit a quadrupole doublet at RT that cannot be distinguished from that of $Fe^{3+}$ in the clay mineral structure. Larger particle sizes yield magnetic patterns. Very well crystallized goethite exhibits sextets with rather narrow lines and a hyperfine field of about 37 T at RT. Intermediate particle sizes yield rather broad spectra with smaller mean fields. They are often so strongly smeared out that only a very broad line with practically no sextet structure is visible. Fortunately, at 4.2 K all goethites exhibit a sextet with narrow lines and a hyperfine field of 49 to 50 T, while hematite at 4.2 K has a field of 53 to 54 T. The hematite patterns at 4.2 K are well distinguishable from the goethite patterns. An additional broad magnetic sextet component that often appears in the 4.2 K spectra is attributed to slowly relaxing $Fe^{3+}$ in clays.

The essence of this is that hematite is usually already seen in the RT spectra, but to distinguish $Fe^{3+}$ in goethite from the $Fe^{3+}$ in the clay one needs to cool to 4.2 K.

Silicate-bound Fe in clays usually yields electric quadrupole doublets, which allow an easy distinction between $Fe^{3+}$ and $Fe^{2+}$. At RT, clay minerals never exhibit magnetic hyperfine splitting. At 4.2 K, the silicate-bound Fe sometimes orders magnetically, but this is rare and occurs only at very large Fe contents. For Fe contents of a few percent only, no magnetic ordering occurs even at 4.2 K. However, the paramagnetic relaxation processes of $Fe^{3+}$ may become slow at low temperatures. Then, magnetic sextet patterns for such Fe species are observable even though there is no magnetic order. Such paramagnetic sextets usually have rather broad lines and hyperfine fields well above 50 T, often up to 55 T. The relaxation of the Fe may, however, also occur in an intermediate time range. In this case, neither a sextet nor a doublet is observable, but a very broad "background" component. In most cases, only part of $Fe^{3+}$ exhibits slow relaxation. In this case, both a broad sextet and a doublet pattern at 4.2 K are observed. $Fe^{2+}$ practically never exhibits slow paramagnetic relaxation, due to its strong spin-lattice relaxation. The spherical half-filled 3d shell of $Fe^{3+}$ with zero orbital angular momentum does not exhibit spin-lattice relaxation and the spin-spin relaxation becomes weak when the Fe is very dilute.

**Equipment**

Transmission spectrometer (Halder Electronics), circular Lucite (Plexiglass) holders with appropriate lids, spatula

**Chemicals**

none

**Brief description**

Absorber preparation: The Mössbauer absorbers were made from the respective particle size fractions without further chemical treatment. About 500 mg of the powder sample material were filled into flat circular Lucite™ (Plexiglass™) holders with appropriate lids. An absorber thickness of 200 $mg/cm^2$ was used for all samples. This is a good compromise between the necessity to use thick absorbers to make up for the small Fe content of the specimens and the necessity to avoid excessive photoelectric attenuation of the 14.4 keV γ-rays in the absorber (Rancourt et al., 1993).

The Mössbauer spectra were taken with a standard transmission spectrometer (Halder Electronics) using a sinusoidal velocity waveform and a source of $^{57}Co$ in a rhodium matrix. The γ-rays were detected with a krypton/$CO_2$ proportional counter. Measurements at 4.2 K were performed in a liquid He bath cryostat with both the source and the absorber immersed into the liquid He. A detailed experimental and methodical description can be found in Wagner and Kyek (2004). The velocity range scanned was about 10 mm/s both at ambient temperature and at 4.2 K. The time required to obtain spectra of reasonably good statistical accuracy was between one and three days.

Data evaluation: Mössbauer spectra of minerals frequently exhibit overlapping peaks. Thus, the particular fitting technique and model assumptions strongly influence the data interpretation. The Mössbauer spectra were least-squares fitted with appropriate superpositions of Lorentzian lines grouped into electric quadrupole doublets or magnetic sextet patterns. In some cases the magnetic patterns are considerably broadened. Such spectral components were fitted with patterns corresponding to a Gaussian distribution of magnetic hyperfine fields around an appropriate median value.

**Error**

Regarding error analysis, the resolution of areas of doublets is quoted to one significant figure after the decimal. Errors of isomer shift and quadrupole splitting are usually ±0.02 mm/s, and hyperfine fields are accurate to about 0.5 T. Mössbauer spectroscopy can generally detect features down to an intensity of roughly 1% of the total Fe. The technique is not suitable for samples containing less than about 0.1 wt% of Fe (Dyar et al., 2006), because at smaller Fe contents the counting times become excessively long.

### 4.2.8 Microscopy

Particle morphology was examined by means of light microscopy and Environmental Scanning Electron Microscopy (ESEM).

With light microscopy the coarsest fraction of the ceramic clays were investigated to visualize particle morphology of large particles and agglomerates.

ESEM is a variety of conventional Scanning Electron Microscopy (SEM) by operating in ‘wet’ mode, which means that it is not necessary to prepare conductive samples by sputtering them, e.g., with gold. Therefore, their original characteristics may be preserved. This feature turns ESEM very suitable for the investigation of moisture-sensitive samples like clay minerals.

The working principle of ESEM is based on the use of water vapor as imaging gas. Water vapor is introduced to the specimen chamber. The primary electron beam penetrates the water vapor, scanning across the surface of the sample. Secondary electrons are generated, as in SEM, but they encounter water vapor molecules, which in turn produce secondary electrons themselves. Thus, the water vapor serves as a cascade amplifier, amplifying the original secondary electron signal from the sample. The amplified secondary electron signal is collected by a gaseous secondary electron detector (GSED). The intensity of the signal is converted into a brighter or darker portion of the image at a given point on the sample as the electron beam is scanning across it.

Additionally, ESEM coupled with an energy-dispersive X-ray fluorescence spectrometer (EDS) permitts simultaneous morphological and elemental studies (Bassin, 1975). EDS detects the X-rays emitted from the specimen when hit by the electron beam. The physical principle of X-ray fluorescence has been described in Section 4.2.4. Standardless EDS provides a quick semi-quantitative estimate of elemental concentration.

Further information can be found in textbooks, e.g. from Goldstein et al. (1992) or Goodhew et al. (2001).

**Equipment**

Optical microscope from Zeiss (Discovery V12), ESEM from Philips (XL 30 FEG) with EDX measurement unit, carbon foil-laminated sample holder, spatula, forceps

**Brief description**

A small amount of the powdered sample was strewn on an adhesive carbon-foil laminated aluminum holder.

The device was operated at an acceleration voltage of 15 kV and a chamber pressure of 1 Torr. For energy dispersive X-ray (EDX) measurements, a liquid nitrogen cooled Sapphire Si(Li) detecting unit from EDAX was used. The EDX-spectra collection time was between 2 and 10 minutes.

**Errors**

Misleading image interpretation due to image distortion at low magnifications (increased scan angle) (Goldstein et al., 1992).

EDX measurements carried out in this study are only semi-quantitative, because of lacking characteristics required for quantitative analysis, such as plane sample surface and reference standards.

# 5 Comprehensive characterization of the paper kaolins

## 5.1 Introduction

The largest use of kaolin is in the production of paper. Annually, about 80% of high-grade kaolin is applied as coating or filler (Harvey and Lagaly, 2006).

As paper filler, kaolin is added to the pulp to fill voids between the wood fibers to improve strength, appearance and printing characteristics of the paper. As paper coating, kaolin is applied to the surface of paper to ensure gloss, smoothness, brightness, opacity, and printability of the paper sheet (Bundy, 1993).

Both types of application require very rigid specifications regarding the brightness, which is mainly influenced by the mineralogical composition of the kaolins employed in the process (Prasad et al., 1991). Kaolins are polymineralic admixtures consisting commonly of kaolinite (occasionally including halloysite, as well as the polytypes dickite and nacrite), mica, illite, smectite, quartz, feldspar, Fe-bearing phases such as goethite, hematite, pyrite, Ti-bearing phases like anatase, rutile, ilmenite, and trace quantities of tourmaline, zircon, kyanite, and a few other heavy minerals (Murray, 2007).

As reported in Chapter 1.3.3, naturally occuring kaolin is often associated with Fe and Ti impurities, which reduce brightness, leading to a decreased economic value and hinder its application (Ryu et al., 1995; Lee et al., 2002; Shelobolina et al., 2005). Currently available physical and chemical processes for kaolin beneficiation are considered energy- and cost-intensive, not sufficiently flexible, and pollutive (Mandal and Banerjee, 2004).

As summarized in Chapter 1.3.5, alternative methods of Fe removal using metal-reducing microorganisms have yielded encouraging results for the refinement of clays. Zegeye et al. (2008) compared the efficiency of different *Shewanella* species for removing Fe from kaolins and found the greatest extents of reduction employing *Shewanella putrefaciens*, able to increase the brightness from 76% to 80%. *Shewanella putrefaciens* was found to reduce both, Fe-oxides as well as silicate-bound Fe (Kostka et al., 1999b), which envisions this microorganism as an ideal candidate for the refinement of kaolins, known to contain both types of “Fe sources” (Jepson,1988).

Aim of the following study is a detailed determination of the mineralogical phase content of three kaolins from the area of Hirschau-Schnaittenbach, Germany, in order to elucidate the effects of microbiological treatment with *Shewanella putrefaciens* on mineralogy as well as on Fe-distribution, as oxide-bound Fe seems to affect the brightness of kaolins more adversely than silicate-bound Fe (Möbius, 1977; Chandrasekhar and Raghavan, 2004).

The sampling technique and sample preparation in terms of microbiological treatment are described in Section 3.1.2. A description of the analytical methods applied to the investigation of the paper kaolins as well as grain-size fractionation are reported in Chapter 4.

## 5.2 Results

### 5.2.1 Grain-size distribution and processing properties-related parameters

The kaolin samples LA540, B4914, and B4915 as well as their microbiologically treated counterparts had very similar mineralogical water contents of about 1% when they arrived in the laboratory from the processing plant.

The following grain-size fractions were gathered from the respective kaolin samples, each before and after the microbiological treatment with *Shewanella putrefaciens*: >20 µm, 2-20 µm, 0.6-2 µm, 0.2-0.6 µm, and <0.2 µm.

Grain-size fractionation was carried out according to the pipette method described in Section 4.2.2 without adding any dispergent agent, as phosphate species – usually employed for dispersion – are known to promote the microbiological activity (Liu et al., 1982) and to extract Fe from moderately crystallized goethite (Bascomb, 1968; Beckett, 1989).

Figure 5.1a-c compares the grain-size distributions of the three kaolin samples before and after the microbiological treatment. For sample B4915, a supplementary processing step was monitored (B4915 K), which consisted of adding the growing medium without the microorganism in order to test its influence on removal efficiency.

In the following, results are presented comparing the grain-size distribution of each sample with the respective microbiologically treated counterpart. Then, the grain-size characteristics of each sample are compared to the untreated as well as treated state.

Figure 5.1a illustrates that the grain-size distributions of LA540 and LA540 MO were characterized by sizes of generally <20 µm. Both samples had a distribution maximum in the fraction 2-20 µm with about half of the total mass. With decreasing grain-size fraction, both samples showed a stepwise reduction of the respective fraction masses, but with different distributions.

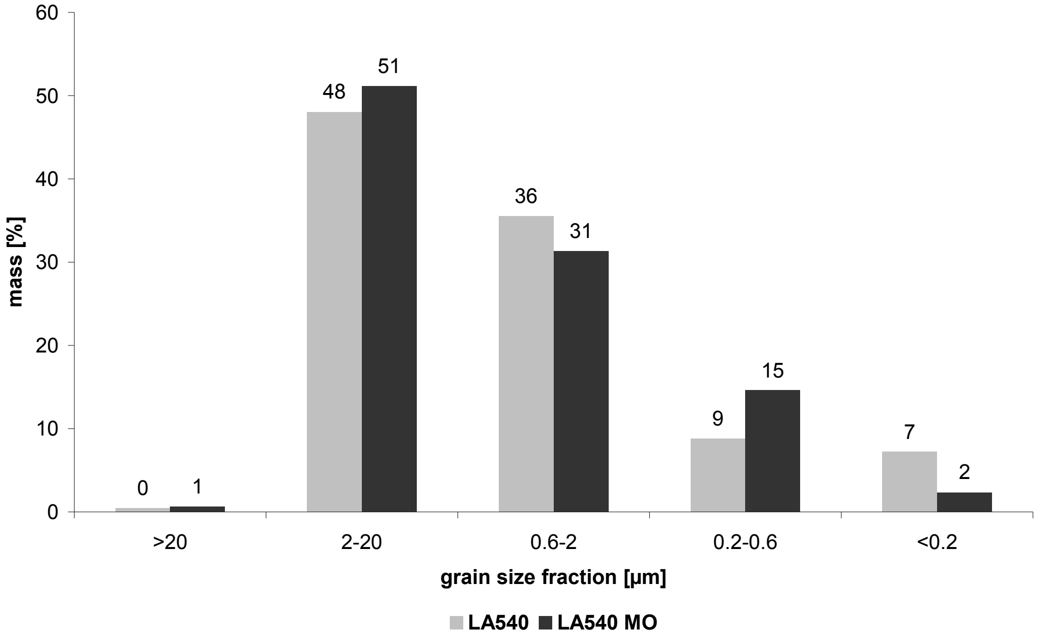

Figure 5.1a: Grain-size distribution of kaolin sample LA540 before (light grey columns) and after treatment with *Shewanella putrefaciens* (LA540 MO, black columns).

The mass distribution of the clay fractions 0.2-0.6 µm and <0.2 µm of LA540 were very similar with 9% and 7%, respectively, whereas LA540 MO yielded a mass enrichment for the fraction 0.2-0.6 µm to 15%, under strong reduction of the smallest fraction <0.2 µm to merely 2%.

As depicted in Figure 5.1b, the grain-size distributions of samples B4914 and B4914 MO strongly differed from each other. The untreated sample B4914 showed a nearly uniform distribution of the grain fractions >20 µm, 2-20 µm, and 0.6-2 µm of about 30%. The mass of the clay fractions <2 µm was 41%. Compared to sample B4914 MO, which had a mass of 55% for the clay fractions, it can be seen that the microbiological treatment resulted in a shift toward finer fractions. Both samples showed small amounts below 2% for the respective <0.2 µm fractions.

Figure 5.1c illustrates that differences between the untreated sample B4915 and the treated samples B4915 K and B4915 MO were observed mainly for the grain-size distribution of the fractions >2 µm. At 22%, B4915 showed a greater mass content in the coarsest >20 µm fraction compared to 3% and 6%, respectively, for the treated counterparts, which had a maximum in the 2-20 µm

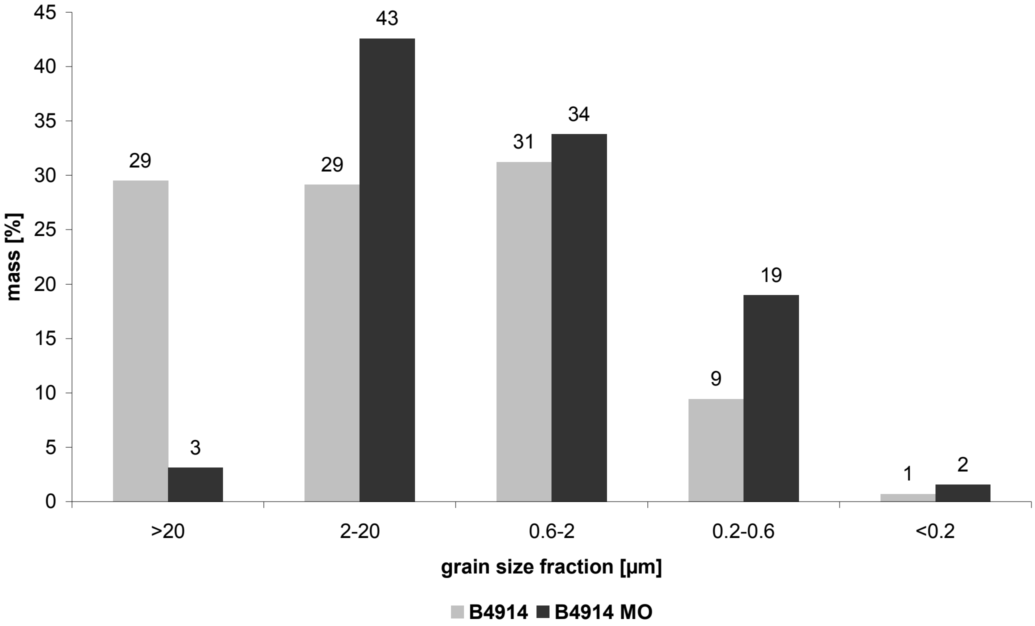

Figure 5.1b: Grain-size distribution of kaolin sample B4914 before (light grey columns) and after treatment with *Shewanella putrefaciens* (B4914 MO, black columns).

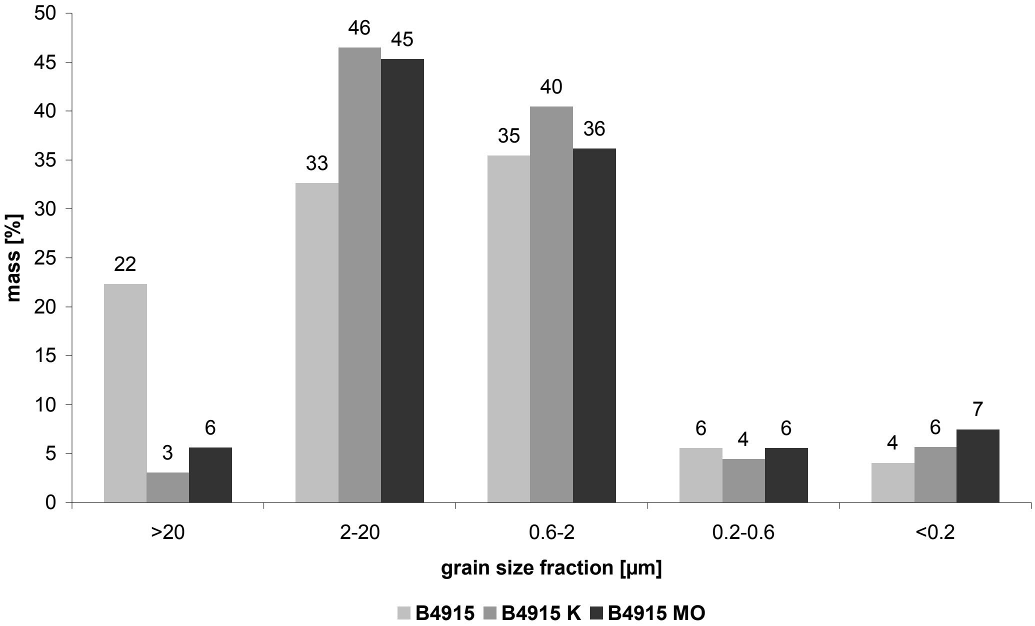

Figure 5.1c: Grain-size distribution of kaolin sample B4915 before (light grey columns), after addition of the growing medium without microorganisms (B4915 K, dark grey columns), and after treatment with *Shewanella putrefaciens* (B4915 MO, black columns).

fraction of about 45%. The distribution of sample B4915 was distended over the middle and fine silt fraction (2-20 µm), and the coarsest clay fraction (0.6-2 µm), whereas the treated samples showed a mass decrease for these fractions. Regarding the coarsest clay fraction, B4915 and B4915 MO had nearly identical values of about 35%. For the clay fractions <0.6 µm, all tested samples showed a similar grain-size distribution, with a slight increase from 10% to 13% for the microbially treated sample B4915 MO.

The comparison of all untreated kaolin samples revealed differences in grain-size distribution concerning the sum of the respective clay fractions (<2 µm), which increased in the order B4914 < B4915 < LA540. Thus at 51%, sample LA540 showed the greatest proportion of clay fraction, followed by B4915 (45%) and B4914 (42%). For all kaolin samples, the largest clay content was observed in the coarsest clay fraction (0.6-2 µm). The most evident difference noted between the untreated samples was for the coarsest fraction >20 µm, which had large masses for B4914 and B4915, but was almost absent in the case of LA540.

Comparing the changes in grain-size distribution caused by microbiological treatment, one can see that mass shifts toward finer fractions were most pronounced for sample B4914, followed by B4915. Sample LA540 seemed to be relatively unaffected by the microbiological treatment in this respect.

pH and electrical conductivity σ were recorded before and after the microbiological treatment for three replicates (Table 5.1). For all tested samples, the standard deviation was s<0.1 for the pH and s<0.5 for the electrical conductivity. The blank values of pH and σ of the deionized water were 6.9 (s=0.1) and 0.5 µS/cm (s=0.2 µS/cm), respectively, determined from 10 replicates.

Table 5.1: pH and electrical conductivity σ of the kaolin samples.

| Sample | pH | σ [µS/cm] |
|---|---|---|
| LA540 | 7.2 | 6.5 |
| LA540 MO | 7.4 | 47.8 |
| B4914 | 7.5 | 3.5 |
| B4914 MO | 6.8 | 58.9 |
| B4915 | 7.0 | 7.3 |
| B4915 MO | 7.0 | 58.1 |
| B4915 K | 6.9 | 56.6 |

All samples had pH values at about circumneutral. The influence of treatment on pH seemed to be non-systematic as sample LA540 showed a slight increase in pH after the microbiological treatment, whereas for sample B4914 the pH decreased from 7.5 to 6.8. In the case of sample B4915, the pH remained nearly constant after the various treatment steps.

Regarding the electrical conductivity, an increase was observed for all samples after the treatment. B4914 showed the strongest increase from 3.5 to 58.9 µS/cm.

The brightness of the kaolins was measured before and after 140 h of bioleaching. Table 5.2 and Figure 5.2 show that all kaolins responded to the treatment by increased brightness values, but the extent of bioleaching was different for the various bulk materials.

Sample B4915, which had the lowest brightness before the treatment, was characterized by a distinct increase in brightness, both for the bacteria-free control sample B4915 K with an increase of 2.7% as well as for the microbially treated sample B4915 MO with an increase of 8.7%. Regarding the $Fe_2O_3$ contents, it can be seen that only a slight decrease of 0.13% occurred after microbial refinement.

Table 5.2: Brightness R457 and $Fe_2O_3$ content obtained from XRF analysis of the bulk samples before and after the treatment with *Shewanella putrefaciens*.

| Sample | Brightness R457 [%] | $Fe_2O_3$ [%] |
|---|---|---|
| LA540 | 68.2 | 1.46 |
| LA540 MO | 72.1 | 1.05 |
| B4914 | 76.5 | 0.78 |
| B4914 MO | 79.2 | 0.75 |
| B4915 | 67.9 | 0.95 |
| B4915 MO | 76.6 | 0.82 |
| B4915 K | 70.6 | 0.82 |

The strongest decrease of the $Fe_2O_3$ content with 0.41% was noted for the sample with the greatest initial value (LA540), which was accompanied by an increase of brightness of 3.9% after bioleaching.

Among the tested samples, B4914, which was characterized by the smallest $Fe_2O_3$ content (0.78%) and a slight decrease of 0.03% after bioleaching, showed the smallest increase in brightness (2.7%).

Additionally, the brightness of each grain-size fraction of sample LA540 prior to bioleaching was measured, in order to detect changes in brightness with mineralogical composition, as the amount of clay minerals was assumed to increase with decreasing particle size. This analysis was exclusively done for kaolin sample LA540, due to the time-consuming fractionation procedure required for about 1 kg of the bulk material. Such a great amount was employed to obtain at least 10 g of each fraction, which were required for the duly measurement of brightness.

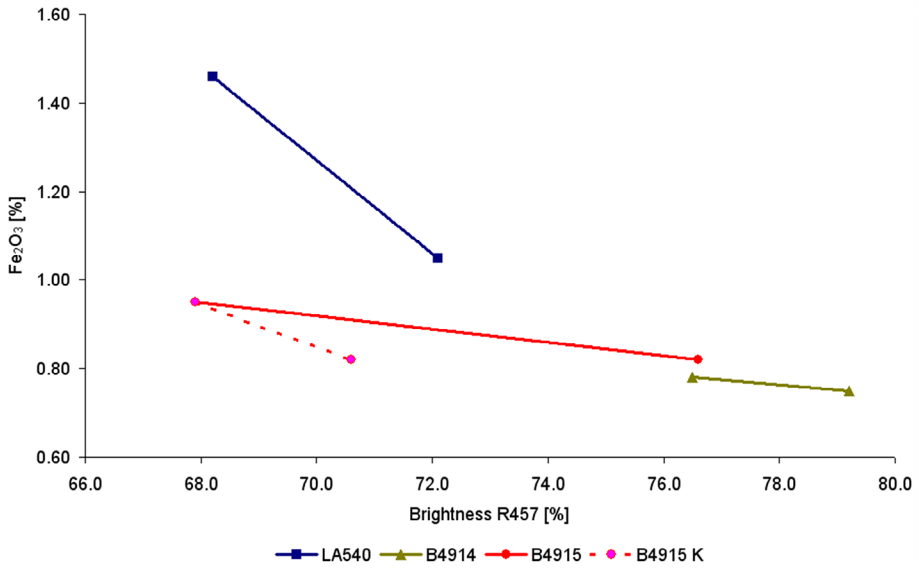

Figure 5.2: Correlation between brightness and $Fe_2O_3$ content before and after the leaching experiment with *Shewanella putrefaciens* of the bulk kaolin samples LA540, B4914, B4915 (bold lines), and the control sample B4915 K (dashed line).

Table 5.3 summarizes the brightness values and $Fe_2O_3$ contents for the bulk material of sample LA540 and the grain-size fractions. The correlations between the respective parameters are represented by Figure 5.3.

Table 5.3: Brightness R457 and $Fe_2O_3$ content of sample LA540 and of the grain-size fractions.

| LA540 | Brightness R457 [%] | $Fe_2O_3$ [%] |
|---|---|---|
| bulk | 68.2 | 1.46 |
| >20 µm | 63.6 | 2.09 |
| 2-20 µm | 78.0 | 0.48 |
| 0.6-2 µm | 74.1 | 1.19 |
| 0.2-0.6 µm | 42.1 | 3.94 |
| <0.2 µm | 36.0 | 4.27 |

Figure 5.3a illustrates the presence of a close ($R^2$=0.99) negative linear correlation between $Fe_2O_3$ content and brightness within the sample set. With the exception of the >20 µm, the brightness decreased with decreasing grain-size fraction, but without any discernable regression type (Figure 5.3b).

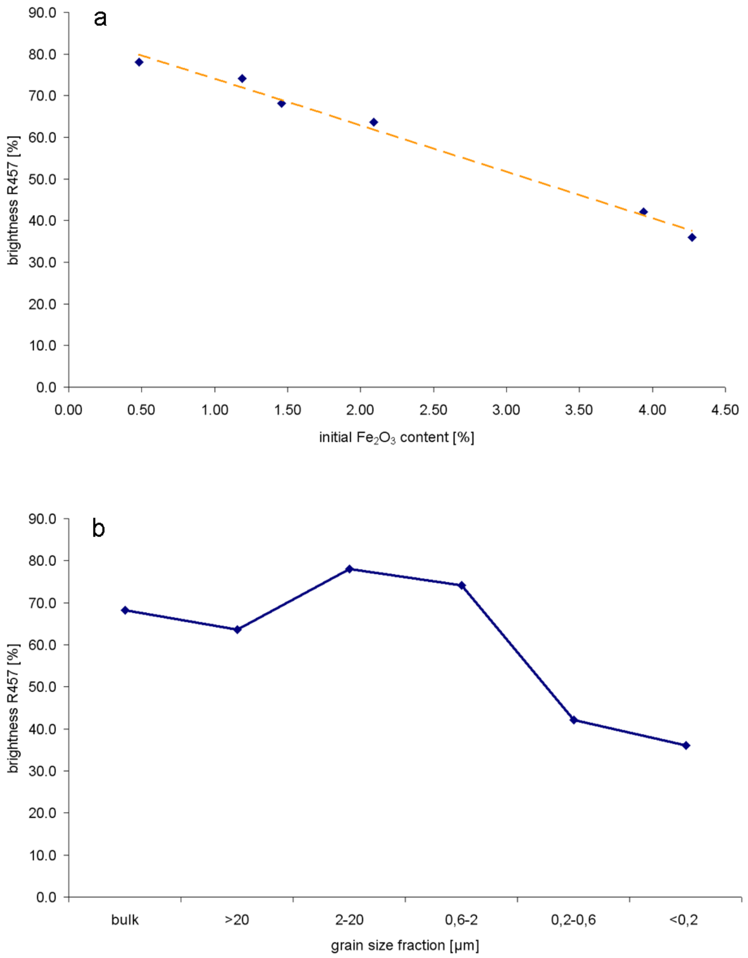

Figure 5.3: Bulk sample and grain-size fractions of kaolin LA540 (a) correlation between $Fe_2O_3$ content and brightness and (b) correlation with brightness.

### 5.2.2 X-ray techniques

All kaolin samples as well as their respective grain-size fractions were investigated by means of XRD and XRF in order to quantify the mineralogical and chemical composition. After phase identification according to their peak positions, the phase content of each sample was determined applying Rietveld analysis. Afterwards, the results were crosschecked with the results from XRF analysis, converting the phase content to element oxides and comparing them to the results from XRF analysis.

Regarding the chemical composition (Table 5.4), discernable differences between bulk materials were found. Sample LA540 was characterized by a higher $SiO_2$ (≈ 59%) and smaller $Al_2O_3$ concentration (≈ 35%) compared to the samples B4914 and B4915, which both showed contents of about 55% $SiO_2$ and 41% $Al_2O_3$, respectively. These differences were also reflected by the microbiologically treated bulk samples.

Table 5.4a: Chemical composition of the kaolin samples LA540 and LA540 MO and their respective grain-size fractions. Values were normalized for loss on ignition (LOI).

| | $SiO_2$ [%] | $Al_2O_3$ [%] | $Fe_2O_3$ [%] | MgO [%] | CaO [%] | $Na_2O$ [%] | $K_2O$ [%] | $TiO_2$ [%] | $P_2O_5$ [%] | LOI [%] |
|---|---|---|---|---|---|---|---|---|---|---|
| LA540 bulk | 58.83 | 34.65 | 1.46 | 0.71 | 0.19 | 0.08 | 3.05 | 0.70 | 0.34 | 11.20 |
| LA540 >20 µm | 57.32 | 33.03 | 2.09 | 0.90 | 0.19 | 0.03 | 5.24 | 0.72 | 0.48 | 11.86 |
| LA540 2-20 µm | 59.57 | 36.90 | 0.48 | 0.16 | 0.06 | 0.06 | 2.32 | 0.48 | 0.07 | 10.92 |
| LA540 0.6-2 µm | 59.57 | 34.50 | 1.19 | 0.52 | 0.19 | 0.06 | 2.37 | 0.92 | 0.69 | 10.82 |
| LA540 0.2-0.6 µm | 55.31 | 30.08 | 3.94 | 1.91 | 0.56 | 0.00 | 6.33 | 1.46 | 0.40 | 10.67 |
| LA540 <0.2 µm | 57.63 | 27.64 | 4.27 | 2.36 | 0.84 | 0.55 | 6.27 | 0.31 | 0.14 | 11.98 |
| LA540 MO bulk | 59.42 | 34.72 | 1.05 | 0.35 | 0.11 | 0.00 | 2.87 | 0.52 | 0.96 | 10.98 |
| LA540 MO >20 µm | 57.50 | 32.30 | 2.28 | 1.08 | 0.22 | 0.01 | 5.29 | 0.70 | 0.62 | 13.07 |
| LA540 MO 2-20 µm | 59.29 | 35.81 | 0.58 | 0.07 | 0.07 | 0.00 | 2.86 | 0.40 | 0.91 | 10.44 |
| LA540 MO 0.6-2 µm | 60.26 | 34.82 | 0.97 | 0.28 | 0.12 | 0.00 | 2.14 | 0.54 | 0.86 | 10.86 |
| LA540 MO 0.2-0.6 µm | 55.12 | 30.01 | 3.52 | 2.23 | 0.95 | 0.18 | 6.25 | 1.37 | 0.37 | 10.61 |
| LA540 MO <0.2 µm | 56.82 | 27.50 | 3.94 | 2.82 | 1.16 | 0.93 | 6.43 | 0.29 | 0.11 | 13.22 |

Table 5.4b: Chemical composition of the kaolin samples B4914 and B4914 MO and their respective grain-size fractions. Values were normalized for loss on ignition (LOI).

| | $SiO_2$ [%] | $Al_2O_3$ [%] | $Fe_2O_3$ [%] | MgO [%] | CaO [%] | $Na_2O$ [%] | $K_2O$ [%] | $TiO_2$ [%] | $P_2O_5$ [%] | LOI [%] |
|---|---|---|---|---|---|---|---|---|---|---|
| B4914 bulk | 54.67 | 41.34 | 0.78 | 0.17 | 0.13 | 0.00 | 2.22 | 0.47 | 0.21 | 12.34 |
| B4914 >20 µm | 54.68 | 42.44 | 0.56 | 0.00 | 0.08 | 0.00 | 1.65 | 0.43 | 0.16 | 12.89 |
| B4914 2-20 µm | 56.11 | 40.08 | 0.61 | 0.07 | 0.09 | 0.00 | 2.66 | 0.27 | 0.10 | 11.88 |
| B4914 0.6-2 µm | 53.49 | 42.42 | 0.90 | 0.24 | 0.15 | 0.00 | 1.91 | 0.58 | 0.32 | 13.14 |
| B4914 0.2-0.6 µm | 53.72 | 39.91 | 1.33 | 0.55 | 0.19 | 0.00 | 3.22 | 0.80 | 0.27 | 12.79 |
| B4914 <0.2 µm | 52.30 | 40.38 | 1.92 | 0.68 | 0.35 | 0.23 | 3.26 | 0.67 | 0.21 | 14.28 |
| B4914 MO bulk | 54.64 | 41.32 | 0.75 | 0.25 | 0.08 | 0.00 | 2.23 | 0.47 | 0.25 | 12.95 |
| B4914 MO >20 µm | 54.94 | 42.10 | 0.53 | 0.00 | 0.07 | 0.00 | 1.72 | 0.44 | 0.20 | 11.94 |
| B4914 MO 2-20 µm | 55.99 | 40.15 | 0.56 | 0.05 | 0.05 | 0.00 | 2.56 | 0.48 | 0.17 | 11.89 |
| B4914 MO 0.6-2 µm | 53.68 | 43.18 | 0.74 | 0.18 | 0.07 | 0.00 | 1.52 | 0.40 | 0.23 | 13.43 |
| B4914 MO 0.2-0.6 µm | 53.49 | 41.31 | 1.15 | 0.51 | 0.12 | 0.00 | 2.49 | 0.56 | 0.37 | 14.48 |
| B4914 MO <0.2 µm | 52.84 | 39.92 | 1.22 | 0.60 | 0.58 | 1.17 | 2.85 | 0.53 | 0.29 | 27.42 |

Table 5.4c: Chemical composition of the kaolin samples B4915, B4915 MO and B4915 K and their respective grain-size fractions. Values were normalized for loss on ignition (LOI).

| | $SiO_2$ | $Al_2O_3$ | $Fe_2O_3$ | MgO | CaO | $Na_2O$ | $K_2O$ | $TiO_2$ | $P_2O_5$ | LOI |
|---|---|---|---|---|---|---|---|---|---|---|
| | [%] | [%] | [%] | [%] | [%] | [%] | [%] | [%] | [%] | [%] |
| B4915 bulk | 54.60 | 40.99 | 0.95 | 0.31 | 0.11 | 0.07 | 2.33 | 0.49 | 0.15 | 12.04 |
| B4915 >20 µm | 54.91 | 42.16 | 0.61 | 0.00 | 0.08 | 0.00 | 1.73 | 0.42 | 0.08 | 12.66 |
| B4915 2-20 µm | 56.12 | 40.14 | 0.64 | 0.06 | 0.09 | 0.00 | 2.58 | 0.29 | 0.07 | 11.97 |
| B4915 0.6-2 µm | 53.50 | 42.13 | 1.05 | 0.26 | 0.15 | 0.00 | 2.00 | 0.58 | 0.32 | 12.92 |
| B4915 0.2-0.6 µm | 53.62 | 40.83 | 1.24 | 0.35 | 0.18 | 0.00 | 2.53 | 0.98 | 0.26 | 13.04 |
| B4915 <0.2 µm | 53.65 | 36.75 | 2.01 | 0.95 | 0.63 | 0.67 | 4.46 | 0.69 | 0.20 | 13.97 |
| B4915 MO bulk | 54.75 | 40.91 | 0.82 | 0.32 | 0.08 | 0.08 | 2.37 | 0.48 | 0.19 | 13.06 |
| B4915 MO >20 µm | 55.85 | 38.55 | 0.97 | 0.22 | 0.08 | 0.00 | 3.39 | 0.70 | 0.23 | 13.28 |
| B4915 MO 2-20 µm | 55.97 | 40.24 | 0.65 | 0.06 | 0.06 | 0.00 | 2.52 | 0.41 | 0.08 | 11.93 |
| B4915 MO 0.6-2 µm | 53.63 | 42.51 | 0.94 | 0.23 | 0.10 | 0.00 | 1.85 | 0.47 | 0.26 | 13.07 |
| B4915 MO 0.2-0.6 µm | 53.51 | 41.77 | 1.16 | 0.33 | 0.13 | 0.00 | 2.17 | 0.55 | 0.35 | 13.69 |
| B4915 MO <0.2 µm | 52.43 | 38.91 | 1.51 | 0.67 | 0.43 | 1.00 | 3.49 | 0.78 | 0.74 | 18.51 |
| B4915 K bulk | 54.67 | 41.03 | 0.82 | 0.32 | 0.07 | 0.07 | 2.38 | 0.49 | 0.15 | 12.26 |
| B4915 K >20 µm | 56.68 | 39.01 | 0.59 | 0.01 | 0.07 | 0.00 | 3.10 | 0.45 | 0.08 | 12.18 |
| B4915 K 2-20 µm | 55.85 | 40.57 | 0.63 | 0.04 | 0.06 | 0.00 | 2.37 | 0.38 | 0.08 | 12.06 |
| B4915 K 0.6-2 µm | 53.60 | 42.35 | 1.01 | 0.23 | 0.10 | 0.00 | 1.87 | 0.55 | 0.27 | 12.92 |
| B4915 K 0.2-0.6 µm | 53.67 | 40.48 | 1.40 | 0.47 | 0.14 | 0.00 | 2.82 | 0.77 | 0.23 | 13.07 |
| B4915 K <0.2 µm | 53.32 | 38.12 | 1.53 | 0.71 | 0.36 | 1.22 | 4.08 | 0.46 | 0.17 | 15.36 |

Concerning the dyeing element oxides, LA540 showed the greatest $Fe_2O_3$ content (1.46%), whereas B4914 and B4915 both had smaller contents of about 0.8%. The microbiological treatment led to a decrease of the bulk materials' $Fe_2O_3$ content, pronounced for sample LA540 and negligible for B4914 and B4915. A tendency of an increasing $Fe_2O_3$ content with decreasing grain-size fraction has been observed, which was analogous for the treated samples. The $TiO_2$ content was also greatest for sample LA540. The other two kaolin samples had equal $TiO_2$ amounts of about 0.5%. With microbiological treatment, the amount of $TiO_2$ decreases slightly within all fractions. For sample B4914, a slight decrease was identified only for the clay fractions. For the respective bulk samples of B4915, the $TiO_2$ content remained nearly constant during the different treatment steps. Throughout the various grain-size fractions, the $TiO_2$ content varied slightly without any apparent tendency.

Regarding the amounts of MgO, CaO and $Na_2O$, an increase toward finer fractions was noted for all kaolins, which became even more pronounced by the microbiological treatment. The bulk material as well as the grain-size fractions of LA540 and LA540 MO showed distinctly greater MgO contents compared to B4914 and B4915 and their treated analogs.

Within all fractionated kaolin samples, the $K_2O$ content follows a bimodal distribution, having its maxima mostly in the fractions >2 µm and <0.6 µm.

After microbiological treatment, B4914 and B4915 were characterized by decreased $K_2O$ values within the clay fractions, whereas the all in all greatest $K_2O$ contents of sample LA540 slightly increased within the finest clay fraction.

For all kaolin samples, the loss on ignition (LOI) had the largest values for the finest clay fraction <0.2 µm, with markedly higher values for the treated counterparts.

XRD analysis revealed the mineralogical composition of the kaolins. For all samples kaolinite, illite, muscovite, orthoclase/microcline, quartz, rutile/anatase, and crandallite have been identified. The presence of I-S mixed layer minerals was separately determined by ODPF from oriented samples (see below). As orthoclase and microcline as well as rutile and anatase could not be attributed unequivocally according to their peak positions, they were summarized as K-feldspar and Ti oxides, respectively.

Then, the quantitative phase content of the bulk materials as well as their grain-size fractions were determined with Rietveld analysis before and after the microbiological treatment.

The results gathered by Rietveld analysis were crosschecked with the chemical composition from XRF analysis. Structural formulae and chemical composition used for the conversion of the mineralogical phase content to element oxides are listed in Table 5.5.

Table 5.5: Structural formulae and chemical composition of the mineralogical phases applied to the crosscheck of XRD and XRF data.

| Phase | Chemical composition [%] | | | | | | | | |
|---|---|---|---|---|---|---|---|---|---|
| *Structural formula* | $SiO_2$ | $Al_2O_3$ | $Fe_2O_3$ | MgO | CaO | $Na_2O$ | $K_2O$ | $TiO_2$ | $P_2O_5$ |
| Kaolinite<br>$Al_2Si_2O_5(OH)_4$ | 54.10 | 45.90 | | | | | | | |
| Muscovite<br>$KAl_2Si_3AlO_{10}(OH,F)_2$ | 47.40 | 40.22 | | | | | 12.38 | | |
| Illite * | 50.90 | 35.76 | 1.06 | 1.07 | | | 11.22 | | |
| K-feldspar<br>$KAlSi_3O_8$ | 64.70 | 18.40 | | | | | 16.90 | | |
| Quartz<br>$SiO_2$ | 100.00 | | | | | | | | |
| Ti oxides<br>$TiO_2$ | | | | | | | | 100.00 | |
| Crandallite<br>$CaAl_3(PO_4)_3\cdot(H_2O)$ | | 43.58 | | | 15.98 | | | | 40.44 |

All structural formulae taken from Downs and Hall-Wallace (2003), except * illite $K_{0.89}(Si_{3.20}Al_{0.80})(Al_{1.85}Fe_{0.05}Mg_{0.10})[O_{10}(OH)_2]$ taken from Środoń et al. (1992).

The deviations resulting from this procedure were then minimized by lowering or raising the amounts of those phases suspected to cause differences between Rietveld analysis and XRF measurements. In an iterative process, the adapted phase content of each sample was again crosschecked with the chemical composition until a minimum deviation was reached. Tables 9.2 a-g in the Appendix compare the deviations resulting from the XRD-XRF crosscheck with those obtained after the iteration (XRD-XRF adapted). A negative deviation denotes overestimation; a positive deviation denotes underestimation of the respective results from Rietveld analysis referred to the element oxide contents gathered from XRF measurements.

The modifications made throughout the various iteration steps were based on the following considerations:

- With decreasing grain-size fraction, the clay mineral content should, in principal, increase, with the consequence that deviations for $K_2O$ in the silt fractions were preferentially ascribed to K-feldspar (orthoclase, microcline) or, for the clay fractions (<2 µm), to illite.
- Furthermore, positive deviations for $K_2O$ were tried to be corrected by adding the muscovite content to those of illite, which led also to more reasonable $Al_2O_3$ values, consistently overestimated by Rietveld analysis.
- Negative $Al_2O_3$ deviations were compensated by decreasing the kaolinite content.
- Deviations for $SiO_2$ were buffered adjusting the quartz content.
- The total amount of $TiO_2$ was assigned to Ti-bearing phases.
- The total amount of $P_2O_5$ was accounted for by crandallite.
- As Fe phases could not be detected by Rietveld analysis due to small $Fe_2O_3$ quantities and distribution diversity as Fe (oxy-hydr)oxides and silicate-bound Fe, the positive deviations of $Fe_2O_3$ remaining after the XRD-XRF crosscheck were attributed to Fe phases.

In order to prove consistency of the modifications made, the amount of clay minerals of the adapted phase contents was then crosschecked with the results from STA measurements (mass loss during dehydroxylation reaction) according to the method described in Section 4.2.5. The results of this crosscheck are reported in Section 5.2.3 (Table 5.8).

Table 5.6 compares the quantification results from Rietveld analysis with the results obtained after the XRD-XRF crosscheck.

Independent of the quantification method and treatment, some general tendencies became evident. All bulk samples contained large amounts of kaolinite, which exceeded 80% for samples B4914 and B4915, but was notably smaller for sample LA540 (>63%). Nearly all samples showed the largest kaolinite amount in the fractions >2 µm. Within the clay size fractions (<2 µm), the kaolinite content decreased with decreasing grain size, whereas the illite

Table 5.6a: Phase content of the kaolin sample LA540 and of the grain-size fractions determined by Rietveld analysis (Rietveld) and after the crosscheck with the results from chemical composition (XRD-XRF adapted).

| LA540 | Quantification method | bulk [%] | >20 µm [%] | 2-20 µm [%] | 0.6-2 µm [%] | 0.2-0.6 µm [%] | <0.2 µm [%] |
|---|---|---|---|---|---|---|---|
| Kaolinite | Rietveld | 67 | 66 | 77 | 65 | 68 | 59 |
| | XRD-XRF adapted | 65 | 57 | 73 | 63 | 30 | 17 |
| Illite | Rietveld | 13 | 8 | 7 | 14 | 14 | 16 |
| | XRD-XRF adapted | 9 | 4 | 5 | 11 | 37 | 58 |
| K-Feldspar | Rietveld | 9 | 18 | 7 | 5 | 10 | 17 |
| | XRD-XRF adapted | 11 | 27 | 10 | 5 | 14 | 0 |
| Quartz | Rietveld | 11 | 8 | 9 | 5 | 6 | 6 |
| | XRD-XRF adapted | 12 | 8 | 11 | 17 | 13 | 21 |
| Ti oxides | Rietveld | 0 | 0 | 0 | 1 | 2 | 1 |
| | XRD-XRF adapted | 1 | 1 | 1 | 1 | 1 | 0 |
| Crandallite | Rietveld | 0 | 0 | 0 | 0 | 0 | 1 |
| | XRD-XRF adapted | 1 | 1 | 0 | 2 | 1 | 0 |
| Fe phases | Rietveld | n.d. | n.d. | n.d. | n.d. | n.d. | n.d. |
| | XRD-XRF adapted | 2 | 2 | 0 | 1 | 4 | 4 |

n.d.: not determinable with the respective method

Table 5.6b: Phase content of the kaolin sample LA540 MO and of the grain-size fractions determined by Rietveld analysis (Rietveld) and after the crosscheck with the results from chemical composition (XRD-XRF adapted).

| LA540 MO | Quantification method | bulk [%] | >20 µm [%] | 2-20 µm [%] | 0.6-2 µm [%] | 0.2-0.6 µm [%] | <0.2 µm [%] |
|---|---|---|---|---|---|---|---|
| Kaolinite | Rietveld | 67 | 79 | 76 | 65 | 60 | 34 |
| | XRD-XRF adapted | 63 | 51 | 67 | 62 | 21 | 32 |
| Illite | Rietveld | 15 | 12 | 7 | 15 | 29 | 44 |
| | XRD-XRF adapted | 9 | 15 | 9 | 12 | 57 | 49 |
| K-Feldspar | Rietveld | 6 | 4 | 4 | 4 | 4 | 10 |
| | XRD-XRF adapted | 10 | 21 | 12 | 5 | 0 | 5 |
| Quartz | Rietveld | 12 | 4 | 12 | 16 | 6 | 11 |
| | XRD-XRF adapted | 14 | 9 | 11 | 18 | 16 | 11 |
| Ti oxides | Rietveld | 0 | 1 | 1 | 0 | 1 | 1 |
| | XRD-XRF adapted | 1 | 1 | 0 | 1 | 1 | 0 |
| Crandallite | Rietveld | 0 | 0 | 0 | 0 | 0 | 0 |
| | XRD-XRF adapted | 2 | 1 | 1 | 2 | 1 | 0 |
| Fe phases | Rietveld | n.d. | n.d. | n.d. | n.d. | n.d. | n.d. |
| | XRD-XRF adapted | 1 | 2 | 0 | 1 | 3 | 3 |

n.d.: not determinable with the respective method

Table 5.6c: Phase content of the kaolin sample B4914 and of the grain-size fractions determined by Rietveld analysis (Rietveld) and after the crosscheck with the results from chemical composition (XRD-XRF adapted).

| B4914 | Quantification method | bulk [%] | >20 µm [%] | 2-20 µm [%] | 0.6-2 µm [%] | 0.2-0.6 µm [%] | <0.2 µm [%] |
|---|---|---|---|---|---|---|---|
| Kaolinite | Rietveld | 86 | 89 | 82 | 78 | 70 | 69 |
| | XRD-XRF adapted | 80 | 86 | 75 | 79 | 66 | 68 |
| Illite | Rietveld | 7 | 4 | 9 | 15 | 23 | 26 |
| | XRD-XRF adapted | 8 | 5 | 10 | 14 | 25 | 29 |
| K-Feldspar | Rietveld | 5 | 5 | 6 | 3 | 3 | 3 |
| | XRD-XRF adapted | 7 | 7 | 9 | 2 | 3 | 0 |
| Quartz | Rietveld | 2 | 2 | 3 | 2 | 3 | 2 |
| | XRD-XRF adapted | 3 | 2 | 5 | 2 | 4 | 0 |
| Ti oxides | Rietveld | 0 | 0 | 0 | 1 | 1 | 0 |
| | XRD-XRF adapted | 0 | 0 | 0 | 1 | 1 | 1 |
| Crandallite | Rietveld | 0 | 0 | 0 | 1 | 1 | 0 |
| | XRD-XRF adapted | 1 | 0 | 0 | 1 | 1 | 0 |
| Fe phases | Rietveld | n.d. | n.d. | n.d. | n.d. | n.d. | n.d. |
| | XRD-XRF adapted | 1 | 1 | 1 | 1 | 1 | 2 |

n.d.: not determinable with the respective method

Table 5.6d: Phase content of the kaolin sample B4914 MO and of the grain-size fractions determined by Rietveld analysis (Rietveld) and after the crosscheck with the results from chemical composition (XRD-XRF adapted).

| B4914 MO | Quantification method | bulk [%] | >20 µm [%] | 2-20 µm [%] | 0.6-2 µm [%] | 0.2-0.6 µm [%] | <0.2 µm [%] |
|---|---|---|---|---|---|---|---|
| Kaolinite | Rietveld | 80 | 76 | 89 | 88 | 77 | 73 |
|  | XRD-XRF adapted | 80 | 82 | 76 | 85 | 74 | 69 |
| Illite | Rietveld | 13 | 9 | 6 | 8 | 17 | 23 |
|  | XRD-XRF adapted | 9 | 9 | 8 | 10 | 18 | 26 |
| K-Feldspar | Rietveld | 5 | 10 | 3 | 2 | 3 | 3 |
|  | XRD-XRF adapted | 7 | 4 | 9 | 2 | 3 | 0 |
| Quartz | Rietveld | 1 | 3 | 2 | 1 | 2 | 1 |
|  | XRD-XRF adapted | 3 | 3 | 5 | 2 | 3 | 3 |
| Ti oxides | Rietveld | 0 | 1 | 0 | 1 | 0 | 0 |
|  | XRD-XRF adapted | 0 | 1 | 0 | 0 | 1 | 1 |
| Crandallite | Rietveld | 1 | 1 | 0 | 0 | 1 | 0 |
|  | XRD-XRF adapted | 1 | 1 | 0 | 1 | 0 | 1 |
| Fe phases | Rietveld | n.d. | n.d. | n.d. | n.d. | n.d. | n.d. |
|  | XRD-XRF adapted | 1 | 0 | 1 | 1 | 1 | 1 |

n.d.: not determinable with the respective method

Table 5.6e: Phase content of the kaolin sample B4915 and of the grain-size fractions determined by Rietveld analysis (Rietveld) and after the crosscheck with the results from chemical composition (XRD-XRF adapted).

| B4915 | Quantification method | bulk [%] | >20 µm [%] | 2-20 µm [%] | 0.6-2 µm [%] | 0.2-0.6 µm [%] | <0.2 µm [%] |
|---|---|---|---|---|---|---|---|
| Kaolinite | Rietveld | 81 | 90 | 83 | 76 | 76 | 77 |
|  | XRD-XRF adapted | 77 | 84 | 76 | 78 | 73 | 55 |
| Illite | Rietveld | 12 | 4 | 7 | 16 | 18 | 16 |
|  | XRD-XRF adapted | 14 | 7 | 9 | 16 | 19 | 37 |
| K-Feldspar | Rietveld | 5 | 4 | 6 | 4 | 3 | 3 |
|  | XRD-XRF adapted | 5 | 6 | 9 | 1 | 2 | 4 |
| Quartz | Rietveld | 2 | 2 | 4 | 2 | 1 | 4 |
|  | XRD-XRF adapted | 4 | 2 | 5 | 3 | 3 | 3 |
| Ti oxides | Rietveld | 0 | 0 | 0 | 1 | 1 | 0 |
|  | XRD-XRF adapted | 0 | 0 | 0 | 1 | 1 | 0 |
| Crandallite | Rietveld | 0 | 0 | 0 | 1 | 1 | 0 |
|  | XRD-XRF adapted | 0 | 0 | 0 | 1 | 1 | 0 |
| Fe phases | Rietveld | n.d. | n.d. | n.d. | n.d. | n.d. | n.d. |
|  | XRD-XRF adapted | 1 | 1 | 1 | 1 | 1 | 1 |

n.d.: not determinable with the respective method

Table 5.6f: Phase content of the kaolin sample B4915 MO and of the grain-size fractions determined by Rietveld analysis (Rietveld) and after the crosscheck with the results from chemical composition (XRD-XRF adapted).

| B4915 MO | Quantification method | bulk [%] | >20 µm [%] | 2-20 µm [%] | 0.6-2 µm [%] | 0.2-0.6 µm [%] | <0.2 µm [%] |
|---|---|---|---|---|---|---|---|
| Kaolinite | Rietveld | 83 | 75 | 84 | 86 | 83 | 77 |
| | XRD-XRF adapted | 77 | 68 | 77 | 81 | 77 | 62 |
| Illite | Rietveld | 10 | 12 | 7 | 11 | 7 | 16 |
| | XRD-XRF adapted | 12 | 14 | 8 | 13 | 16 | 27 |
| K-Feldspar | Rietveld | 5 | 8 | 6 | 2 | 6 | 3 |
| | XRD-XRF adapted | 6 | 11 | 9 | 2 | 2 | 3 |
| Quartz | Rietveld | 2 | 4 | 3 | 1 | 3 | 3 |
| | XRD-XRF adapted | 4 | 5 | 4 | 2 | 2 | 4 |
| Ti oxides | Rietveld | 0 | 1 | 0 | 0 | 0 | 0 |
| | XRD-XRF adapted | 0 | 1 | 0 | 0 | 1 | 1 |
| Crandallite | Rietveld | 0 | 0 | 0 | 0 | 1 | 1 |
| | XRD-XRF adapted | 0 | 1 | 0 | 1 | 1 | 2 |
| Fe phases | Rietveld | n.d. | n.d. | n.d. | n.d. | n.d. | n.d. |
| | XRD-XRF adapted | 1 | 1 | 1 | 1 | 1 | 1 |

n.d.: not determinable with the respective method

Table 5.6g: Phase content of the kaolin sample B4915 K and of the grain-size fractions determined by Rietveld analysis (Rietveld) and after the crosscheck with the results from chemical composition (XRD-XRF adapted).

| B4915 K | Quantification method | bulk [%] | >20 µm [%] | 2-20 µm [%] | 0.6-2 µm [%] | 0.2-0.6 µm [%] | <0.2 µm [%] |
|---|---|---|---|---|---|---|---|
| Kaolinite | Rietveld | 81 | 82 | 85 | 81 | 70 | 85 |
| | XRD-XRF adapted | 77 | 73 | 78 | 80 | 69 | 58 |
| Illite | Rietveld | 12 | 6 | 7 | 12 | 24 | 11 |
| | XRD-XRF adapted | 13 | 8 | 8 | 12 | 24 | 33 |
| K-Feldspar | Rietveld | 5 | 8 | 5 | 4 | 4 | 3 |
| | XRD-XRF adapted | 6 | 13 | 9 | 3 | 1 | 3 |
| Quartz | Rietveld | 2 | 4 | 3 | 2 | 1 | 1 |
| | XRD-XRF adapted | 3 | 5 | 4 | 2 | 4 | 5 |
| Ti oxides | Rietveld | 0 | 0 | 0 | 0 | 0 | 0 |
| | XRD-XRF adapted | 0 | 0 | 0 | 1 | 1 | 0 |
| Crandallite | Rietveld | 0 | 0 | 0 | 1 | 1 | 0 |
| | XRD-XRF adapted | 0 | 0 | 0 | 1 | 1 | 0 |
| Fe phases | Rietveld | n.d. | n.d. | n.d. | n.d. | n.d. | n.d. |
| | XRD-XRF adapted | 1 | 1 | 1 | 1 | 1 | 1 |

n.d.: not determinable with the respective method

content continuously increased with decreasing grain size throughout all fractions.

Comparing the results for quantification of kaolinite obtained by Rietveld analysis with those of the crosscheck (XRD-XRF adapted), the latter values were smaller, in particular for the clay size fractions, whereas the crosschecked illite contents exceeded the results from Rietveld analysis for the clay size fractions.

The overall smaller clay contents (sum of kaolinite and illite) of the adapted quantification from the XRD-XRF crosscheck were balanced by greater K-feldspar and quartz contents. Thus, reversed deviations between quantification results from Rietveld analysis and XRD-XRF crosscheck were noted for K-feldspar and quartz. For the bulk material as well as the silt fractions, nearly all kaolinites showed higher K-feldspar and quartz contents after the crosscheck. Regarding the clay fractions, the respective K-feldspar contents were below the results from Rietveld analysis, whereas the quartz contents gathered from XRD-XRF crosscheck were mostly higher.

The contents of Ti oxide and crandallite varied generally between 0% and 1%. Slight variations between the tested kaolins obtained from XRF analyses disappeared owing to rounding. Thus, quantitative XRD analyses did not resolve sufficiently the Ti oxide and crandallite contents in order to deduce correlations referred to grain-size distribution.

For reasons mentioned above, Rietveld analysis yielded no results for the abundance of Fe phases in terms of Fe (oxy-hydr)oxides. Therefore, their contents were derived from the XRD-XRF crosscheck. After microbiological treatment, decreasing Fe contents were observed only for sample LA540, whereas the $Fe_2O_3$-poorer samples B4914 and B4915 had values of 1%, both before and after treatment.

In order to detect the presence of swellable components, XRD patterns of EG-solvated oriented samples of all clay fractions were recorded and compared with the respective air-dried (AD) and heat-treated samples (375 °C). Figure 5.4 shows the XRD patterns of the various clay fractions of sample LA540. The XRD patterns for the coarsest clay fraction (0.6-2 µm) exhibited strong reflections at 7.14 Å and 3.57 Å from kaolinite, and a non-rational series of basal reflections with d(001) at about 10 Å. These values varied slightly from a rational series for illite and are diagnostic for I-S mixed-layered species.

After EG solvation, changes in the diffraction patterns of all samples were observed that were less pronounced for the samples of the coarsest clay fraction and well pronounced for the clay fractions <0.6 µm. Peak shift in the region between 7 and 8° 2θ and broadening of the peak at 17.7° 2θ indicated the presence of a smectitic component. The identification of I-S mixed-layered species was confirmed by the heat-treated samples, whose whose XRD patterns resembled a physical mixture of a pure illite and kaolinite.

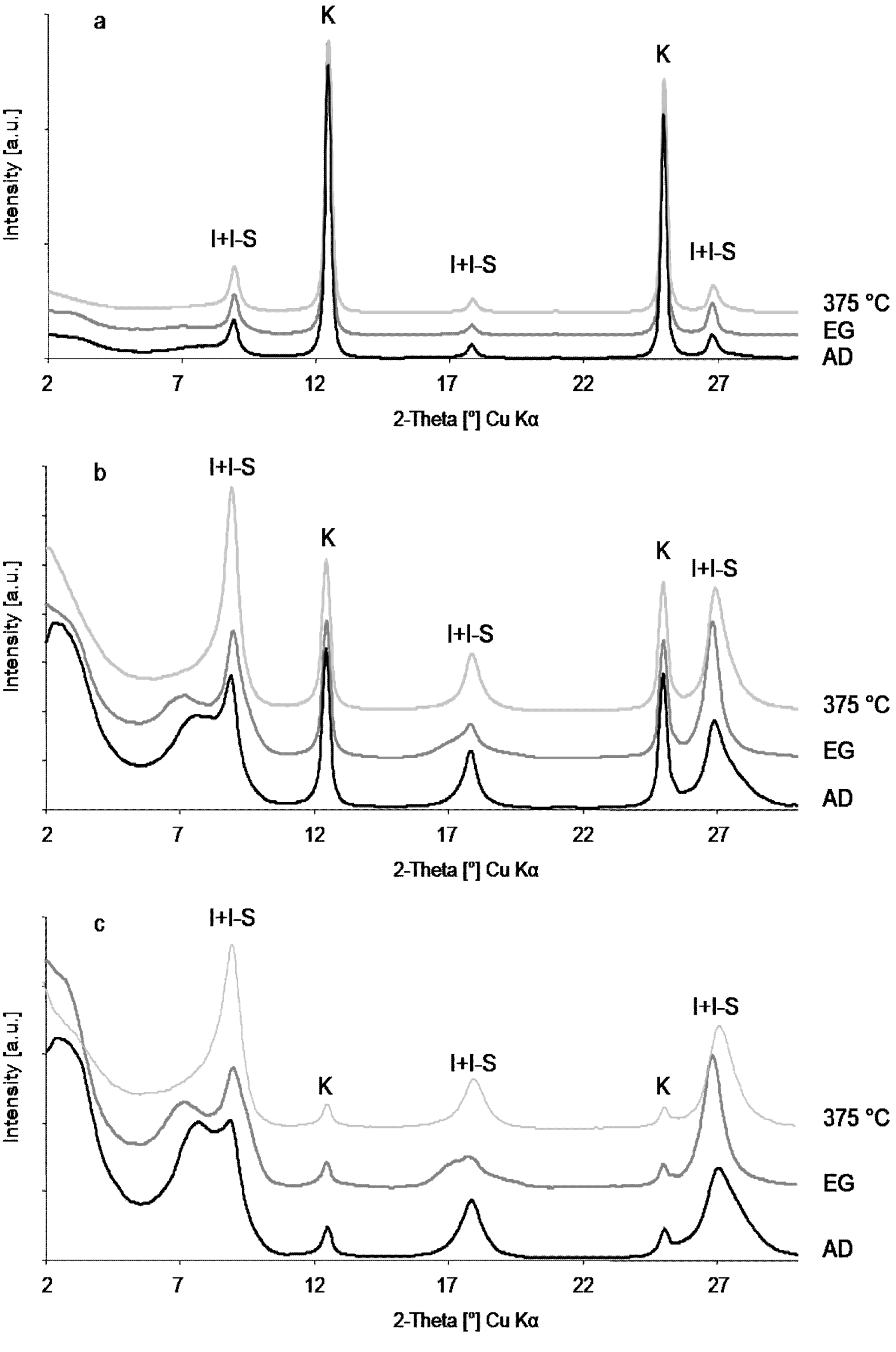

Figure 5.4: XRD patterns of sample LA540 from oriented preparation of the grain sizes (a) 0.6-2 µm, (b) 0.2-0.6 µm, (c) <0.2 µm, in the air-dried state (AD), after EG-solvation (EG) and heat-treatment (375 °C).

Furthermore, a shift of the relative intensities was observed with decreasing grain-size fraction. The intensity of the illite and I-S mixed-layers reflections increased, whereas the intensities of the kaolinite peaks strongly decreased.

Regarding phase identification, the clay samples of the microbiologically treated analogue LA540 MO showed identical features. However, the relative peak intensities did not change with decreasing grain size as observed for the clay samples of LA540. The XRD patterns of the respective EG-solvated samples of all kaolins are shown in Figures 5.5-5.7.

The clay fractions of the kaolinite samples B4914 and B4915 as well as their treated counterparts were characterized by nearly identical peak positions, displaying the presence of kaolinite and illite. Under EG-solvation, the samples demonstrated only slight peak shifts (<0.2 Å) and broadening events (<1 Å). The relative peak intensities of kaolinite and illite (plus eventual I-S mixed-layered species) barely did not change thoughout the various grain-size fractions.

In order to identify the mixed-layer phases and to quantify the phase content of the clay fractions, one-dimensional XRD pattern fitting (ODPF) was carried out. The experimental and the calculated XRD patterns are shown in Figures 5.5-5.7. Several I-S mixed-layer structure models were tested to simulate the experimental XRD patterns. A good coincidence of positions, intensities, and profiles was achieved for all kaolin samples with an I-S model, in which smectite and illite layers are interstratified with some tendency to segregation.

For samples LA540 and LA540 MO, the best fits were achieved by a physical mixture of discrete illite and *R1* I(0.80)/S in addition to kaolinite, whereas B4914 and B4915 as well as their treated counterparts were successfully described by the same physical mixture, but with a lower smectitic component portion in the mixed-layer (*R3* I(0.9)/S).

The accuracy of the fitting procedure was demonstrated by the satisfactory agreement between the experimental and calculated patterns, resulting in $R_p$ values <10%.

Disagreement between experimental and calculated profiles was observed for the low-angle part, probably because of the influence of instrumental factors and particularly of Lorentz-polarization effects (Sakharov et al., 1999). This low-angle range was therefore excluded prior to the fitting procedure.

Table 5.7 illustrates that the quantification results gathered with ODPF reflected numerically the observations made of the comparison of XRD patterns from oriented sample preparations. With decreasing grain-size fraction, a strong decrease of kaolinite and an increase of I-S were detected for the clay samples of LA540 and LA540 MO. A decreasing illite content was also observed for

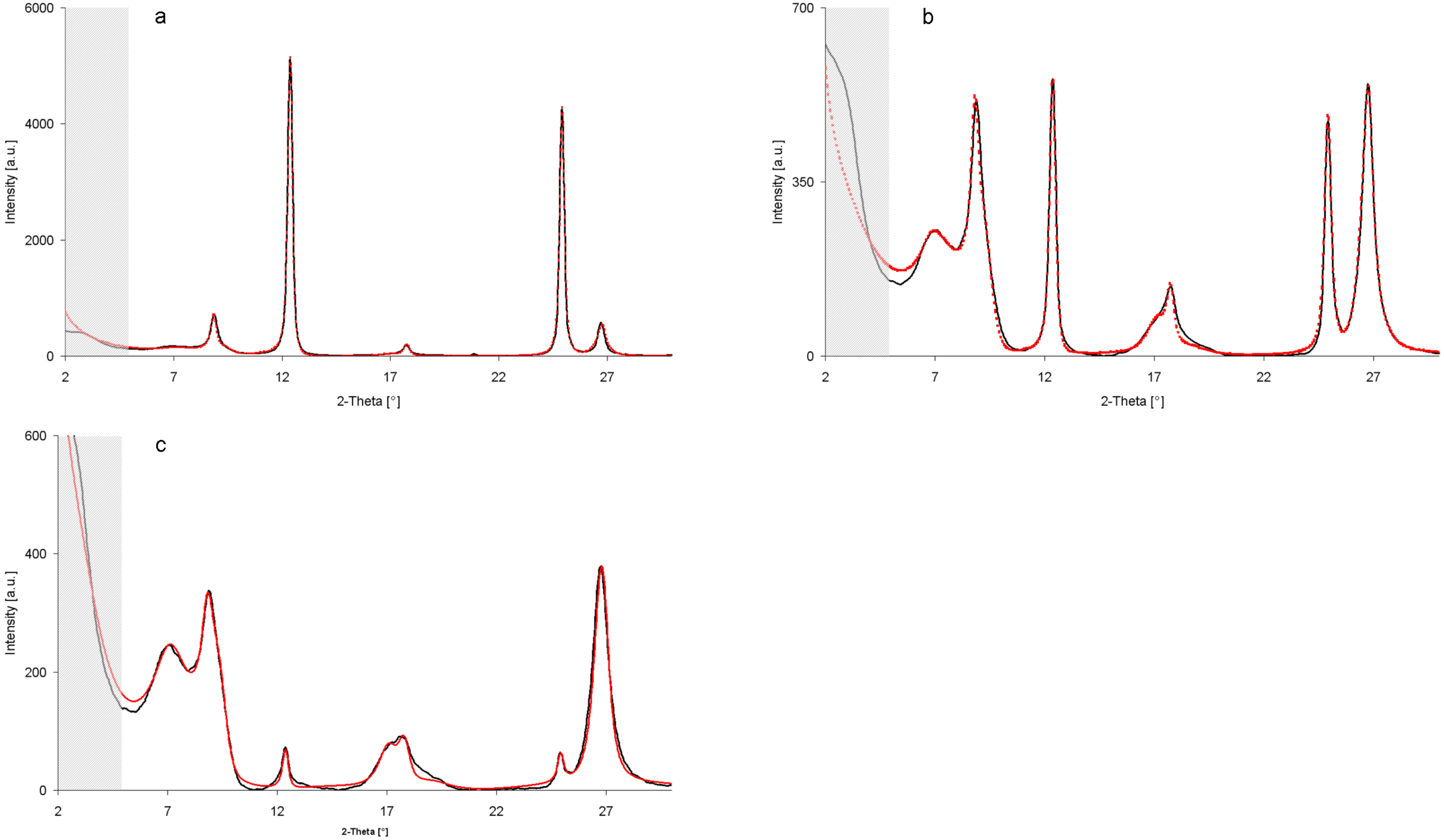

Figure 5.5: One-dimensional XRD pattern fitting for clay fractions from sample LA540. Experimental (solid line) and simulated (dashed line) XRD patterns of the Ca-saturated, EG-sovated oriented samples of the size fractions (a) 0.6-2 µm, (b) 0.2-0.6 µm, (c) <0.2 µm. The shaded areas were excluded from the fit.

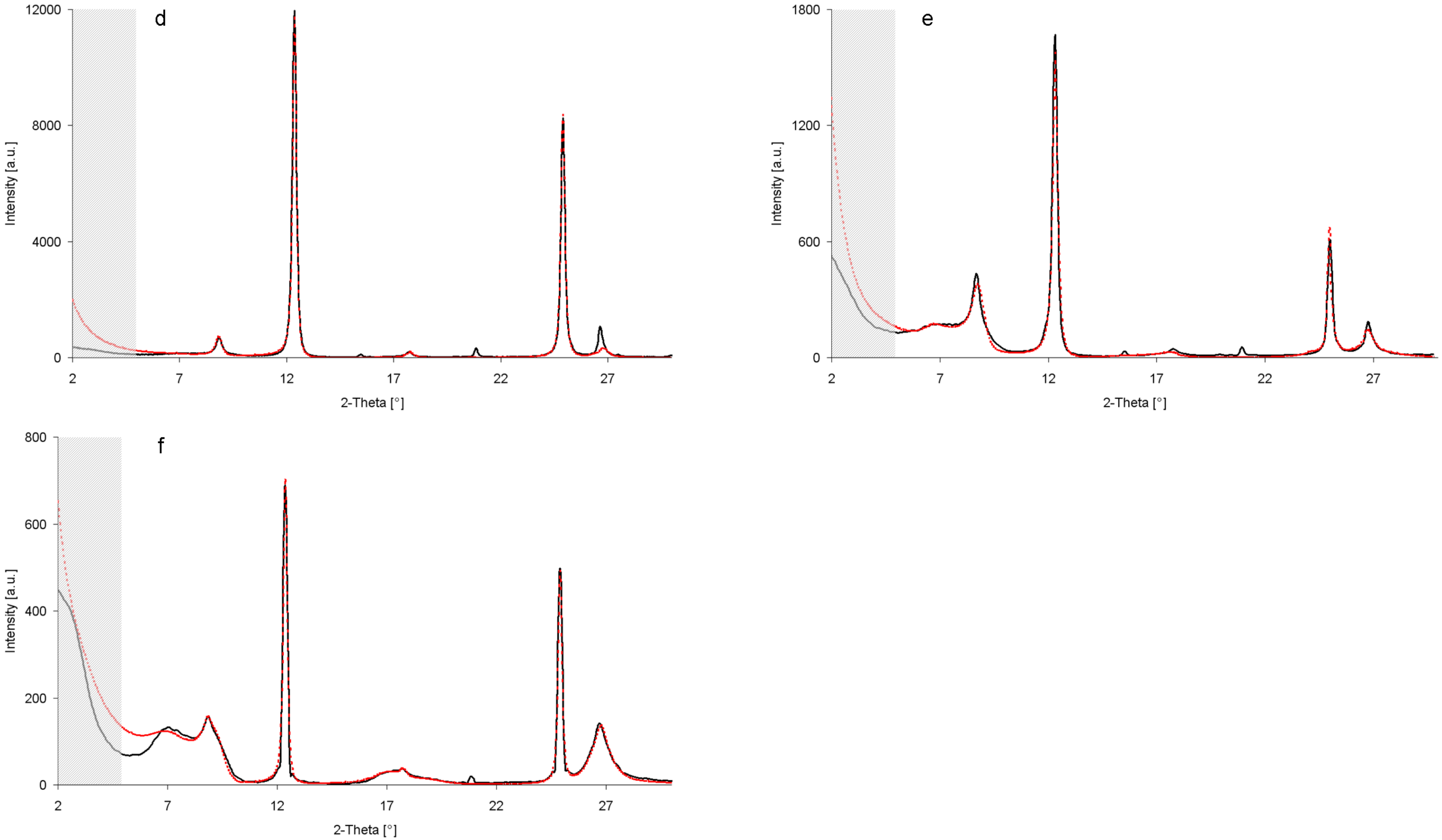

Continuation of Figure 5.5: One-dimensional XRD pattern fitting from clay fractions of sample LA540 MO. Experimental (solid line) and simulated (dashed line) XRD patterns of the Ca-saturated, EG-sovated oriented samples of the size fractions (d) 0.6-2 µm, (e) 0.2-0.6 µm, (f) <0.2 µm. The shaded areas were excluded from the fit.

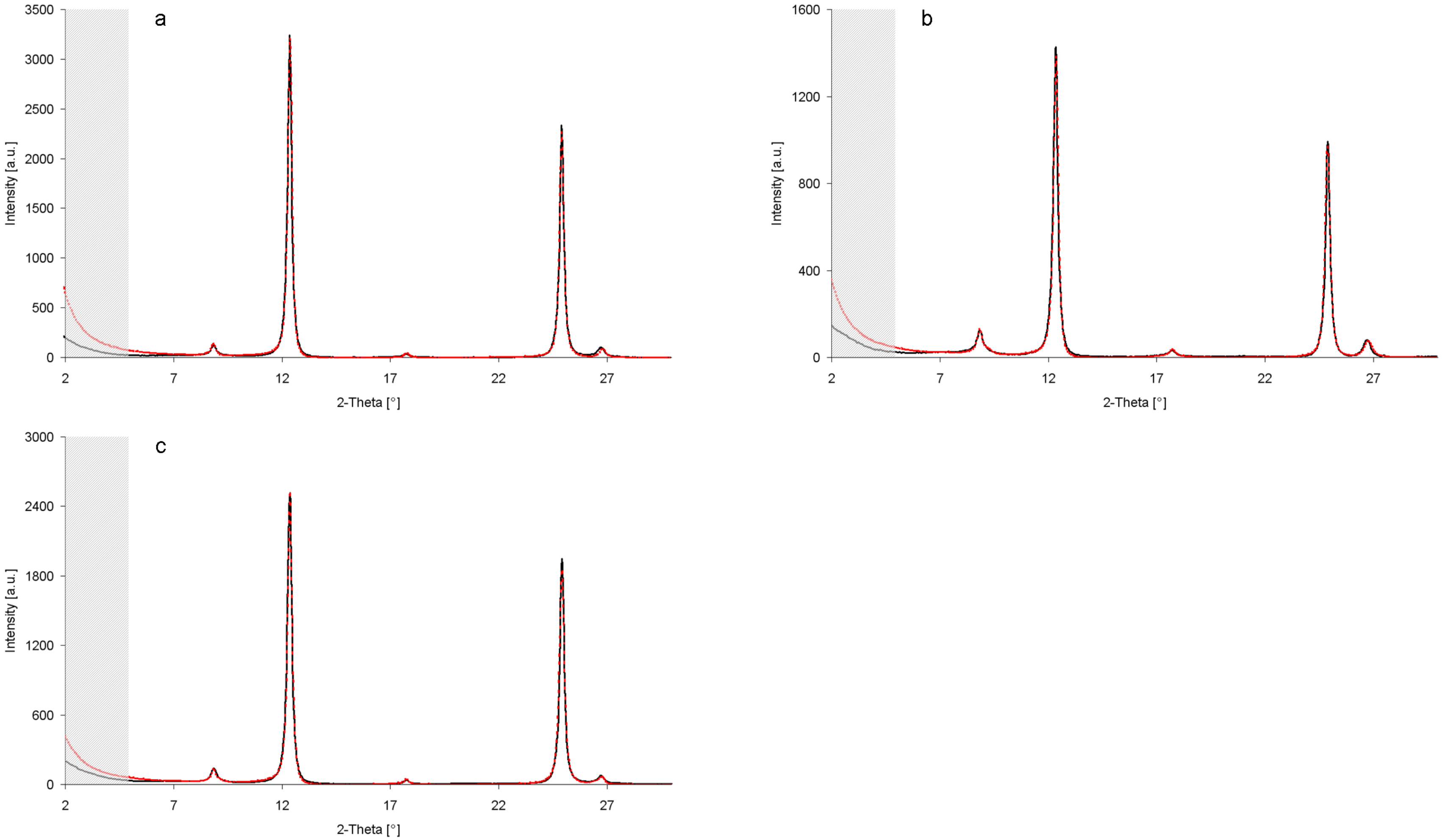

Figure 5.6: One-dimensional XRD pattern fitting for clay fractions from sample B4914. Experimental (solid line) and simulated (dashed line) XRD patterns of the Ca-saturated, EG-sovated oriented samples of the size fractions (a) 0.6-2 µm, (b) 0.2-0.6 µm, (c) <0.2 µm. The shaded areas were excluded from the fit.

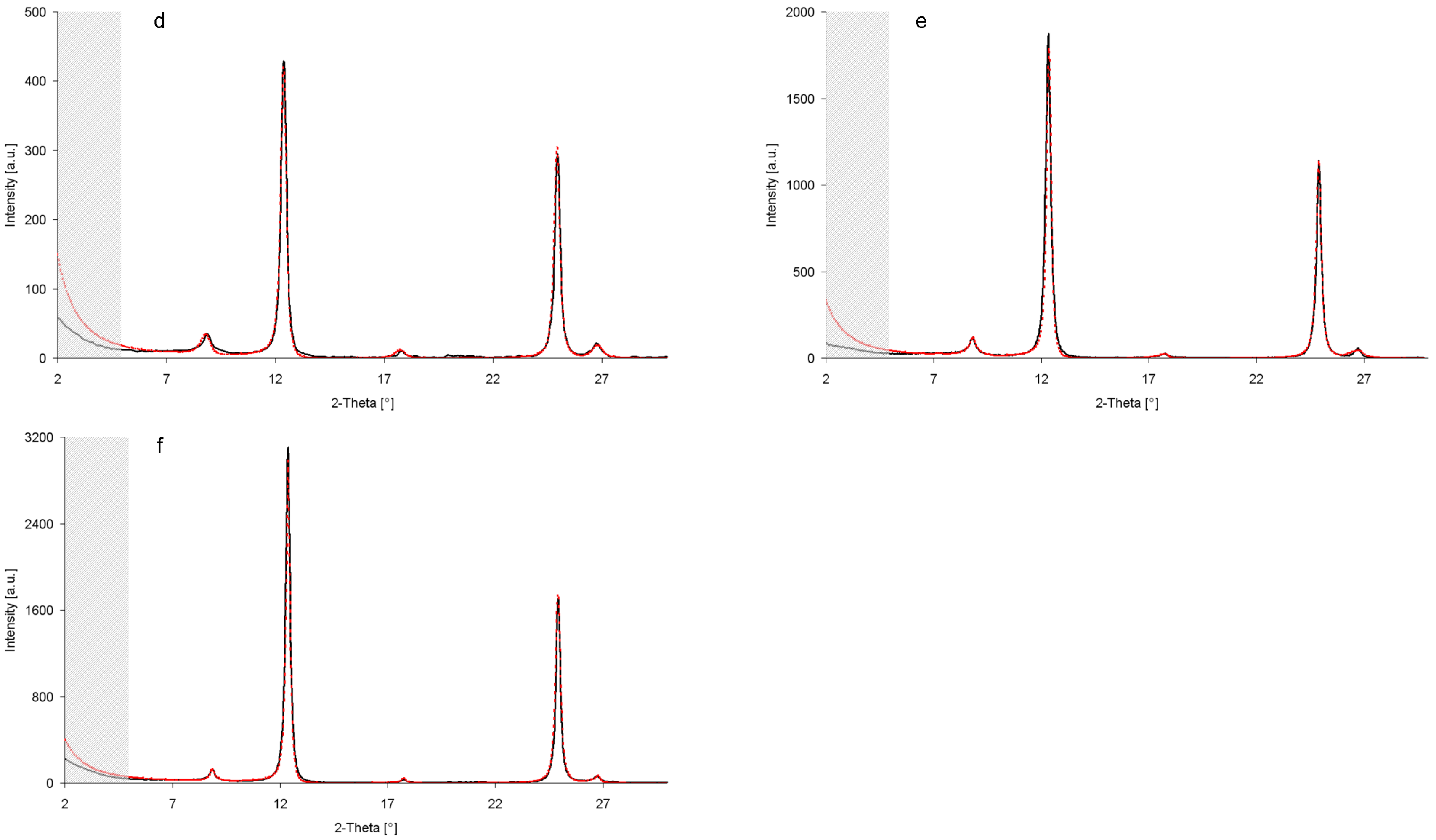

Continuation of Figure 5.6: One-dimensional XRD pattern fitting for clay fractions from sample B4914 MO. Experimental (solid line) and simulated (dashed line) XRD patterns of the Ca-saturated, EG-sovated oriented samples of the size fractions (d) 0.6-2 µm, (e) 0.2-0.6 µm, (f) <0.2 µm. The shaded areas were excluded from the fit.

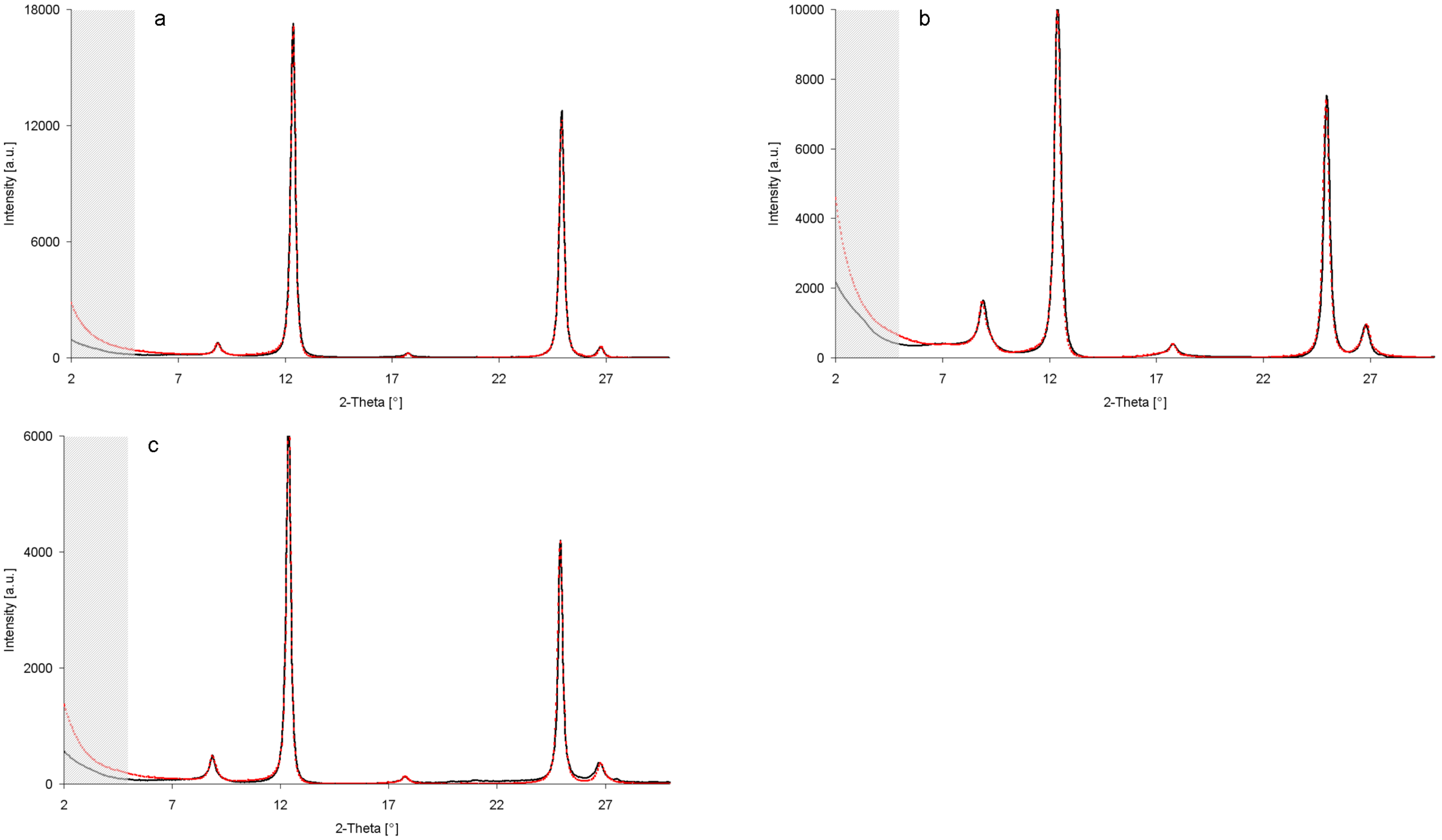

Figure 5.7: One-dimensional XRD pattern fitting for clay fractions from sample B4915. Experimental (solid line) and simulated (dashed line) XRD patterns of the Ca-saturated, EG-sovated oriented samples of the size fractions (a) 0.6-2 µm, (b) 0.2-0.6 µm, (c) <0.2 µm. The shaded areas were excluded from the fit.

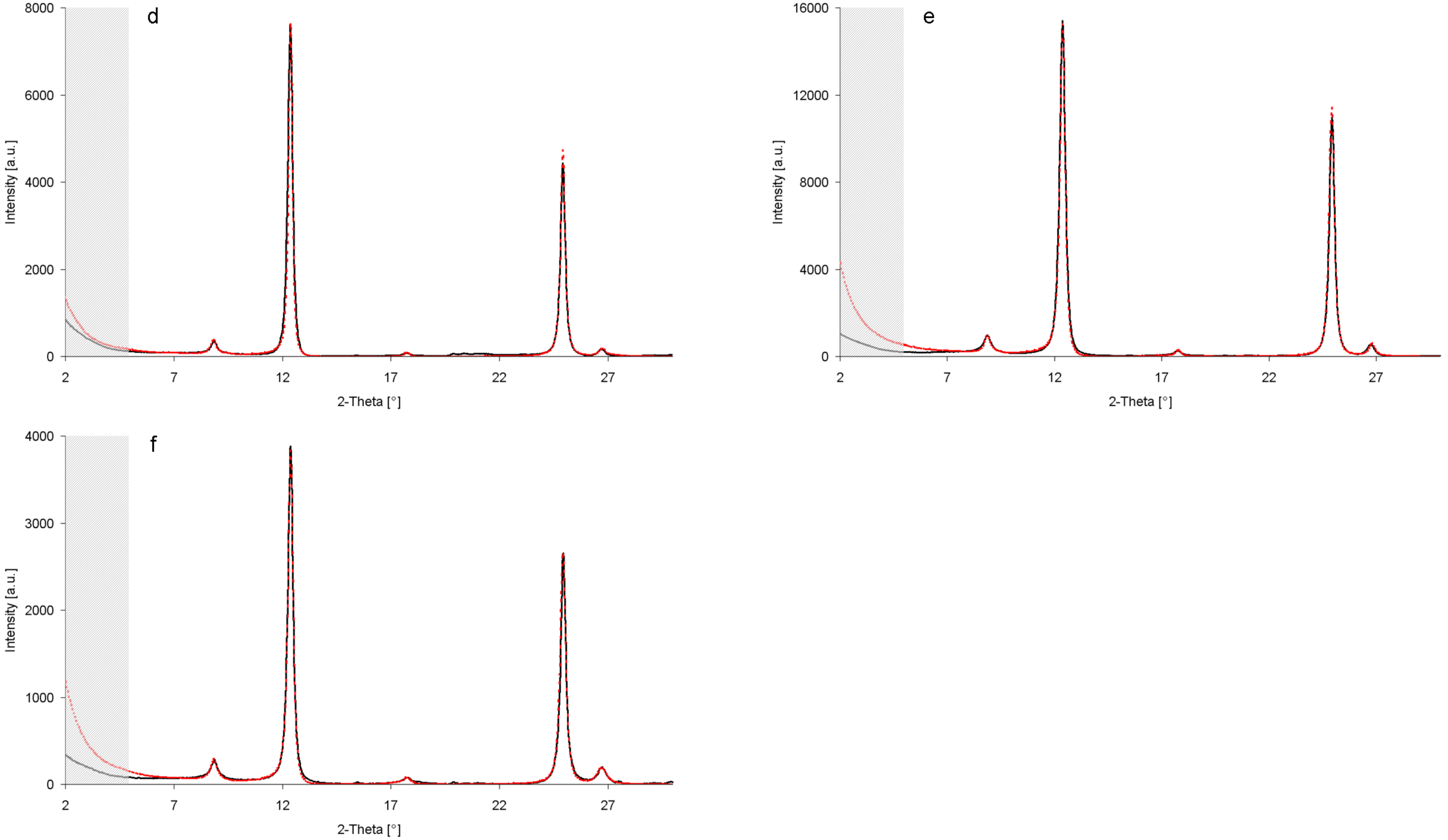

Continuation of Figure 5.7: One-dimensional XRD pattern fitting for clay fractions from sample B4915 MO. Experimental (solid line) and simulated (dashed line) XRD patterns of the Ca-saturated, EG-sovated oriented samples of the size fractions (d) 0.6-2 µm, (e) 0.2-0.6 µm, (f) <0.2 µm. The shaded areas were excluded from the fit.

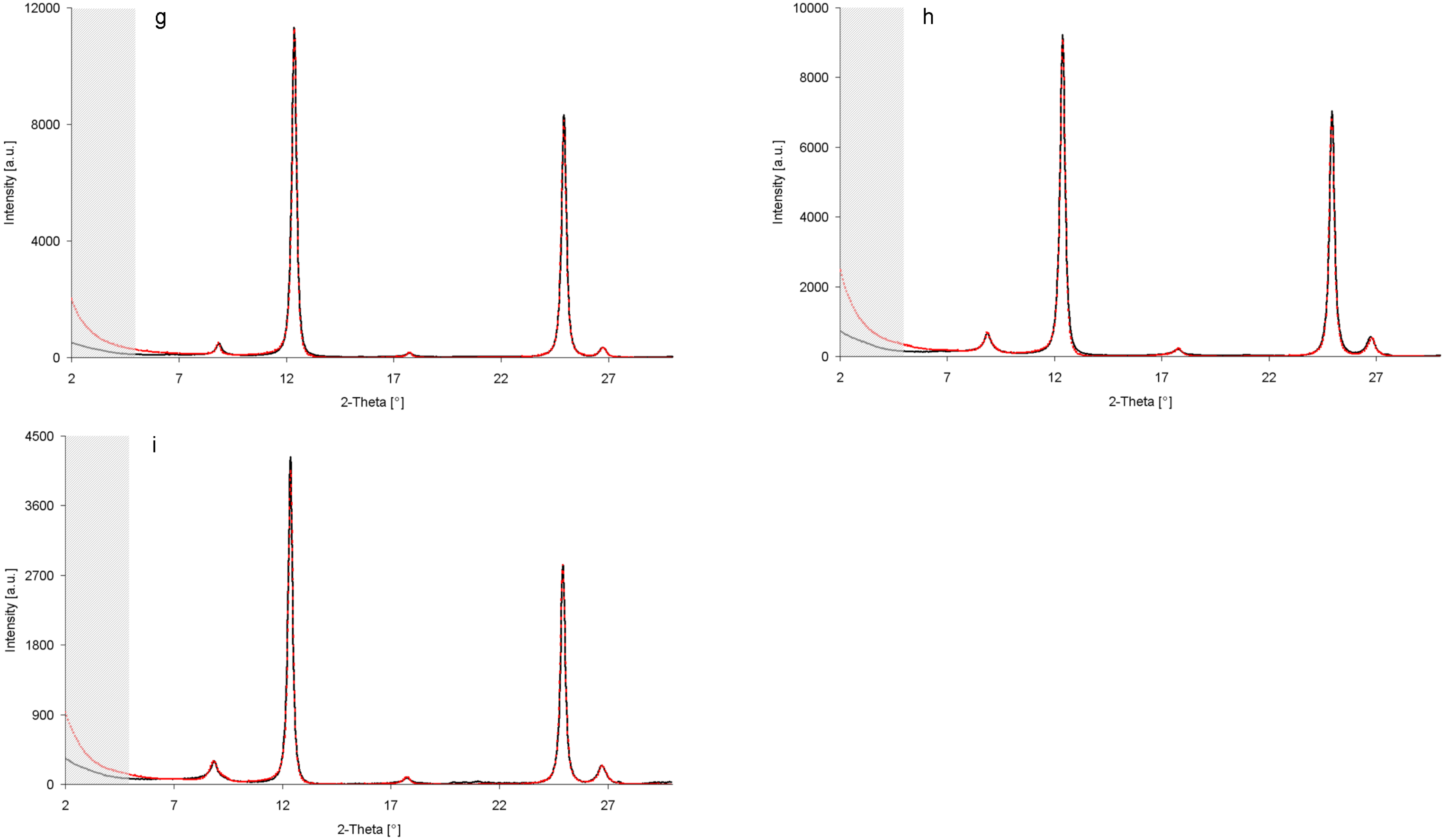

Continuation of Figure 5.7: One-dimensional XRD pattern fitting for clay fractions from sample B4915 K. Experimental (solid line) and simulated (dashed line) XRD patterns of the Ca-saturated, EG-sovated oriented samples of the size fractions (g) 0.6-2 µm, (h) 0.2-0.6 µm, (i) <0.2 µm. The shaded areas were excluded from the fit.

Table 5.7a: Quantification results from one-dimensional XRD profile fitting for the clay fractions of sample LA540. $W_a$: portion of the component that appears at first in the mixed-layer mineral.

| LA540 | 0.6-2 µm [%] | 0.2-0.6 µm [%] | <0.2 µm [%] |
|---|---|---|---|
| Kaolinite | 64 | 11 | 12 |
| I-S | 4 | 72 | 82 |
| -Reichweite | *R1* | *R1* | *R1* |
| -$W_a$ | 0.80 | 0.80 | 0.80 |
| Illite | 32 | 17 | 6 |

Table 5.7b: Quantification results from one-dimensional XRD profile fitting for the clay fractions of sample LA540 MO. $W_a$: portion of the component that appears at first in the mixed-layer mineral.

| LA540 MO | 0.6-2 µm [%] | 0.2-0.6 µm [%] | <0.2 µm [%] |
|---|---|---|---|
| Kaolinite | 86 | 61 | 42 |
| I-S | 4 | 18 | 49 |
| -Reichweite | *R1* | *R1* | *R1* |
| -$W_a$ | 0.80 | 0.80 | 0.80 |
| Illite | 10 | 21 | 9 |

Table 5.7c: Quantification results from one-dimensional XRD profile fitting for the clay fractions of sample B4914. $W_a$: portion of the component that appears at first in the mixed-layer mineral.

| B4914 | 0.6-2 µm<br>[%] | 0.2-0.6 µm<br>[%] | <0.2 µm<br>[%] |
|---|---|---|---|
| Kaolinite | 86 | 81 | 76 |
| I-S | 0 | 8 | 10 |
| -Reichweite | *R3* | *R3* | *R3* |
| -$W_a$ | 0.90 | 0.90 | 0.90 |
| Illite | 14 | 11 | 14 |

Table 5.7d: Quantification results from one-dimensional XRD profile fitting for the clay fractions of sample B4914 MO. $W_a$: portion of the component that appears at first in the mixed-layer mineral.

| B4914 MO | 0.6-2 µm<br>[%] | 0.2-0.6 µm<br>[%] | <0.2 µm<br>[%] |
|---|---|---|---|
| Kaolinite | 74 | 84 | 83 |
| I-S | 16 | 2 | 4 |
| -Reichweite | *R3* | *R3* | *R3* |
| -$W_a$ | 0.90 | 0.90 | 0.90 |
| Illite | 10 | 14 | 13 |

Table 5.7e: Quantification results from one-dimensional XRD profile fitting for the clay fractions of sample B4915. $W_a$: portion of the component that appears at first in the mixed-layer mineral.

| B4915 | 0.6-2 µm<br>[%] | 0.2-0.6 µm<br>[%] | <0.2 µm<br>[%] |
|---|---|---|---|
| Kaolinite | 84 | 63 | 84 |
| I-S | 3 | 18 | 13 |
| -Reichweite | *R3* | *R3* | *R3* |
| -$W_a$ | 0.90 | 0.90 | 0.90 |
| Illite | 13 | 19 | 3 |

Table 5.7f: Quantification results from one-dimensional XRD profile fitting for the clay fractions of sample B4915 MO. $W_a$: portion of the component that appears at first in the mixed-layer mineral.

| B4915 MO | 0.6-2 µm<br>[%] | 0.2-0.6 µm<br>[%] | <0.2 µm<br>[%] |
|---|---|---|---|
| Kaolinite | 90 | 88 | 74 |
| I-S | 5 | 6 | 19 |
| -Reichweite | *R3* | *R3* | *R3* |
| -$W_a$ | 0.90 | 0.90 | 0.90 |
| Illite | 5 | 6 | 7 |

Table 5.7g: Quantification results from one-dimensional XRD profile fitting for the clay fractions of sample B4915 K. $W_a$: portion of the component that appears at first in the mixed-layer mineral.

| B4915 K | 0.6-2 µm [%] | 0.2-0.6 µm [%] | <0.2 µm [%] |
|---|---|---|---|
| Kaolinite | 77 | 75 | 75 |
| I-S | 8 | 20 | 10 |
| -Reichweite | *R3* | *R3* | *R3* |
| -$W_a$ | 0.90 | 0.90 | 0.90 |
| Illite | 15 | 5 | 15 |

sample LA540. For sample LA540 MO, however, the illite content yielded its maximum in the middle clay fraction (0.2-0.6 µm).

The clay fractions of B4914 and B4915 as well as their treated analogs showed higher kaolinite contents of about 80%. Throughout the clay size fractions, the phase contents did not change as strongly as observed for LA540 and LA540 MO.

Comparing B4914 and B4914 MO, it was not possible to identify a general trend concerning the changes of phase content with decreasing grain size. For B4914, the kaolinite content decreased under simultaneous increase of I-S, whereas B4914 MO showed an opposite trend. However, both samples showed similar values regarding the illite contents.

Likewise within the sample group of B4915, no general correlation between phase content and grain-size fraction could be established. With respect to sample group B4914, the range of variation was more pronounced.

### 5.2.3 Simultaneous Thermal Analysis

According to the method described in Section 4.2.5, the results from the adapted XRD-XRF crosscheck were re-examined comparing the measured mass loss during dehydroxylation reaction ($\Delta m\ T_{DHXmeas}$) between 400 and 900 °C from TG curves with a calculated mass loss ($\Delta m\ T_{DHXcalc}$) gathered from quantification results. As no smectitic components were determined by Rietveld analysis, equation 4.15 comprises merely two coefficients, with x for kaolinite and y for illite.

Deviations between $\Delta m\ T_{DHXmeas}$ and $\Delta m\ T_{DHXcalc}$ were expressed by Δ-values: negative Δ-values indicated overestimation of the clay mineral contents gathered by the adapted XRD-XRF crosscheck related to STA measurements and positive Δ-values denoted underestimation. Δ-values, then, were tried to be minimized adjusting the clay minerals content. Afterwards, this adapted phase content was again crosschecked with the chemical composition from XRF analysis.

Before going into detail on the results from crosscheck, the values from TG measurements ($\Delta m\ T_{DHXmeas}$) between 400 and 900 °C are shortly reviewed (Table 5.8). Comparing the bulk material of all kaolins before and after the microbiological treatment, slightly increased values for $\Delta m\ T_{DHXmeas}$ (<0.4%) were noted for the treated samples. With decreasing grain size, all untreated kaolins exhibited a reduction in mass loss, whereas the treated samples showed either unsystematic (B4914 MO, B4915 K) or inverted trends (B4915 MO). After microbiological treatment, the respective values for $\Delta m\ T_{DHXmeas}$ were found to be increased, particularly those of the clay fractions.

Table 5.8 compares the quantification results from the STA crosscheck (XRD-XRF adapted-STA) with the results, which were the most consistent after the XRF crosscheck (STA adapted-XRF). Samples with Δ-values <±0.10 were not

Table 5.8a: Validation of the clay content for sample LA540 from the adapted XRD-XRF crosscheck and for the adapted STA and XRF crosschecked values, comparing the measured mass loss (Δm $T_{DHXmeas}$) during the dehydroxylation reaction with the calculated mass loss (Δm $T_{DHXcalc}$). x and y are the mass fractions of the 1:1 and 2:1 layer silicates. Δ: deviation between measured and calculated mass loss Δm $T_{DHX}$.

| LA540 | Quantification method | Kaolinite x | Illite y | Δm $T_{DHX\ calc}$ [%] | Δm $T_{DHX\ meas}$ [%] | Δ [%] |
|---|---|---|---|---|---|---|
| bulk | XRD-XRF adapted-STA | 0.65 | 0.09 | 9.48 | 9.44 | -0.04 |
| | STA adapted-XRF | 0.65 | 0.09 | 9.48 | 9.44 | -0.04 |
| >20 µm | XRD-XRF adapted-STA | n.d. | n.d. | n.d. | n.d. | n.d. |
| | STA adapted-XRF | n.d. | n.d. | n.d. | n.d. | n.d. |
| 2-20 µm | XRD-XRF adapted-STA | 0.73 | 0.05 | 10.41 | 10.68 | 0.27 |
| | STA adapted-XRF | 0.73 | 0.06 | 10.46 | 10.68 | 0.22 |
| 0.6-2 µm | XRD-XRF adapted-STA | 0.63 | 0.11 | 9.30 | 9.68 | 0.38 |
| | STA adapted-XRF | 0.60 | 0.21 | 9.34 | 9.68 | 0.34 |
| 0.2-0.6 µm | XRD-XRF adapted-STA | 0.30 | 0.35 | 5.80 | 5.91 | 0.11 |
| | STA adapted-XRF | 0.30 | 0.35 | 5.80 | 5.91 | 0.11 |
| <0.2 µm | XRD-XRF adapted-STA | 0.17 | 0.58 | 5.05 | 5.74 | 0.69 |
| | STA adapted-XRF | 0.18 | 0.58 | 5.18 | 5.74 | 0.56 |

n.d.: not determined due to lack of sample

Table 5.8b: Validation of the clay content for sample LA540 MO from the adapted XRD-XRF crosscheck and for the adapted STA and XRF crosschecked values, comparing the measured mass loss ($\Delta m\ T_{DHXmeas}$) during the dehydroxylation reaction with the calculated mass loss ($\Delta m\ T_{DHXcalc}$). x and y are the mass fractions of the 1:1 and 2:1 layer silicates. Δ: deviation between measured and calculated mass loss $\Delta m\ T_{DHX}$.

| LA540 MO | Quantification method | Kaolinite x | Illite y | $\Delta m\ T_{DHX\ calc}$ [%] | $\Delta m\ T_{DHX\ meas}$ [%] | Δ [%] |
|---|---|---|---|---|---|---|
| bulk | XRD-XRF adapted-STA | 0.63 | 0.09 | 9.20 | 9.74 | 0.54 |
| | STA adapted-XRF | 0.64 | 0.09 | 9.34 | 9.74 | 0.40 |
| >20 µm | XRD-XRF adapted-STA | 0.51 | 0.15 | 7.81 | 13.09 | 5.28 |
| | STA adapted-XRF | 0.51 | 0.15 | 7.81 | 13.09 | 5.28 |
| 2-20 µm | XRD-XRF adapted-STA | 0.67 | 0.09 | 9.76 | 11.54 | 1.78 |
| | STA adapted-XRF | 0.67 | 0.09 | 9.76 | 11.54 | 1.78 |
| 0.6-2 µm | XRD-XRF adapted-STA | 0.65 | 0.12 | 9.62 | 9.69 | 0.07 |
| | STA adapted-XRF | 0.65 | 0.12 | 9.62 | 9.69 | 0.07 |
| 0.2-0.6 µm | XRD-XRF adapted-STA | 0.21 | 0.57 | 5.56 | 8.21 | 2.65 |
| | STA adapted-XRF | 0.21 | 0.57 | 5.56 | 8.21 | 2.65 |
| <0.2 µm | XRD-XRF adapted-STA | 0.32 | 0.49 | 7.18 | 10.53 | 3.35 |
| | STA adapted-XRF | 0.32 | 0.49 | 7.18 | 10.53 | 3.35 |

Table 5.8c: Validation of the clay content for sample B4914 from the adapted XRD-XRF crosscheck and for the adapted STA and XRF crosschecked values, comparing the measured mass loss (Δm $T_{DHXmeas}$) during the dehydroxylation reaction with the calculated mass loss (Δm $T_{DHXcalc}$). x and y are the mass fractions of the 1:1 and 2:1 layer silicates. Δ: deviation between measured and calculated mass loss Δm $T_{DHX}$.

| B4914 | Quantification method | Kaolinite x | Illite y | Δm $T_{DHX\ calc}$ [%] | Δm $T_{DHX\ meas}$ [%] | Δ [%] |
|---|---|---|---|---|---|---|
| bulk | XRD-XRF adapted-STA | 0.80 | 0.08 | 11.53 | 11.67 | 0.14 |
| | STA adapted-XRF | 0.81 | 0.08 | 11.67 | 11.67 | 0.00 |
| >20 µm | XRD-XRF adapted-STA | 0.86 | 0.05 | 12.23 | 12.45 | 0.22 |
| | STA adapted-XRF | 0.87 | 0.06 | 12.41 | 12.45 | 0.04 |
| 2-20 µm | XRD-XRF adapted-STA | 0.75 | 0.10 | 10.92 | 11.30 | 0.38 |
| | STA adapted-XRF | 0.77 | 0.11 | 11.25 | 11.30 | 0.05 |
| 0.6-2 µm | XRD-XRF adapted-STA | 0.79 | 0.14 | 11.67 | 11.98 | 0.31 |
| | STA adapted-XRF | 0.81 | 0.14 | 11.94 | 11.98 | 0.04 |
| 0.2-0.6 µm | XRD-XRF adapted-STA | 0.66 | 0.25 | 10.36 | 10.88 | 0.52 |
| | STA adapted-XRF | 0.68 | 0.28 | 10.78 | 10.88 | 0.10 |
| <0.2 µm | XRD-XRF adapted-STA | n.d. | n.d. | n.d. | n.d. | n.d. |
| | STA adapted-XRF | n.d. | n.d. | n.d. | n.d. | n.d. |

n.d.: not determined due to lack of sample

Table 5.8d: Validation of the clay content for sample B4914 MO from the adapted XRD-XRF crosscheck and for the adapted STA and XRF crosschecked values, comparing the measured mass loss (Δm $T_{DHXmeas}$) during the dehydroxylation reaction with the calculated mass loss (Δm $T_{DHXcalc}$). x and y are the mass fractions of the 1:1 and 2:1 layer silicates. Δ: deviation between measured and calculated mass loss Δm $T_{DHX}$.

| B4914 MO | Quantification method | Kaolinite x | Illite y | Δm $T_{DHX\ calc}$ [%] | Δm $T_{DHX\ meas}$ [%] | Δ [%] |
|---|---|---|---|---|---|---|
| bulk | XRD-XRF adapted-STA | 0.80 | 0.09 | 11.57 | 12.02 | 0.45 |
| | STA adapted-XRF | 0.82 | 0.11 | 11.95 | 12.02 | 0.07 |
| >20 µm | XRD-XRF adapted-STA | 0.82 | 0.09 | 11.85 | 13.20 | 1.35 |
| | STA adapted-XRF | 0.82 | 0.09 | 11.85 | 13.20 | 1.35 |
| 2-20 µm | XRD-XRF adapted-STA | 0.76 | 0.08 | 10.97 | 11.58 | 0.61 |
| | STA adapted-XRF | 0.79 | 0.11 | 11.53 | 11.58 | 0.05 |
| 0.6-2 µm | XRD-XRF adapted-STA | 0.85 | 0.10 | 12.32 | 12.51 | 0.19 |
| | STA adapted-XRF | 0.86 | 0.11 | 12.50 | 12.51 | 0.01 |
| 0.2-0.6 µm | XRD-XRF adapted-STA | 0.74 | 0.18 | 11.15 | 12.07 | 0.92 |
| | STA adapted-XRF | 0.74 | 0.18 | 11.15 | 12.07 | 0.92 |
| <0.2 µm | XRD-XRF adapted-STA | 0.69 | 0.26 | 10.82 | 15.54 | 4.72 |
| | STA adapted-XRF | 0.69 | 0.26 | 10.82 | 15.54 | 4.72 |

Table 5.8e: Validation of the clay content for sample B4915 from the adapted XRD-XRF crosscheck and for the adapted STA and XRF crosschecked values, comparing the measured mass loss (Δm $T_{DHXmeas}$) during the dehydroxylation reaction with the calculated mass loss (Δm $T_{DHXcalc}$). x and y are the mass fractions of the 1:1 and 2:1 layer silicates. Δ: deviation between measured and calculated mass loss Δm $T_{DHX}$.

| B4915 | Quantification method | Kaolinite x | Illite y | Δm $T_{DHX\ calc}$ [%] | Δm $T_{DHX\ meas}$ [%] | Δ [%] |
|---|---|---|---|---|---|---|
| bulk | XRD-XRF adapted-STA | 0.77 | 0.14 | 11.39 | 11.26 | -0.13 |
| | STA adapted-XRF | 0.77 | 0.12 | 11.29 | 11.26 | -0.03 |
| >20 µm | XRD-XRF adapted-STA | 0.84 | 0.07 | 12.04 | 12.10 | 0.06 |
| | STA adapted-XRF | 0.84 | 0.07 | 12.04 | 12.10 | 0.06 |
| 2-20 µm | XRD-XRF adapted-STA | 0.76 | 0.09 | 11.02 | 11.12 | 0.10 |
| | STA adapted-XRF | 0.76 | 0.10 | 11.06 | 11.12 | 0.06 |
| 0.6-2 µm | XRD-XRF adapted-STA | 0.78 | 0.16 | 11.62 | 11.54 | -0.08 |
| | STA adapted-XRF | 0.78 | 0.14 | 11.53 | 11.54 | 0.01 |
| 0.2-0.6 µm | XRD-XRF adapted-STA | 0.73 | 0.19 | 11.06 | 10.86 | -0.20 |
| | STA adapted-XRF | 0.70 | 0.23 | 10.83 | 10.86 | 0.03 |
| <0.2 µm | XRD-XRF adapted-STA | 0.55 | 0.37 | 9.38 | 10.39 | 1.01 |
| | STA adapted-XRF | 0.55 | 0.38 | 9.42 | 10.39 | 0.97 |

Table 5.8f: Validation of the clay content for sample B4915 MO from the adapted XRD-XRF crosscheck and for the adapted STA and XRF crosschecked values, comparing the measured mass loss (Δm $T_{DHXmeas}$) during the dehydroxylation reaction with the calculated mass loss (Δm $T_{DHXcalc}$). x and y are the mass fractions of the 1:1 and 2:1 layer silicates. Δ: deviation between measured and calculated mass loss Δm $T_{DHX}$.

| B4915 MO | Quantification method | Kaolinite x | Illite y | Δm $T_{DHX\ calc}$ [%] | Δm $T_{DHX\ meas}$ [%] | Δ [%] |
|---|---|---|---|---|---|---|
| bulk | XRD-XRF adapted-STA | 0.77 | 0.14 | 11.39 | 11.37 | -0.02 |
| | STA adapted-XRF | 0.77 | 0.14 | 11.39 | 11.37 | -0.02 |
| >20 µm | XRD-XRF adapted-STA | 0.68 | 0.14 | 10.13 | 10.99 | 0.86 |
| | STA adapted-XRF | 0.69 | 0.12 | 10.18 | 10.99 | 0.81 |
| 2-20 µm | XRD-XRF adapted-STA | 0.77 | 0.08 | 11.11 | 11.41 | 0.30 |
| | STA adapted-XRF | 0.77 | 0.09 | 11.16 | 11.41 | 0.25 |
| 0.6-2 µm | XRD-XRF adapted-STA | 0.81 | 0.13 | 11.90 | 11.95 | 0.05 |
| | STA adapted-XRF | 0.81 | 0.13 | 11.90 | 11.95 | 0.05 |
| 0.2-0.6 µm | XRD-XRF adapted-STA | 0.77 | 0.16 | 11.48 | 11.73 | 0.25 |
| | STA adapted-XRF | 0.75 | 0.19 | 11.34 | 11.73 | 0.39 |
| <0.2 µm | XRD-XRF adapted-STA | 0.62 | 0.27 | 9.89 | 12.39 | 2.50 |
| | STA adapted-XRF | 0.62 | 0.27 | 9.89 | 12.39 | 2.50 |

Table 5.8g: Validation of the clay content for sample B4915 K from the adapted XRD-XRF crosscheck and for the adapted STA and XRF crosschecked values, comparing the measured mass loss (Δm $T_{DHXmeas}$) during the dehydroxylation reaction with the calculated mass loss (Δm $T_{DHXcalc}$). x and y are the mass fractions of the 1:1 and 2:1 layer silicates. Δ: deviation between measured and calculated mass loss Δm $T_{DHX}$.

| B4915 K | Quantification method | Kaolinite x | Illite y | Δm $T_{DHX\ calc}$ [%] | Δm $T_{DHX\ meas}$ [%] | Δ [%] |
|---|---|---|---|---|---|---|
| bulk | XRD-XRF adapted-STA | 0.77 | 0.13 | 11.34 | 11.30 | -0.04 |
| | STA adapted-XRF | 0.77 | 0.13 | 11.34 | 11.30 | -0.04 |
| >20 µm | XRD-XRF adapted-STA | 0.73 | 0.08 | 10.55 | 11.23 | 0.68 |
| | STA adapted-XRF | 0.72 | 0.12 | 10.60 | 11.23 | 0.63 |
| 2-20 µm | XRD-XRF adapted-STA | 0.78 | 0.08 | 11.25 | 11.44 | 0.19 |
| | STA adapted-XRF | 0.78 | 0.09 | 11.30 | 11.44 | 0.14 |
| 0.6-2 µm | XRD-XRF adapted-STA | 0.80 | 0.12 | 11.71 | 11.74 | 0.03 |
| | STA adapted-XRF | 0.80 | 0.12 | 11.71 | 11.74 | 0.03 |
| 0.2-0.6 µm | XRD-XRF adapted-STA | 0.69 | 0.24 | 10.73 | 10.91 | 0.18 |
| | STA adapted-XRF | 0.70 | 0.22 | 10.78 | 10.91 | 0.13 |
| <0.2 µm | XRD-XRF adapted-STA | 0.58 | 0.33 | 9.61 | 11.11 | 1.50 |
| | STA adapted-XRF | 0.58 | 0.36 | 9.75 | 11.11 | 1.36 |

considered in this crosscheck, as deviations were sufficiently small and could not be further meliorated. For all Δ-values <1.00, improvements were mainly achieved by increasing the illite content at the expense of the K-feldspar content and/or by a slight increase of the kaolinite content. For samples with Δ-values >1.00, no improvements could be achieved, as the corrected values (in terms of Δ → 0) were no more consistent with the results from XRF analysis. Evidently, the greatest Δ-values were observed for the treated samples. The quantification results after the XRD-XRF adapted-STA crosscheck are reported in Table 5.9.

In order to test the structural order of kaolinite and to detect structural changes due to microbiological treatment, PA curves were recorded for all bulk samples and compared with kaolinite-rich samples of different degrees of structural order (Figure 5.8). In order to ensure comparability of the results, all data were normalized to the kaolinite content gathered from XRD-XRF-STA crosscheck of the respective sample.

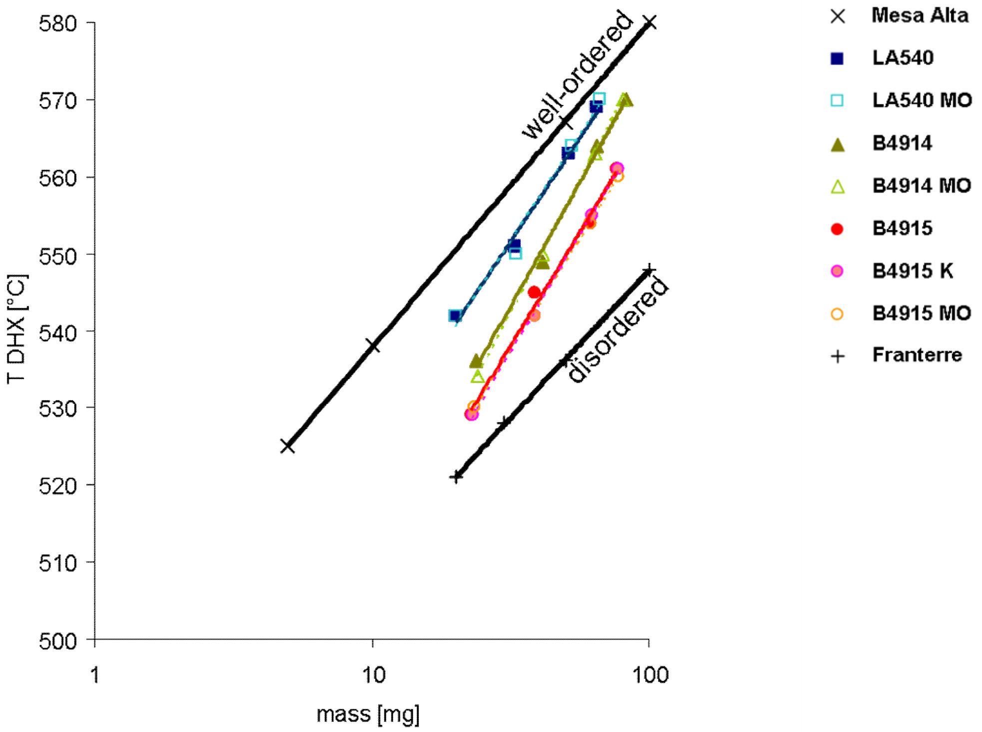

Figure 5.8: PA curves to estimate the structural disorder of kaolinite of the samples LA540, B4914 and B4915 before (filled markers) and after the microbiological treatment (open markers).

The data of a well-ordered kaolinite (Mesa Alta) and of a highly disordered kaolinite (Franterre) as thresholds were taken from Smykatz-Kloss (1974). According to the relative position of the PA curves, the degree of structural

Table 5.9a: Phase content of the kaolin sample LA540 and of the grain-size fractions gathered from XRD-XRF-STA crosscheck.

| LA540 | bulk<br>[%] | >20 µm<br>[%] * | 2-20 µm<br>[%] | 0.6-2 µm<br>[%] | 0.2-0.6 µm<br>[%] | <0.2 µm<br>[%] |
|---|---|---|---|---|---|---|
| Kaolinite | 65 | 57 | 73 | 60 | 30 | 18 |
| Illite | 9 | 4 | 6 | 21 | 35 | 58 |
| K-Feldspar | 11 | 27 | 9 | 0 | 15 | 0 |
| Quartz | 12 | 8 | 11 | 16 | 14 | 20 |
| Ti oxides | 1 | 1 | 1 | 1 | 1 | 0 |
| Crandallite | 1 | 1 | 0 | 1 | 1 | 0 |
| Fe phases | 1 | 2 | 0 | 1 | 4 | 4 |

* not STA crosschecked due to lack of sample

Table 5.9b: Phase content of the kaolin sample LA540 MO and of the grain-size fractions gathered from XRD-XRF-STA crosscheck.

| LA540 MO | bulk<br>[%] | >20 µm<br>[%] | 2-20 µm<br>[%] | 0.6-2 µm<br>[%] | 0.2-0.6 µm<br>[%] | <0.2 µm<br>[%] |
|---|---|---|---|---|---|---|
| Kaolinite | 64 | 51 | 67 | 65 | 21 | 32 |
| Illite | 9 | 15 | 9 | 12 | 57 | 49 |
| K-Feldspar | 11 | 21 | 12 | 4 | 1 | 5 |
| Quartz | 13 | 9 | 11 | 16 | 16 | 11 |
| Ti oxides | 1 | 1 | 1 | 1 | 1 | 0 |
| Crandallite | 1 | 1 | 0 | 1 | 1 | 0 |
| Fe phases | 1 | 2 | 0 | 1 | 3 | 3 |

Table 5.9c: Phase content of the kaolin sample B4914 and of the grain-size fractions gathered from XRD-XRF-STA crosscheck.

| B4914 | bulk [%] | >20 µm [%] | 2-20 µm [%] | 0.6-2 µm [%] | 0.2-0.6 µm [%] | <0.2 µm [%] * |
|---|---|---|---|---|---|---|
| Kaolinite | 81 | 87 | 77 | 81 | 68 | 68 |
| Illite | 8 | 6 | 11 | 14 | 28 | 30 |
| K-Feldspar | 7 | 6 | 8 | 1 | 1 | 0 |
| Quartz | 2 | 2 | 4 | 2 | 2 | 0 |
| Ti oxides | 0 | 0 | 0 | 0 | 0 | 0 |
| Crandallite | 1 | 0 | 0 | 1 | 0 | 0 |
| Fe phases | 1 | 1 | 1 | 1 | 1 | 2 |

* not STA crosschecked due to lack of sample

Table 5.9d: Phase content of the kaolin sample B4914 MO and of the grain-size fractions gathered from XRD-XRF-STA crosscheck.

| B4914 MO | bulk [%] | >20 µm [%] | 2-20 µm [%] | 0.6-2 µm [%] | 0.2-0.6 µm [%] | <0.2 µm [%] |
|---|---|---|---|---|---|---|
| Kaolinite | 82 | 82 | 79 | 86 | 74 | 69 |
| Illite | 11 | 9 | 11 | 11 | 18 | 26 |
| K-Feldspar | 5 | 4 | 5 | 1 | 3 | 1 |
| Quartz | 1 | 3 | 4 | 1 | 3 | 3 |
| Ti oxides | 0 | 1 | 0 | 0 | 1 | 0 |
| Crandallite | 0 | 1 | 0 | 0 | 0 | 0 |
| Fe phases | 1 | 0 | 1 | 1 | 1 | 1 |

Table 5.9e: Phase content of the kaolin sample B4915 and of the grain-size fractions gathered from XRD-XRF-STA crosscheck.

| B4915 | bulk [%] | >20 µm [%] | 2-20 µm [%] | 0.6-2 µm [%] | 0.2-0.6 µm [%] | <0.2 µm [%] |
|---|---|---|---|---|---|---|
| Kaolinite | 77 | 84 | 76 | 78 | 70 | 55 |
| Illite | 12 | 7 | 10 | 14 | 23 | 38 |
| K-Feldspar | 6 | 6 | 9 | 3 | 1 | 1 |
| Quartz | 4 | 2 | 4 | 2 | 4 | 3 |
| Ti oxides | 0 | 0 | 0 | 1 | 1 | 1 |
| Crandallite | 0 | 0 | 0 | 1 | 0 | 1 |
| Fe phases | 1 | 1 | 1 | 1 | 1 | 1 |

Table 5.9f: Phase content of the kaolin sample B4915 MO and of the grain-size fractions gathered from XRD-XRF-STA crosscheck.

| B4915 MO | bulk [%] | >20 µm [%] | 2-20 µm [%] | 0.6-2 µm [%] | 0.2-0.6 µm [%] | <0.2 µm [%] |
|---|---|---|---|---|---|---|
| Kaolinite | 77 | 69 | 77 | 81 | 75 | 62 |
| Illite | 14 | 12 | 9 | 13 | 19 | 27 |
| K-Feldspar | 5 | 11 | 9 | 2 | 2 | 3 |
| Quartz | 3 | 5 | 4 | 2 | 2 | 4 |
| Ti oxides | 0 | 0 | 0 | 0 | 1 | 1 |
| Crandallite | 0 | 0 | 0 | 1 | 0 | 2 |
| Fe phases | 1 | 1 | 1 | 1 | 1 | 1 |

Table 5.9g: Phase content of the kaolin sample B4915 K and of the grain-size fractions gathered from XRD-XRF-STA crosscheck.

| B4915 K | bulk [%] | >20 µm [%] | 2-20 µm [%] | 0.6-2 µm [%] | 0.2-0.6 µm [%] | <0.2 µm [%] |
|---|---|---|---|---|---|---|
| Kaolinite | 77 | 72 | 78 | 80 | 70 | 58 |
| Illite | 13 | 12 | 9 | 12 | 22 | 36 |
| K-Feldspar | 6 | 11 | 8 | 3 | 2 | 0 |
| Quartz | 3 | 4 | 4 | 2 | 3 | 5 |
| Ti oxides | 0 | 0 | 0 | 1 | 1 | 0 |
| Crandallite | 0 | 0 | 0 | 1 | 1 | 0 |
| Fe phases | 1 | 1 | 1 | 1 | 1 | 1 |

disorder increased slightly in the sequence: LA540 < B4914 < B4915. The PA curves of the treated analogues plotted extremely close to the respective untreated samples. The sharp and intense recrystallization peaks of all bulk samples displayed by DSC curves indicated an overall ordered kaolinite structure.

As further testing tool for the determination of structural disorder, the Hinckley index (Hinckley, 1963) was applied. Unfortunately, this method did not yield unique results as the diagnostic peaks were poorly resolved. This, in turn, caused difficulties in determination of peak heights due to ambiguous background correction. Therefore, the Hinckley index was discarded as a method to determine the degree of structural order.

### 5.2.4 CEC measurements

For all tested kaolin samples, the cation exchange capacity was determined by means of the Cu-trien method at pH 7 and compared to the sum of exchanged cations gathered from ICP-OES measurements. Afterwards, the measured CEC was corrected as outlined in Section 4.2.6 in order to calculate the content of swellable components $w_{sc}$ (sum of smectite and smectitic layers in I-S) using equation 4.19. The results are reported in Table 5.10.

Except for sample B4914, the CEC increased with decreasing grain size and under a strong increase in the clay fractions <0.6 µm. This trend was well-pronounced for sample LA540 and LA540 MO, which exhibited the greatest overall CEC within the tested kaolins, followed by B4915 and its treated analogues.

Regarding the measured CEC of the bulk samples and the <0.6 µm clay fractions with treatment, all samples showed variations of ±2 meq/100g, which is within the measurement accuracy.

The comparison between the amount of exchanged cations in the exchanging solution and the CEC revealed that the interlayer of the swellable components was dominated by $Ca^{2+}$ and $Mg^{2+}$. With a deviation of ±2 meq/100 g, the sum of exchangeable cations (∑) was in the range of the measured CEC for LA540, B4914 MO, as well as for several fractions of sample LA540 MO and sample group B4915. The bulk material and the silt fractions of sample B4914 showed somewhat larger deviations. Unsystematic deviations of ∑ and CEC were noted for the clay fractions <0.6 µm of LA540 MO and sample group B4915.

Regarding the contents of the swellable components $w_{sc}$ for the respective bulk samples, it can be seen that LA540 showed the greatest values (6%), followed by B4914 (3%). For B4915 as well as for the treated counterparts, no swellable components were found. After bioleaching, $w_{sc}$ decreased slightly for sample LA540 and was absent for B4914 MO. The trend of lower $w_{sc}$ values after microbiological treatment was also observed for the respective grain-size

Table 5.10a: Amount of exchangeable cations and CEC measurements (CEC meas) of the bulk material of LA540 and LA540 MO and of the respective grain-size fractions.

| Sample | bulk [meq/100g] | >20 µm [meq/100g] | 2-20 µm [meq/100g] | 0.6-2 µm [meq/100g] | 0.2-0.6 µm [meq/100g] | <0.2 µm [meq/100g] |
|---|---|---|---|---|---|---|
| LA540 | | | | | | |
| $Na^+$ | 0 | n.d. | 0 | 0 | 0 | 0 |
| $Mg^{2+}$ | 2 | n.d. | 0 | 0 | 7 | 9 |
| $K^+$ | 1 | n.d. | 0 | 2 | 1 | 3 |
| $Ca^{2+}$ | 5 | n.d. | 2 | 3 | 16 | 26 |
| Σ | 8 | n.d. | 2 | 5 | 24 | 38 |
| CEC meas | 10 | n.d. | 4 | 6 | 25 | 38 |
| CEC corr | 5 | n.d. | 0 | 1 | 19 | 30 |
| $w_{sc}$ [%] | 6 | n.d. | 0 | 1 | 24 | 38 |
| LA540 MO | | | | | | |
| $Na^+$ | 0 | n.d. | 0 | 0 | 0 | 1 |
| $Mg^{2+}$ | 2 | n.d. | 1 | 4 | 4 | 9 |
| $K^+$ | 1 | n.d. | 0 | 1 | 1 | 4 |
| $Ca^{2+}$ | 5 | n.d. | 2 | 2 | 10 | 21 |
| Σ | 8 | n.d. | 3 | 6 | 15 | 35 |
| CEC meas | 9 | n.d. | 4 | 6 | 25 | 37 |
| CEC corr | 4 | n.d. | 0 | 2 | 19 | 29 |
| $w_{sc}$ [%] | 5 | n.d. | 0 | 3 | 24 | 36 |

CEC corr: corrected CEC according to equation 4.18. $w_{sc}$: content of swellable components from CEC measurements; n.d.: not determined due to lack of sample.

Table 5.10b: Amount of exchangeable cations and CEC measurements (CEC meas) of the bulk material of B4914 and B4914 MO and of the respective grain-size fractions.

| Sample | bulk [meq/100g] | >20 µm [meq/100g] | 2-20 µm [meq/100g] | 0.6-2 µm [meq/100g] | 0.2-0.6 µm [meq/100g] | <0.2 µm [meq/100g] |
|---|---|---|---|---|---|---|
| B4914 | | | | | | |
| $Na^+$ | 0 | 0 | 0 | 0 | 0 | n.d. |
| $Mg^{2+}$ | 1 | 0 | 1 | 1 | 1 | n.d. |
| $K^+$ | 0 | 0 | 0 | 0 | 0 | n.d. |
| $Ca^{2+}$ | 1 | 1 | 1 | 1 | 3 | n.d. |
| Σ | 2 | 1 | 2 | 2 | 4 | n.d. |
| CEC meas | 7 | 6 | 7 | 3 | 4 | n.d. |
| CEC corr | 2 | 1 | 2 | 0 | 0 | n.d. |
| $w_{sc}$ [%] | 3 | 1 | 3 | 0 | 0 | n.d. |
| B4914 MO | | | | | | |
| $Na^+$ | 1 | 0 | 0 | 0 | 0 | 3 |
| $Mg^{2+}$ | 3 | 0 | 1 | 2 | 4 | 5 |
| $K^+$ | 0 | 0 | 0 | 0 | 0 | 1 |
| $Ca^{2+}$ | 1 | 1 | 0 | 1 | 1 | 2 |
| Σ | 5 | 1 | 1 | 3 | 5 | 11 |
| CEC meas | 5 | 1 | 2 | 2 | 6 | 10 |
| CEC corr | 0 | 0 | 0 | 0 | 1 | 4 |
| $w_{sc}$ [%] | 0 | 0 | 0 | 0 | 1 | 5 |

CEC corr: corrected CEC according to equation 4.18. $w_{sc}$: content of swellable components from CEC measurements; ; n.d.: not determined due to lack of sample.

Table 5.10c: Amount of exchangeable cations and CEC measurements (CEC meas) of the bulk material of B4915, B4915 MO and B4915 K and of the respective grain-size fractions.

| Sample | bulk [meq/100g] | >20 µm [meq/100g] | 2-20 µm [meq/100g] | 0.6-2 µm [meq/100g] | 0.2-0.6 µm [meq/100g] | <0.2 µm [meq/100g] |
|---|---|---|---|---|---|---|
| B4915 | | | | | | |
| $Na^+$ | 0 | 0 | 0 | 0 | 0 | 0 |
| $Mg^{2+}$ | 1 | 1 | 0 | 1 | 1 | 1 |
| $K^+$ | 0 | 0 | 0 | 0 | 0 | 0 |
| $Ca^{2+}$ | 1 | 1 | 1 | 1 | 1 | 1 |
| Σ | 2 | 2 | 1 | 2 | 2 | 2 |
| CEC meas | 3 | 3 | 1 | 2 | 4 | 18 |
| CEC corr | 0 | 0 | 0 | 0 | 0 | 12 |
| $w_{sc}$ [%] | 0 | 0 | 0 | 0 | 0 | 15 |
| B4915 MO | | | | | | |
| $Na^+$ | 1 | 1 | 0 | 2 | 3 | 4 |
| $Mg^{2+}$ | 3 | 2 | 2 | 3 | 2 | 4 |
| $K^+$ | 0 | 0 | 0 | 0 | 0 | 2 |
| $Ca^{2+}$ | 1 | 2 | 2 | 2 | 1 | 2 |
| Σ | 5 | 5 | 4 | 7 | 6 | 12 |
| CEC meas | 3 | 2 | 3 | 4 | 5 | 17 |
| CEC corr | 0 | 0 | 0 | 0 | 0 | 11 |
| $w_{sc}$ [%] | 0 | 0 | 0 | 0 | 0 | 14 |

CEC corr: corrected CEC according to equation 4.18. $w_{sc}$: content of swellable components from CEC measurements.

Continuation of Table 5.10c:

| B4915 K | bulk<br>[meq/100g] | >20 µm<br>[meq/100g] | 2-20 µm<br>[meq/100g] | 0.6-2 µm<br>[meq/100g] | 0.2-0.6 µm<br>[meq/100g] | <0.2 µm<br>[meq/100g] |
|---|---|---|---|---|---|---|
| $Na^+$ | 1 | 1 | 1 | 0 | 1 | 4 |
| $Mg^{2+}$ | 3 | 2 | 2 | 2 | 2 | 4 |
| $K^+$ | 1 | 1 | 1 | 0 | 0 | 2 |
| $Ca^{2+}$ | 1 | 1 | 2 | 2 | 2 | 3 |
| Σ | 6 | 5 | 6 | 4 | 5 | 13 |
| CEC meas | 3 | 3 | 3 | 4 | 4 | 19 |
| CEC corr | 0 | 0 | 0 | 0 | 0 | 13 |
| $w_{sc}$ [%] | 0 | 0 | 0 | 0 | 0 | 17 |

CEC corr: corrected CEC according to equation 4.18. $w_{sc}$: content of swellable components from CEC measurements.

fractions of B4914, whereas the values for the grain-size fractions of LA540 remained nearly constant with treatment.

For all samples, a general increase of $w_{sc}$ with decreasing grain-size fraction was observed, which was independent from treatment.

### 5.2.5 Mössbauer spectroscopy

Information on Fe distribution was gained through Mössbauer spectroscopy. For all kaolin samples, the oxide-bound Fe was identified as goethite as the spectra from measurements at 4.2 K exhibited a sextet of narrow lines and a hyperfine field of 49 to 50 T. The relative Fe distribution gathered from Mössbauer spectroscopy was related to the total $Fe_2O_3$ content from XRF measurements, giving rise to an absolute Fe distribution (Table 5.11).

The Fe distribution characteristics for each sample was expressed by the ratio of silicate-bound Fe to oxide-bound Fe as goethite. All samples yielded distribution ratios >1, which means that the Fe was predominantly silicate-bound. However, large differences between the samples were observed with respect to Fe concentrations. The comparison of the bulk samples showed that the smallest Fe distribution ratios were recorded for LA540 and its microbiologically treated counterpart, with 7 and 9, respectively. With 250 times more silicate-bound than oxide-bound Fe, the bulk sample of B4914 had the largest distribution ratio, which strongly decreased after microbiological treatment. The distribution ratio of B4915 increased slightly from 17 to 35 for the control sample B4915 K and strongly increased after microbiological treatment.

With respect to grain-size distribution, no general tendency could be established for the distribution ratios. LA540 showed a slight increase toward the clay size fractions, whereas the distribution ratios of LA540 MO remained nearly constant for all size fractions. Sample B4914 showed the greatest values for the coarsest fraction as well as for the <0.6 µm clay fractions. The opposite trend was found for B4914 MO. For B4915 and B4915 MO, the maximum of distribution ratios were observed for the 2-20 µm and 0.6-2 µm fractions, whereas sample B4915 K showed an inverse trend.

In order to elucidate the effect of microbiological treatment on Fe distribution, the distribution ratios of the respective bulk samples and of the various grain-size fractions were set in relation, giving rise to the relative Fe depletion $\Psi$. Figure 5.9 indicates that relative Fe depletion occurred within sample group LA540 both, for goethite ($\Psi<1$) and silicate-bound Fe ($\Psi>1$). The amount of goethite was found to be reduced for the bulk sample and the grain-size fractions >0.6 µm, whereas for the grain-size fractions <0.6 µm, depletion took place within the silicate structure. Regarding the sample group B4914, Fe depletion occurred entirely at the expense of the silicate-bound Fe. Merely for the 0.6-2 µm fraction, no change was detected with microbiological treatment.

Table 5.11a: Fe distribution determined by Mössbauer spectroscopy related to the $Fe_2O_3$ content from XRF analysis of the kaolin samples LA540 and LA540 MO and their respective grain-size fractions.

| Sample | | relative Fe distribution | | absolute Fe distribution | | |
|---|---|---|---|---|---|---|
| | $Fe_2O_3$ [%] | Goethite [%] | silicate-bound Fe [%] | Goethite [%] | silicate-bound Fe [%] | silicate-bound Fe/ Goethite |
| LA540 | | | | | | |
| bulk | 1.46 | 13.0 | 87.0 | 0.19 | 1.27 | 7 |
| >20 µm | 2.09 | 13.0 | 87.0 | 0.27 | 1.82 | 7 |
| 2-20 µm | 0.48 | 17.7 | 82.3 | 0.08 | 0.40 | 5 |
| 0.6-2 µm | 1.19 | 13.1 | 86.9 | 0.16 | 1.03 | 7 |
| 0.2-0.6 µm | 3.94 | 7.4 | 92.6 | 0.29 | 3.65 | 13 |
| <0.2 µm | 4.27 | 8.8 | 91.2 | 0.38 | 3.90 | 10 |
| LA540 MO | | | | | | |
| bulk | 1.05 | 9.7 | 90.3 | 0.10 | 0.95 | 9 |
| >20 µm | 2.28 | n.d. | n.d. | n.d. | n.d. | n.d. |
| 2-20 µm | 0.58 | n.d. | n.d. | n.d. | n.d. | n.d. |
| 0.6-2 µm | 0.97 | 10.4 | 89.6 | 0.10 | 0.86 | 9 |
| 0.2-0.6 µm | 3.52 | 11.3 | 88.7 | 0.40 | 3.12 | 8 |
| <0.2 µm | 3.94 | 10.4 | 89.6 | 0.41 | 3.53 | 9 |

n.d.: not determined due to lack of sample

Table 5.11b: Fe distribution determined by Mössbauer spectroscopy related to the $Fe_2O_3$ content from XRF analysis of the kaolin samples B4914 and B4914 MO and their respective grain-size fractions.

| Sample | $Fe_2O_3$ [%] | relative Fe distribution<br>Goethite [%] | silicate-bound Fe [%] | absolute Fe distribution<br>Goethite [%] | silicate-bound Fe [%] | silicate-bound Fe/ Goethite |
|---|---|---|---|---|---|---|
| B4914 | | | | | | |
| bulk | 0.78 | 0.4 | 99.6 | 0.003 | 0.77 | 250 |
| >20 µm | 0.56 | 0.2 | 99.8 | 0.001 | 0.56 | 499 |
| 2-20 µm | 0.61 | 0.9 | 99.1 | 0.01 | 0.60 | 110 |
| 0.6-2 µm | 0.90 | 1.2 | 98.8 | 0.01 | 0.89 | 82 |
| 0.2-0.6 µm | 1.33 | 0.6 | 99.4 | 0.01 | 1.33 | 166 |
| <0.2 µm | 1.92 | 0.5 | 99.5 | 0.01 | 1.91 | 199 |
| B4914 MO | | | | | | |
| bulk | 0.75 | 1.2 | 98.8 | 0.01 | 0.74 | 82 |
| >20 µm | 0.53 | n.d. | n.d. | n.d. | n.d. | n.d. |
| 2-20 µm | 0.56 | 1.3 | 98.7 | 0.01 | 0.55 | 76 |
| 0.6-2 µm | 0.74 | 1.2 | 98.8 | 0.01 | 0.73 | 82 |
| 0.2-0.6 µm | 1.15 | 2.3 | 97.7 | 0.03 | 1.12 | 42 |
| <0.2 µm | 1.22 | 1.8 | 98.2 | 0.02 | 1.20 | 55 |

n.d.: not determined due to lack of sample

Table 5.11c: Fe distribution determined by Mössbauer spectroscopy related to the $Fe_2O_3$ content from XRF analysis of the kaolin samples B4915, B4915 MO and B4915 K and their respective grain-size fractions.

| Sample | $Fe_2O_3$ [%] | relative Fe distribution<br>Goethite [%] | silicate-bound Fe [%] | absolute Fe distribution<br>Goethite [%] | silicate-bound Fe [%] | silicate-bound Fe/ Goethite |
|---|---|---|---|---|---|---|
| B4915 | | | | | | |
| bulk | 0.95 | 5.5 | 94.5 | 0.05 | 0.90 | 17 |
| >20 µm | 0.61 | 6.9 | 93.1 | 0.04 | 0.57 | 13 |
| 2-20 µm | 0.64 | 3.3 | 96.7 | 0.02 | 0.62 | 29 |
| 0.6-2 µm | 1.05 | 2.7 | 97.3 | 0.03 | 1.02 | 36 |
| 0.2-0.6 µm | 1.24 | 4.4 | 95.6 | 0.05 | 1.19 | 22 |
| <0.2 µm | 2.01 | 5.3 | 94.7 | 0.11 | 1.90 | 18 |
| B4915 MO | | | | | | |
| bulk | 0.82 | 0.8 | 99.2 | 0.01 | 0.81 | 124 |
| >20 µm | 0.97 | 3.3 | 96.7 | 0.03 | 0.94 | 29 |
| 2-20 µm | 0.65 | 1.0 | 99.0 | 0.01 | 0.64 | 99 |
| 0.6-2 µm | 0.94 | 0.5 | 99.5 | 0.00 | 0.93 | 199 |
| 0.2-0.6 µm | 1.16 | 1.1 | 98.9 | 0.01 | 1.15 | 90 |
| <0.2 µm | 1.51 | 1.3 | 98.7 | 0.02 | 1.49 | 76 |
| B4915 K | | | | | | |
| bulk | 0.82 | 2.8 | 97.2 | 0.02 | 0.80 | 35 |
| >20 µm | 0.59 | 3.6 | 96.4 | 0.02 | 0.57 | 27 |
| 2-20 µm | 0.63 | 4.6 | 95.4 | 0.03 | 0.60 | 21 |
| 0.6-2 µm | 1.01 | 5.7 | 94.3 | 0.06 | 0.95 | 17 |
| 0.2-0.6 µm | 1.40 | 4.3 | 95.7 | 0.06 | 1.34 | 22 |
| <0.2 µm | 1.53 | 2.6 | 97.4 | 0.04 | 1.49 | 37 |

In contrast, sample group B4915 showed consistently Ψ-values <1, which means that Fe depletion occurred exclusively by means of goethite. The control sample B4915 K exhibited all types of Fe depletion: within the bulk sample as well as for the coarsest and the finest fraction, where Fe depletion took place for goethite. No changes were observed for the 0.2-0.6 µm fraction, whereas a decrease of the silicate-bound Fe was recorded for the fractions 2-20 µm and 0.6-2 µm.

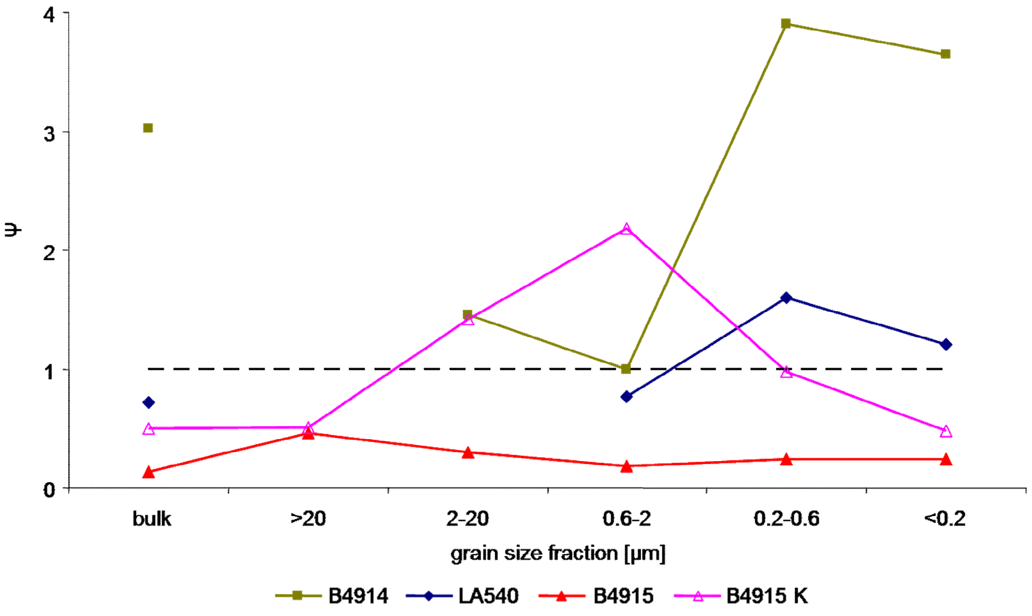

Figure 5.9: Relative Fe depletion Ψ for the bulk samples and the grain-size fractions of LA540, B4914, and B4915. The dashed horizontal line marks the boundary between Fe depletion events by means of goethite (Ψ<1) or silicate-bound Fe (Ψ>1).

### 5.2.6 Electron microscopy

The influence of microbial treatment on particle morphology in terms of particle shape, particle size and aggregate structure was examined by means of ESEM. All bulk samples contained mainly kaolinite as well as sparse amounts of quartz and K-feldspar. Only LA540 and LA540 MO were found to contain greater quantities of quartz and K-feldspar (Figure 5.10a). At a magnification of up to 20000x, isolated needle-like goethite crystals were identified by their morphology as well as by EDX measurements.

Independent from treatment, the particle shape of kaolinite ranged from hexagonal and pseudo-hexagonal crystallites to crystallites with jagged and irregular edges (Figure 5.10a). Some of the kaolinite platelets showed evidence of curve-shaped surfaces (Figures 5.10b and 5.10c).

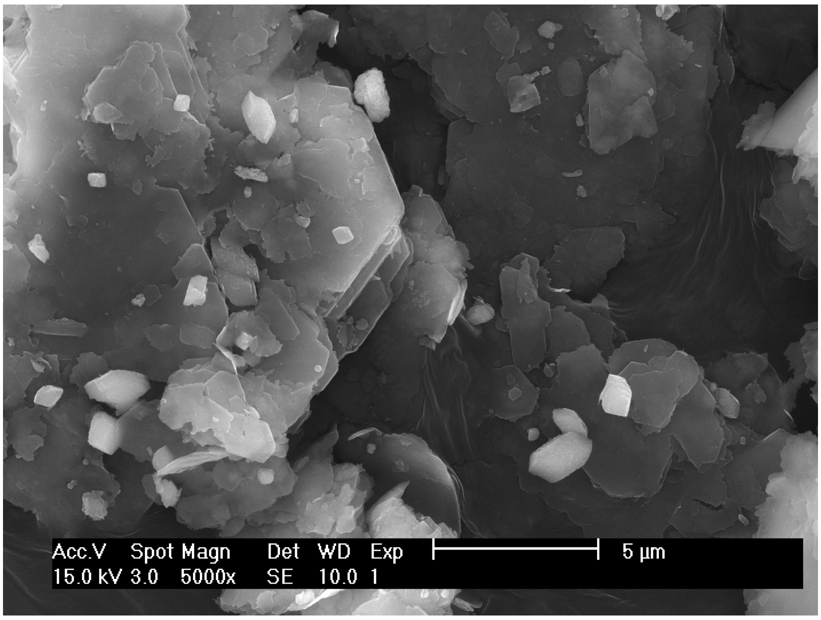

Figure 5.10a: SEM micrograph of sample LA540 demonstrates the greater abundance of quartz with respect to the other samples as well as the coexsistence of different particle shapes, which ranged from hexagonal and pseudo-hexagonal crystallites (left side of the picture) to crystallites with jagged and irregular edges (right side).

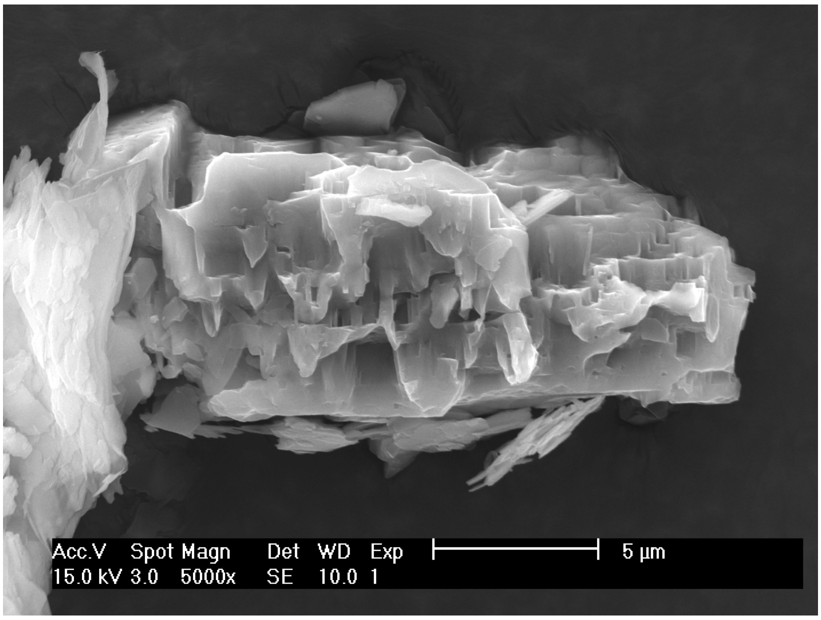

Figure 5.10b: SEM micrograph of sample B4915, with evidence of curve-shaped kaolinite platelets (upper left part of the picture) and strongly altered K-feldspar.

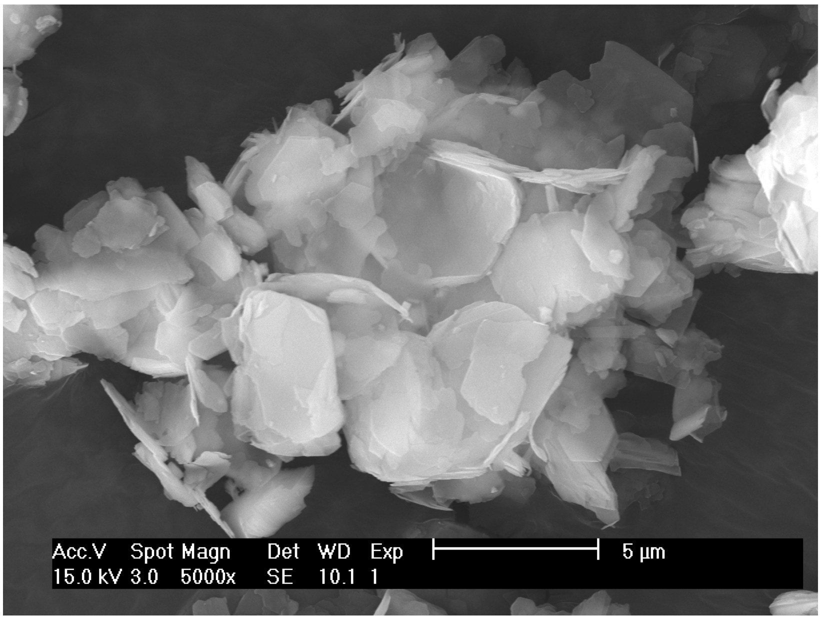

Figure 5.10c: SEM micrograph of sample B4914 MO revealing kaolinite with curve-shaped surfaces (central part of the picture) and kaolinite crystallites consisting of only few 1:1 silicate layers.

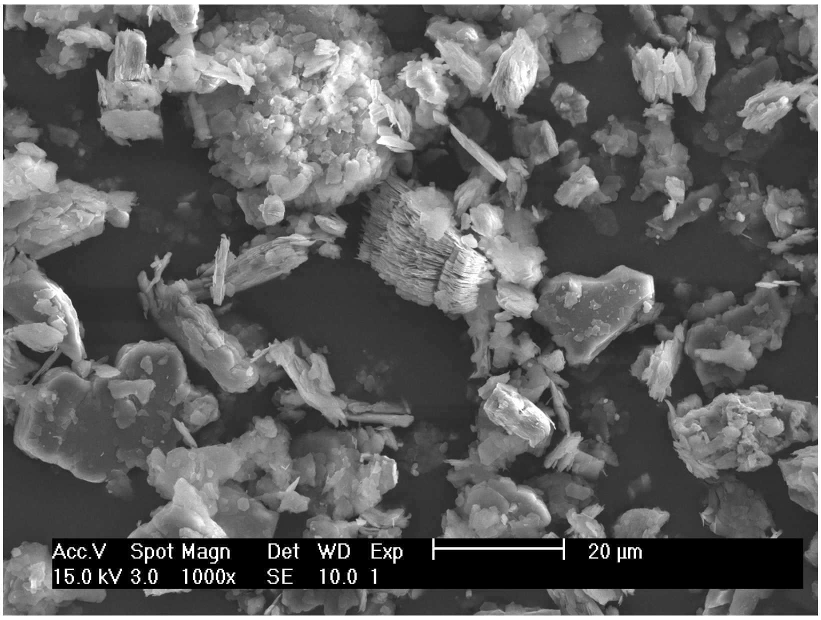

Figure 5.10d: SEM micrograph of sample B4915 MO at low magnification, indicating an average particle size of 20 µm as well as the coexistence of various kaolinite aggregation forms like “booklets” (central part of the picture), larger agglomerates (upper part) and associations of only few platelets (e.g., upper central part).

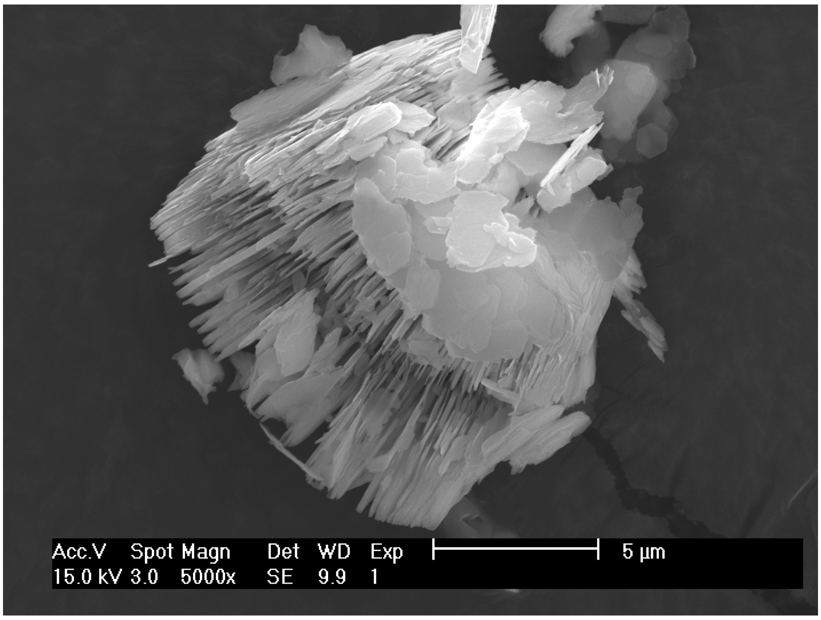

Figure 5.10e: SEM micrograph of sample B4915 K, which shows a multi-layer stacked kaolinite particle (“booklet”) in association with jagged-edge thin kaolinite platelets.

The surfaces of the K-feldspar crystallites were characterized by fractures and dissolution pores, indicating extensive alteration (Figure 5.10b).

No changes as a consequence of microbiological treatment was observed for the average particle size of the bulk samples, which was in the range of 20 µm (Figure 5.10d).

Different types of kaolinite aggregate structures were identified, coexisting in all bulk samples, regardless of the treatment step. Kaolinite platelets were arranged as face-to-face multi-layered stacks (“booklets”) (Figures 5.10d and 5.10e), as chaotically oriented agglomerates of smaller particles (Figure 5.10d), or as association of only few platelets (Figures 5.10c and 5.10e).

### 5.2.7 Summary of the results

In the following, the results obtained from the various methods described above, are summarized acoording to their significance to bioleaching and to the determination of the mineralogical phase content of the paper kaolins.

*Bioleaching*

Information on bioleaching of the paper kaolins with *Shewanella putrefaciens* was obtained by spectrophotometry, XRF, and Mössbauer spectroscopy. The results were evaluated and compared according to the following brightness-related parameters as summarized in Table 5.12:

- initial $Fe_2O_3$ content: amount of $Fe_2O_3$ prior to bioleaching gathered from XRF analysis (Table 5.2)

- extent of Fe reduction: percentage of Fe decrease after treatment, calculated according to (1-$Fe_2O_3$ final/$Fe_2O_3$ initial)*100%
- initial brightness: value of brightness R457 before treatment
- brightness enhancement $\Delta$: differential amount of the brightness prior to and after treatment
- Fe depletion $\Psi$: place of Fe depletion in terms of goethite ($\Psi<1$) or silicate-bound Fe ($\Psi>1$) (Figure 5.9)
- Fe removal efficiency: relation of the extent of Fe reduction to brightness enhancement $\Delta$ expressed by the slope m of the respective straight lines from the slope-intercept form $y=mx+b$ (Figure 5.2)

Comparing the order of samples established for each parameter (Table 5.12) and as illustrated in Figure 5.11 in terms of "pattern recognition", the following correlations became evident:

(1) a strong positive correlation between the initial $Fe_2O_3$ content and the extent of Fe reduction, thus, the larger the amount of $Fe_2O_3$, the larger the extent of Fe reduction; (2) a direct correlation between the initial brightness and $\Psi$, as the sample with the smallest brightness (B4915) showed the largest depletion of oxide-bound Fe; an inverse correlation between $\Psi$ and (3) the initial $Fe_2O_3$ content and (4) the extent of Fe reduction, as the silicate-bound sample B4914 showed, for both parameters, the smallest values; (5) a strong correlation between $\Delta$ and $\Psi$, as the largest brightness enhancement was achieved for B4915, the sample with mainly oxide-bound Fe as depletion source, whereas it was the smallest for the Fe silicate-bound sample B4914; an inverse correlation between Fe removal efficiency and (6) initial $Fe_2O_3$ content and, thus, (7) the extent of Fe reduction; a week inverse correlation between initial brightness and both (8) the initial $Fe_2O_3$ content and (9) the extent of Fe reduction, as the sample with the smallest values for both parameters (B4914) showed the largest initial brightness, but the other kaolin samples did not reflect this trend; (10) an inverse correlation of initial brightness and brightness enhancement for the samples B4914 and B4915.

### *Quantification results*

The phase content of the paper kaolins prior to and after bioleaching was determined by a multi-method approach, crosschecking the results gathered from XRD, XRF and STA measurements. In order to ensure comparability of these results with the quantification results from ODPF, only the portion of clay minerals from the XRD-XRF-STA crosscheck was considered (Table 5.9). Therefore, ODPF results were normalized to the quantification results from the XRD-XRF-STA crosscheck. The three phases determined by ODPF (kaolinite, I-S, illite) were converted to four phases (kaolinite, smectite layers, illite, and illite layers), subdividing the I-S content according to the respective $W_a$ values (Table

5.13). With the normalized ODPF values, the maximum mass loss $\Delta m\ T_{DHXcalc}$ was calculated according to equation 4.14 and compared with the measured results ($\Delta m\ T_{DHXmeas}$). For this calculation, the quantification results of the original three phases from ODPF were converted to three coefficients x, y, z, with x for kaolinite, y for the smectite layers, and z for the sum of illite and illite layers.

Comparing the Δ values as an assessment tool for quantification, differences between the data sets deduced from the diverse methods (XRD-XRF-STA and ODPF) were remarkable. In general, from ODPF greater positive Δ values were derived, implying underestimation of the clay minerals content.

The greatest positive deviations were observed for the <0.6 µm fractions of LA540 and LA540 MO, which contained larger amounts of smectite layers. For the respective clay fractions of LA540, an underestimation of kaolinite and an overestimation of illite plus illite layers was noted. The tendency to underestimate the kaolinite content was enhanced with increasing amounts of smectite layers.

In contrast, for the clay fractions of sample LA540 MO, the respective kaolinite contents from ODPF were either in good agreement with the results from the XRD-XRF-STA crosscheck or distinctly larger, like in the case of fraction 0.2-0.6 µm, which, in turn, led to a smaller Δ value. The increasing amount of smectite layers with decreasing size fraction was compensated by smaller illite plus illite layers contents.

The clay fractions of B4914 and B4915 as well as their treated counterparts were characterized by small smectite layers contents of 2% or less. The generally greater kaolinite contents determined by ODPF induced neither negative Δ values, denoting overestimation, nor smaller positive deviations, indicating a greater consistency in the quantification results of ODPF and STA measurements. The largest positive Δ values were produced from samples with smaller kaolinite amounts with respect to the results from the XRD-XRF-STA crosscheck.

Differences between the smectite layer content determined by ODPF and CEC measurements (Table 5.10) were very significant for the <0.2 µm fractions as well as for the 0.2-0.6 µm fractions of LA540 and LA540 MO. The smectite layers content deduced from CEC exceeded the quantification results from ODPF by a factor of more than three. For the coarsest clay fraction of all samples and for the 0.2-0.6 µm fraction of the sample groups B4914 and B4915, results from ODPF and CEC were in the same range.

Table 5.12: Summary of the results for the brightness-related parameters before and after bioleaching of the paper kaolins with *Shewanella putrefaciens*.

| Parameter | LA540 | B4914 | B4915 | B4915 K | Order |
|---|---|---|---|---|---|
| initial $Fe_2O_3$ content [%] | 1.46 | 0.78 | 0.95 | 0.95 | B4914 < B4915 = B4915 K < LA540 |
| Extent of Fe reduction [%] | 28 | 4 | 14 | 14 | B4914 < B4915 = B4915 K < LA540 |
| initial brightness [%] | 68.2 | 76.5 | 67.9 | 67.9 | B4915 = B4915 K < LA540 < B4914 |
| Brightness enhancement Δ [%] | 3.9 | 2.7 | 8.7 | 2.7 | B4914 = B4915 K < LA540 < B4915 |
| Fe depletion Ψ | 0.72 | 3.02 | 0.14 | 0.49 | B4915 < B4915 K < LA540 < B4914 |
| Fe removal efficiency | -0.1051 | -0.0111 | -0.0149 | -0.0481 | LA540 < B4915 K < B4915 < B4914 |

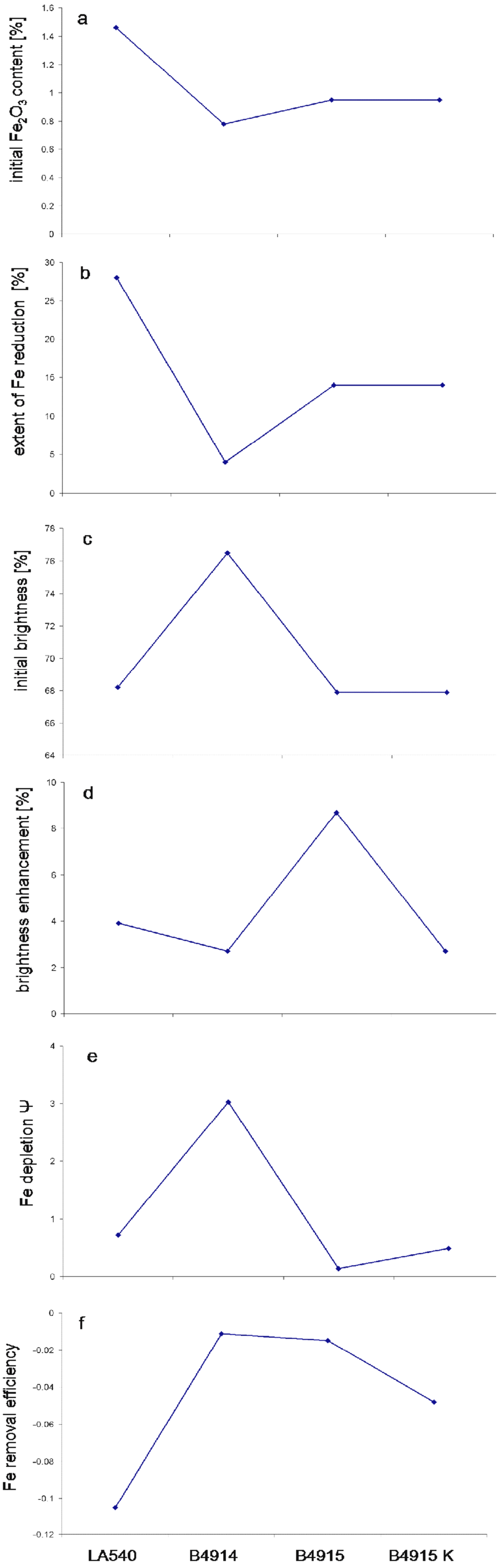

Figure 5.11: Pattern recognition of the parameters used for the evaluation of bioleaching (a) initial $Fe_2O_3$ content, (b) extent of Fe reduction, (c) initial brightness, (d) brightness enhancement Δ, (e) Fe depletion Ψ, and (f) Fe removal efficiency of the bulk samples.

Table 5.13a: Quantification by XRD-XRF-STA crosscheck and by one-dimensional XRD profile modeling (ODPF) of the clay fractions of LA540 and LA540 MO compared with the maximum mass loss Δm $T_{DHX}$. norm: normalized value; conv.: converted value from phase reduction.

| Sample | Quantification method | Kaolinite [%] | Smectite layers [%] | Illite [%] | Illite layers [%] | ∑ [%] | Δm $T_{DHXcalc}$ [%] | Δm $T_{DHXmeas}$ [%] | Δ [%] |
|---|---|---|---|---|---|---|---|---|---|
| LA540 | | | | | | | | | |
| 0.6-2 µm | XRD-XRF-STA | 60 | n.d. | 21 | n.d. | 81 | 9.34 | 9.68 | 0.34 |
| | ODPF | 64 | 1 | 32 | 3 | 100 | - | - | - |
| | ODPF conv., norm. | 52 | 1 | 26 | 2 | 81 | 8.59 | 9.68 | 1.09 |
| 0.2-0.6 µm | XRD-XRF-STA | 30 | n.d. | 35 | n.d. | 65 | 5.80 | 5.91 | 0.11 |
| | ODPF | 11 | 14 | 17 | 58 | 100 | - | - | - |
| | ODPF conv., norm. | 7 | 9 | 11 | 38 | 65 | 3.67 | 5.91 | 2.24 |
| <0.2 µm | XRD-XRF-STA | 18 | n.d. | 58 | n.d. | 76 | 5.18 | 5.74 | 0.56 |
| | ODPF | 12 | 16 | 6 | 66 | 100 | - | - | - |
| | ODPF conv., norm. | 9 | 12 | 5 | 50 | 76 | 4.37 | 5.74 | 1.37 |
| LA540 MO | | | | | | | | | |
| 0.6-2 µm | XRD-XRF-STA | 65 | n.d. | 12 | n.d. | 77 | 9.62 | 9.69 | 0.07 |
| | ODPF | 86 | 1 | 10 | 3 | 100 | - | - | - |
| | ODPF conv., norm. | 66 | 1 | 8 | 2 | 77 | 9.72 | 9.69 | -0.03 |
| 0.2-0.6 µm | XRD-XRF-STA | 21 | n.d. | 57 | n.d. | 78 | 5.56 | 8.21 | 2.65 |
| | ODPF | 61 | 4 | 21 | 14 | 100 | - | - | - |
| | ODPF conv., norm. | 48 | 3 | 16 | 11 | 78 | 8.08 | 8.21 | 1.61 |
| <0.2 µm | XRD-XRF-STA | 32 | n.d. | 49 | n.d. | 81 | 7.18 | 10.53 | 3.35 |
| | ODPF | 42 | 10 | 9 | 39 | 100 | - | - | - |
| | ODPF conv., norm. | 34 | 8 | 7 | 32 | 81 | 6.92 | 10.53 | 3.61 |

n.d.: not detectable with the respective method

Table 5.13b: Quantification by XRD-XRF-STA crosscheck and by one-dimensional XRD profile modeling (ODPF) of the clay fractions of B4914 and B4914 MO compared with the maximum mass loss Δm $T_{DHX}$. norm: normalized value; conv.: converted value from phase reduction.

| Sample | Quantification method | Kaolinite [%] | Smectite layers [%] | Illite [%] | Illite layers [%] | ∑ [%] | Δm $T_{DHXcalc}$ [%] | Δm $T_{DHXmeas}$ [%] | Δ [%] |
|---|---|---|---|---|---|---|---|---|---|
| B4914 | | | | | | | | | |
| 0.6-2 µm | XRD-XRF-STA | 81 | n.d. | 14 | n.d. | 95 | 11.94 | 11.98 | 0.04 |
| | ODPF | 86 | 0 | 14 | 0 | 100 | - | - | - |
| | ODPF conv., norm. | 82 | 0 | 13 | 0 | 95 | 12.04 | 11.98 | -0.06 |
| 0.2-0.6 µm | XRD-XRF-STA | 68 | n.d. | 28 | n.d. | 96 | 10.78 | 10.88 | 0.10 |
| | ODPF | 81 | 1 | 11 | 7 | 100 | - | - | - |
| | ODPF conv., norm. | 78 | 1 | 10 | 7 | 96 | 11.71 | 10.88 | -0.83 |
| <0.2 µm | XRD-XRF-STA | 68 | n.d. | 30 | n.d. | 98 | 10.87 | n.d.* | n.d.* |
| | ODPF | 76 | 1 | 14 | 9 | 100 | - | - | - |
| | ODPF conv., norm. | 74 | 1 | 14 | 9 | 98 | 11.43 | n.d.* | n.d.* |
| B4914 MO | | | | | | | | | |
| 0.6-2 µm | XRD-XRF-STA | 86 | n.d. | 11 | n.d. | 97 | 12.50 | 12.51 | 0.01 |
| | ODPF | 74 | 2 | 10 | 14 | 100 | - | - | - |
| | ODPF conv., norm. | 72 | 2 | 10 | 13 | 97 | 11.20 | 12.51 | 1.31 |
| 0.2-0.6 µm | XRD-XRF-STA | 74 | n.d. | 18 | n.d. | 92 | 11.15 | 12.07 | 0.92 |
| | ODPF | 84 | 0 | 14 | 2 | 100 | - | - | - |
| | ODPF conv., norm. | 77 | 0 | 13 | 2 | 92 | 11.43 | 12.07 | 0.64 |
| <0.2 µm | XRD-XRF-STA | 69 | n.d. | 26 | n.d. | 95 | 10.82 | 15.54 | 4.72 |
| | ODPF | 83 | 0 | 13 | 4 | 100 | - | - | - |
| | ODPF conv., norm. | 79 | 0 | 12 | 4 | 95 | 11.76 | 15.54 | 3.78 |

n.d.: not detectable with the respective method, *n.d.: not determined due to lack of sample

Table 5.13c: Quantification by XRD-XRF-STA crosscheck and by one-dimensional XRD profile modeling (ODPF) of the clay fractions of B4915, B4915 MO and B4915 K compared with the maximum mass loss Δm $T_{DHX}$. norm: normalized value; conv.: converted value from phase reduction.

| Sample | Quantification method | Kaolinite [%] | Smectite layers [%] | Illite [%] | Illite layers [%] | ∑ [%] | Δm $T_{DHXcalc}$ [%] | Δm $T_{DHXmeas}$ [%] | Δ [%] |
|---|---|---|---|---|---|---|---|---|---|
| B4915 | | | | | | | | | |
| 0.6-2 µm | XRD-XRF-STA | 78 | n.d. | 14 | n.d. | 92 | 11.53 | 11.54 | 0.01 |
| | ODPF | 84 | 0 | 13 | 3 | 100 | - | - | - |
| | ODPF conv., norm. | 77 | 0 | 12 | 3 | 92 | 11.34 | 11.54 | 0.20 |
| 0.2-0.6 µm | XRD-XRF-STA | 70 | n.d. | 23 | n.d. | 93 | 10.83 | 10.86 | 0.03 |
| | ODPF | 63 | 2 | 19 | 16 | 100 | - | - | - |
| | ODPF conv., norm. | 58 | 2 | 18 | 15 | 93 | 9.71 | 10.86 | 1.15 |
| <0.2 µm | XRD-XRF-STA | 55 | n.d. | 38 | n.d. | 93 | 9.42 | 10.39 | 0.97 |
| | ODPF | 84 | 1 | 3 | 12 | 100 | - | - | - |
| | ODPF conv., norm. | 78 | 1 | 3 | 11 | 93 | 11.57 | 10.39 | -1.18 |
| B4915 MO | | | | | | | | | |
| 0.6-2 µm | XRD-XRF-STA | 81 | n.d. | 13 | n.d. | 94 | 11.90 | 11.95 | 0.05 |
| | ODPF | 90 | 1 | 5 | 4 | 100 | - | - | - |
| | ODPF conv., norm. | 84 | 1 | 5 | 4 | 94 | 12.18 | 11.95 | -0.23 |
| 0.2-0.6 µm | XRD-XRF-STA | 75 | n.d. | 19 | n.d. | 94 | 11.34 | 11.73 | 0.39 |
| | ODPF | 88 | 1 | 6 | 5 | 100 | - | - | - |
| | ODPF conv., norm. | 82 | 1 | 6 | 5 | 94 | 11.99 | 11.73 | -0.26 |
| <0.2 µm | XRD-XRF-STA | 62 | n.d. | 27 | n.d. | 89 | 10.03 | 12.39 | 2.36 |
| | ODPF | 74 | 2 | 7 | 17 | 100 | - | - | - |
| | ODPF conv., norm. | 66 | 2 | 6 | 15 | 89 | 10.27 | 12.39 | 2.12 |

n.d.: not detectable with the respective method

Continuation of Table 5.13c:

| Sample | Quantification method | Kaolinite [%] | Smectite layers [%] | Illite [%] | Illite layers [%] | ∑ [%] | $\Delta m\ T_{DHXcalc}$ [%] | $\Delta m\ T_{DHXmeas}$ [%] | Δ [%] |
|---|---|---|---|---|---|---|---|---|---|
| B4915 K | | | | | | | | | |
| 0.6-2 µm | XRD-XRF-STA | 80 | n.d. | 12 | n.d. | 92 | 11.71 | 11.74 | 0.03 |
| | ODPF | 77 | 1 | 15 | 7 | 100 | - | - | - |
| | ODPF conv., norm. | 71 | 1 | 14 | 6 | 92 | 10.87 | 11.74 | 0.87 |
| 0.2-0.6 µm | XRD-XRF-STA | 70 | n.d. | 22 | n.d. | 92 | 10.78 | 10.91 | 0.13 |
| | ODPF | 75 | 2 | 5 | 18 | 100 | - | - | - |
| | ODPF conv., norm. | 68 | 2 | 5 | 17 | 92 | 10.60 | 10.91 | 0.31 |
| <0.2 µm | XRD-XRF-STA | 58 | n.d. | 36 | n.d. | 94 | 9.75 | 11.11 | 1.36 |
| | ODPF | 75 | 1 | 15 | 9 | 100 | - | - | - |
| | ODPF conv., norm. | 71 | 1 | 14 | 8 | 94 | 10.97 | 11.11 | 0.14 |

n.d.: not detectable with the respective method

## 5.3 Discussion

### 5.3.1 Physical and chemical parameters

In the following, the influence of microbiological treatment with *Shewanella putrefaciens* on grain-size distribution, pH, electrial conductivity, and brightness-related parameters is discussed.

As shown in Figure 5.1, changes in grain-size distribution occurred by bioleaching. These changes are well pronounced for the kaolin samples B4914 and B4915 and less distinct for LA540. The general trend of a mass shift toward smaller fractions after the treatment can be attributed to the following factors: (1) changes in the aggregate structure due to a dispersion stabilization effect caused by soluble salts as reported by Baird and Walz (2007), who observed that in the absence of any additives, kaolinite particles quickly aggregate and settle. When salt is added, however, the dispersions begin to stabilize, resulting in lower settling velocities. Furthermore, the microorganism itself was found to influence the aggregate structure of clays by the secretion of extracellular polysaccharides that induced local binding of clay particles, referred to as polysaccharide-mediated aggregation, according to Dorioz et al. (1993); (2) particle disaggregation by the removal of cementing Fe oxides (Colombo and Torrent, 1991; Cornell and Schwertmann, 2003); (3) particle fragmentation by microbial attack as stated by Styriaková and Styriak (2000), and Styriaková et al. (2003).

As the control sample B4915 K shows the same distribution trend as the microbiologically treated samples, the shift toward smaller grain sizes seems to be mainly affected by the soluble salt content of the reducing media (Table 3.3) rather than to polysaccharide-mediated aggregation. Moreover, the presence of soluble salts is reflected by the larger electrical conductivity of the treated samples (Table 5.1). Changes of the floc architecture with pH can be excluded, as the pH remained nearly constant after bioleaching. The constancy of pH is in accordance with experiments carried out by Kim et al. (2005) using *Shewanella oneidensis*, but in contrast to observations of Lee et al. (2002) and Styriaková et al. (2003), who both reported a decrease in pH from circumneutral to pH 4 after bioleaching of kaolin samples, which was attributed to the production of acid metabolites. However, these kaolin refinement experiments were carried out with unspecified indigenous (autochtonous) microorganisms (Lee et al., 2002) or with *Bacillus cereus* in the case of Styriaková et al. (2003). Thus, these results may not be fully transferable to the kaolins of this study treated with *Shewanella putrefaciens*.

Regarding the Fe distribution derived from Mössbauer spectroscopy (Table 5.11), the effect of Fe oxide removal on grain-size distribution seems to play a minor role, as the sample with the greatest oxide-bound Fe content (LA540) showed the slightest change in grain-size distribution after biological treatment.

Likewise, the option of particle defragmentation by microbial attack is questionable, as no evidence for particle defragmentation after bioleaching was observed by SEM investigations (Figure 5.10). On the contrary, Styriaková and Styriak (2000) deduced from XRD intensity studies that the decrease of the 3.33 Å peak was induced by the destruction of the mica structure, which led, in turn, to the enrichment of bioleached kaolin samples by fine-grained fractions. This observation could not be ascertained for the kaolin samples under investigation as peak intensity did not change with bioleaching.

The microbially induced enhancement in kaolin brightness stated by various authors (e.g., Lee et al., 2002, Guo et al., 2010) was also detected for the samples investigated in this study (Table 5.2 and Figure 5.2).

In order to facilitate the comparison of the brightness-related parameters, values from previous studies dedicated to microbial leaching of kaolins were summarized (Table 5.14) and compared with the results of this study (Figure 5.12). The reduction rate is not included due to missing bioleaching treatment times of several studies.

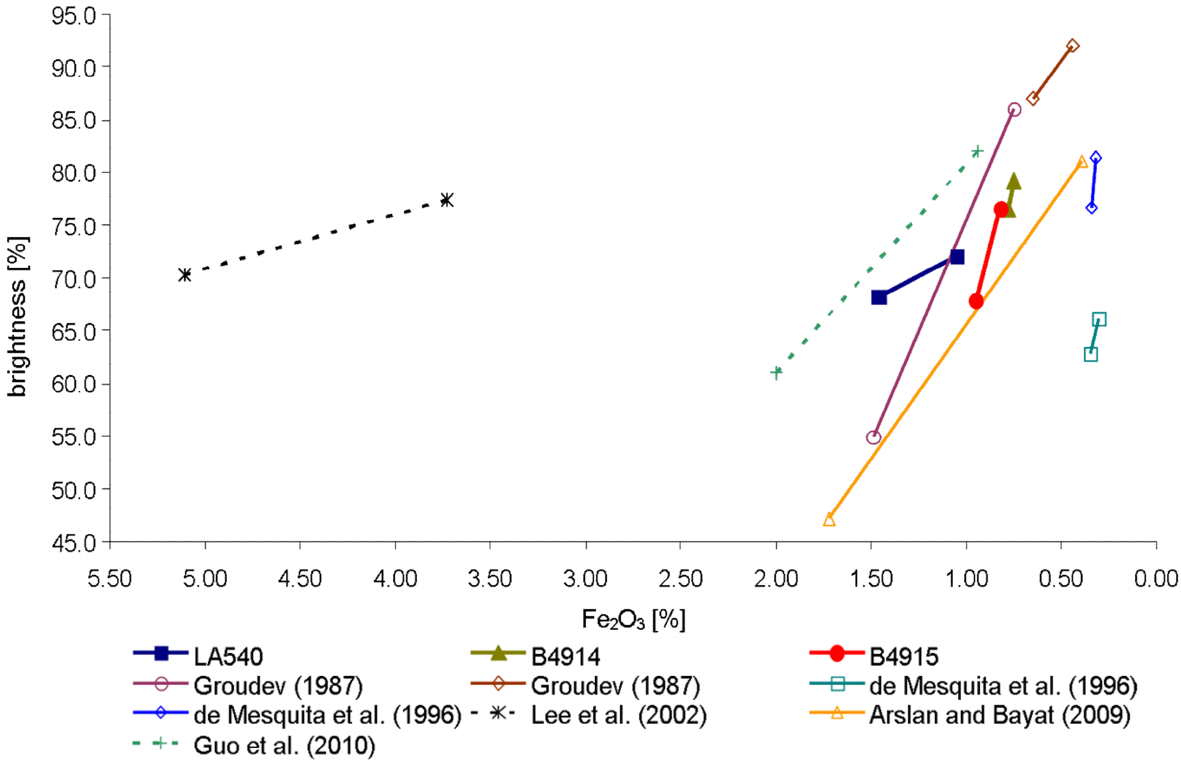

Figure 5.12: Comparison of the Fe removal efficiency from various studies on bioleaching of kaolin. Bold lines with filled markers: samples employed in this study; thin dashed lines with open markers: bioleaching studies using autochtonous microorganisms; thin solid lines with open markers: bioleaching studies using *Aspergillus niger*.

Table 5.14 shows that there is no straight relationship between brightness enhancement Δ and type of microorganism used for bioleaching, but some tendencies are discernable: the greatest Δ-values (>20%) were reached using *Aspergillus niger* and by an authochtonous species, whereas with *Shewanella putrefaciens* only Δ-values below 10% were achieved.

With respect to the slopes of straight lines (Figure 5.12), three sample groups can be distinguished regarding the Fe removal efficiency. A numerical translation of this observation is made by setting up linear equations in the form y=mx+b, where m is the slope of the line, which indicates the leaching efficiency and b is the y-intercept, which designates the $Fe_2O_3$ content for a brightness of 0%. However, note that the measurement of brightness does not yield valid results for values lower than 30% (Huber, 2010, personal communication).

According to the slope m and the y-intercept b, the kaolin samples can be distinguished into three groups as shown in Table 5.15. Type I is characterized by steep slopes with values less than -0.1, which means a strong depletion of the $Fe_2O_3$ content associated with a small increase in brightness, thus, a relatively low bioleaching efficiency. Types II and III are characterized by flatter slopes with values between -0.05 and -0.024, indicating a smaller extent of Fe reduction, but accompanied by a larger increase in brightness and, therefore, a larger bioleaching efficiency, which is even more pronounced for type III, with m≤-0.015. The division in three groups is justified by the marked gaps between them.

The classification illustrates the diversity of the kaolin samples under investigation regarding their predisposition to bioleaching. For type I kaolin LA540, the extent of $Fe_2O_3$ reduction is in the same range with the results reported by Lee et al. (2002). Despite of the same Fe removal efficiency, the increase in brightness obtained for LA540 of about 4% is smaller with respect to the enhancement of about 7% yielded by Lee et al. (2002). The bacteria-free sample B4915 K – classified as type II – shows a greater leaching efficiency with respect to LA540, leading to a brightness enhancement of 2.7%, which is the smallest increase within this group. An enhancement of 2.7% is also reached for sample B4914 – classified as type III – due to the much larger leaching efficiency. Sample B4915 is characterized by the greatest brightness enhancement of all type III kaolins.

The inverse correlation between Fe removal efficiency and initial $Fe_2O_3$ content as well as the extent of Fe reduction (Figure 5.12), observed for the three microbiologically treated paper kaolins, is mostly in accordance with results from literature. With respect to samples from literature with initial $Fe_2O_3$ contents greater than LA540, the sample of Lee et al. (2002) is in the same range of Fe removal efficiency (type I), whereas the samples of Groudev (1987), Arslan and Bayat (2009), and Guo et al. (2010) show larger efficiencies (type II). For samples within the group showing the greatest Fe removal efficiency (type III), the initial $Fe_2O_3$ contents are in the same range with those of B4914 and B4915 (<1.00%) or even smaller (samples of de Mesquita et al., 1996), whereas the sample studied by Groudev (1987) shows a slightly lower Fe removal efficiency, being classified as type II kaolin.

The observation of an inverse correlation between Fe removal efficiency and extent of Fe reduction is confirmed by the samples of de Mesquita et al. (1996), which are in the same range with B4914 and B4915. Samples with lower Fe removal efficiencies (types I and II) generally show Fe reductions to a larger extent, whereas the overall largest extents of Fe reduction are found for type II kaolins (samples of Groudev, 1987; Arslan and Bayat, 2009; Guo et al., 2010). Taking into account the data from the authors mentioned above, there seems to be only a tendential relationship between these two parameters, as great differences between the values for the extent of Fe reduction are already evident within one classification group (type II and III).

The correlation of initial $Fe_2O_3$ content and extent of Fe reduction, as observed for the three paper kaolins, has also been reported for bioreduced smectites (Ernstsen et al., 1998; Gates et al., 1998). However, transferring this correlation to the samples from literature, one can see that this trend is generally not reflected (Table 5.14).

The inverse relationship of Fe removal efficiency and kaolinite crystallinity established by Mockovciaková et al. (2008) is consistent with the findings of the present study, as the “well-ordered” sample LA540 (Figure 5.8) shows the smallest Fe removal efficiency, whereas the most “disordered” sample B4915 is characterized by the greatest Fe removal efficiency.

The observation of a weak correlation between initial $Fe_2O_3$ content and initial brightness agrees with the results of Möbius (1977), Galán et al. (1996), and Chandrasekhar and Raghavan (2004). On the contrary, Galazzo et al. (1986) reported a strong correlation between these two parameters, which is as well observed for the grain-size fractions of sample LA540 (Figure 5.3). Möbius (1977) concluded that the dyeing capacity of Fe solely depends on Fe distribution on different phases. Assuming that oxide-bound Fe affects the kaolin brightness more adversely than silicate-bound Fe, irrespective of the total Fe concentration, as stated by Jepson (1988) and Chandrasekhar and Raghavan (2004), the initial brightness of the three paper kaolins should correlate with the Fe distribution ratios prior to bioleaching (Table 5.11). This correlation is found for sample B4914, but not for LA540 and B4915, as the latter is characterized by both, a greater amount of silicate-bound Fe as well as $Fe_2O_3$ content, but with a slightly smaller brightness than sample LA540.

Table 5.14: Comparison of the $Fe_2O_3$ content and brightness of different kaolins before (initial) and after microbial refinement (final) as well as the resulting brightness enhancement (Δ).

| Microorganism | $Fe_2O_3$ content |  |  | Brightness |  |  | Author |
|---|---|---|---|---|---|---|---|
|  | initial [%] | final [%] | extent [%] | initial [%] | final [%] | Δ [%] |  |
| *Aspergillus niger* | 0.65-1.49* | 0.44-0.75* | 32-50 | 55-87[a] | 86-92[a] | 31-5 | Groudev (1987) |
|  | 0.35 | 0.30 | 14 | 62.9 | 66.2 | 3.3 | de Mesquita et al. (1996) |
|  | 0.34 | 0.32 | 6 | 76.7 | 81.4 | 4.7 | de Mesquita et al. (1996) |
|  | 11.11 | 6.33 | 43 | n.d. | n.d. | n.d. | Hosseini et al. (2007) |
|  | 1.72 | 0.39 | 77 | 47.2 | 81.1 | 33.9 | Arslan and Bayat (2009) |
| authochtonous | 5.11 | 3.73 | 27 | 70.3 | 77.4 | 7.1 | Lee et al. (2002) |
|  | 2.00 | 0.94 | 53 | 61[b] | 82[b] | 21 | Guo et al. (2010) |
| *Bacillus* sp. | 0.92 | 0.52 | 43 | n.d. | n.d. | n.d. | Styriaková and Styriak (2000) |
|  | 1.43 | 1.22 | 15 | n.d. | n.d. | n.d. | Styriaková and Styriak (2000) |
| *Bacillus cereus* | 1.17 | 0.58 | 49 | n.d. | n.d. | n.d. | Styriaková et al. (2003) |
| *Shewanella putrefaciens* | n.i. | n.i. | n.i. | 76 | 80 | 4 | Zegeye et al. (2008) |
|  | 1.46 | 1.05 | 28 | 68.2 | 72.1 | 3.9 | LA540 |
|  | 0.78 | 0.75 | 4 | 76.5 | 79.2 | 2.7 | B4914 |
|  | 0.95 | 0.82 | 14 | 67.9 | 76.6 | 8.7 | B4915 |
|  | 0.95 | 0.82 | 14 | 67.9 | 70.6 | 2.7 | B4915 K |

n.d.: not determined; n.i.: no information; *) results from ten different kaolins, not individually attributed to a respective brightness value; a) referred as not further specifed “whiteness”; b) colometric determined whiteness index

As this inverse behavior of the brightness trend for LA540 and B4915 is not explicable by their Fe distribution, the presence of further staining components or phases has to be considered such as $TiO_2$, which becomes staining by means of the titania effect, as reported in Chapter 1.3.3 (Weaver, 1976). Möbius (1977) found an inverse relationship between $TiO_2$ content and brightness, which is not reflected by the samples investigated in this study, as the sample with the poorest brightness (B4915) shows a lower $TiO_2$ content (Table 5.4) than LA540 (slightly greater brightness, but larger $TiO_2$ content).

Moreover, the sample with the greatest initial brightness (B4914) has nearly the same $TiO_2$ content as B4915. This absence of correlation between $TiO_2$ content and brightness is in accordance with results of Galazzo et al. (1986), deduced from Q-mode factor analysis.

Table 5.15: Classification of microbiologically treated kaolin samples on the basis of linear equations with slope m and y-intercept b, listed in order of decreasing m-values as evaluation tool for the Fe removal efficiency.

| Sample | m | b | Classification |
|---|---|---|---|
| Lee et al. (2002) | -0.1944 | 18.77 | Type I |
| LA540 | -0.1051 | 8.63 | |
| Guo et al. (2010) | -0.0505 | 5.08 | Type II |
| B4915 K | -0.0481 | 4.22 | |
| Groudev (1987) | -0.0420 | 4.30 | |
| Arslan and Bayat (2009) | -0.0392 | 3.57 | |
| Groudev (1987) | -0.0239 | 2.80 | |
| de Mesquita et al. (1996) | -0.0152 | 1.30 | Type III |
| B4915 | -0.0149 | 1.96 | |
| B4914 | -0.0111 | 1.63 | |
| de Mesquita et al. (1996) | -0.0043 | 0.67 | |

In addition to Fe and Ti impurities, the presence of further clay minerals influences the optical properties of kaolins (Prasad et al., 1991). The results from brightness measurements of single grain-size fractions show that a decrease in particle size correlates with decreasing brightness values (Figure 5.3), which, in turn, are linked to an increasing clay mineral content (Table 5.9).

### 5.3.2 Mineralogical parameters

In the following, the results from quantitative phase analysis collected by a multi-method approach are discussed.

Regarding the deviations between the element oxides from XRF measurements and the oxide-converted Rietveld values (Table 9.2 in the Appendix), larger deviations for all samples were observed in the $SiO_2$, $Al_2O_3$,

$Fe_2O_3$, and $K_2O$ contents, which generally increase in smaller particle size fractions.

The mostly negative deviations in $SiO_2$ and $Al_2O_3$ contents are caused by different factors: (1) the application of ODPF revealed the presence of I-S mixed-layer minerals, which could not have been detected by Rietveld analysis due to the lack of an appropriate structural model. This effect was emphasized for the I-S enriched clay fractions, for which the clay content was consistently overestimated by Rietveld analysis, and particularly pronounced for the clay fractions <0.6 µm of LA540 and LA540 MO, and for sample group B4915, which exhibited larger amounts of I-S mixed-layer minerals compared to B4914 and B4914 MO; (2) the structural formulae and chemical composition used for the conversion of the mineralogical phase content to element oxides (Table 5.5) represent an “ideal” stoichiometry and, therefore, do not consider further varieties of isomorphous substitutions; (3) the choice of structural models in the Rietveld code, which was motivated by the achievement of $R_{wp}$ values as small as possible. Kleeberg (2005) compared the quantification results obtained from different structural models of a kaolin sample from the Hirschau-Schnaittenbach area and found a *hkl*-dependent broadening model, including stacking faults to be the most suitable for the structural refinement of kaolinite. Simpler models failed due to an overestimation of the muscovite content that did partially “absorb” the intensity of the broadened kaolinite peaks.

For the samples investigated in this study, the application of such a broadening model seems to tendentially overestimate the kaolinite content. However, the amount of clay minerals (sum of kaolinite and illite) for the clay fractions obtained from Rietveld analysis was found to be in good agreement with the quantification results deduced from the adapted values, STA, and ODPF. As a consequence, Rietveld analysis gives a reasonable approximation of clay content, and is, therefore, a fair estimate of the ratio of clay minerals to non-clay minerals. Larger deviations between the quantification results were noticed for sample group LA540, probably because of the greater I-S mixed-layer content compared to the other kaolin samples as exhibited by ODPF.

The deviation in $Fe_2O_3$ content is explicable by the fact that Fe-bearing phases at such low concentrations could not be identified by XRD with Cu*K*α radiation due to significant background fluorescence resulting in a poor peak resolution (Bland et al., 2004). However, also an attempt using Co*K*α radiation failed. Moreover, Mössbauer spectroscopy (Table 5.11) showed that most of the Fe is silicate-bound, which again reduces the XRD-detectable portion.

The Rietveld quantification of the K-bearing minerals was carried out using a combination of different structural models. For the quantification of K-feldspar, an orthoclase and a microcline model were used simultaneously, as the coexistence of both phases were reported for kaolins from the Hirschau-Schnaittenbach area

(Köster, 1974). As both phases are polymorphs (e.g., Rösler, 1991), the oxide conversion (Table 5.5) was carried out by adding the quantification results. For the K-bearing clay minerals, two structural models (muscovite 2M1 and illite 1Mc) were used to account for different parageneses (Köster, 1974) as well as for a better fit.

The oxide conversion for muscovite was performed using a structural model with 1.00 $K^+$/FU and for illite on the basis of a high-K-illite structural model (0.89 $K^+$/FU), in order to account for the illite layers in I-S mixed-layer minerals (Środoń et al., 1992). Despite of the use of a high-K-illite structural model, deviations in $K_2O$ content were mainly positive, thus, underestimated by Rietveld analysis, and negative for some clay fractions.

Therefore, in the following iteration steps (XRD-XRF adapted), the $K_2O$ content of the various silt fractions was preferentially accounted for by K-feldspar and, with decreasing grain sizes, by illite, leading to a minimization of the $K_2O$-deviations. This adaption is in accordance to common knowledge, and as stated by Dutz (2002), of a decreasing K-feldspar content with decreasing particle size fraction, with a simultaneous increase of the illite content. Moreover, this adaption led to smaller quantification results for kaolinite and, thus, to lower deviations in the $Al_2O_3$ and $SiO_2$ contents.

The adapted quantification results are in good agreement with the results from STA measurements (Table 5.8) as deviations between measured and calculated mass loss during dehydroxylation were below 1% for all untreated samples. The greatest positive deviations were generally found for the clay size fractions, reflecting the lack of the smectitic components not included in the results deduced from Rietveld analysis, but detected by XRD measurements from oriented samples (Figure 5.4), ODPF (Figures 5.5-5.7 and Table 5.7), and from CEC measurements (Table 5.10).

The all in all larger deviations of the treated samples are not solely explicable by a lacking smectitic component as some samples exceeded the maximum allowable mass loss ($\Delta m\ T_{DHX\ meas}$) for kaolins of 13.95%, which correspond to 100% kaolinite. The DSC curves of the respective treated samples showed a weak broad exothermic peak between 300-400 °C, which became more pronounced with decreasing particle size fraction (data not shown). By means of Evolved Gas Analysis (EGA), the release of $CO_2$ was detected within this T-interval, indicating the presence of organic compounds (Siewert, 1995), attributable to the organic constituents of the reducing media in terms of lactate, AQDS, and the microorganism itself (Table 3.3).

An explanation for the larger deviations is given by the interference between the oxidation reaction from organic matter (200-500 °C) and the dehydroxylation reaction, which was found to occur as above 400 °C (Ulery and Drees, 2008).

However, the interference between the two reactions has no implication for the quantifaction results, as deviations >1.00% were not further adapted in the STA crosscheck, because of the greater inconsistency with the results from XRF analysis.

The remarkable differences in the phase content between the grain-size fractions of all kaolin samples prior to and after bioleaching may be attributed to the following reasons in terms of (1) microbially induced formation or transformation of minerals by a solid-state or dissolution-precipitation reaction mechanism (Chapter 1.3.5) as reported for kaolins by Styriaková and Styriak (2000), Styriaková et al. (2003), and Styriaková and Lovás (2007), for smectitic samples by serveral authors (e.g., Kim et al., 2004; Stucki; 2009), and for illite (Kukkudapu et al., 2006); (2) dispersion effects, causing mass shifts during sample fractionation, as grain-size fractionation was carried out without addition of a dispergent agent in order to prevent affection of metabolic activities of the microorganisms (Liu et al., 1982; Shelobolina et al., 2004).

Microbially induced mineral transformations were reported to result in the destruction of mica under formation of illite (Styriaková and Styriak, 2000; Styriaková et al., 2003) or to induce the in situ conversion of smectite to illite (Kim et al., 2004). Regarding the paper kaolins, no unequivocal evidence for mineral transformation can be provided as no changes have occurred with microbiological treatment for the phase content of the bulk samples or for the particle morphology as demostrated by SEM. This is in contrast to SEM observations by Styriaková and Styriak (2000) and Styriaková et al. (2003), and Roy et al. (2010), who found mineral surfaces to be altered after bioleaching. On the contrary, Lee et al. (2002) did not detect any morphological modifications after microbial refinement.

An increase in CEC due to $Fe^{3+}$-reduction in the structure of the swellable components as reported by several authors (e.g., Kostka et al., 1999b; Gates et al., 1998; Stucki, 2006) was not detected for the bioleached kaolin samples.

However, possible changes in the phase content by mineral transformation reactions can be neither confirmed nor completely excluded as the accuracy of the quantification results may be to low to detected any effects.

Moreover, as discussed in Section 5.3.1, changes in grain-size distribution after bioleaching are also attributable to changes in the aggregate structure due to dispersion stabilization effects, induced by the increased soluble salt concentration by means of the reducing media (Baird and Walz, 2007) and by polysaccharide-mediated aggregation (Dorioz et al., 1993). The resulting mass shifts lead, in turn, to changes in the phase content of the respective grain-size fractions. Therefore, not all the changes in the mineralogical composition can be interpreted solely as the result of microbial $Fe^{3+}$-reduction, as already stated by Shelobolina et al. (2004).

Concerning the paper kaolins investigated in this study, the identification of bio-available Fe depletion sources is obfuscated due to the complexity of factors that impacts the comparability of the respective grain-size fractions prior to and after bioleaching.

Results from Mössbauer spectroscopy indicate the presence of mostly silicate-bound Fe. Thus, potential Fe depletion sources for the three paper kaolins are kaolinite, illite, and I-S mixed layer minerals.

Regarding kaolinite as an Fe depletion source, indirect proof for the presence of silicate-bound Fe was provided by the generation of PA curves, as kaolinites with high degree of structural disorder were found to contain more octahedral $Fe^{3+}$ than those with a well-ordered structure (Herbillon et al., 1976; Mestdagh et al., 1980). The relative positions of the PA curves (Figure 5.8) indicate different degrees of structural disorder of the three kaolins in the order LA540 < B4914 < B4915, which did not change with bioleaching.

However, the comparison of the PA curves gathered from the highly-disordered ceramic clays (Figure 6.4) indicates the presence of principally well-ordered kaolinite structures, which is also evidenced by the sharp and intense recrystallization reactions at $T \approx 1000$ °C obtained from DSC measurements, reported for kaolinites with a well-ordered structure (Jasmund and Lagaly, 1993). This means that the respective kaolinite structures may contain merely low amounts of structural $Fe^{3+}$, which were not subject to microbial reduction, as shown by the steady PA curves detected prior to and after bioleaching.

Therefore, $Fe^{3+}$-reduction seems to be restrained to the 2:1 layer silicates in terms of illite and I-S mixed-layer minerals. On the basis of the data acquired in this study, a further differentiation is not possible.

Literature data favor smectitic components to be the easiest reducible among the 2:1 layer silicates due to the lower layer charge with respect to illite (Seabaugh et al., 2006; Dong et al., 2009a; 2009b). The smectitic components are a highly Fe depletion source, as the extent of Fe reduction correlates with the amount of smectitic components, which was found to increase in the order B4914 < B4915 < LA540.

Discussing these observations in the light of the parameters gathered for the characterization of bioleaching, the following conclusions result:

(1) the enhancement of kaolin brightness Δ depends primarily on the place of Fe depletion Ψ, and not on the $Fe_2O_3$ content, as the various Fe depletion sources contribute to a different extent to brightness. The reduction of goethite generally increases kaolin brightness, whereas it should be adversely affected by Fe reduction in smectite due to color changes by reduction from yellow to dark green or blue color (Kostka et al., 1996; O'Reilly et al., 2006). In contrast, the reduction of $Fe^{3+}$ in the illite structure should positively contribute to brightness, as Shen and Stucki (1994) observed color changes from dark gray to white.

However, color is not solely a function of the Fe oxidation state since changes principally depend on complex light scattering and chromophoric absorption phenomena caused by particle size, Fe site coordination, Fe clustering, and other factors (Stucki, 2011).

(2) Regarding the Fe distribution of the studied kaolin samples, the enhancement of brightness is mainly caused by the reduction of oxide-bound Fe and less affected by the reduction of silicate-bound Fe, as the largest increase in brightness is correlated with oxide-bound Fe depletion (B4915), whereas the smallest increase in brightness was yielded by kaolin sample B4914, for which Fe depletion was found to occur exclusively within the silicate structure. For kaolin sample LA540, which showed both types of Fe depletion, the brightness enhancement was between the values of B4914 and B4915.

(3) The different Fe removal efficiencies, which were large for B4914 and B4915, but small for LA540, seem to be explicable by a the fact that the reduced Fe largely remains inside the silicate structure as reported in various studies dedicated to structural Fe reduction and reoxidation of 2:1 layer silicates (e.g., Lee et al., 2006; Ribeiro et al., 2009). This is in accordance with observations made for sample B4914, for which Fe depletion was shown to take place solely in the silicate structure, as well as for sample LA540, characterized by the largest goethite amount and a “concomitant Fe depletion”. On the other hand, for sample B4915 it was shown that Fe depletion occurred for the oxide-bound Fe, which is in contrast to the assumption outlined above. However, a “concomitant Fe depletion” seems to be very probable as sample B4915 contains only little goethite, but showed the largest extent of Fe reduction. Moreover, mass shifts during grain-size fractionation may influence the comparability of the respective Fe distribution-ratios prior to and after bioleaching, leading to imprecise $\Psi$ values.

(4) The reduction of silicate-bound Fe should be restrained to the 2:1 layer silicates, as no evidence for structural changes have been detected for kaolinite with bioleaching.

(5) The correlation between the amount of smectitic components and extent of Fe reduction suggests that $Fe^{3+}$-reduction preferentially takes place in the swellable components of the I-S mixed layers. On the contrary, the more pronounced staining effect reported for Fe-reduced smectites suggests illite as the source of Fe depletion. Illite loses its dyeing capacity by Fe reduction, resulting in an increased brightness, as was also observed for the goethite-free kaolin sample B4914.

## 5.4 Conclusions

The removal of $Fe^{3+}$ impurities from paper kaolins with different brightness qualities by a Fe-reducing culture of *Shewanella putrefaciens* was investigated on the basis of a comprehensive mineralogical characterization. The combination of various quantification methods revealed differences in the character and amount of I-S mixed layer minerals, which were found to correlate positively with the extent of Fe reduction. The determination of the Fe distribution prior to and after bioleaching indicated that

(1) *Shewanella putrefaciens* is capable to reduce both, oxide-bound Fe as well as silicate-bound Fe

(2) the enhancement of brightness is mainly caused by the reduction of oxide-bound Fe and less affected by the reduction of silicate-bound Fe. Thus, brightness enhancement of kaolins is a function of the place of Fe depletion

(3) the microbiologically induced removal of the silicate-bound Fe seems to occur mainly in the structure of the 2:1 layer silicates, as no evidence of structural changes was observed for kaolinite

(4) the generally assumed correlation of kaolin brightness and $Fe_2O_3$ content is not strictly valid and always should be seen in the context of Fe distribution in terms of oxide/silicate Fe as well as $Fe^{2+}/Fe^{3+}$

(5) the impact of the $TiO_2$ content on brightness remains unclear as no correlation was found between these two parameters

(6) changes in rheology was caused by bioleaching, leading to mass shifts during grain-size fractionation.

However, the attribution of single parameters to brightness enhancement still remains challenging due to the number and complexity of interactions arising from kaolin composition, in terms of $Fe_2O_3$ content, Fe distribution, amount and kind of clay minerals, particle size distribution, kaolinite crystallinity, as well as the presence of further staining components, such as $TiO_2$ or organic compounds, which were all shown to influence the kaolin brightness.

# 6 Comprehensive characterization of the ceramic clays

Results of this study were published in Petrick et al. (2011) Character and amount of I-S mixed-layer minerals and physical-chemical parameters of two ceramic clays from Westerwald, Germany: Implications for processing properties. *Clays and Clay Minerals* **59**, 58-74.

## 6.1 Introduction

Common practice for the industrial assessment of ceramic clays consists of determining two parameters only: particle-size distribution and chemical composition. This rapid procedure should provide information on clay working properties and determine the end-use as ceramic masses or slurries. Due to the frequent failure of assigning properties of clays on the basis of this procedure, the clay processing industry finds itself constrained to reconsider common evaluation strategies.

It is well-known that mineralogical composition controls ceramic processing-related properties, as described in Chapter 1.4. For that reason, it is astonishing that mineralogy is widely neglected in the industrial assessment of ceramic clays.

Aim of the following study is to demonstrate that a careful determination of the mineralogical phase content provides valuable additional information on the processing behavior of ceramic clays, as especially quantitative minor constituents exert a strong effect on processing properties (Schüller, 1980).

In this context, two ceramic clays (W1 and W2) from the Westerwald area, Germany, were investigated. According to industrial assessment, W1 and W2 are characterized by nearly identical chemical compositions and particle size distributions, but show different working properties in terms of extruding behavior (generally also referred as “plasticity” according to Göhlert and Uebel, 2007) and making moisture content. A phenomenological description and properties-related parameters of W1 and W2 are summarized in Table 3.4 (Chapter 3.2).

In order to elucidate the different behavior, both clays were investigated in detail by a multi-method approach combining physical-chemical and mineralogical methods. The combination of different analytical methods (XRF, STA, CEC) in addition to Rietveld analysis of XRD patterns allows an approximation of the mineralogical phase content.

In such a multi-method approach, a new analytical tool applied for the first time to ceramic clays is represented by one-dimensional XRD profile fitting (ODPF), previously mainly used for oil exploration-related identification of mixed-layer minerals and clay mineral parageneses (e.g., Środoń, 1981; Drits et al., 1997b; Lindgreen et al., 2000; McCarty et al., 2008; Lanson et al., 2009). This technique enables the characterization of complex samples, consisting of discrete clay minerals and mixed-layer phases.

However, also the application of one-dimensional modeling not always provides an unambiguous determination of the actual structure as several structural models may fit the experimental data equally well (Drits, 1987; Sakharov et al., 1999; McCarty et al., 2004). Fitting results have to be critically evaluated by comparing them with chemical and mineralogical analyses in order to obtain a consistent characterization.

## 6.2 Results

### 6.2.1 Grain-size distribution and processing properties-related parameters

The two studied samples had very similar water contents: W1=13.4% (s=0.4%), W2=13.7% (s=1.0%), when they arrived in the laboratory from the processing plant.

Considerable differences in grain-size distribution were observed between the pathways (Table 6.1). The use of Na-pyrophosphate led to a mass shift toward finer grain-size fractions, which was strongly emphasized in the fraction <0.6 µm for both samples. Independently from the pathway, W1 was characterized by a greater content in the clay-size fractions <2 µm.

Table 3.2 (Chapter 3.2) illustrates that W1, referred to be plastic, had a larger making moisture content and extrusion pressure compared to the less-plastic sample W2.

pH values of W1 and W2 were very similar within standard deviation: 6.1 (s=0.8) for W1 and 6.9 (s=0.7) for W2. The soluble salt concentration in terms of anions $SO_4^{2-}$ and $Cl^-$ was 479 mg/kg (s=171 mg/kg) and 116 mg/kg (s=13 mg/kg), respectively, for W1, and 37 mg/kg (s=8 mg/kg) and 79 mg/kg (s=5 mg/kg), respectively, for sample W2. The overall soluble salt concentration of W1 was greater and this was reflected by a much greater electrical conductivity σ, 400 µS/cm (s=99 µS/cm) compared to 51 µS/cm (s=11 µS/cm) for W2.

Table 6.1: Grain-size distribution of the samples W1 and W2 with and without Na-pyrophosphate as dispergent agent, obtained from different methods.

| Grain-size fraction | with dispersant Sedigraph (pathway 1) | | with dispersant pipette procedure (pathway 1) | | without dispersant pipette procedure (pathway 2) | |
|---|---|---|---|---|---|---|
| | W1 | W2 | W1 | W2 | W1 | W2 |
| [µm] | [%] | [%] | [%] | [%] | [%] | [%] |
| >63 | 1 | 3 | 2 | 5 | 2 | 5 |
| 20-63 | 10 | 12 | 18 | 17 | 19 | 21 |
| 2-20 | 29 | 31 | 27 | 28 | 31 | 31 |
| 0.6-2 | 10 | 13 | 10 | 21 | 24 | 39 |
| <0.6 | 50 | 41 | 43 | 29 | 24 | 4 |

### 6.2.2 X-ray techniques

Investigation of the bulk material revealed that W1 and W2 had very similar chemical compositions (Table 6.2) and phase contents (Table 6.3).

Table 6.3 summarizes the quantitative phase content of the bulk materials and their clay fractions 0.6-2 µm and <0.6 µm. The samples were mainly composed of quartz, kaolinite, illite, swellable components (as I-S mixed-layer minerals and/or discrete smectite), orthoclase, plagioclase, rutile, as well as small quantities of Fe-bearing phases.

As expected, the amount of layer silicates increased with decreasing grain size, whereas the amount of quartz decreased. The amount of feldspar and rutile remained constant within the various grain-size fractions.

In order to check the quantification results from Rietveld analysis, the mineralogical phase content was converted to chemical composition in terms of element oxides. Afterwards, these values were compared with the chemical composition from XRF measurements.

Figure 6.1 represents the relative deviation between the two data sets. A positive deviation means an underestimation by Rietveld quantification; a negative deviation denotes overestimation.

Table 6.2: Chemical composition of the bulk material of W1 and W2 and their respective clay fractions 0.6-2 µm and <0.6 µm. Normalized values according to loss on ignition (LOI).

| | Chemical composition [%] | | | | | |
|---|---|---|---|---|---|---|
| | W1 bulk | W2 bulk | W1 0.6-2 µm | W2 0.6-2 µm | W1 <0.6 µm | W2 <0.6 µm |
| $SiO_2$ | 74.79 | 75.27 | 57.24 | 53.86 | 52.93 | 52.66 |
| $Al_2O_3$ | 19.40 | 18.94 | 33.12 | 36.55 | 38.50 | 39.33 |
| $Fe_2O_3$ | 1.54 | 1.44 | 1.99 | 2.24 | 2.71 | 1.95 |
| MgO | 0.43 | 0.45 | 0.72 | 0.81 | 0.79 | 0.89 |
| CaO | 0.28 | 0.22 | 0.37 | 0.36 | 0.61 | 0.63 |
| $Na_2O$ | 0.12 | 0.09 | 0.28 | 0.21 | 0.25 | 0.24 |
| $K_2O$ | 2.11 | 2.34 | 4.14 | 4.33 | 3.30 | 3.99 |
| $TiO_2$ | 1.32 | 1.25 | 2.15 | 1.65 | 0.93 | 0.31 |
| LOI | 6.25 | 5.63 | 9.42 | 10.30 | 12.70 | 12.24 |

Table 6.3: Quantitative phase content of the bulk material and the fractions 0.6-2 µm and <0.6 µm determined with Rietveld analysis.

| Phase | Structure model | Phase content [%] | | | | | |
|---|---|---|---|---|---|---|---|
| | AutoQuan® | W1 bulk | W2 bulk | W1 0.6-2 µm | W2 0.6-2 µm | W1 <0.6 µm | W2 <0.6 µm |
| Quartz | Quartz | 43 ± 2 | 46 ± 2 | 12 ± 1 | 7 ± 1 | 2 ± 1 | 2 ± 1 |
| Kaolinite | disordered Kaolinite | 21 ± 3 | 20 ± 2 | 42 ± 5 | 51 ± 5 | 55 ± 5 | 60 ± 5 |
| Illite | Muscovite 2M1<br>Illite 1Mc | 20 ± 2 | 19 ± 2 | 24 ± 2 | 22 ± 3 | 21 ± 3 | 19 ± 3 |
| Swellable components* | Smectite1wCa | 12 ± 3 | 11 ± 3 | 17 ± 3 | 16 ± 3 | 18 ± 3 | 16 ± 4 |
| Feldspar | Orthoclase<br>Plagioclase An16 | 3 ± 1 | 3 ± 1 | 3 ± 1 | 3 ± 1 | 3 ± 1 | 3 ± 1 |
| Rutile | Rutile | 1 ± 1 | 1 ± 1 | 2 ± 1 | 1 ± 1 | 1 ± 1 | 0 |
| Fe-phases** | | n.q. | n.q. | n.q. | n.q. | n.q. | n.q. |

*discrete smectite + contribution from I-S mixed-layer minerals, **goethite, hematite, marcasite and siderite below XRD detection limit, n.q.: not quantified

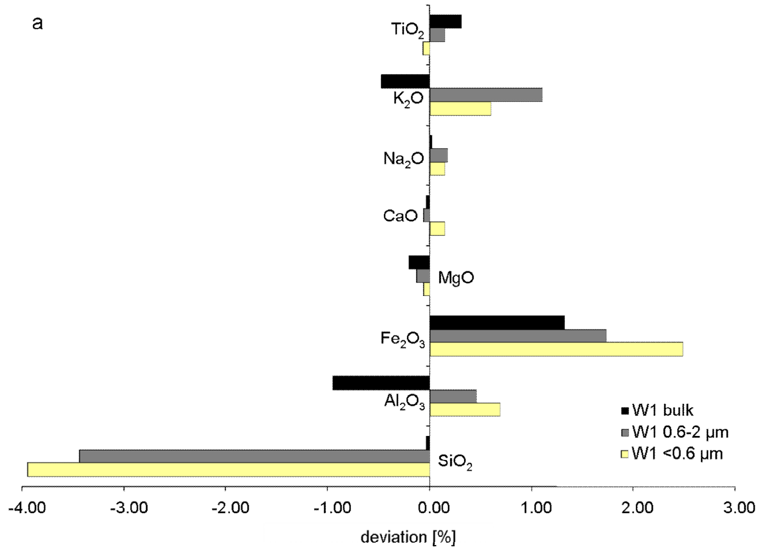

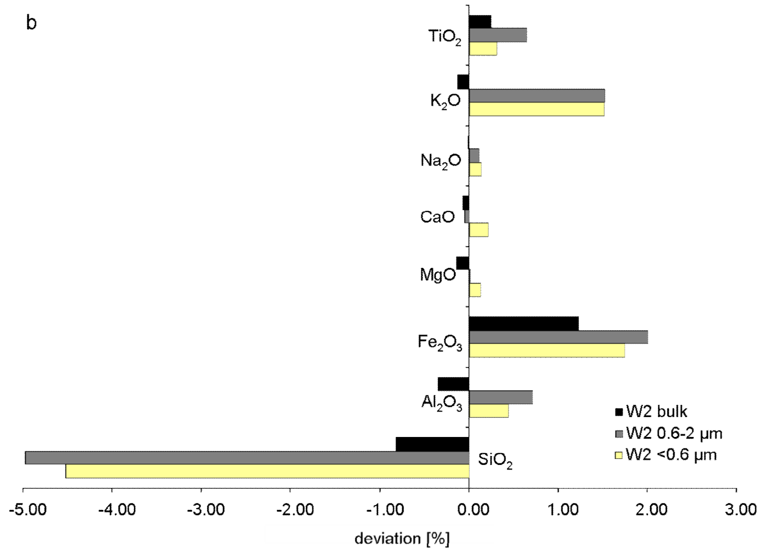

Figure 6.1: Relative deviation between chemical composition, calculated from Rietveld analysis and measured by XRF, for the bulk material and the clay fractions of (a) W1 and (b) W2.

In the clay fractions of both samples, a considerable increase in terms of deviation was noted. For W1, the increase was magnified in the <0.6 µm fraction, whereas W2 exhibited the strongest deviations in the 0.6-2 µm size fraction. The $Al_2O_3$ content showed both, overestimation for the bulk materials and underestimation for the clay fractions.

The XRD patterns of the clay fractions (0.6-2 µm and <0.6 µm) from oriented-sample preparation look very similar at first glance (Figure 6.2) with strong reflections at 7.14 Å and 3.57 Å from kaolinite and a non-rational series of basal reflections with d(001) at about 10 Å. These values differed slightly from a rational series for illite and are diagnostic for I-S mixed-layered species.

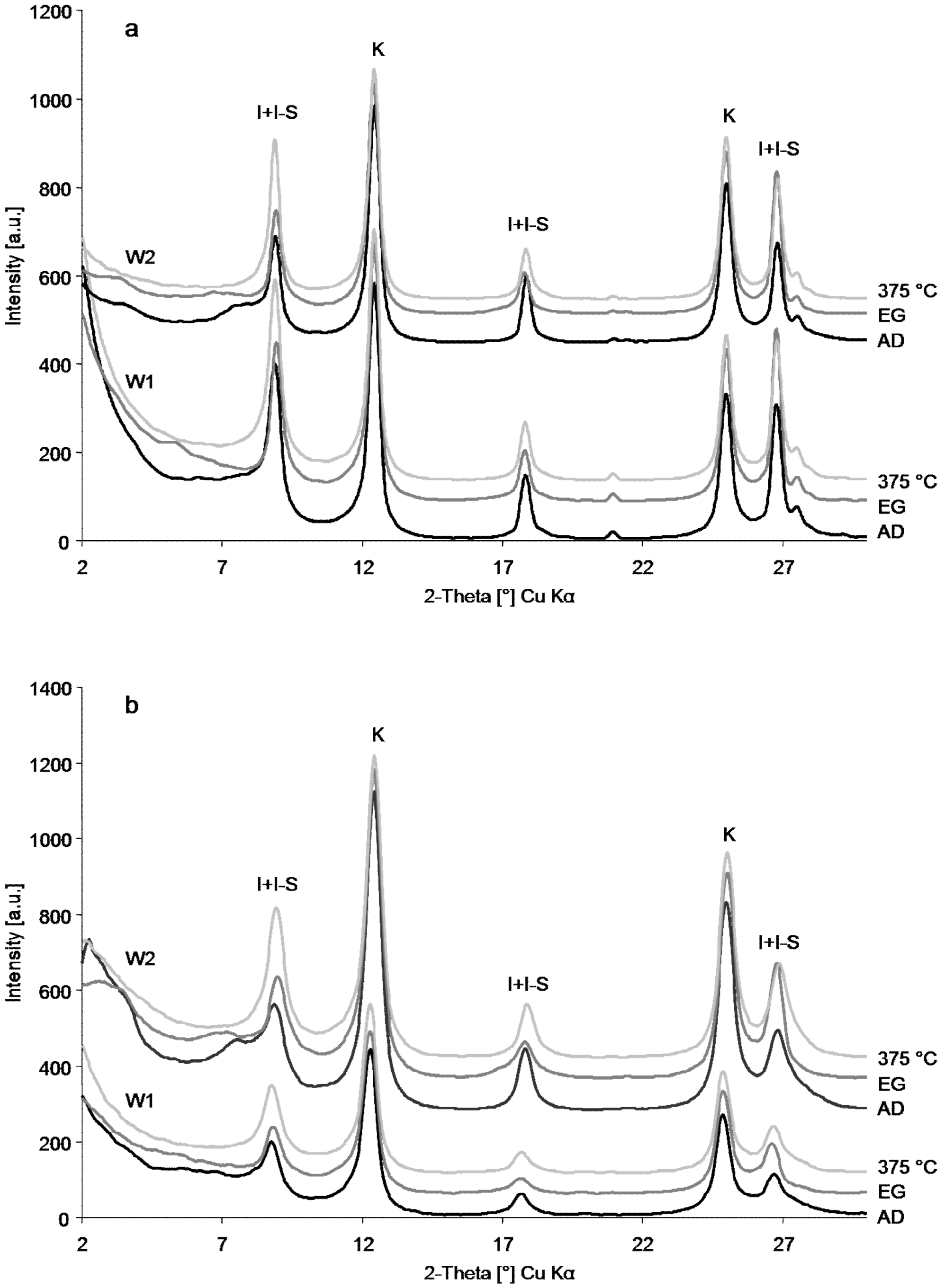

Figure 6.2: XRD diffraction patterns from oriented samples. Comparison between the samples W1 and W2 in air-dried state (AD), after treatment with ethylenglycol (EG) and heat-treated (375 °C) for the fractions (a) 0.6-2 µm and (b) <0.6 µm.

After EG solvation, changes in the diffraction patterns of all samples were noted: peak shift in the region between 7 and 8° 2θ and broadening of the peak at 17.7° 2θ indicated the presence of a smectite component. The identification of I-S mixed-layered species was confirmed by the heat-treated samples, the XRD patterns of which resembled a physical mixture of a pure illite and kaolinite.

The morphology of the I-S basal reflections was different for the clay fractions of W1 and W2. Both samples of W1 had a poorly resolved shoulder on the low-angle side of the peak near 9° 2θ (10 Å), which is diagnostic of long-range ordering *R*>1 (Moore and Reynolds, 1997). Both samples of W2 had a well-resolved shoulder at 11.7 Å, which shifted to 12.4 Å under EG solvation.

All in all, the peaks were sharper and more intense in the case of W2 <0.6 µm, indicating a more ordered structure, unlike W1.

Identification of the mixed-layer phases was carried out by one-dimensional XRD pattern fitting (ODPF). The experimental and the calculated XRD patterns (Figure 6.3) were compared using several structure models. A good coincidence of positions, intensities, and profiles was achieved for both clay samples with an I-S model, in which smectite and illite layers are interstratified with some tendency to segregation.

Both experimental XRD patterns of the clay fractions of W1 were described successfully by a physical mixture of discrete smectite and *R3* I(0.9)/S, whereas the clay fractions of W2 were characterized by a greater proportion of smectite in the mixed-layer (*R1* I(0.85)/S for W2 0.6-2 µm and *R1* I(0.80)/S for W2 <0.6 µm), but smaller amounts of discrete smectite or no smectite in the case of W2 <0.6 µm (Table 6.4).

The accuracy of the fitting procedure was demonstrated by the satisfactory agreement between the experimental and calculated patterns, which was $R_p$=7.14% for sample W1 0.6-2 µm and $R_p$=7.20% for W2 0.6-2 µm, as well as $R_p$=7.88% for W1 <0.6 µm and $R_p$=8.71% for W2 <0.6 µm.

Disagreement between experimental and calculated profiles was, however, observed for the low-angle part, probably because of the influence of instrumental factors and, in particular, Lorentz-polarization effects (Sakharov et al., 1999).

For both samples, the degree of structural disorder of kaolinite seems high, as the diagnostic XRD peaks (data not shown) were so poorly resolved that no Hinckley index could be determined.

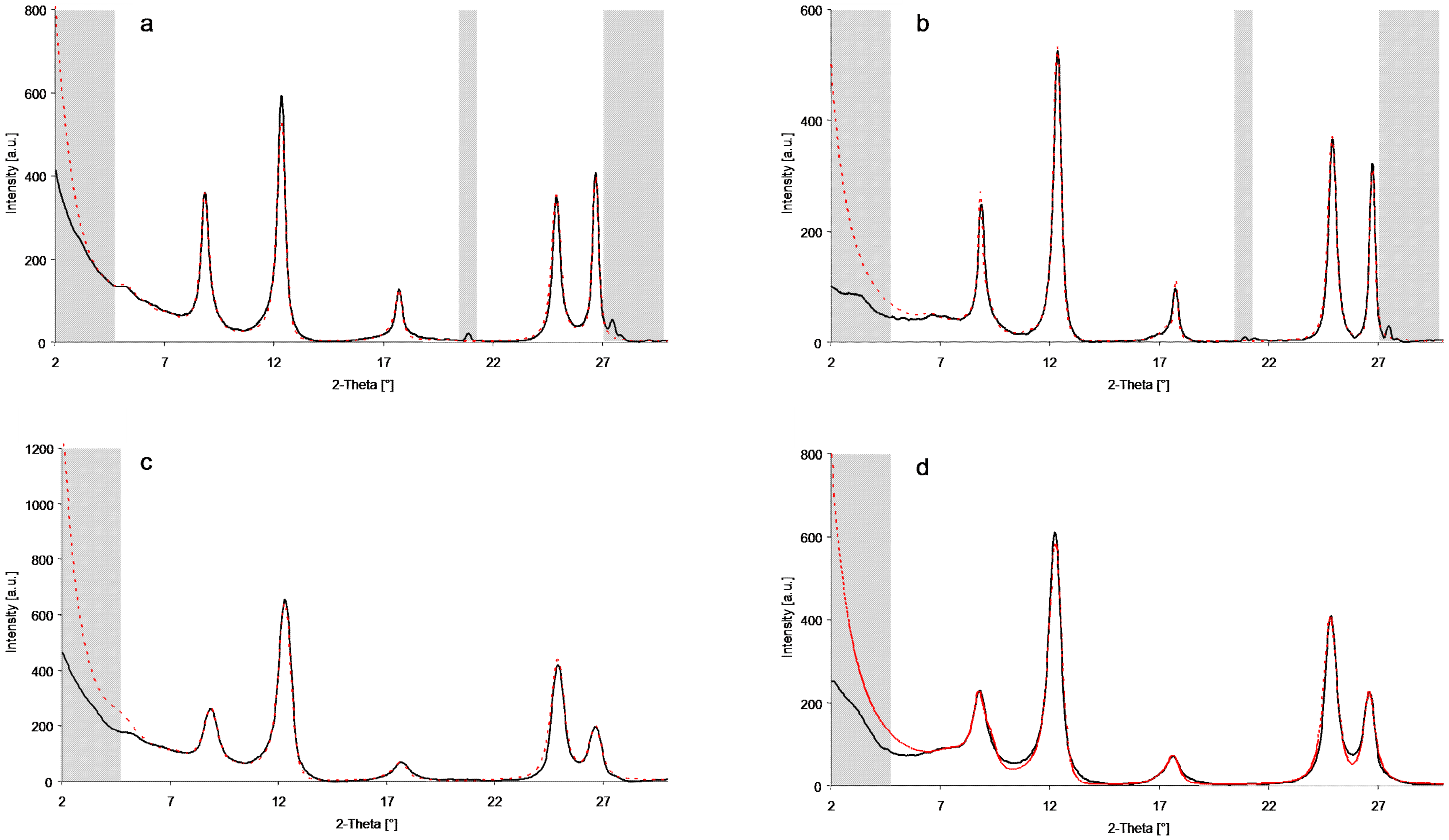

Figure 6.3: Experimental (solid lines) and calculated (dashed lines) XRD patterns of the Ca-saturated, EG solvated samples from oriented preparation of the fractions (a) W1 0.6-2 µm, (b) W2 0.6-2 µm, (c) W1 <0.6 µm and (d) W2 <0.6 µm. The shaded areas were excluded from the fit.

Table 6.4: Quantification results from one-dimensional XRD profile fitting. $W_a$: portion of the component that appears first in the mixed-layer mineral.

| | W1 0.6-2 µm [%] | W2 0.6-2 µm [%] | W1 <0.6 µm [%] | W2 <0.6 µm [%] |
|---|---|---|---|---|
| Kaolinite | 44 | 48 | 57 | 63 |
| Smectite | 4 | 2 | 4 | 0 |
| I-S | 31 | 19 | 32 | 22 |
| -Reichweite | *R3* | *R1* | *R3* | *R1* |
| -$W_a$ | 0.90 | 0.85 | 0.90 | 0.80 |
| Illite | 21 | 31 | 7 | 15 |

### 6.2.3 Simultaneous Thermal Analysis

From equation 4.15 (Section 4.2.5), the maximum clay content was estimated, comparing the measured mass loss during dehydroxylation reaction ($\Delta m\ T_{DHXmeas}$) between 400 and 900 °C from TG curves with a calculated mass loss ($\Delta m\ T_{DHXcalc}$) based on the quantification results from Rietveld analysis.

Within the tested groups, the smallest positive delta value indicated the most appropriate set of coefficients. Table 6.5 shows that the best match between calculated and experimental data was achieved for both bulk samples considering the mean values as coefficients. For the clay fractions of W1 and W2, the smallest delta values were obtained by a set of coefficients generated from negative standard deviations.

The mass loss during dehydroxylation ($\Delta m\ T_{DHX}$) was slightly greater for the bulk sample of W1. In case of the clay fractions, W2 showed somewhat greater values.

The DSC curves of both samples showed four endothermic and two exothermic effects (Table 6.6). Except the first dehydration reaction, the bulk material of W2 had slightly greater peak temperatures of thermal reaction than those of W1. For both clays, the peak of the second dehydration reaction was only resolved as a weak shoulder.

Differences between the two samples were observed in the peak temperature of the recrystallization reaction, which was notably lower for W1 (958-974 °C) compared with W2 (975-981 °C). The recrystallization reaction of W1 varied with grain size, whereas it remained nearly constant for W2. In both sets of samples, the recrystallization peaks were neither sharp nor intense.

For the grain size fraction <0.6 µm of W1 and W2, PA curves were recorded and compared with kaolinite-rich samples of different degrees of structural disorder (Figure 6.4). The data of a well-ordered kaolinite (Mesa Alta) and of a highly disordered kaolinite (Franterre) as thresholds were taken from Smykatz-Kloss (1974). For comparison and to discern device-specific effects, sample LA540 employed for the study of paper kaolins (Chapter 5) was included in the analysis. W1 and W2 plotted close to the PA curve of the disordered kaolinite sample Franterre, whereas W1 was closer than W2.

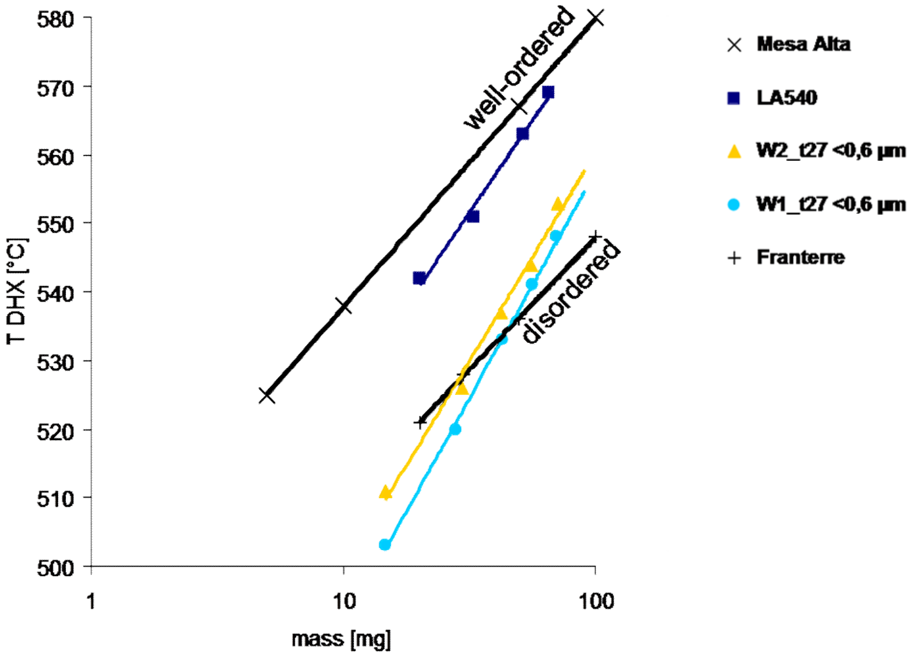

Figure 6.4: PA curves to estimate the degree of structural disorder of kaolinite of the samples W1<0.6 µm and W2<0.6 µm. Black bold lines: PA curves of a well-ordered and a disordered kaolinite as bounderies taken from Smykatz-Kloss (1974).

### 6.2.4 CEC measurements

The CEC was determined by the Cu-trien method at pH 7. The measured values were 9 meq/100g and 7 meq/100g for the bulk material of W1 and W2, respectively, and increased within the clay fractions (0.6-2 µm, <0.6 µm) from 10 meq/100g to 19 meq/100g for W1 and from 12 meq/100g to 18 meq/100g for W2.

The content of swellable components (sum of smectite and smectitic layers in I-S) was calculated according to equation 4.19 (Section 4.2.6). The results are reported in Table 6.7.

Comparing the amount of exchanged cations in the exchanging solution with the CEC (Table 6.7) revealed that the interlayer of the swellable components is dominated by $Ca^{2+}$ and $Mg^{2+}$. The sum of exchangeable cations (∑) was in the range of the measured CEC for both sets of samples.

Table 6.5: Estimation of the maximum possible clay content by comparing the measured mass loss (Δm $T_{DHXmeas}$) during the dehydroxylation reaction with the calculated mass loss (Δm $T_{DHXcalc}$). x, y, z are the average mass fractions with their standard deviations (-s, +s) of the 1:1 and 2:1 layer silicates from Rietveld analysis. Δ: deviation between measured and calculated mass loss Δm $T_{DHX}$.

| Sample | Kaolinite x | Smectite + smectitic layers in ML y | Illite + illitic layers in ML z | Δm $T_{DHX\ calc}$ [%] | Δm $T_{DHX\ meas}$ [%] | Δ [%] |
|---|---|---|---|---|---|---|
| W1 bulk | 0.21 | 0.12 | 0.20 | 4.43 | 4.52 | 0.09 |
| W1 bulk -s | 0.18 | 0.09 | 0.18 | 3.77 | 4.52 | 0.75 |
| W1 bulk +s | 0.24 | 0.15 | 0.22 | 5.08 | 4.52 | -0.56 |
| W2 bulk | 0.20 | 0.11 | 0.19 | 4.19 | 4.31 | 0.12 |
| W2 bulk -s | 0.18 | 0.08 | 0.17 | 3.68 | 4.31 | 0.63 |
| W2 bulk +s | 0.22 | 0.14 | 0.21 | 4.71 | 4.31 | -0.40 |
| W1 0.6-2 µm | 0.42 | 0.17 | 0.24 | 7.78 | 7.16 | -0.62 |
| W1 0.6-2 µm -s | 0.37 | 0.14 | 0.22 | 6.85 | 7.16 | 0.31 |
| W1 0.6-2 µm +s | 0.47 | 0.20 | 0.26 | 8.72 | 7.16 | -1.56 |
| W2 0.6-2 µm | 0.51 | 0.16 | 0.22 | 8.90 | 7.94 | -0.96 |
| W2 0.6-2 µm -s | 0.46 | 0.13 | 0.19 | 7.92 | 7.94 | 0.02 |
| W2 0.6-2 µm +s | 0.56 | 0.19 | 0.25 | 9.88 | 7.94 | -1.94 |
| W1 <0.6 µm | 0.55 | 0.18 | 0.21 | 9.50 | 8.98 | -0.52 |
| W1 <0.6 µm -s | 0.50 | 0.15 | 0.18 | 8.52 | 8.98 | 0.46 |
| W1 <0.6 µm +s | 0.60 | 0.21 | 0.24 | 10.48 | 8.98 | -1.50 |
| W2 <0.6 µm | 0.60 | 0.16 | 0.19 | 10.01 | 9.08 | -0.93 |
| W2 <0.6 µm -s | 0.55 | 0.12 | 0.16 | 8.99 | 9.08 | 0.09 |
| W2 <0.6 µm +s | 0.65 | 0.20 | 0.22 | 11.04 | 9.08 | -1.96 |

Table 6.6: Peak temperatures of thermal reactions from STA measurements of bulk materials and the clay fractions 0.6-2 µm and <0.6 µm.

| Reaction | dehydration | | oxidation organic | dehydroxylation | α→β-quartz transition | recrystallization |
|---|---|---|---|---|---|---|
| Character | endothermic | | exothermic | endothermic | endothermic | exothermic |
| Peak temperature | T [°C] | | T [°C] | T [°C] | T [°C] | T [°C] |
| W1 | 101 | 162 | 322 | 527 | 576 | 965 |
| W2 | 92 | 163 | 347 | 532 | 576 | 981 |
| W1 0.6-2 µm | 104 | 169 | 328 | 544 | n.o. | 974 |
| W2 0.6-2 µm | 105 | 173 | 340 | 550 | n.o. | 980 |
| W1 <0.6 µm | 116 | 175 | 337 | 547 | n.o. | 958 |
| W2 <0.6 µm | 108 | 171 | 353 | 552 | n.o. | 975 |

n.o.: not observed

### 6.2.5 Microscopic techniques and Mössbauer spectroscopy

Investigation of the coarsest fraction >63 µm by optical microscopy revealed yellowish-brown, Fe-coated agglomerates, to be abundant in W2 but rarely found in W1. Analysis by ESEM coupled with EDX confirmed that these coatings were rich in Fe. Sample W1 showed sporadic coatings consisting of crystals with a flat, tabular habit with “cockscomb” growth, typical of marcasite (Rösler, 1991).

The distribution of Fe was established by Mössbauer spectroscopy (Table 6.8). The bulk sample of W2 contained four times more oxide-bound Fe than did sample W1. For sample W1, the ratio of silicate-bound Fe to oxide-bound Fe remained almost constant with decreasing grain size, whereas this ratio increased in case of sample W2.

### 6.2.6 Summary of the quantification results

The layer silicate content of the ceramic clays W1 and W2 was determined by a multi-method approach, in order to crosscheck the quantification results from Rietveld analysis and ODPF. In Table 6.9 the quantification results of the clay fractions from Rietveld analysis, ODPF and STA measurements are compared.

To ensure comparability, only the portion of clay minerals from Rietveld analysis was considered. Therefore, ODPF results were normalized to the mean values (conv., norm. mv) from Rietveld analysis, as well as to the Rietveld quantification results after subtracting the standard deviation (conv., norm. -s).

The four phases determined by ODPF (kaolinite, smectite, I-S, and illite) were converted to five phases (kaolinite, smectite, smectite layers, illite, and illite layers), subdividing the I-S content according to the respective $W_a$ values.

With the normalized ODPF values, the maximum mass loss $\Delta m\ T_{DHXcalc}$ was calculated from equation 4.15 (Section 4.2.5) and compared with the measured results ($\Delta m\ T_{DHXmeas}$). For this calculation, the quantification results of the originally four phases from ODPF were reduced to the three discrete “end-member phases” kaolinite, smectite and illite, summing up the content of smectite and smectite layers, and the content of illite and illite layers.

For sample W1 0.6-2 µm, the kaolinite content varied between 32 and 42% in the tested methods. For the appropriate $\Delta$ values, the smallest quantification result of 32% from ODPF corresponded to a large positive $\Delta$ value of 0.80 (always in combination with the other coefficients), denoting underestimation. A kaolinite content of 42% from Rietveld analysis (mean value) yielded the largest negative $\Delta$ value of -0.62, implying overestimation.

Comparing the quantification results of all clay fraction samples, some general tendencies became evident: the strongest variability in phase content was noted for smectite, with Rietveld quantification results being remarkably greater than those obtained by ODPF. The quantification results from Rietveld analysis (mv) led always to the largest negative Δ values; the largest positive Δ values were produced from results from ODPF (conv., norm. -s).

On the basis of the Δ value as an assessment tool for quantification, data sets generated from Rietveld analysis (-s) and ODPF (conv., norm. mv) were in the same range. Rietveld quantification results (mv) as well as the results from ODPF (conv., norm. -s) induced large Δ values, which indicated a greater inconsistency of the quantification results obtained from different methods.

The contents of swellable components from CEC measurements (Table 6.7) were closer to the results from ODPF in case of both 0.6-2 µm fractions, whereas for both <0.6 µm fractions the results were closer to those from Rietveld analysis.

## 6.3 Discussion

### 6.3.1 Physical and chemical parameters

In the following, the influence of grain-size distribution as well as pH, electrical conductivity and soluble salt concentration on processing properties of ceramic clay masses are discussed.

As shown in Table 6.1, grain-size distribution depends heavily on the kind of dispersant and the method employed.

The use of Na-pyrophosphate leads to a mass shift toward smaller particle sizes, which is caused by the destruction of aggregates and the formation of discrete particles. The absorption of pyrophosphate on particles increases the negative charges and their dispersibility in water (Jeanroy and Guillet, 1981).

The samples investigated responded very differently to the Na-pyrophosphate treatment, and this cannot be explained by an electrostatic stabilization effect alone. Comparing the values of the different methods, the mass fraction of the sample W2 <0.6 µm without dispersant increased by a factor of about ten after the treatment with Na-pyrophosphate. Simultaneously, the content of the fraction 0.6-2 µm shrank to about one third. For sample W1, the redistribution of grain sizes with Na-pyrophosphate was less drastic: the respective <2 µm fractions differed from each other by a factor of two.

Microscopic investigations and Mössbauer spectroscopy (Table 6.8) showed differences in Fe distribution for the two samples. In the case of sample W1, the Fe was largely silicate-bound, whereas for W2 it was mostly oxide-bound. The greater amount of oxide-bound Fe of W2 is mainly visible as yellowish-brown goethite-rich coatings, which tend to aggregate smaller particles, giving the impression of a larger grain size.

The influence of Fe oxides on the aggregation behavior of clays is well-known (e.g., Colombo and Torrent, 1991; Cornell and Schwertmann, 2003). Bascomb (1968) reported that pyrophosphate is capable to extract Fe from moderately crystallized goethite.

Table 6.7: Amount of exchangeable cations and CEC measurements (CEC meas) of the bulk material and the clay fractions 0.6-2 µm and <0.6 µm. %CEC: ratio of the sum of exchangeable cations (Σ) to measured CEC. CEC corr: corrected CEC according to equation 2. $w_{sc}$: content of swellable components from CEC measurements.

| Cation | W1 bulk [meq/100g] | W2 bulk [meq/100g] | W1 0.6-2 µm [meq/100g] | W2 0.6-2 µm [meq/100g] | W1 <0.6 µm [meq/100g] | W2 <0.6 µm [meq/100g] |
|---|---|---|---|---|---|---|
| $Na^+$ | 0 | 0 | 0 | 0 | 0 | 0 |
| $Mg^{2+}$ | 3 | 2 | 2 | 3 | 5 | 4 |
| $K^+$ | 0 | 0 | 1 | 0 | 1 | 1 |
| $Ca^{2+}$ | 7 | 5 | 6 | 6 | 12 | 12 |
| Σ | 10 | 7 | 9 | 9 | 18 | 17 |
| CEC meas | 9 | 7 | 10 | 12 | 19 | 18 |
| percentage CEC [%] | 111 | 100 | 90 | 76 | 95 | 97 |
| CEC corr | 6 | 4 | 6 | 7 | 13 | 12 |
| $w_{sc}$ [%] | 8 | 5 | 7 | 9 | 17 | 15 |

Table 6.8: Iron distribution from Mössbauer spectroscopy of the bulk materials and the fractions <0.6 µm.

| Sample | silicate-bound iron [%] | oxide-bound iron [%] |
|---|---|---|
| W1 bulk | 88 | 12 |
| W1 <0.6 µm | 90 | 10 |
| W2 bulk | 49 | 51 |
| W2 <0.6 µm | 77 | 23 |

Table 6.9: Quantification by Rietveld analysis (Rietveld) and one-dimensional XRD profile modeling (ODPF) compared with the maximum mass loss Δm $T_{DHX}$. mv: mean value; -s: quantification value after subtracting the standard deviation; norm: normalized value; conv.: converted value from phase reduction.

| Sample | Quantification method | Kaolinite | Smectite | Smectite layers | Illite | Illite layers | ∑ | Δm $T_{DHXcalc}$ | Δm $T_{DHXmeas}$ | Δ |
|---|---|---|---|---|---|---|---|---|---|---|
| | | [%] | [%] | [%] | [%] | [%] | [%] | [%] | [%] | [%] |
| W1 0.6-2 µm | Rietveld mv | 42 | 17 | n.d. | 24 | n.d. | 83 | 7.78 | 7.16 | -0.62 |
| | Rietveld -s | 37 | 14 | n.d. | 22 | n.d. | 73 | 6.85 | 7.16 | 0.31 |
| | ODPF | 44 | 4 | 3 | 21 | 28 | 100 | - | - | - |
| | ODPF conv., norm. mv | 37 | 3 | 3 | 17 | 23 | 83 | 7.29 | 7.16 | -0.13 |
| | ODPF conv., norm. -s | 32 | 3 | 2 | 15 | 21 | 73 | 6.36 | 7.16 | 0.80 |
| W2 0.6-2 µm | Rietveld mv | 51 | 16 | n.d. | 22 | n.d. | 89 | 8.90 | 7.94 | -0.96 |
| | Rietveld -s | 46 | 13 | n.d. | 19 | n.d. | 78 | 7.92 | 7.94 | 0.02 |
| | ODPF | 48 | 2 | 3 | 31 | 16 | 100 | - | - | - |
| | ODPF conv., norm. mv | 43 | 2 | 3 | 27 | 14 | 89 | 8.13 | 7.94 | -0.19 |
| | ODPF conv., norm. -s | 38 | 2 | 2 | 24 | 12 | 78 | 7.06 | 7.94 | 0.88 |

Continuation of Table 6.9:

| Sample | Quantification method | Kaolinite [%] | Smectite [%] | Smectite layers [%] | Illite [%] | Illite layers | ∑ [%] | Δm $T_{DHXcalc}$ [%] | Δm $T_{DHXmeas}$ [%] | Δ [%] |
|---|---|---|---|---|---|---|---|---|---|---|
| W1 <0.6 µm | Rietveld mv | 55 | 18 | n.d. | 21 | n.d. | 94 | 9.50 | 8.98 | -0.52 |
| | Rietveld -s | 50 | 15 | n.d. | 18 | n.d. | 83 | 8.52 | 8.98 | 0.46 |
| | ODPF | 57 | 4 | 3 | 7 | 29 | 100 | - | - | - |
| | ODPF conv., norm. mv | 53 | 4 | 3 | 7 | 27 | 94 | 9.42 | 8.98 | -0.44 |
| | ODPF conv., norm. -s | 47 | 3 | 3 | 6 | 24 | 83 | 8.31 | 8.98 | 0.67 |
| W2 <0.6 µm | Rietveld mv | 60 | 16 | n.d. | 19 | n.d. | 95 | 10.01 | 9.08 | -0.93 |
| | Rietveld -s | 55 | 12 | n.d. | 16 | n.d. | 83 | 8.99 | 9.08 | 0.09 |
| | ODPF | 63 | 0 | 4 | 15 | 18 | 100 | - | - | - |
| | ODPF conv., norm. mv | 59 | 0 | 4 | 14 | 17 | 95 | 9.93 | 9.08 | -0.85 |
| | ODPF conv., norm. -s | 52 | 0 | 3 | 13 | 15 | 83 | 8.77 | 9.08 | 0.31 |

The application of pyrophosphate leads to the destruction of micro-aggregates and the dispersion of clayey and colloidal cements (Pansu and Gautheyrou, 2006). A summary of the mechanisms of the action of pyrophosphate is given by Beckett (1989).

According to Ongley et al. (1981), the different kinds of treatments give rise to an absolute and to an effective grain-size distribution. The contrast between these two states plays an important role, as both exert a strong influence on the rheological properties of clays, not only in ceramics but also in paper industry (Grafton, 1968) or sediment dynamics (Walling and Moorehead, 1989).

Furthermore, the measuring method itself affects the results. The present data confirm that the Sedigraph method for particle-size analysis consistently yields a finer size distribution than the pipette method (Buchan et al., 1993; Hotchkiss, 1994). However, independent of the analytical method, both data sets from treatment with and without Na-pyrophosphate illustrate the different aggregation characteristics of W1 and W2, which are jointly responsible for the processing properties.

Significant differences between the two samples are noticeable in the soluble salt concentration. W1 releases >12 times as much sulfate, which is also reflected by its greater electrical conductivity. The sulfate release is probably caused by oxidation of marcasite (Rimstidt and Vaughan, 2003), as marcasite is the only sulfide-bearing mineral found in the samples. The greater $SO_4^{2-}$ concentration in W1 is in accord with the detection of marcasite during the ESEM analysis. The small amount of sulfate released by W2, combined with the information from Mössbauer spectroscopy, plus the observation of yellowish-brown Fe-coatings, indicate that the iron is largely oxide-bound, presumably as goethite.

The larger soluble salt concentration of W1 explains the greater degree of dispersibility of the raw material in water. Penner and Lagaly (2001) showed that multivalent anions up to high salt concentrations exert a pronounced liquefying effect on kaolinite-rich dispersions, as anions recharge the edges and cancel the edge(+)/face(-) interaction (Rand and Melton, 1977; van Olphen, 1977), resulting in a reduced viscosity.

The influence of pH on the clay suspensions cannot be taken into consideration for the different processing properties of W1 and W2, as the values are the same for both clays within the standard deviations.

Kromer and Rose (1994) stated that an increasing amount of swelling clay minerals prevent liquefaction of clays, so that the differences in processing properties of W1 and W2, with respect to the extrusion pressure and making moisture content, are made more complex by the interaction of the physical-chemical parameters with the mineralogical phase content.

### 6.3.2 Mineralogical parameters

Regarding the bulk samples, the deviations between the element oxides from XRF measurements and the oxide-converted Rietveld values were <0.5% for all tested element oxides.

Larger deviations were noted for the $SiO_2/Al_2O_3$-ratio and in the $Fe_2O_3$ content for the two samples. The deviation in $Fe_2O_3$ content is explicable by the fact that Fe-bearing phases at such low concentrations could not be identified by XRD with Cu*K*α radiation due to significant background fluorescence resulting in a poor peak resolution (Bland et al., 2004).

Moreover, Mössbauer spectroscopy showed that some of the Fe is silicate-bound, which again reduces the XRD-detectable portion.

Furthermore, indirect proof for the presence of silicate-bound Fe was provided by the generation of PA curves (Figure 6.4). Kaolinites with high degree of structural disorder were found to contain more octahedral $Fe^{3+}$ than those with a well-ordered structure (Herbillon et al., 1976; Mestdagh et al., 1980).

The presence of highly-disordered kaolinite is also reflected in STA measurements by the weak recrystallization reaction at low temperatures. Such thermal behavior is typical of clays from the Westerwald, which are known to contain highly-disordered kaolinite (Lippmann, 1960; Jasmund and Lagaly, 1993). All tested methods indicated consistently that the kaolinite in sample W1 has a greater degree of structural disorder.

Deviations in the $SiO_2/Al_2O_3$-ratio were caused by the lack of an appropriate structural model for I-S mixed-layer minerals within the Rietveld code and correlation of clay mineral phases. This effect was pronounced for the clay fractions, where the $SiO_2$ content was overestimated and the $Al_2O_3$ content was underestimated consistently.

The clay fraction samples of W1 and W2 show positive deviations in the $K_2O$ content, implying underestimation of the K-bearing phases by Rietveld analysis. This may have been caused by an inappropriate illite structural model as well as an incorrect quantification result for illite and/or orthoclase. The Rietveld quantification was carried out by a combination of two structural models (muscovite 2M1 and illite 1Mc), because of the better fit. The oxide conversion was done on the basis of a high K-illite structural model (0.89 $K^+$/FU) according to Środoń et al. (1992). Even setting stoichiometry to the maximum value of 1 $K^+$/FU, the positive $K_2O$-deviation decreases only slightly, suggesting an underestimation of illite and/or orthoclase by Rietveld analysis.

An increase of the illite content together with a decrease in the feldspar content is to be expected with decreasing particle size (Dultz, 2002). The results from the present Rietveld analysis show nearly constant values for illite and feldspar within the various fractions, whereas ODPF show an increase in the illite layer content with decreasing particle size.

Balancing the deviations, a plausible explanation for the positive deviations in the $Al_2O_3$ and $K_2O$ contents and the negative deviations of $SiO_2$ for the clay fractions is given by an overestimation of smectitic components coupled with a simultaneous underestimation of the kaolinite and illite contents and/or feldspar content by Rietveld analysis.

For the bulk material of W1 and W2, the quartz and kaolinite contents seem to be slightly underestimated, whereas the illite content and the content of swellable components appear to be overestimated.

The results from CEC measurements of both bulk samples and the 0.6-2 µm clay fractions reflect also the tendency to overestimate swellable components by Rietveld analysis. For both clay fractions <0.6 µm, the amounts of swellable components from CEC measurements and Rietveld analysis are very similar, while the results for the 0.6-2 µm samples match the contents gathered from ODPF better.

The results from STA measurements correspond, in the case of sample W1 <0.6 µm, slightly better with the results from ODPF, whereas for sample W2 <0.6 µm the results from STA measurements and Rietveld analysis correlate better.

However, both, the structure and the amount of swellable minerals in ceramic clays, influence significantly the water binding, the size of delaminated particles and their spatial movement, and the distribution of the material during processing. Because of their smaller layer charge, in contrast to illite, the swellable components are thought to act like “predetermined breaking-points”. Figure 6.5 illustrates the delamination behavior and resulting water-accessible surfaces of *R1* and *R3* I-S mixed-layer minerals compared to pure smectite.

Delamination is expected to occur not only in suspensions, but also in wet ceramic clay masses under high shear stress, as applied during extrusion.

According to this model, plasticity of W1 is caused by the presence of discrete smectite, which acts as a lubricant compensating the lower delamination potential of the *R3* I-S particles. In contrast, the *R1* I-S particles of W2 form stockier stacks of 2:1 layers by delamination, and these cannot enter interparticle spaces, resulting in lower plasticity during processing at the same operational load.

The greater plasticity of W1 results in a greater dry-bending strength as well as in an increased making moisture content and extrusion pressure, which, in turn, increase energy consumption during the drying and firing process.

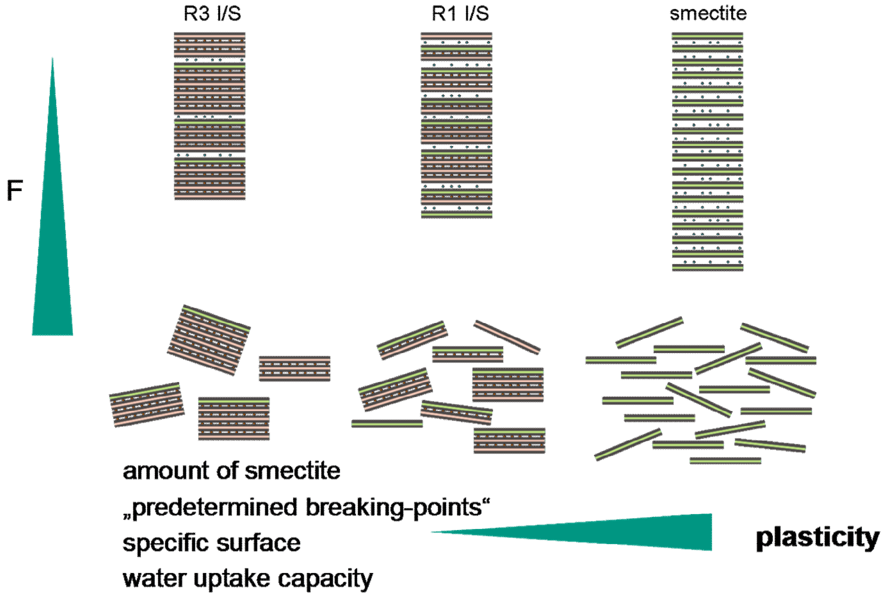

Figure 6.5: Relation between the structure and ordering principle of 2:1 layer silicates and delamination behavior affecting processing properties. F is the applied force.

## 6.4 Conclusions

The processing properties of ceramic clays are influenced by the interaction of different material parameters. The present study show that the two investigated ceramic clays differed in terms of the following parameters:

(1) effective grain-size distribution
(2) soluble-salt concentration
(3) particle agglomeration by Fe-coatings
(4) abundance of discrete smectite
(5) amount and degree of ordering of I-S mixed-layer minerals.

The qualitative delamination model deduced from the structural information gives an indication of how the swellable components may influence the processing properties of ceramic clays. With increasing amounts of swellable layers, the number of “predetermined breaking-points” increases, and so, too, does the number of water-accessible surfaces. As a consequence, microstructural modifications are facilitated for clay systems containing larger amounts of swellable components, which may in turn result in greater plasticity.

Further studies are required to quantify the contribution of each parameter to workability, with special attention paid to the swellable components. Challenges remain in terms of quantitative determination of all material parameters due to the small concentrations of components and/or inappropriate structural models for Rietveld quantification of mixed-layer minerals in complex mineral admixtures.

Processing properties of ceramic clays can be predicted only by means of a multi-method approach as detailed information on the phase content seems to be the only way to elucidate the differences in ceramic clays that are graded as being the same according to traditional quality assessment of industrial raw clays.

# 7 Summary and final conclusions

A comprehensive mineralogical investigation of three paper kaolins and two ceramic clays and their respective grain-size fractions was carried out to elucidate the processing properties with regard to possible microbially induced quality enhancement. The study was aimed at contributing to the long-term objective of developing an assessment scheme for quality evaluation of industrially used clays.

The necessity of such expert systems is shown by the large number of studies dedicated to the deduction of mineralogical key parameters in order to understand bulk material properties (e.g., Lagaly, 1989; Galán et al., 1998; Taboada et al., 2006) or to elucidate special properties of single clay constituents, such as smectites (e.g., studies of Dong, Kostka, or Stucki) or kaolinites (e.g., studies of Murray).

As described in the introduction (Chapter 1), this issue still remains very challenging due to the complexity of factors, which influence clay properties. For that reason, conventional industrial clay assessment is solely based on the deduction of mineralogical parameters from chemical composition and grain-size distribution, which was shown not to be sufficient for the evaluation of processing properties in terms of kaolin brightness and plasticity of ceramic clays. In order to overcome this complexity, the characterization of the samples investigated in this study was based on a multi-method approach, consisting in the detection of relevant physical-chemical as well as mineralogical parameters.

Regarding the paper kaolins, the study demonstrated the feasibility of removing $Fe^{3+}$ impurities by a Fe-reducing culture of *Shewanella putrefaciens*. For the various kaolin samples, the microbial treatment led to different degrees of brightness enhancement, which were shown to be a function of the respective mineralogical composition in terms of different Fe depletion sources. The results indicated that *Shewanella putrefaciens* is capable to reduce both, oxide-bound

Fe as well as silicate-bound Fe, whereas the impact on brightness was larger for the reduction of oxide-bound Fe and smaller for the reduction of silicate-bound Fe. Considering the place of microbially induced reduction for the silicate-bound Fe, the depletion seemed to occur in the 2:1 layer silicates, since no evidence of structural changes was observed for kaolinite.

On the basis of the results obtained, further identification of Fe depletion sources within the group of 2:1 layer silicates in terms of illite and swellable components was not possible. The correlation between the amount of smectitic components and extent of Fe reduction found for the kaolin samples in this study suggests that $Fe^{3+}$-reduction preferably takes place in the swellable components of the I-S mixed layers. In contrast, the more pronounced staining effect found for smectites with reduced Fe is indicative of illite being the source of Fe depletion, with illite losing its dyeing capacity by Fe reduction, which, in turn, should result in an increased brightness.

With the knowledge of different Fe depletion sources, the generally assumed correlation of kaolin brightness and $Fe_2O_3$ content is at most valid if the Fe is completely oxide-bound. This is not the case for kaolins since they contain considerable amounts of Fe-bearing 2:1 layer silicates. As the reduced silicate-bound Fe largely remains inside the silicate structure, the total $Fe_2O_3$ content decreases only slightly with bioleaching and, thus, does not serve as an indicator of kaolin brightness. Therefore, brightness should be always seen in the context of Fe distribution in terms of oxide versus silicate Fe as well as in the context of the ratio $Fe^{2+}/Fe^{3+}$. On these grounds, the Fe removal efficiency may be used as an indicator of Fe distribution, as this parameter correlates well with the mineralogical differences of the various kaolin samples in terms of different Fe depletion sources. The Fe removal efficiency was shown to be high for the samples with silicate-bound Fe (B4914 and B4915), but low for sample LA540, which was characterized by a larger amount of oxide-bound Fe.

However, attributing single parameters to brightness enhancement still remains challenging due to the number and complexity of interactions arising from the kaolin composition in terms of $Fe_2O_3$ content, Fe distribution, amount and kind of clay minerals, particle size distribution, kaolinite crystallinity, as well as the presence of further staining components such as $TiO_2$ or organic compounds, which were all shown to influence the kaolin brightness.

The observed changes in rheology occurred with bioleaching, which led to mass shifts during grain-size fractionation of the investigated kaolin samples, should be taken into account in future industrial applications since an adequate rheology of kaolin suspensions represents a crucial factor of paper making. Further studies are needed to evaluate the influence of microbiological treatment on the rheology of kaolin suspensions.

Regarding the different processing properties of the ceramic clays, which were classified into the same grade, according to common industrial assessment in terms of chemical composition and grain-size distribution, the present study indicated that plasticity is the result of various interacting material parameters, which were found to differ for the two investigated ceramic clays.

Grain-size distribution was found to depend heavily on the dispersion method employed, either using Na-pyrophosphate according to industrial standard sample preparation or solely deionized water. The different treatments prior to grain-size fractionation gave rise to an absolute and to an effective grain-size distribution, since the application of pyrophosphate led to the destruction of Fe-bearing micro-aggregates and the dispersion of clayey and colloidal cements. The distinction in absolute and effective grain-size distribution represents an important concept, as the evaluation of processing properties, according to industrial standards, is based on results obtained from sample preparation with Na-pyrophosphate, thus, on absolute grain-size distribution. Ceramic clays, however, are processed without any additional dispersant agent. Therefore, evaluation of processing behavior should rather be deduced from values gathered from effective grain-size distribution and not, as hitherto, from absolute grain-size distribution.

Particle agglomeration effects, contributing to the different grain-size distribution characteristics of the two ceramic clays were further traced by the determination of the Fe distribution, which illustrated that the more plastic sample W1 had mostly silicate-bound Fe, whereas the less plastic sample W2 was also characterized by the presence of oxide-bound Fe coatings, tending to aggregate smaller particles and giving the impression of a larger grain size.

By means of ODPF, it was shown that the investigated ceramic clays differed in the abundance of discrete smectite as well as in the amount and degree of ordering of I-S mixed-layer minerals. On the basis of both, the structure and the amount of swellable minerals, a qualitative delamination model was derived in order to explain the different working properties of the samples. Within this model, the swellable components, in contrast to illite, are thought to act like “predetermined breaking-points”, due to their smaller layer charge. With increasing amount of the swellable components, that is, increasing number of “predetermined breaking-points”, the probability of delamination events increases. Delamination leads to the creation of water-accessible surfaces and, therefore, water binding increases. Delamination is expected to occur not only in suspensions, but also in wet ceramic clay masses under high shear stress, as applied during extrusion. As a consequence, microstructural modifications are facilitated for clay systems containing larger amounts of swellable components, which may in turn result in greater plasticity.

However, further studies are required to quantify the contribution of each parameter to workability, with special attention paid to the swellable components. Challenges remain in terms of quantitative determination of all material parameters due to the low concentrations of components and/or inappropriate structural models for Rietveld quantification of mixed-layer minerals in complex mineral admixtures.

Regardless of the respective clay system, this study illustrated that the characterization of paper kaolins and ceramic clays for understanding the processing properties can be gained only by means of a multi-method approach as detailed information on the phase content seems to be the only way to elucidate compositional and structural differences, which were not detectable by common industrial evaluation methods.

The combination of various quantification methods revealed that both, the Fe distribution in terms of oxide-bound Fe and silicate-bound Fe and the swellable components found in I-S mixed-layer silicates or in form of smectites, have a strong impact on brightness as well as on the plasticity of clays.

Therefore, future quality assessment of raw clay properties’ should take into account these two key parameters. Nevertheless, decision-making for clay grade-classification on the basis of mineralogical phase analysis remains challenging due to the partial inconsistency of the quantification results obtained by XRD analysis using the Rietveld method and ODPF as well as STA and CEC. The deduction of a generally valid clay assessment scheme is additionally complicated by the high variability of clay systems and, thus, mineralogical composition, which have been shown to vary notably even in one single mining area.

However, to conclude with the words of Galán et al. (1998), “the industrial properties of kaolin cannot be predicted from other basic properties such as mineralogy because they are intricately related to one another.” This means that the long-term objective of developing an assessment scheme for the quality evaluation of industrially used clays can only be reached by further efforts dedicated to a detailed determination of the quantitative phase content.

# 8 References

Ahn, J. H. and Peacor, D. R. (1986a) Transmission and analytical electron microscopy of the smectite-to-illite transition. *Clays and Clay Minerals* **34**, 165-179.

Ahn, J. H. and Peacor, D. R. (1986b) Transmission electron microscope data for rectorite: Implications for the origin and structure of "fundamental particles". *Clays and Clay Minerals* **34**, 180-186.

Altaner, S. P., Hower, J., Whitney, G., and Aronson, J. (1984) Model for K-bentonite formation: Evidence from zoned K-bentonites in the disturbed belt, Montana. *Geology* **12**, 412-415.

Altaner, S. P. and Bethke, C. M. (1998) Interlayer order in illite/smectite. *American Mineralogist* **73**, 766-774.

Ammann, L., Bergaya, F., and Lagaly, G. (2005) Determination of the cation exchange capacity of clays with copper complexes revisited. *Clay Minerals* **40**, 441-453.

Andreola, F., Castellini, E., Manfredini, T., and Romagnoli, M. (2004) The role of sodium hexametaphosphate in the dissolution process of kaolinite and kaolin. *Journal of the European Ceramic Society* **24**, 2113-2124.

Andreola, F., Castellini, E., Ferreira, J. M. F., Olhero, S., and Romagnoli, M. (2006) Effect of sodium hexametaphosphate and ageing on the rheological behaviour of kaolin dispersions. *Applied Clay Science* **31**, 56-64.

Anonymous (2001) Reviewing the concept of paper brightness. Axiphos GmbH http://www.axiphos.com/BrightnessReview.pdf, Loerrach, Germany.

Arslan, V. and Bayat, O. (2009) Removal of Fe from kaolin by chemical leaching and bioleaching. *Clays and Clay Minerals* **57**, 787-794.

Atterberg, A. (1912) Die mechanische Bodenanalyse und die Klassifikation der Mineralböden Schwedens. *Internationale Mittelungen für Bodenkunde* **2**, 312-342.

AutoQuan (2003) Seifert Analytical X-ray. Agfa NDT Pantak Seifert GmbH & Co. KG, Ahrensburg.

Bachir, C. (2009) The influence on calcination temperature on structure and magnetic properties of pillared clays. Doctoral Thesis, pp. 157. Universität Karlsruhe.

Bahranowski, K., Serwicka, E. M., Stoch, L., and Strycharski, P. (1993) On the possibility of removal of nonstructural iron from kaolinite-group minerals. *Clay Minerals* **28**, 379-391.

Bailey, S. W. (1982) Nomenclature for regular interstratifications. *American Mineralogist* **67**, 394-398.

Bailey, S. W. (1984) Crystal chemistry of the true mica. In: Bailey, S. W. (Ed.), *Micas, Reviews in Mineralogy*. Mineralogical Society of America, pp. 13-60.

Bailey, S. W., Alietti, A., Formoso, M. L. L., Konta, J., Köster, H. M., Mackenzie, R. C., Morgan, D. J., Mumpton, F. A., Nagasawa, K., Paquet, H., Rausell-Colom, J. A., and Zvyagin, B. B. (1986) Report of the AIPEA Nomenclature Committee (Illite-Glauconite-Volkonskoite). Supplement to the AIPEA Newsletter, Bailey et al. (1984). *AIPEA Newsletter* **22**, 1-3.

Bain, J. A. (1971) A plasticity chart as an aid to the identification and assessment of industrial clays. *Clay Minerals* **9**, 1-17.

Baird, J. C. and Walz, J. Y. (2007) The effects of added nanoparticles on aqueous kaolinite suspensions II. Rheological effects. *Journal of Colloid and Interface Science* **306**, 411-420.

Bajpai, P. (2005) Enrivonmentally benign approaches. Elsevier, Amsterdam, pp. 277.

Balan, E., Allard, T., Boizot, B., Morin, G., and Muller, J.-P. (2000) Quantitative measurement of paramagnetic $Fe^{3+}$ in kaolinite. *Clays and Clay Minerals* **48**, 439-445.

Bartusch, R. and Händle, F. (2007) Laminations in extrusion. In: Händle, F. (Ed.), *Extrusion in Ceramics*. Springer, Berlin Heidelberg, pp. 187-210.

Bascomb, C. L. (1968) Distribution of pyrophosphate - Extractable iron and organic carbon in soils of various groups. *Journal of Soil Science* **19**, 251-268.

Bassin, N. J. (1975) Suspended marine clay minerals identification by scanning electron microscopy and energy-dispersive X-ray analysis. *Limnology and Oceanography* **20**, 133-137.

Batchelder, M. and Cressey, G. (1998) Rapid, accurate phase quantification of clay-bearing samples using a position-sensitive X-ray detector. *Clays and Clay Minerals* **46**, 183-194.

Bauberger, W. and Haunschild, H. (1960) Erläuterungen zur Geologischen Karte von Bayern 1:25 000, Blatt Nr. 6438 Schnaittenbach. Bayerisches Geologisches Landesamt, München, pp. 127.

Beckett, P. H. T. (1989) The use of extractants in studies on trace metals in soils, sewage sludges, and sludge-treated soils. In: Stewart, B. A. (Ed.), *Advances in Soil Science*. Springer-Verlag, New York, pp. 143-176.

Bell, T. E. (1986) Microstructure in mixed-layer illite/smectite and its relationship to the reaction of smectite to illite. *Clays and Clay Minerals* **34**, 146-154.

Bergaya, F., Theng, B. K. G., and Lagaly, G. (2006) Handbook of Clay Science. Elsevier, Oxford Amsterdam, pp. 1224.

Bergmann, J. and Kleeberg, R. (1998) Rietveld analysis of disordered layer silicates. *Materials Science Forum* **278-281**, 300-305.

Bergmann, J., Friedel, P., and Kleeberg, R. (1998) BGMN - A new fundamental parameters based Rietveld program for laboratory X-ray sources, its use in quantitative analysis and structure investigations. Commission of Powder Diffraction. *International Union of Crystallography CPD Newsletter* **20**, 5-8.

Berthelin, J., Leyval, C., and Mustin, C. (2004) Environmental Mineralogy: Microbial Interactions, Anthropogenic Influences, Contaminated Land and Waste Management. Mineralogical Society of Great Britain & Ireland, London, pp. 414.

Besson, G., Bookin, A. S., Dainyak, L. G., Rautureau, M., Tsipursky, S., Tchoubar, C., and Drits, V. A. (1983) Use of diffraction and Mössbauer methods for the structural and crystallochemical characterization of nontronite. *Journal of Applied Crystallography* **16**, 374-383.

Bethke, C. M. and Altaner, S. P. (1986) Layer-by-layer mechanism of smectite illitization and application to a new rate law. *Clays and Clay Minerals* **34**, 136-145.

Bethke, C. M., Vergo, N., and Altaner, S. P. (1986) Pathways of smectite illitization. *Clays and Clay Minerals* **34**, 125-135.

Beyer, D., Görsch, K., and Zehnsdorf, A. (2011) Bericht zum Teilvorhaben 3: Amplifikation und verfahrenstechnische Prozessoptimierung zur Produktion mikrobiologisch aufbereiteter Tone. *Entwicklung neuer Aufbereitungstechnologien für tonmineralische Rohstoffe durch gezielte Nutzung und Steuerung mikrobiologischer Reaktionen*, Leipzig, pp. 86.

Bischoff, P. (2004) Einfluss von bakteriellen extrazellulären Polysacchariden auf die Rheologie industriell genutzter keramischer Massen. Institut für Mineralogie und Geochemie, Karlsruhe, pp. 18.

Bish, D. L. and Howard, S. A. (1988) Quantitative phase analysis using the Rietveld method. *Journal of Applied Crystallography* **21**, 86-91.

Bish, D. L. and Reynolds , R. C. (1989) Sample preparation for X-ray diffraction. *Reviews in Mineralogy and Geochemistry* **20**, 73-99.

Blanc, P., Legendre, O., and Gaucher, E. C. (2007) Estimate of clay minerals amounts from XRD pattern modeling: The Arquant model. *Physics and Chemistry of the Earth* **32**, 135-144.

Bland, P. A., Cressey, G., and Menzies, O. N. (2004) Modal mineralogy of carbonaceous chondrites by X-ray diffraction and Mössbauer spectroscopy. *Meteroritic & Planetary Science* **39**, 3-16.

Bonneville, S., Behrends, T., Van Cappellen, P., Hyacinthe, C., and Röling, W. F. M. (2006) Reduction of Fe(III) colloids by *Shewanella putrefaciens*: A kinetic model. *Geochimica et Cosmochimica Acta* **70**, 5842-5854.

Bookin, A. S., Dainyak, L. G., and Drits, V. A. (1978) Interpretation of the Mössbauer spectra iron(3+)-containing layered silicates based on structural modeling. *Physics and Chemistry of Minerals* **3**, 58-59.

Borggaard, O. K. (1988) Phase identification by selective dissolution techniques. In: Stucki, J. W., Goodman, B. A., and Schwertmann, U. (Eds.), *Iron in soils and clay minerals*. D. Reidel, Dordrecht, pp. 83-98.

Bosch, J., Fritzsche, A., and Meckenstock, R. U. (2007) Nanosized iron(hydroxy)oxide particles are readily reduced by iron-reducing microorganisms, *European Geoscience Union*. Geophysical Research Abstracts, Vienna, pp.

Bosecker, K. (1997) Bioleaching: Metal solubilization by microorganisms. *FEMS Microbiology Reviews* **20**, 591-604.

Brigatti, M. F., Galán, E., and Theng, B. K. G. (2006) Structures and mineralogy of clay minerals. In: Bergaya, F., Theng, B. K. G., and Lagaly, G. (Eds.), *Handbook of clay science*. Elsevier, Oxford Amsterdam, pp. 19-86.

Brindley, G. W. (1945) A theory of X-ray absorption in mixed powders. *Philosophical Magazine* **36**, 347-369.

Brindley, G. W. and Pedro, G. (1972) Report of the AIPEA Nomenclature Committee. *AIPEA Newsletter* **7**, 8-13.

Brindley, G. W. and Brown, G. (1980) Crystal structures of clay minerals and their X-ray identification. Mineralogical Society of Great Britain, London, pp. 495.

Brindley, G. W., Kao, C.-C., Harrison, J. L., Lipsicas, M., and Raythatha, R. (1986) Relation between structural disorder and other characteristics of kaolinites and dickites. *Clays and Clay Minerals* **34**, 239-249.

Bristow, J. A. (1994) What is ISO brightness? *Tappi Journal* **77**, 174-178.

Brombacher, C., Bachofen, R., and Brandl, H. (1997) Biohydrometallurgical processing of solids: A patent review. *Applied Microbiology and Biotechnology* **48**, 577-587.

Buchan, G. D., Grewal, K. S., Claydon, J. J., and McPherson, R. J. (1993) A comparison of sedigraph and pipette methods for soil particle-size analysis. *Australian Journal of Soil Research* **31**, 407-417.

Bundy, W. M. (1993) The diverse industrial applications of kaolins. In: Murray, H. H., Bundy, W. M., and Harvey, C. C. (Eds.), *Kaolin, Genesis and Utilizations*. The Clay Minerals Society, Bloomington, Indiana, pp. 43-73.

Burgstaller, W. and Schinner, F. (1993) Leaching of metals with fungi. *Journal of Biotechnology* **27**, 91-116.

Cameselle, C., Nunez, M. J., Lema, J. M., and Pais, J. (1995) Leaching of iron by a spent fermentation liquor: Influence of temperature, pH, agitation and citric acid concentration. *Journal of Industrial Microbiology* **14**, 288-292.

Cameselle, C., Ricart, M. T., Núnez, M. J., and Lema, J. M. (2003) Iron removal from kaolin. Comparison between "in situ" and "two-stage" bioleaching processes. *Hydrometallurgy* **68**, 97-105.

Cardile, C. M. (1989) Tetrahedral iron in smectite: A critical commentary. *Clays and Clay Minerals* **37**, 185-188.

Cervini-Silva, J., Kostka, J. E., Larson, R. A., Stucki, J. W., and Wu, J. (2003) Dehydrochlorination of 1,1,1-trichloroethane and pentachloroethane by microbially reduced ferruginous smectite. *Environmental Toxicology and Chemistry* **22**, 1046-1050.

Chandrasekhar, S. and Raghavan, P. (1999) Characterization of ancillary minerals in Kutch kaolin during size classification. In: Sastry, S. R. S., Mohanty, S., and Mohapatra, B. K. (Eds.), *Proceedings of the International Symposium on Beneficiation, Agglomeration and Environment*. Allied Publishers, New Delhi, pp. 24-31.

Chandrasekhar, S. and Raghavan, P. (2004) A novel approach to correlate brightness of kaolin with the iron and titanium contents. In: Rao, G. V. and Misra, V. N. (Eds.), *Mineral Processing Technology*. Sunil Sachdev, New Delhi, pp. 253-260.

Chandrasekhar, S. and Ramaswamy, S. (2006) Iron minerals and their influence on the optical properties of two Indian kaolins. *Applied Clay Science* **33**, 269-277.

Chapelle, F. H. and Lovley, D. R. (1990) Rates of microbial metabolism in deep coastal plain aquifers. *Applied and Environmental Microbiology* **56**, 1865-1874.

Chipera, S. J. and Bish, D. L. (2002) FULLPAT: A full-pattern quantitative analysis program for X-ray powder diffraction using measured and calculated patterns. *Journal of Applied Crystallography* **35**, 744-749.

Colmer, A. R. and Hinkle, M. E. (1947) The role of microorganisms in acid mine drainage: A preliminary report. *Science* **106**, 253-256.

Colombo, C. and Torrent, J. (1991) Relationsship between aggregation and iron oxides in Terra Rossa soils from southern Italy. *Catena* **18**, 51-59.

Cornell, R. M. and Schwertmann, U. (2003) The iron oxides: structure, properties, reactions, occurrences, and uses. Wiley-VCH, Weinheim, pp. 664.

Coyne, L. M. and Banin, A. (1986) Effect of adsorbed iron on thermoluminescence and electron spin resonance spectra of Ca-Fe-exchanged montmorillonite. *Clays and Clay Minerals* **34**, 645-650.

Crosby, N. T. and Patel, I. (1995) General principles of good sampling practice. The Royal Society of Chemistry, Cambridge, pp. 68.

Cuadros, J. and Altaner, S. P. (1998) Characterization of mixed-layer illite-smectite from bentonites using microscopic, chemical, and X-ray methods: Constraints on the smectite-to-illite transformation mechanism. *American Mineralogist* **83**, 762-774.

de Mesquita, L. M. S., Rodrigues, T., and Gomes, S. S. (1996) Bleaching of Brazilian kaolins using organic acids and fermented medium. *Mineral Engineering* **9**, 965-971.

DIN 19261 (2000) pH-Messung, Messverfahren mit Verwendung potentiometrischer Zellen.

DIN 4022 (1987) Baugrund und Grundwasser.

DIN 5033-9 (1982) Farbmessung; Weißstandard für Farbmessung und Photometrie.

DIN 6164 (1980) DIN-Farbkarte; Festlegung der Farbmuster.

DIN 66115 (1983) Partikelgrößenanalyse; Sedimentationsanalyse im Schwerefeld; Pipette-Verfahren.

DIN 19683-2 (1973) Physikalische Laboruntersuchungen - Bestimmung der Korngrößenzusammensetzung nach Vorbehandlung mit Natriumpyrophosphat.

DIN 38414-4 (1984) German standard methods for the examination of water, waste water and sludge; sludge and sediments (group S); determination of leachibility by water (S 4).

Dohrmann, R., Rüping, K. B., Kleber, M., Ufer, K., and Jahn, R. (2009) Variation of preferred orientation in oriented clay mounts as a result of sample preparation and composition. *Clays and Clay Minerals* **57**, 686-694.

Dolcater, D. L., Syers, J. K., and Jackson, M. L. (1970) Titanium as free oxide and substituted forms in kaolinites and other soil minerals. *Clays and Clay Minerals* **18**, 71-79.

Dondi, M., Guarini, G., Raimondo, M., and Salucci, F. (2003) Influence of mineralogy and particle size on the technological properties of ball clays for porcelain stoneware tiles. *Tile & Brick International* **20**, 2-11.

Dondi, M., Iglesias, C., Dominguez, E., Guarini, G., and Raimondo, M. (2008) The effect of kaolin properties on their behaviour in ceramic processing as illustrated by a range of kaolins from the Santa Cruz and Chubut Provinces, Patagonia (Argentina). *Applied Clay Science* **40**, 143-158.

Dong, H., Fredrickson, J. K., Kennedy, D. W., Zachara, J. M., Kukkadapu, R. K., and Onstott, T. C. (2000) Mineral transformation associated with the microbial reduction of magnetite. *Chemical Geology* **169**, 299-318.

Dong, H., Kukkadapu, R. K., Fredrickson, J. K., Zachara, J. M., Kennedy, D. W., and Kostandarithes, H. M. (2003a) Microbial reduction of structural Fe(III) in illite and goethite. *Environmental Science and Technology* **37**, 1268-1276.

Dong, H., Kostka, J. E., and Kim, J. (2003b) Microscopic evidence for microbial dissolution of smectite. *Clays and Clay Minerals* **51**, 502-512.

Dong, H., Jaisi, D. P., Kim, J., and Zhang, G. (2009a) Microbe-clay mineral interaction. *American Mineralogist* **94**, 1505-1519.

Dong, H., Ji, S., Yang, J., Bishop, M. E., and Zhang, G. (2009b) Microbial reduction of iron in smectite (nontronite), mixed-layer smectite/illite, and illite: Correlating the rate and extent of bioreduction with layer charge and expandability, *46th Clay Mineral Society Annual Meeting*, Billings, Montana, pp. 113.

Dong, H., Jaisi, D. P., Zhang, G., and Kim, J. W. (2009c) Microbe-clay interactions and implications for environmental remediation. 237th Annual Meeting of the American Chemical Society, Salt Lake City.

Dorioz, J. M., Robert, M., and Chenu, C. (1993) The role of roots, fungi and bacteria on clay particle organization. An experimental approach. *Geoderma* **56**, 179-194.

Downs, R. T. and Hall-Wallace, M. (2003) The *American Mineralogist* crystal structure database. *American Mineralogist* **88**, 247-250.

Drits, V. A. (1987) Mixed-layer minerals: Diffraction methods and structural features. In: Schultz, L. G., van Olphen, H., and Mumpton, F. A. (Eds.), *Proceedings of the International Clay Conference*, Denver, 1985. The Clay Minerals Society, Bloomington, Indiana, Denver, pp. 33-45.

Drits, V. A. (2003) Structural and chemical heterogeneneity of layer silicates and clay minerals. *Clay Minerals* **38**, 403-432.

Drits, V. and Sakharov, B. A. (1976) X-ray structural analysis of mixed-layer minerals. *Transactions of Academy of Sciences U.S.S.R. (in russia)* **295**, pp. 252.

Drits, V. A. and Tchoubar, C. (1990) X-ray diffraction by disordered lamellar structures: Theory and application to microdevided silicates and carbons. Springer-Verlag, Berlin Heidelberg, pp. 371.

Drits, V., Varaxina, V., Sakharov, B. A., and Plancon, A. (1994) A simple technique for identification of one-dimensional powder X-ray diffraction patterns for mixed-layer illite-smectites and other interstratified minerals. *Clays and Clay Minerals* **42**, 382-390.

Drits, V. A., Besson, G., and Muller, F. (1995) An improved model for structural transformations of heat-treated aluminous dioctahedral 2:1 layer silicates. *Clays and Clay Minerals* **43**, 718-731.

Drits, V. A., Środoń, J., and Eberl, D. D. (1997a) XRD measurement of mean crystallite thickness of illite and illite/smectite: Reappraisal of the Kubler index and the Scherrer equation. *Clays and Clay Minerals* **45**, 461-475.

Drits, V. A., Sakharov, B. A., Lindgreen, H., and Salyn, A. L. (1997b) Sequential structure transformation of illite-smectite-vermiculite during diagenesis of Upper Jurassic shales from the Northern Sea and Denmark. *Clay Minerals* **32**, 351-371.

Dudek, T. and Środoń, J. (1996) Identification of illite/smectite by X-ray powder diffraction taking into account the lognormal distribution of crystal thickness. *Geologia Carpathica - Clays* **5**, 21-32.

Dultz, S. (2002) Effects of parent material and weathering on feldspar content in different particle size fractions from forest soils in NW Germany. *Geoderma* **106**, 63-81.

Dyar, M. D., Agresti, D. G., Schaefer, M. W., Grant, C. A., and Sklute, E. C. (2006) Mössbauer spectroscopy of earth and planetary materials. *Annual Review of Earth and Planetary Sciences* **34**, 83-125.

Eberl, D. D. and Środoń, J. (1988) Ostwald ripening and interparticle-diffraction effects for illite crystals. *American Mineralogist* **73**, 1335-1345.

Eberl, D. D., Środoń, J., Lee, M., Nadeau, P. H., and Northrop, H. R. (1987) Sericite from the Silverton caldera, Colorado: Correlation among structure, composition, origin, and particle thickness. *American Mineralogist* **72**, 914-934.

Eberl, D. D., Środoń, J., Kralik, M., Taylor, B., and Peterman, Z. (1990) Ostwald ripening of clays and metamorphic minerals. *Science* **248**, 474-477.

Ebitani, K., Ide, M., Mitsudome, T., Mizugaki, T., and Kaneda, K. (2002) Creation of a chain-like cationic iron species in montmorillonite as a highly active heterogeneous catalyst for alkane oyxgenations using

Ehrlich, H. L. (1996) How microbes influence mineral growth and dissolution. *Chemical Geology* **132**, 5-9.

Ehrlich, H. L. (1998) Geomicrobiology: its significance for geology. *Earth-Science Reviews* **45**, 45-60.

Elsass, F. (2006) Transmission electron microscopy. In: Bergaya, F., Theng, B. K. G., and Lagaly, G. (Eds.), *Handbook of clay science*. Elsevier, Oxford Amsterdam, pp. 939-963.

Emmerich, K. (2009) A contribution to the understanding of structure-functionality-relation of clay minerals and clays in technical and geotechnical applications. Habilitation Thesis, pp. 167. University of Karlsruhe.

Emmerich, K., Wolters, F., Kahr, G., and Lagaly, G. (2009) Clay profiling: The classification of montmorillonites. *Clays and Clay Minerals* **57**, 104-114.

Erb, W. J. and Krystek, M. P. (1996) Weighting function for the calculation of ISO brightness. *Tappi Journal* **79**, 279-282.

Ernstsen, V., Gates, W. P., and Stucki, J. W. (1998) Microbial reduction of structural iron in clays - A renewable source of reduction capacity. *Journal of Environmental Quality* **27**, 761-766.

Farmer, V. C. and Russell, J. D. (1964) The infrared spectra of layer silicates. *Spectrochimica Acta* **20**, 1149-1173.

Favre, F., Tessier, D., Abdelmoula, M., Genin, J. M., Gates, W. P., and Boinvin, P. (2002) Iron reduction and changes in cation exchange capacity in intermittently waterlogged soil. *European Journal of Soil Science* **53**, 175-183.

Favre, F., Bogdal, C., Gavillet, S., and Stucki, J. W. (2006) Changes in the CEC of a soil smectite-kaolinite clay fraction as induced by structural iron reduction and iron coatings dissolution. *Applied Clay Science* **34**, 95-104.

Ferrage, E., Lanson, B., Sakharov, B. A., and Drits, V. (2005) Investigation of smectite hydration properties by modeling experimental X-ray diffraction patterns: Part I. Montmorillonite hydration properties. *American Mineralogist* **90**, 1358-1374.

Ferrage, E., Kirk, C. A., Cressey, G., and Cuadros, J. (2007) Dehydration of Ca-montmorillonite at the crystal scale. Part I: Structure evolution. *American Mineralogist* **92**, 994-1006.

Frederickson, J. K., McKinley, J. P., Nierzwicki-Bauer, S. A., White, D. C., Ringelberg, D. B., Rawson, S. A., Li, S.-M., and Bjornstad, B. N. (1995) Microbial community structure and biogeochemistry of Miocene subsurface sediments: Implications for long-term microbial survival. *Molecular Ecology* **4**, 619-626.

Friedrich, S., Platonova, N. P., Karavaiko, G. I., Stichel, E., and Glombitza, F. (1991) Chemical and microbiological solubilization of silicates. *Acta Biotechnologica* **11**, 187-196.

Furukawa, Y. and O'Reilly, S. E. (2007) Rapid precipitation of amorphous silica in experimental systems with nontronite (NAu-1) and *Shewanella oneidensis* MR-1. *Geochimica et Cosmochimica Acta* **71**, 363-377.

Gaidzinski, R., Osterreicher-Cunha, P., Duailibi, J., and Tavares, L. M. (2009) Modification of clay properties by ageing: Role of indigenous microbiota and implications for ceramic processing. *Applied Clay Science* **43**, 98-102.

Gaite, J.-M., Ermakoff, P., Allard, T., and Muller, J. P. (1997) Paramagnetic $Fe^{3+}$: A sensitive probe for disorder in kaolinite. *Clays and Clay Minerals* **45**, 496-505.

Galán, E., Aparicio, P., Miras, A., Michailidis, K., and Tsirambides, A. (1996) Technical properties of compounded kaolin sample from Griva (Macedonia, Greece). *Applied Clay Science* **10**, 477-490.

Galán, E., Aparicio, P., González, I., and Miras, A. (1998) Contribution of multivariate analysis to the correlation of some properties of kaolin with its mineralogical and chemical composition. *Clay Minerals* **33**, 65-75.

Galazzo, J. L., Cerro, R. L., and Depetris, P. J. (1986) Factors affecting the physical and chemical properties of argentine kaolins. *Applied Clay Science* **1**, 255-264.

Gates, W. P. (2008) Cation mass-valence sum (CM-VS) approach to assigning OH-bending bands in dioctahedral smectites. *Clays and Clay Minerals* **56**, 10-22.

Gates, W. P., Wilkinson, H. T., and Stucki, J. W. (1993) Swelling properties of microbially reduced ferruginous smectite. *Clays and Clay Minerals* **41**, 360-364.

Gates, W. P., Jaunet, A.-M., Tessier, D., Cole, M. A., Wilkinson, H. T., and Stucki, J. W. (1998) Swelling and texture of iron-bearing smectites reduced by bacteria. *Clays and Clay Minerals* **46**, 487-497.

Glasauer, S., Weidler, P. G., Langley, S., and Beveridge, T. J. (2003) Controls on Fe reduction and mineral formation by a subsurface bacterium. *Geochimica et Cosmochimica* **67**, 1277-1288.

Göhlert, K. and Uebel, M. (2007) Test method for plasticity and extrusion behaviour. In: Händle, F. (Ed.), *Extrusion in Ceramics*. Springer, Berlin Heidelberg, pp. 347-362.

Goldstein, J., Newbury, D. E., Joy, D. C., Lyman, C. E., Echlin, P., Lifshin, E., Sawyer, L., and Michael, J. R. (1992) Scanning electron microscopy and X-ray microanalysis. Plenum Press, New York, pp. 820.

Goodhew, P. J., Humphreys, F. J., and Beanland, R. (2001) Electron microscopy and analysis. Taylor & Francis, London, pp. 251.

Goodman, B. A., Russell, J. D., Fraser, A. R., and Woodhams, F. D. (1976) A Mössbauer and IR spectroscopy study of the structure of nontronite. *Clays and Clay Minerals* **24**, 53-59.

Grafton, D. R. (1968) The effect of clay-adhesive interaction on the structure of coatings. The Institute of Paper Chemistry, Lawrence University, Wisconsin, Appleton, Wisconsin.

Grim, R. E. (1950) Modern concepts of clay materials. *Journal of Geology* **50**, 225-275.

Grim, R. E. (1968) Applied Clay Mineralogy. McGraw Hill, New York, pp. 422.

Grim, R. E. and Güven, N. (1978) Bentonites - Geology, Mineralogy, Properties and Uses. Elsevier, Amsterdam New York, pp. 256.

Grim, R. E., Bray, R. H., and Bradley, W. F. (1937) The mica and argillaceous sediments. *American Mineralogist* **22**, 813-829.

Grizelj, A., Tibljas, D., Kovacic, M., and Spanic, D. (2011) Diagenesis of Miocene pelitic sedimentary rocks in the Sava Depression (Croatia). *Clay Minerals* **46**, 59-72.

Groudev, S. N. (1987) Use of heterotrophic microorganisms in mineral biotechnology. *Acta Biotechnologica* **7**, 299-306.

Groudev, S. N. (2001) Biobeneficiation of mineral raw materials. In: Kawatra, S. K. and Natarajan, K. A. (Eds.), *Mineral biotechnology: Microbial aspects of mineral beneficiation, metal extraction, and environmental control*. Society for Mining, Metallurgy, and Exploration, Inc. (SME), Littleton, Colorado, pp. 263.

Gualtieri, A. F., Moen, A., and Nicholson, D. G. (2000) XANES study of the local environment of iron in natural kaolinites. *European Journal of Mineralogy* **12**, 17-23.

Guggenheim, S. and Martin, R. T. (1995) Definition of clay and clay mineral. Joint report of the AIPEA nomenclature and CMS nomenclature committees. *Clays and Clay Minerals* **43**, 255-256.

Guggenheim, S., Bain, D. C., Bergaya, F., Brigatti, M. F., Drits, V., Eberl, D. D., Formoso, M. L. L., Galán, E., Merriman, R. J., Peacor, D. R., Stanjek, H., and Watanabe, T. (2002) Report of the Association Internationale pour l'Etude des Argiles (AIPEA) Nomenclature Committee for 2001: Order, disorder and crystallinity in phyllosilicates and the use of the 'Cristallinity Index'. *Clay Minerals* **37**, 389-393.

Guggenheim, S., Adams, J. M., Bain, D. C., Bergaya, F., Brigatti, M. F., Drits, V. A., Formoso, M. L. L., Galán, E., Kogure, T., and Stanjek, H. (2006) Summary of recommendations of Nomenclature Committees relevant to clay mineralogy: Report of the Association Internationale pour l'Etude des Argiles (AIPEA) Nomenclature Committee for 2006. *Clays and Clay Minerals* **54**, 761-772.

Guo, M., Lin, Y., Xu, X., and Chen, Z. (2010) Bioleaching of iron from kaolin using Fe(III)-reducing bacteria with various carbon nitrogen sources. *Applied Clay Science* **48**, 379-383.

Guthrie, G. D. J. and Veblen, D. R. (1989) High-resolution transmission electron microscopy of mixed-layer illite/smectite: Computer simulations. *Clays and Clay Minerals* **37**, 1-11.

Gysau, D. (2006) Fillers for paints, *European Coatings Literature*. Vincentz Network GmbH & Co. KG, Hannover, Germany, pp. 199.

Harris, D. C. (1991) Quantitative chemical analysis. W.H. Freeman and Company, New York, pp. 782.

Harvey, C. C. and Lagaly, G. (2006) Clays in industry: Conventional applications. In: Bergaya, F., Theng, B. K. G., and Lagaly, G. (Eds.), *Handbook of clay science*. Elsevier, Oxford Amsterdam, pp. 501-540.

Haus, R. (2002) Zur Geologie und Mineralogie der Kaolinlagerstätte Hirschau-Schnaittenbach/Oberpfalz. In: Störr, M. (Ed.), *Kaolin-Ton-Feldspatbergbau und Keramik-Industrie der Oberpfalz*. Verlag der Gesellschaft für Geowissenschaften e.V., Berlin, pp. 19-30.

Hauser-Fuhlberg, M. (2005) Einlagerung von Initiator-/Monomer-Molekülen in Kaolinit für eine polymergesteuerte Delamination zur Herstellung von Nanokompositen, pp. 145. Universität Fridericiana Karlsruhe.

Hemminger, W. F. and Cammenga, H. K. (1989) Methoden der Thermischen Analyse. Anleitungen fur die chemische Laboratiumspraxis. Springer Verlag, Heidelberg, pp. 299.

Hendricks, S. B. and Teller, E. (1942) X-ray interference in partially ordered layer lattices. *Journal of Chemical Physics* **10**, 147-167.

Henningsen, D. (1981) Sedimentpetrographie. In: Bender, F. (Ed.), *Angewandte Geowissenschaften*. Enke, Stuttgart, pp. 295-310.

Henseleit, R. and Huber, S. (2002) Die Aufbereitung von Kaolin, Feldspat und Quarz in den Anlagen der Amberger Kaolinwerke Eduard Kick GmbH & Co. KG. In: Störr, M. (Ed.), *Kaolin-Ton-Feldspatbergbau und Keramik-Industrie der Oberpfalz*. Verlag der Gesellschaft für Geowissenschaften e.V., Berlin, pp. 31-48.

Herbillon, A. J., Mestagh, M. M., Vielvoye, L., and Derouane, E. G. (1976) Iron in kaolinite with special reference to kaolinite from tropical soils. *Clay Minerals* **11**, 201-220.

Hernandez, M. E., Kappler, A., and Newman, D. K. (2004) Phenazines and other redox-active antibiotics promote microbial mineral reduction. *Applied And Environmental Microbiology* **70**, 921-928.

Hillier, S. (2000) Accurate quantitative analysis of clay and other minerals in sandstones by XRD: comparison of a Rietveld and a reference intensity ratio (RIR) method and the importance of sample preparation. *Clay Minerals* **35**, 291-302.

Hiltmann, W. and Stribrny, B. (1998) Tonmineralogie und Bodenphysik. In: Hiltmann, W. and Stribrny, B. (Eds.), *Handbuch zur Erkundung des Untergrundes von Deponien und Altlasten*. Springer-Verlag, Berlin Heidelberg New York, pp. 297.

Hinckley, D. N. (1963) Variability in "crystallinity" values among the kaolin deposits of the coastal plain of Georgia and South Carolina. *Clays and Clay Minerals* **11**, 229-235.

Hofmann, U. (1961) Geheimnisse des Tons. *Berichte der Deutschen Keramischen Gesellschaft* **38**, 201-207.

Hofmann, U. (1962) Die Tonminerale und die Plastizität des Tons. *Keramische Zeitschrift* **14**, 14-19.

Hofmann, U. and Weiss, A. (1968) Röntgenographischer Nachweis der Tonminerale und der begleitenden Minerale. In: Bilke, W. (Ed.), *Handbuch der Keramik*. Verlag Schmid, Freiburg/Brsg.

Hofmann, U., Endell, K., and Wilm, D. (1933) Kristallstruktur und Quellung von Montmorillonit. *Zeitschrift für Kristallographie* **86**, 340-347.

Hölzgen, M. and Quirmbach, P. (2007) Additives for extrusion. In: Händle, F. (Ed.), *Extrusion in Ceramics*. Springer, Berlin Heidelberg, pp. 211-220.

Hotchkiss, R. (1994) Evaluation of pipet and X-ray procedures for determining particle-size distributions of sediment. U.S. Geological Survey, Office of Water Data Coordination, Reston, Virginia.

Howard, S. A. and Preston, K. D. (1989) Profile fitting of powder diffraction patterns. In: Bish, D. L. and Post, J. E. (Eds.), *Modern Powder Diffraction*. Mineralogical Society of America, Washington, D.C., pp. 217-276.

Hower, J., Eslinger, E., Hower, M., and Perry, E. (1976) Mechanism of burial metamorphism of argillaceous sediments: 1. Mineralogical and chemical evidence. *Geological Society of America Bulletin* **87**, 725-737.

Hubert, F., Caner, L., Meunier, A., and Lanson, B. (2009) Advances in characterization of soil clay mineralogy using X-ray diffraction: From decomposition to profile fitting. *European Journal of Soil Science* **60**, 1093-1105.

Huggett, J. M., McCarty, D. K., Calvert, C. C., Gale, A. S., and Kirk, C. (2006) Serpentine-nontronite-vermiculite mixed-layer clay from the Weches Formation, Claiborne Group, Middle Eocene, Northeast Texas. *Clays and Clay Minerals* **54**, 101-115.

Hughes, J. C. and Brown, G. (1979) A crystallinity index for soil kaolins and relation to parent rock, climate and soil maturity. *Journal of Soil Science* **30**, 557-563.

Hurst, V. J. and Pickering Jr, S. M. (1997) Origin and classification of coastal plain kaolins, Southeastern USA, and the role of groundwater and microbial action. *Clays and Clay Minerals* **45**, 274-285.

Iannicelli, J. (1976) High extraction magnetic filtration of kaolin clay. *Clays and Clay Minerals* **24**, 64-68.

Inoue, A. and Kitagawa, R. (1994) Morphological characteristics of illitic clay minerals from a hydrothermal system. *American Mineralogist* **79**, 700-711.

Inoue, A., Watanabe, T., Kohyama, N., and Brusewitz, A. (1990) Characterization of illitization of smectite in bentonite beds at Kinnekulle, Sweden. *Clays and Clay Minerals* **38**, 241-249.

ISO 2469 (2007) Paper, board, and pulps. Measurement of diffuse reflectance factor. *International Organization of Standardization*.

ISO 2470 (2009) Paper and board. Measurement of diffuse blue reflectance factor (ISO brightness). *International Organization for Standardization*.

Jadgozinski, H. (1949) Eindimensionale Fehlordnung in Kristallen und ihr Einfluss auf die Röntgeninterferenzen. I. Berechnung des Fehlordnungsgrades aus den Röntgenintensitäten. *Acta Crystallographica* **2**, 201-207.

Jaisi, D. P., Kukkadapu, R. K., Eberl, D. D., and Dong, H. (2005) Control of Fe(III) site occupancy on the rate and extent of microbial reduction of Fe(III) in nontronite. *Geochimica et Cosmochimica Acta* **69**, 5429-5440.

Jaisi, D. P., Dong, H., and Liu, C. (2007a) Influence of biogenic Fe(II) on the extent of microbial reduction of Fe(III) in clay minerals nontronite, illite, and chlorite. *Geochimica et Cosmochimica Acta* **71**, 1145-1158.

Jaisi, D. P., Dong, H., and Liu, C. (2007b) Kinetics analysis of microbial reduction of Fe(III) in nontronite. *Environmental Science and Technology* **41**, 2437-2444.

Jaisi, D. P., Dong, H., Kim, J. W., He, Z., and Morton, J. P. (2007c) Particle aggregation kinetics during microbial reduction of Fe(III) in nontronite. *Clays and Clay Minerals* **55**, 96-107.

Jansen, E., Schäfer, W., and Will, G. (1994) *R* values in analysis of powder diffraction data using Rietveld refinement. *Journal of Applied Crystallography* **27**, 492-496.

Jasmund, K. and Lagaly, G. (1993) Tonminerale und Tone: Struktur, Eigenschaften, Anwendungen und Einsatz in Industrie und Umwelt. Steinkopff, Darmstadt, pp. 490.

Jeanroy, E. and Guillet, B. (1981) The occurence of suspended ferruginous particles in pyrophosphate extracts of some soil horizons. *Geoderma* **26**, 95-105.

Jepson, W. B. (1984) Kaolins: Their properties and uses. *Philosophical Transactions of the Royal Society of London* **311**, 411-432.

Jepson, W. B. (1988) Structural iron in kaolinites and in associated ancillary minerals. In: Stucki, J. W., Goodman, B. A., and Schwertmann, U. (Eds.), *Iron in soils and clay minerals*. D. Riedel Publishing Company, Dordrecht, pp. 467-536.

Johnston, J. H. and Cardile, C. M. (1987) Iron substitution in montmorillonite, illite, and glauconite by $^{57}$Fe Mössbauer spectroscopy. *Clays and Clay Minerals* **35**, 170-176.

Kaisersberger, E. (1979) Gas analytical methods of thermal analysis in comparison. *Thermochimica Acta* **29**, 215-220.

Kämpfer, S. (1991) Biotechnology: State-of-the art and prospects for possible applications in ceramics technologies. *Tile & Brick International* **7**, 229-230.

Kashefi, K., Shelobolina, E. S., Elliott, W. C., and Lovley, D. R. (2008) Growth of thermophilic and hyperthermophilic Fe(III)-reducing microorganisms on a ferruginous smectite as the sole electron acceptor. *Applied And Environmental Microbiology* **74**, 251-258.

Kaufhold, S. (2001) Untersuchung zur Eignung von natürlich alterierten sowie mit Oxalsäure aktivierten Bentoniten als Bleicherde für Pflanzenöle. Doctoral Thesis, pp. 178. RWTH Aachen.

Kaufhold, S. and Penner, D. (2006) Applicability of the SER method for quality control of clays from the German 'Westerwald'. *Applied Clay Science* **32**, 53-63.

Kaufhold, S., Dohrmann, R., Ufer, K., and Meyer, F. M. (2002) Comparison of methods for the quantification of montmorillonite in bentonites. *Applied Clay Science* **22**, 145-151.

Khaled, E. M. and Stucki, J. W. (1991) Fe oxidation state effects on cation fixation in smectites. *Soil Science Society of America Journal* **55**, 550-554.

Kim, J., Dong, H., Seabaugh, J., Newell, S. W., and Eberl, D. D. (2004) Role of microbes in the smectite-to-illite reaction. *Science* **303**, 830-832.

Kim, J.-W., Furukawa, Y., Dong, H., and Newell, S. W. (2005) The effect of microbial Fe(III) reduction on smectite flocculation. *Clays and Clay Minerals* **53**, 572-579.

Kleeberg, R. (2005) Outcomes of the second Reynolds Cup in quantitative mineral analysis. In: Dohrmann, R. and Kaufhold, S. (Eds.), *Contributions of the annual meeting DTTG*, Celle, pp. 26-35.

Kleeberg, R. (2009a) State-of-the-art and trends in quantitative phase analysis of geological and raw materials. *Z. Kristallogr. Suppl.* **30**, 47-52.

Kleeberg, R. (2009b) Basics of the Rietveld method, BGMN/AutoQuan, *3rd International Workshop of the German Clay Group (DTTG)*. Institute for Geotechnical Engineering, ETH Zurich, pp.

Kogel, J. E., Pickering Jr, S. M., Shelobolina, E. S., Chowns, T., Yuan, J., and Avant Jr, D. M. (2002) The Georgia Kaolins: Geology and Utilization. Society for Mining, Metallurgy, and Exploration, Inc. (SME), Littleton, Colorado, pp. 84.

Komlos, J., Kukkadapu, R. K., Zachara, J. M., and Jaffe, P. R. (2007) Biostimulation of iron reduction and subsequent oxidation of sediment containing Fe-silicates and Fe-oxides: Effect of redox cycling on Fe(III) bioreduction. *Water Research* **41**, 2996-3004.

Konhauser, K. O. (1998) Diversity of bacterial iron mineralization. *Earth-Science Reviews* **43**, 91-121.

Köster, H. M. (1974) Ein Beitrag zur Geochemie und Entstehung der Oberpfälzischen Kaolin-Feldspat-Lagerstätten. *Geologische Rundschau* **63**, 655-689.

Köster, H. M. and Tillmann, H. (1975) Kaolin und Tonvorkommen in der Oberpflalz. *Der Aufschluß* **26**, 289-306.

Koster van Groos, A. F. and Guggenheim, S. (1984) The effect of pressure on the dehydration reaction of interlayer water in Na-montmorillonite (SWy-1). *American Mineralogist* **69**, 872-879.

Kostka, J. E. and Nealson, K. H. (1995) Dissolution and reduction of magnetite by bacteria. *Environmental Science & Technology* **29**, 2535-2540.

Kostka, J. E., Stucki, J. W., Nealson, K. H., and Wu, J. (1996) Reduction of structural Fe(III) in smectite by a pure culture of *Shewanella putrefaciens* strain MR-1. *Clays and Clay Minerals* **44**, 522-529.

Kostka, J. E., Haefele, E., Viehweger, R., and Stucki, J. W. (1999a) Respiration and dissolution of iron(III)-containing clay minerals by bacteria. *Environmental Science and Technology* **33**, 3127-3133.

Kostka, J. E., Wu, J., Nealson, K. H., and Stucki, J. W. (1999b) The impact of structural Fe(III) reduction by bacteria on the surface chemistry of smectite clay minerals. *Geochimica et Cosmochimica* **63**, 3705-3713.

Krasnodebska-Ostrega, B., Paldyna, J., Kowalska, J., Jedynak, L., and Golimowski, J. (2009) Fractionation study in bioleached metallurgy wastes using six-step sequential extraction. *Journal of Hazardous Materials* **167**, 128-135.

Kroll, J. M. and Borchert, W. (1969) Geologisch-petrographische Untersuchungen an westdeutschen Kaolinlagerstätten -VIII: Kaolinsandstein von Hischau-Schnaittenbach. *Berichte der Deutschen Keramischen Gesellschaft* **46**, 496-500.

Krolla-Sidenstein, P., Kaden, R., Emmerich, K., Petrick, K., He, L., and Gliemann, H. (2009) Methods characterising microbial community composition during clay maturation. In: Fiore, S., Belviso, C., and Giannossi, M. L. (Eds.), *14th International Clay Conference*, Castellaneta Marina, Italy, pp. 693.

Kromer, H. (1980) Tertiary clays in the Westerwald area. *Geologisches Jahrbuch, Reihe D* **Heft D39**, 69-84.

Kromer, H. and Schüller, K.-H. (1973) Eigenschaften von Kaolinen für die Keramik und als Füllstoff. *Ber. DKG* **50**, 39-41.

Kromer, H. and Rose, D. (1994) Der Einfluß des Stoffbestandes auf das Verflüssigungsverhalten von Tonen. *Ber. DKG* **71**, 245-249.

Kübler, B. (1964) Les argiles, indicateurs de metamorphisme. *Revue de l'Institut Francaise du Petrole* **19**, 1093-1112.

Kukkadapu, R. K., Zachara, J. M., Smith, S. C., Fredrickson, J. K., and Chongxuan, L. (2001) Dissimilatory bacterial reduction of Al-substituted goethite in subsurface sediments. *Geochimica et Cosmochimica Acta* **65**, 2913-2924.

Kukkadapu, R. K., Zachara, J. M., Fredrickson, J. K., McKinley, J. P., Kennedy, D. W., Smith, S. C., and Dong, H. (2006) Reductive biotransformation of Fe in shale-limestone saprolite containing Fe(III) oxides and Fe(II)/Fe(III) phyllosilicates. *Geochimica et Cosmochimica Acta* **70**, 3662-3676.

Kulikov, O. L. and Hornung, K. (2001) A simple geometrical solution to the surface fracturing problem in extrusion processes. *Journal of the Non-Newtonian Fluid Mechanics* **98**, 107-115.

Lagaly, G. (1981) Characterization of clays by organic compounds. *Clay Minerals* **16**, 1-21.

Lagaly, G. (1989) Principles of flow of kaolin and bentonite dispersions. *Applied Clay Science* **4**, 105-123.

Lagaly, G. (1993) Layer charge determination by alkylammonium ions. In: Mermut, A. R. (Ed.), *CMS Workshop Lectures*. The Clay Mineral Society, Boulder, CO.

Lagaly, G. (2006) Colloid clay science. In: Bergaya, F., Theng, B. K. G., and Lagaly, G. (Eds.), *Handbook of clay science*. Elsevier, Oxford Amsterdam, pp. 141-245.

Lahav, N. (1990) Preparation of stable suspensions of delaminated kaolinite by combined dimethylsulfoxide-ammonium fluoride treatment. *Clays and Clay Minerals* **38**, 219-222.

Lanson, B. (2005) Crystal structure of mixed-layer minerals and their X-ray identification: New insights from X-ray diffraction profile modeling. *Clay Science* **12**, 1-5.

Lanson, B., Sakharov, B. A., Claret, F., and Drits, V. (2009) Diagenetic smectite-to-illite transition in clay-rich sediments: A reappraisal of X-ray diffraction results using the multi-specimen method. *American Journal of Science* **6**, 476-516.

Lear, P. R. and Stucki, J. W. (1989) Effects of iron oxidation state on the specific surface area of nontronite. *Clays and Clay Minerals* **37**, 547-552.

Lee, E. Y., Cho, K.-S., and Ryu, H. W. (2002) Microbial refinement of kaolin by iron-reducing bacteria. *Applied Clay Science* **22**, 47-53.

Lee, J. H., Ahn, J. H., and Peacor, D. R. (1985) Textures in layered silicates; progessive changes through diagensis and low-temperature metamorphism. *Journal of Sedimentary Research* **55**, 532-540.

Lee, J. V., Gibson, D. M., and Shewan, J. M. (1977) A numerical taxonomic study of some *Pseudomonas*-like marine bacteria. *Journal of General Microbiology* **98**, 439-451.

Lee, K., Kostka, J. E., and Stucki, J. W. (2006) Comparisons of structural Fe reduction in smectites by bacteria and dithionite: An infrared spectroscopic study. *Clays and Clay Minerals* **54**, 195-208.

Li, Y. L., Zhang, G., Yang, J., Deng, B., and Vali, H. (2004) Dissolution of nontronite NAu-2 by a sulfate-reducing bacterium. *Geochimica et Cosmochimica Acta* **68**, 3251-3260.

Lide, D. R. (2009) CRC Handbook of Chemistry and Physics. Taylor and Francis, Boca Raton London New York, pp. 2804.

Lindberg, J. D., Douglass, R. E., and Garvey, D. M. (1994) Absorption-coefficient-determination method for particulate materials. *Applied Optics* **33**, 4314-4319.

Lindgreen, H., Jacobsen, H., and Jakobsen, H. J. (1991) Diagenetic structural transformations in North Sea Jurassic illite-smectite. *Clays and Clay Minerals* **39**, 54-69.

Lindgreen, H., Drits, V., Sakharov, B. A., Salyn, A. L., Wrang, P., and Dainyak, L. G. (2000) Illite-smectite structural changes during metamorphism in Cambrian Alum shales from the Baltic sea. *American Mineralogist* **85**, 1223-1238.

Lins, G. and Blazek, V. (1980) Die DIN-Farbenkarte 6164 zur anschaulichen Farbkennzeichnung bei der gerichtlichen Leichenöffnung. *Zeitschrift für Rechtsmedizin* **86**, 49-57.

Lippmann, F. (1960) Über eine Apparatur zur Differentialthermoanalyse (DTA). *Keramische Zeitschrift* **11**, 475-480, 524-528, 570-573.

Liu, C., Kota, S., Zachara, J. M., Fredrickson, J. K., and Brinkman, C. K. (2001) Kinetic analysis of the bacterial reduction of goethite. *Environmental Science & Technology* **35**, 2482-2490.

Liu, C.-L., Hart, N., and Peck Jr., H. D. (1982) Inorganic pyrophosphate: Energy source for sulfate-reducing bacteria of the Genus *Desulfotomaculum*. *Science* **23**, 363-364.

Liu, D. H. F. and Lipták, B. G. (1997) Environmental Engineers' Handbook. CRC Press, New York, pp. 1449.

Lombardi, G. (1980) For better Thermal Analysis. *International Conference on Thermal Analysis* (ICTA), Rome, pp. 24.

Loomis, G. A. (1938) Grain size of whiteware clays as determined by the Andreasen pipette. *Fortieth Annual Meeting of the American Ceramic Society*. The American Ceramic Society, New Orleans.

Lovley, D. R. and Philips, E. J. P. (1988) Novel mode of microbial energy metabolism: organic carbon oxidation coupled to dissimilatory reduction of iron or manganese. *Applied And Environmental Microbiology* **54**, 1472-1480.

Lovley, D. R., Coates, J. D., Blunt-Harris, E. L., Philips, E. J. P., and Woodward, J. C. (1996) Humic substances as electron acceptors for microbial respiration. *Nature* **382**, 445-448.

Luca, V. and Cardile, C. M. (1989) Improved detection of tetrahedral $Fe^{3+}$ in nontronite SWa-1 by Mössbauer spectroscopy. *Clay Minerals* **24**, 555-560.

Lutz, D. (2007) Scenarios of extrusion. In: Händle, F. (Ed.), *Extrusion in Ceramics*. Springer, Berlin Heidelberg, pp. 173-186.

Luu, Y.-S. and Ramsay, J. A. (2003) Review: Microbial mechanisms of accessing insoluble Fe(III) as an energy source. *World Journal of Microbiology & Biotechnology* **19**, 215-225.

MacEwan, D. M. C. (1956) Fourier transform methods for studying scattering from lamellar systems: I. A direct method for analyzing interstratified mixtures. *Kolloidzeitschrift* **149**, 96-108.

MacEwan, D. M. C. (1958) Fourier transform methods for studying scattering from lamellar systems: II. The calculation of X-ray diffraction effects for various types of interstratification. *Kolloidzeitschrift* **156**, 61-67.

Maciejewski, M., Müller, C. A., Tschan, R., Emmerich, W. D., and Baiker, A. (1997) Novel pulse thermal analysis method and its potential for investigating gas-solid reactions. *Thermochimica Acta* **295**, 167-182.

Madejová, J. (2003) FTIR techniques in clay mineral studies. *Vibrational Spectroscopy* **31**, 1-10.

Madejová, J., Komadel, P., and Cicel, B. (1994) Infrared study of octahedral site populations in smectites. *Clay Minerals* **29**, 319-326.

Malengreau, N., Muller, J. P., and Calas, G. (1994) Fe-speciation in kaolins; a diffuse reflectance study. *Clays and Clay Minerals* **42**, 137-147.

Malengreau, N., Muller, J. P., and Calas, G. (1995) Spectroscopic approach for investigating the status and mobility of Ti in kaolinitic minerals. *Clays and Clay Minerals* **43**, 615-621.

Malengreau, N., Bedidi, A., Muller, J. P., and Herbillon, A. J. (1996) Spectroscopic control of iron oxide dissolution in two ferralitic soils. *European Journal of Soil Science* **47**, 13-20.

Mandal, S. K. and Banerjee, P. C. (2004) Iron leaching from China clay with oxalic acid: effect of different physico-chemical parameters. *International Journal of Mineral Processing* **74**, 263-270.

Manfredini, T., Pellacani, G. C., Pozzi, P., and Bonamartini Corradi, A. (1990) Monomeric and oligomeric phosphates as deflocculants of concentrated aqueous clay suspensions. *Applied Clay Science* **5**, 193-201.

Martin, R. T., Bailey, S. W., Eberl, D. D., Fanning, D. S., Guggenheim, S., Kodama, H., Pevear, D. R., Środoń, J., and Wicks, F. J. (1991) Report of the Clay Minerals Society Nomenclature Committee: Revised classification of clay materials. *Clays and Clay Minerals* **39**, 333-335.

McCarty, D. K. (2002) Quantitative mineral analysis of clay-bearing mixtures: the Reynolds Cup contest. *International Union of Crystallography CPD Newsletter* **27**, 12-15.

McCarty, D. K., Drits, V. A., Sakharov, B. A., Zviagina, B. B., Ruffell, A., and Wach, G. (2004) Heterogeneous mixed-layer clays from the Cretaceous greensand, Isle of Wight, southern England. *Clays and Clay Minerals* **52**, 552-575.

McCarty, D. K., Sakharov, B. A., and Drits, V. A. (2008) Early clay diagenesis in gulf coast sediments: New insights from XRD profile modeling. *Clays and Clay Minerals* **56**, 359-379.

Mehra, O. P. and Jackson, M. L. (1960) Iron oxide removal from soils and clays by a dithionite-citrate system buffered with sodium bicarbonate. *Clays and Clay Minerals* **7**, 317-327.

Meier, L. P. and Kahr, G. (1999) Determination of the cation exchange capacity (CEC) of clay minerals using the complexes of copper (II) ion with triethylenetetramine and tetraethylenepentamine. *Clays and Clay Minerals* **47**, 386-388.

Menger-Krug, E., Kaden, R., Krolla-Sidenstein, P., Emmerich, K., Petrick, K., and Obst, U. (2008) Biological processes during maturation. In: Skowronski, A. (Ed.), *4th Mid-European Clay Conference*, Zakopane (Poland), pp. 113.

Méring, J. (1949) L'interprétation des rayons X dans les systèmes à stratification désordonnée. *Acta Crystallographica* **2**, 371-377.

Mermet, J.-M. and Poussel, E. (1995) ICP Emission Spectrometers: 1995 Analytical figures of merit. *Applied Spectroscopy* **49**, 12A-18A.

Mestdagh, M. M., Vielvoye, L., and Herbillon, A. J. (1980) Iron in kaolinite: II. The relationship between kaolinite crystallinity and iron content. *Clay Minerals* **15**, 1-13.

Meunier, A. (2005) Clays. Springer, Berlin Heidelberg New York, pp. 472.

Mitchell, M. (1998) An introduction to genetic algorithms. Bradford Book-The MIT Press, Cambridge, Massachusetts, pp. 221.

Möbius, C. H. (1977) Der Einfluß von Eisen und Titan auf den Weißgrad der Kaoline. *Das Papier* **31**, 223-228.

Mockovciaková, A., Styriaková, I., Skvarla, J., and Kozáková, I. (2008) Characterization of changes of low and high defect kaolinite alfter bioleaching. *Applied Clay Science* **39**, 202-207.

Moore, D. M. and Reynolds Jr., R. C. (1997) X-ray diffraction and the identification and analysis of clay minerals. Oxford University Press, New York, pp. 378.

Mörtel, H. and Heimstädt, K. (1996) Microbial problems in ceramic slurries and green bodies. In: Heitz, E., Flemming, C. A., and Sand, W. (Eds.), *Microbially influenced corrosion of materials*. Springer-Verlag, Berlin Heidelberg, pp. 360-375.

Mössbauer, R. (1958) Kernresonanzfluoreszenz von Gammastrahlung in $Ir^{191}$. *Zeitschrift für Physik* **151**, 124-143.

Müller-Vonmoos, M. and Loken, T. (1989) The shearing behaviour of clays. *Applied Clay Science* **4**, 125-141.

Müller-Vonmoos, M., Honold, P., and Kahr, G. (1985) Das Scherverhalten reiner Tone, *Mitteilungen des Instituts für Grundbau und Bodenmechanik*. ETH-Zürich, pp. 128.

Müller, B., Burgstaller, W., Strasser, H., Zanella, H., and Schinner, F. (1995) Leaching of zinc from an industrial filter dust with *Penicillium, Pseudomonas* and *Corynebacterium*: citric acid is the leaching agent rather than amino acids. *Journal of Industrial Microbiology & Biotechnology* **14**, 208-212.

Müller, W. (2008) Mechanische Grundoperationen und ihre Gesetzmäßigkeiten. Oldenbourg Wissenschaftsverlag, München, pp. 316.

Murad, E. (1987) Mössbauer spectra of nontronites: Structural implications and characterization of associated iron oxides. *Zeitschrift für Pflanzenernährung und Bodenkunde* **150**, 279-285.

Murad, E. (1988) Properties and behavior of iron oxides as determined by Mössbauer spectroscopy. In: Stucki, J. W., Goodman, B. A., and Schwertmann, U. (Eds.), *Iron in soils and clay minerals*. D. Reidel, Dordrecht, pp. 309-350.

Murad, E. (1999) Clays and clay minerals: What can Mössbauer spectroscopy do to help understand them? In: Kodama, H., Mermut, A. R., and Torrance, J. K. (Eds.), *Clays for our future-Proceedings of the 11th International Clay Conference, Ottawa, Canada, 1997*. ICC97 Organizing Committee, Ottawa, pp. 207-213.

Murray, H. H. (1980) Major kaolin processing developments. *International Journal of Mineral Processing* **7**, 263-274.

Murray, H. H. (1988) Kaolin minerals: Their genesis and occurrences. *Mineralogical Society of America Reviews in Mineralogy* **19**, 67-90.

Murray, H. H. (2000) Traditional and new applications for kaolin, smectite, and palygorskite: A general overview. *Applied Clay Science* **17**, 207-221.

Murray, H. H. (2007) Applied Clay Mineralogy. Occurences, processing and application of kaolins, bentonite, palygorskite-sepiolite, and common clays, *Developments in Clay Science*. Elsevier, Amsterdam, pp. 180.

Murray, H. H. and Keller, W. D. (1993) Kaolins, kaolins and kaolins. In: Murray, H. H., Bundy, W. M., and Harvey, C. C. (Eds.), *Kaolin genesis and utilization*. The Clay Minerals Society, Boulder Colorado, pp. 1-24.

Myers, C. R. and Nealson, K. H. (1990) Respiration-linked proton translocation coupled to anaerobic reduction of manganese(IV) and iron(III) in *Shewanella putrefaciens* MR-1. *Journal of Bacteriology* **172**, 6232-6238.

Nadeau, P. H. (1985) The physical dimension of fundamental clay particles. *Clay Minerals* **20**, 499-514.

Nadeau, P. H. (1987) Clay particle engineering: A potential new technology with diverse applications. *Applied Clay Science* **2**, 83-93.

Nadeau, P. H. (1998) Fundamental particles and the advancement of geoscience: response to "implications of TEM data for the concept of fundamental particles". *The Canadian Mineralogist* **36**, 1409-1414.

Nadeau, P. H., Tait, J. M., McHardy, W. J., and Wilson, M. J. (1984a) Interstratified XRD characteristics of physical mixtures of elementary clay particles. *Clay Minerals* **19**, 67-76.

Nadeau, P. H., Wilson, M. J., McHardy, W. J., and Tait, J. M. (1984b) Interstratified clays as fundamental particles. *Science* **225**, 923-925.

Nadeau, P. H., Wilson, M. J., McHardy, W. J., and Tait, J. M. (1984c) Interparticle diffraction: A new concept for interstratified clays. *Clay Minerals* **19**, 757-769.

Naguib, N. (2010) Synthese und Charakterisierung von hochporösen magnetischen Nanopartikeln auf der Basis von Montmorillonite. Doctoral Thesis, pp. 240. Universität Karlsruhe.

Nealson, K. H. and Saffarini, D. (1994) Iron and manganese in anaerobic respiration: Environmental significance, physiology, and regulation. *Annual Review of Microbiology* **48**, 311-343.

Nevin, K. P. and Lovley, D. R. (2000) Potential for nonenzymatic reduction of Fe(III) via electron shuttling in subsurface sediments. *Environmental Science & Technology* **34**, 2472-2478.

Nevin, K. P. and Lovley, D. R. (2002) Mechanisms for Fe(III) oxide reduction in sedimentary environments. *Geomicrobiological Journal* **19**, 141-159.

Niederbudde, E.-A., Stanjek, H., and Emmerich, K. (2002) Tonminerale Methodik. In: Blume, H. P., Felix-Henningsen, P., Fischer, W. R., Frede, H. G., Horn, R., and Stahr, K. (Eds.), *Handbuch der Bodenkunde*. ecomed Verlag, Landsberg, pp. 38.

Norrgran, D. A. and Orlich, J. N. (1988) Fundamentals of high intensity magnetic separation as applied to industrial minerals. *Minerals and Metallurgical Processing* **5**, 1-11.

Norrish, K. (1954) The swelling of montmorillonite. *Disc. Farad. Soc.* **18**, 120-134.

Oberlin, A. and Couty, R. (1970) Conditions of kaolinite formation during alteration of some silicates by water at 200 °C. *Clays and Clay Minerals* **18**, 347-356.

Odom, I. E. (1984) Smectite clay minerals: Properties and uses. *Philosophical Transactions of the Royal Society of London*. Series A, Mathematical and Physical Sciences **311**, 391-409.

Olson, G. J., Brierley, J. A., and Brierley, C. L. (2003) Bioleaching review part B: Progress in bioleaching: applications of microbial processes by the minerals industries. *Applied Microbiology and Biotechnology* **63**, 249-257.

Omotoso, O., McCarty, D. K., Hillier, S., and Kleeberg, R. (2006) Some successful approaches to quantitative mineral analysis as revealed by the 3rd Reynolds Cup Contest. *Clays and Clay Minerals* **54**, 748-760.

Ongley, E. D., Bynoe, M. C., and Percival, J. B. (1981) Physical and geochemical characteristics of suspended solids, Wilton Creek, Ontario. *Canadian Journal of Earth Science* **18**, 1365-1379.

O'Reilly, S. E., Furukawa, Y., and Newell, S. W. (2006) Dissolution and microbial Fe(III) reduction of nontronite (NAu-1). *Chemical Geology* **235**, 1-11.

Ortega, A. (1997) CRTA or TG? *Thermochimica Acta* **298**, 205-214.

Pansu, M. and Gautheyrou, J. (2006) Handbook of Soil Analysis. Springer-Verlag, Berlin Heidelberg New York, pp. 993.

Paterson, E. and Swaffield, R. (1987) Thermal Analysis. In: Wilson, M. J. (Ed.), *A Handbook of Determinative Methods in Clay Mineralogy*. Blackie & Son, London, pp. 99-132.

Penner, D. and Lagaly, G. (2001) Influence of anions on the rheological properties of clay mineral dispersions. *Applied Clay Science* **19**, 131-142.

Petit, S., Madejaová, J., Decarreau, A., and Martin, F. (1999) Characterization of octahedral substitutions in kaolinites using near infrared spectroscopy. *Clays and Clay Minerals* **47**, 103-108.

Petrick, K. (2007) Vergleich von STA-Messungen und FTIR-spektroskopischen Messungen zur Strukturbestimmung der Oktaederschicht von Montmorillonit. Diplomarbeit, pp. 165. Universität Karlsruhe (TH).

Petrick, K., Emmerich, K., Menger-Krug, E., Kaden, R., Dieterle, M., Kuch, P., Diedel, R., Peuker, M., and Krolla-Sidenstein, P. (2008) Why do two apparently similar German ceramic clays display different rheological properties during maturation? In: Skowronski, A. (Ed.), *4th Mid-European Clay Conference*, Zakopane, Poland, pp. 128.

Petrick, K., Diedel, R., Peuker, M., Dieterle, M., Kuch, P., Kaden, R., Krolla-Sidenstein, P., Schuhmann, R., and Emmerich, K. (2011) Character and amount of I-S mixed-layer minerals and physical-chemical parameters of two ceramic clays from Westerwald, Germany: Implications for processing properties. *Clays and Clay Minerals* **59**, 58-74.

Peuker, M., Diedel, R., Petrick, K., Menger-Krug, E., Kaden, R., Emmerich, K., Schuhmann, R., Dieterle, M., Kuch, P., Huber, S., Fischer, H., Beyer, D., Zehnsdorf, A., and Krolla-Sidenstein, P. (2009) Investigation of the clay maturing process as basis for property-enhancing utilization and control of microbiological reactions. In: Fiore, S., Belviso, C., and Giannossi, M. L. (Eds.), *14th International Clay Conference*, Castellaneta Marina, Italy, pp. 122.

Pevear, D. R. and Schuette, J. F. (1993) Inverting the NEWMOD X-ray Diffraction Forward Model for Clay Minerals Using Genetic Algorithms. In: Reynolds Jr. , R. C. and Walker, J. R. (Eds.), *CMS Workshop Lectures-Computer Applications to X-Ray Powder Diffraction Analysis of Clay Minerals*, Boulder, pp. 19-41.

Pfefferkorn, K. (1924) Ein Beitrag zur Bestimmung der Plastizität in Tonen und Kaolinen. *Sprechsaal* **57**, 297-299.

Phillips, E. J. P., Lovley, D. R., and Roden, E. E. (1993) Composition of non-microbially reducible Fe(III) in aquatic sediments. *Applied And Environmental Microbiology* **59**, 2727-2729.

Plancon, A. and Tchoubar, C. (1977) Determination of structural defects in phyllosilicates by X-ray diffraction. II. Nature and proportion of defects in natural kaolinites. *Clays and Clay Minerals* **25**, 436-450.

Plancon, A. and Zacharie, C. (1990) An expert system for the structural characterzation of kaolinites. *Clay Minerals* **25**, 249-260.

Plancon, A. and Drits, V. A. (2000) Phase analysis of clays using an expert system and calculation programs for X-ray diffraction by two- and three-component mixed-layer minerals. *Clays and Clay Minerals* **48**, 57-62.

Plancon, A., Giese, R. F., and Snyder, R. (1988) The Hinckley index for kaolinites. *Clay Minerals* **23**, 249-260.

Powell, P. S. (1996) Ball clay basics. *American Ceramic Society Bulletin* **75**, 74-76.

Pradhan, D., Pal, S., Sukla, L. B., Roy Chaudhury, G., and Das, T. (2008) Bioleaching of low-grade copper ore using indigenous microorganisms. *Indian Journal of Chemical Technology* **15**, 588-592.

Prasad, M. S., Reid, K. J., and Murray, H. H. (1991) Kaolin: processing, properties and applications. *Applied Clay Science* **6**, 87-119.

Raghavan, P., Chandrasekhar, S., and Damodaran, A. D. (1997) Value addition of paper coating grade kaolins by the removal of ultrafine coloring impurities. *International Journal of Mineral Processing* **50**, 307-316.

Ramamurthy, A. V. (1986) Wall slip in viscous fluids and influence of materials of construction. *Journal of Rheology* **30**, 337-357.

Rancourt, D. G. (1999) Mössbauer spectroscopy in clay science. In: Kodama, H., Mermut, A. R., and Torrance, J. K. (Eds.), *Clays for our future-Proceedings of the 11th International Clay Conference, Ottawa, Canada, 1997*. ICC97 Organizing Committee, Ottawa, pp. 201-205.

Rancourt, D. G., McDonald, A. M., Lalonde, A. E., and Ping, J. Y. (1993) Mössbauer absorber thickness for accurate site populations in Fe-bearing minerals. *American Mineralogist* **78**, 1-7.

Rand, B. and Melton, I. E. (1977) Particle interactions in aqueous kaolinite suspensions: I. Effect of pH and electrolyte upon the mode of particle interaction in homoionic sodium kaolinite suspensions. *Journal of Colloid and Interface Science* **60**, 308-320.

Reynolds, R. C. (1980) Interstratified clay minerals. In: Brindley, G. W. and Brown, G. (Eds.), *Crystal structures of clay minerals and their X-ray identification*. Mineralogical Society, London, pp. 249-304.

Reynolds, R. C. (1985) NEWMOD - A computer program for the calculation of one-dimensional X-ray diffraction patterns of mixed-layered clays, Hanover, NH, USA.

Reynolds Jr., R. C. (1992) X-ray diffraction studies of illite/smectite from rocks, <1 µm randomly oriented powders, and <1 µm oriented powder aggregates: The absence of laboratory-induced artifacts. *Clays and Clay Minerals* **40**, 387-396.

Reynolds, R. C. and Hower, J. (1970) The nature of interlayering in mixed-layer illite-montmorillonite. *Clays and Clay Minerals* **18**, 25-36.

Ribeiro, F. R., Fabris, J. D., Kostka, J. E., Komadel, P., and Stucki, J. W. (2009) Comparisons of structural iron reduced in smectites by bacteria and dithionite: II. A variable-temperature Mössbauer spectroscopic study of Garfield nontronite. *Pure Applied Chemistry* **81**, 1499-1509.

Rieder, M., Cavazzini, G., D'Yakonov, Y. S., Frank-Kamenetskii, V. A., Gottardi, G., Guggenheim, S., Koval, P. V., Müller, G., Neiva, A. M. R., Radoslovich, E. W., Robert, J.-L., Sassi, F. P., Takeda, H., Weiss, Z., and Wones, D. R. (1998) Nomenclature of the micas. *Clays and Clay Minerals* **46**, 586-595.

Rietveld, H. M. (1967) Line profiles of neutron powder-diffraction peaks for structure refinement. *Acta Crystallographica* **22**, 151-152.

Rietveld, H. M. (1969) A profile refinement method for nuclear and magnetic structures. *Journal of Applied Crystallography* **2**, 65-71.

Rimstidt, J. D. and Vaughan, D. J. (2003) Pyrite oxidation: A state-of-the-art assessment of the reaction mechanism. *Geochimica et Cosmochimica Acta* **67**, 873-880.

Roden, E. E. and Zachara, J. M. (1996) Microbial reduction of crystalline iron(III) oxides: Influence of oxide surface area and potential for cell growth. *Environmental Science & Technology* **30**, 1618-1628.

Rösler, H. J. (1991) Lehrbuch der Mineralogie. Deutscher Verlag für Grundstoffindustrie, Leipzig, pp. 844.

Roy, A., Singh, S. K., Banerjee, P. C., Dana, K., and Das, S. K. (2010) Bio-beneficiation of kaolin and feldspar and its effect on fired characteristics of triaxial porcelain. *Bulletin of Material Science* **33**, 333-338.

Royer, R. A., Burgos, W. D., Fisher, A. S., Unz, R. F., and Dempsey, B. A. (2002a) Enhancement of biological reduction of hematite by electron shuttling and Fe(II) complexation. *Environmental Science & Technology* **36**, 1939-1946.

Ryu, H. W., Cho, K.-S., Chang, Y. K., Kim, S. D., and Mori, T. (1995) Refinement of low-grade clay by microbial removal of sulfur and iron compounds using *Thiobacillus ferrooxidans*. *Journal of Fermentation and Bioengineering* **80**, 46-52.

Sakharov, B. A., Lindgreen, H., Salyn, A. L., and Drits, V. A. (1999) Determination of illite-smectite structures using multispecimen X-ray diffraction profile fitting. *Clays and Clay Minerals* **47**, 555-566.

Saller, M. (1999) Germany's minerals reviewed. *Industrial Minerals* **383**, 25-39.

Salmang, H. and Scholze, H. (2007) Keramik. In: Telle, R. (Ed.). Springer-Verlag, Berlin Heidelberg, pp. 1148.

Sánchez, C. J., Parras, J., and Carretero, M. I. (2002) The effect of maturation upon the mineralogical and physicochemical properties of illitc-smectitic clays for pelotherapy. *Clay Minerals* **37**, 457-463.

Sarikaya, Y. and Staley, J. T. (1994) Design and processing of materials by biomimicking, *3rd year's report*. University of Washington, Seattle, pp. 63.

Sawhney, B. L. (1972) Selective sorption and fixation of cations by clay minerals: A review. *Clays and Clay Minerals* **20**, 93-100.

Schejbal, F. (1978) Westerwälder Tone heute, Teil 4: Der Wettbewerb, die Zukunftsaussichten. *Keramische Zeitschrift* **30**, 362-364.

Schmidt, H. (1979) Physikalische und chemische Untersuchungsverfahren in der Grobkeramik. *Sprechsaal* **112**, 477-484.

Schmidt, H. (1981) Chemische und physikalische Reaktionen in grobkermischen Scherben beim Brennen. *Ziegelindustrie* **34**, 387-397, 431-442.

Schreyer, W., Medenbach, O., Abraham, K., Gerbert, W., and Müller, W. F. (1982) Kulkeite, a new metamorphic phyllosilicate mineral: Ordered 1:1 chlorite/talc mixed-layer. *Contributions to Mineralogy and Petrology* **80**, 103-109.

Schroeder, P. A. and Pruett, R. J. (1996) Fe ordering in kaolinite: Insights from $^{29}$Si and $^{27}$Al MAS NMR spectroscopy. *American Mineralogist* **81**, 26-38.

Schroeder, P. A., Pruett, R. J., and Hurst, V. J. (1998) Effects of secondary iron phases on kaolinite $^{27}$Al MAS NMR spectra. *Clays and Clay Minerals* **46**, 429-435.

Schüller, K.-H. (1980) Die Bedeutung untergeordneter Bestandteile bei technologischen Prozessen. *Fortschr. Mineral.* **58**, 79-105.

Schwertmann, U. (1988) Occurence and formation of iron oxides in various pedoenvironments. In: Stucki, J. W., Goodman, B. A., and Schwertmann, U. (Eds.), *Iron in soils and clay minerals*. D. Reidel, Dordrecht, pp. 267-308.

Schwertmann, U., Friedl, J., Pfab, G., and Gehring, A. U. (1995) Iron substitution in soil and synthetic anatase. *Clays and Clay Minerals* **43**, 599-606.

Scott, R. P. W. (1995) Technique and practice of chromatography, *Chromatographic science series*. Marcel Dekker, INC, New York, pp. 416.

Seabaugh, J. L., Dong, H., Kukkadapu, R. K., Eberl, D. D., Morton, J. P., and Kim, J. W. (2006) Microbial reduction of Fe(III) in the Fithian and Muloorina illites: Contrasting extents and rates of bioreduction. *Clays and Clay Minerals* **54**, 67-79.

Shau, Y.-H., Peacor, D. R., and Essene, E. J. (1990) Corrensite and mixed-layer chlorite-corrensite in metabasalts from Northern Taiwan: TEM/AEM, EMPA, XRD and optical studies. *Contributions to Mineralogy and Petrology* **105**, 123-142.

Shelobolina, E. S., Vanpraagh, C. G., and Lovley, D. R. (2003) Use of ferric and ferrous iron containing minerals for respiration by *Desulfitobacterium frappieri*. *Geomicrobiology Journal* **20**, 143-156.

Shelobolina, E. S., Anderson, R. T., Vodyanitskii, Y. N., Sivtsov, A. V., Yuretich, R., and Lovley, D. R. (2004) Importance of clay size minerals for Fe(III) respiration in a petroleum-contaminated aquifer. *Geobiology* **2**, 67-76.

Shelobolina, E. S., Pickering Jr, S. M., and Lovley, D. R. (2005) Fe-cycle bacteria from industrial clays mined in Georgia, USA. *Clays and Clay Minerals* **53**, 580-586.

Shen, S. and Stucki, J. W. (1994) Effects of iron oxidation state on the fate and behaviour of potassium in soils. In: Havlin, J. L. and Jacobsen, J. S. (Eds.), *Soil Testing: Prospects for Improving Nutrient Recommendations*. Soil Science of America, SSSA Special Publication, Madison, Wisconsin, pp. 173-185.

Shutov, V., Drits, V., and Sakharov, B. A. (1969) On the mechanism of a postsedimentary transformation of montmorillonite into hydromica, *Proceedings of the International Clay Conference*. Israel University Press, Tokyo, pp. 523-531.

Siewert, C. (1995) Ökosystemorientierte Grundlagen der Humusqualitätsbestimmung, Teil 3 (Methodische Grundlagen): Veränderungen thermogravimetrischer Charakteristika der organischen Bodensubstanz bei biologischer Umsetzung. *Archives of Agronomy and Soil Science* **39**, 53-68.

Skopp, J. M. (2002) Physical properties of primary particles. In: Warrick, A. W. (Ed.), *Soil physics companion*. CRC Press, Boca Raton, pp. 389.

Smith, D. K., Johnson Jr, G. G., Scheible, W., Wims, A. M., Johnson, J. L., and Ullmann, G. (1987) Quantitative powder diffraction method using the full diffraction pattern. *Powder Diffraction* **2**, 73-77.

Smykatz-Kloss, W. (1974) Differential Thermal Analysis. Springer-Verlag, Berlin Heidelberg, pp. 185.

Środoń, J. (1981) X-ray identification of randomly interstratified illite-smectite in mixtures with discrete illite. *Clay Minerals* **16**, 297-304.

Środoń, J. (1999) Nature of mixed-layer clays and mechanisms of their formation and alteration. *Annual Review of Earth and Planetary Sciences* **27**, 19-53.

Środoń, J. (2006) Identification and quantitative analysis of clay minerals. In: Bergaya, F., Theng, B. K. G., and Lagaly, G. (Eds.), *Handbook of clay science*. Elsevier, Oxford Amsterdam, pp. 765-787.

Środoń, J. and Eberl, D. D. (1984) Illite. In: Bailey, S. W. (Ed.), *Micas*. Mineralogical Society of America, Washington D.C., pp. 495-544.

Środoń, J., Morgan, D. J., Eslinger, E., Eberl, D. D., and Karlinger, M. (1986) Chemistry of illite-smectite and end-member illite. *Clays and Clay Minerals* **34**, 368-378.

Środoń, J., Andreoli, C., Elsass, F., and Robert, M. (1990) Direct high-resolution transmission electron microscopic measurement of expandability of mixed-layer illite/smectite in bentonite rock. *Clays and Clay Minerals* **38**, 373-379.

Środoń, J., Elsass, F., McHardy, W. J., and Morgan, D. J. (1992) Chemistry of illite-smectite inferred from TEM measurements of fundamental particles. *Clay Minerals* **27**, 137-158.

Środoń, J., Drits, V., McCarty, D. K., Hsieh, J. C. C., and Eberl, D. D. (2001) Quantitative X-ray diffraction analysis of clay-bearing rocks from random preparations. *Clays and Clay Minerals* **49**, 514-528.

Stanjek, H. and Marchel, C. (2008) Linking the redox cycles of Fe oxides and Fe-rich clay minerals: an example from a palaeosol of the Upper Freshwater Molasse. *Clay Minerals* **43**, 69-82.

Steudel, A. (2008) Selection strategy and modification of layer silicates for technical applications. Doctoral Thesis, pp. 258. Universität Karlsruhe.

Stixrude, L. and Peacor, D. R. (2002) First-principles study of illite-smectite and implications for clay mineral systems. *Nature* **420**, 165-168.

Stokes, G. G. (1845) On the theories of the internal friction in fluids in motion, and of the equilibrium and motion of elastic solids. *Transactions, Cambridge Philosophical Society* **8**, 287-342.

Störr, M. (1983) Die Kaolinlagerstätten der Deutschen Demokratischen Republik, *Schriftenreihe für geologische Wissenschaften*. Akademie Verlag, Berlin, pp. 226.

Störr, M. and Schwerdtner, G. (1979) Geologie, Mineralogie und Technologie der DDR. *Zeitschrift für Angewandte Geologie* **25**, 505-514.

Strunz, H. (1941) Mineralogische Tabellen. Eine Klassifikation der Mineralien auf kristallchemischer Grundlage. Akademische Verlagsgesellschaft, Leipzig, pp. 287.

Stubican, V. and Roy, R. (1961) A new approach to assignment of infrared absorption bands in layer-structure silicates. *Z. Kristallogr.* **15**, 200-214.

Stucki, J. W. (1988) Iron in smectites. In: Stucki, J. W., Goodman, B. A., and Schwertmann, U. (Eds.), *Iron in soils and clay minerals*. D. Reidel, Dordrecht, pp. 625-675.

Stucki, J. W. (2006) Properties and behavior of clay minerals. In: Bergaya, F., Theng, B. K. G., and Lagaly, G. (Eds.), *Handbook of clay science*. Elsevier, Oxford Amsterdam, pp. 423-475.

Stucki, J. W. (2009) Iron redox reactions in smectites, *46th Clay Minerals Society Annual Meeting*, Billings, Montana, pp. 47.

Stucki, J. W. (2011) A review of the effects of iron redox cycles on smectite properties. *C.R. Geoscience* **343**, 199-209.

Stucki, J. W. and Lear, P. R. (1989) Variable oxidation states of Fe in the crystal structure of smectite clay minerals. In: Coyne, L. M., McKeever, S. W. S., and Blake, D. E. (Eds.), *Spectroscopic characterization of minerals and their surfaces*. American Chemical Society, Washington, pp. 330-358.

Stucki, J. W. and Kostka, J. E. (2006) Microbial reduction of iron in smectite. *Comptes Rendus Geoscience* **338**, 468-475.

Stucki, J. W., Lee, K., Goodman, B. A., and Kostka, J. E. (2007) Effects of in situ biostimulation on iron mineral speciation in a sub-surface soil. *Geochimica et Cosmochimica Acta* **71**, 835-843.

Styriaková, I. and Styriak, I. (2000) Iron removal from kaolins by bacterial leaching. *Ceramics-Silikáty* **44**, 135-141.

Styriaková, I. and Lovás, M. (2007) Biological purification of silicate minerals. *Advanced Materials Research* **20-21**, 126-129.

Styriaková, I., Styriak, I., Nandakumar, M. P., and Mattiasson, B. (2003) Bacterial destruction of mica during bioleaching of kaolin and quartz sands by *Bacillus cereus*. *World Journal of Microbiology & Biotechnology* **19**, 583-590.

Sukla, L. B., Panchanadikar, V. V., and Kar, R. N. (1993) Microbial leaching of lateric nickel ore. *World Journal of Microbiology & Biotechnology* **9**, 255-257.

Taboada, J., Rivas, T., Saavedra, M. A., Araújo, M., and Argüelles, A. (2006) A fuzzy expert system application to the evaluation of ceramic- and paper-quality kaolin. *Applied Clay Science* **33**, 287-297.

Talibudeen, O. and Goulding, K. W. T. (1983) Apparent charge heterogeneity in kaolins in relation to their 2:1 phyllosilicate content. *Clays and Clay Minerals* **31**, 137-142.

Taylor, G. L., Ruotsala, A. P., and Keeling, R. O. (1968) Analysis of iron in layer silicates by Mössbauer spectroscopy. *Clays and Clay Minerals* **16**, 381-391.

Taylor, J. C. (1985) Technique and performance of powder diffraction in crystal structure studies. *Australian Journal of Physics* **38**, 519-538.

Thamdrup, B. (2000) Bacterial manganese and iron reduction in aquatic sediments. In: Schink, B. (Ed.), *Advances in microbial ecology*. Kluwer/Plenum, New York, pp. 41-84.

Theng, B. K. G., Churchman, G. J., Whitton, J. S., and Claridge, G. G. C. (1984) Comparison of intercalation methods for differentiating halloysite from kaolinite. *Clays and Clay Minerals* **32**, 249-258.

Tomita, T., Kawasaki, S., Nagaoka, T., Sato, K., and Watari, K. (2008) Environmentally benign processing of ceramics by extrusion with various clay minerals as inorganic binders. *Journal of the Ceramic Society of Japan* **116**, 224-229.

Toro, L., Paponetti, B., Veglio, F., and Marabini, A. (1992) Removal of iron from kaolin ores using different microorganisms. The role of organic acids and ferric iron reductase. *Particulate Science and Technology* **10**, 201-208.

Tributh, H. and Lagaly, G. (1986) Aufbereitung und Identifizierung von Boden- und Lagerstättentonen. II. Korngrößenanalyse und Gewinnung der Tonsubfraktionen. *GIT Fachzeitschrift für das Laboratorium* **30**, 771-776.

Tricky, R. (1973) Mise auf point d'une technique de coupes minces pour l'étude des minéraux argileux par microscopie et microdiffraction électronique. PhD thesis, pp. 143. Louis Pasteur University.

Tsipursky, S. and Drits, V. A. (1984) The distribution of octahedral cations in the 2:1 layers of dioctahedral smectites. *Clay Minerals* **19**, 177-193.

Ufer, K., Roth, G., Kleeberg, R., Stanjek, H., Dohrmann, R., and Bergmann, J. (2004) Description of X-ray powder pattern of turbostratically disordered layer structures with a Rietveld compatible approach. *Zeitschrift für Kristallographie* **219**, 519-527.

Ufer, K., Stanjek, H., Roth, G., Dohrmann, R., Kleeberg, R., and Kaufhold, S. (2008) Quantitative phase analysis of bentonites by the Rietveld method. *Clays and Clay Minerals* **56**, 272-282.

Ufer, K., Kleeberg, R., Bergmann, J., and Dohrmann, R. (2009) Structurally based modelling of the X-ray diffraction patterns of illite/smectite mixed layer minerals within the Rietveld method. In: Fiore, S., Belviso, C., and Giannossi, M. L. (Eds.), *14th International Clay Conference*, Castellaneta Marina, Italy, pp. 603.

Ulery, A. L. and Drees, L. R. (2008) Methods of soil analysis: Mineralogical methods, *SSSA Book Series*. Soil Science Society of America, Madison, Wisconsin, pp. 677.

van Olphen, H. (1977) An introduction to clay colloid chemistry: For clay technologists, geologists, and soil scientists. Wiley, New York, pp. 318.

Velde, B. and Meunier, A. (2008) The origin of clay minerals in soils and weathered rocks. Springer-Verlag, Berlin Heidelberg, pp. 406.

Venugopal, B. R., Ravishankar, N., and Rajamathi, M. (2008) Interstratification of trioctahedral and dioctahedra smectites through delamination and costacking. *Journal of Colloid and Interface Science* **324**, 80-84.

Vogt, S. and Vogt, R. (2004) Relationship between minerals and the industrial manufacturing properties of natural clay deposits and the clay bodies produced from them for the heavy clay industrie: Part 2. Manufacturing properties, utilization estimates and clay body optimization. In: Müller, W. and Fischer, A. (Eds.), *Z.I. Jahrbuch*, pp. 78-103.

Wagner, F. E. and Kyek, A. (2004) Mössbauer spectroscopy in archeology: Introduction and experimental considerations. *Hyperfine Interactions* **154**, 5-33.

Walling, D. E. and Moorehead, P. W. (1989) The particle size characteristics of fluvial suspended sediment: An overview. *Hydrobiologia* **176/177**, 125-149.

Watson, J. H. P. (1994) Status of superconducting magnetic separation in the minerals industry. *Minerals Engineering* **7**, 737-746.

Weaver, C. E. (1976) The nature of $TiO_2$ in kaolinite. *Clays and Clay Minerals* **24**, 215-218.

Weaver, C. E., Wampler, J. M., and Pecuil, T. E. (1967) Mössbauer analysis of iron in clay minerals. *Science* **156**, 504-508.

Webb, P. A. (2004) The perseverance of the sedigraph method of particle sizing. Micrometrics.

Weber, K. A., Achenbach, L. A., and Coates, J. D. (2006) Microorganisms pumping iron: anaerobic mocrobial iron oxidation and reduction. *Nature* **4**, 752-764.

Weiss, A. (1958) Über das Kationenaustauschvermögen der Tonminerale II. Der Kationenaustausch bei den Glimmer-, Vermikulit- und Montmorillonitgruppe. *Zeitschrift für Anorganische und Allgemeine Chemie* **297**, 257-286.

Weiss, A. (1963) Ein Geheimnis des chinesischen Porzellans. *Angewandte Chemie* **75**, 755-762.

Weiss, A. (1989) About sealing of waste disposals by clays with special consideration of organic compounds in percolating water. *Applied Clay Science* **4**, 193-209.

Weiss, A. and Frank, R. (1961) Über den Bau der Gerüste in thixotropen Gelen. *Zeitschrift für Naturforschung* **16b**, 141-142.

Weiss, A. and Russow, J. (1963) Über die Lage der austauschbaren Kationen bei Kaolinit, *Proceedings of the International Clay Conference*, Stockholm, pp. 203-213.

White, W. A. (1949) Atterberg plastic limits of clay minerals. *American Mineralogist* **34**, 508-512.

Whitney, G. and Northrop, H. R. (1987) Diagenesis and fluid flow in the San Juan Basin, New Mexico -regional zonation in the mineralogy and stable isotope composition of clay minerals in sandstone. *American Journal of Science* **287**, 353-382.

Whittaker, H. (1939) Effect of particle size on plasticity of kaolinite. *Journal of the American Ceramic Society* **22**, 16-23.

Wiegmann, J., Kranz, G., Horte, C.-H., Graul, J., and Doberenz, C. (1978) Beziehungen zwischen den petrologischen Charakteristika und den keramisch-technischen Eigenschaften von Kaolinen mit nennenswerten Gehalten an Illit-Smectit-Wechsellagerungsmineralen. *Silikattechnik* **29**, 263-267.

Wiles, D. B. and Young, R. A. (1981) A new computer program for Rietveld analysis of X-ray powder diffraction patterns. *Journal of Applied Crystallography* **14**, 149-151.

Will, G. (2006) Powder Diffraction: The Rietveld method and the Two-Stage method. Springer-Verlag, Berlin Heidelberg, pp. 224.

Wingender, J., Neu, T. R., and Flemming, H.-C. (1999) Microbial extracellular polymeric substances. Characterization, structure and function. Springer-Verlag, Berlin Heidelberg New York, pp. 258.

Winkler, H. G. F. (1954) Bedeutung der Korngrößenverteilung auf die stofflichen Eigenschaften grobkeramischer Erzeugnisse. *Ber. Dtsch. Keram. Ges.* **31**, 337-343.

Wloka, M., Rehage, H., Flemming, H.-C., and Wingender, J. (2004) Rheological properties of viscoelastic biofilm extracellular polymeric substances and comparison to the behavior of calcium alginate gels. *Colloid and Polymer Science* **282**, 1067-1076.

Wolters, F. (2005) Classification of montmorillonites. PhD thesis, pp. 169. Universität Karlsruhe.

Wolters, F., Lagaly, G., Kahr, G., Nüesch, R., and Emmerich, K. (2009) A comprehensive characterization of dioctahedral smectites. *Clays and Clay Minerals* **57**, 115-133.

Worrall, W. E. (1986) Clays and ceramic raw materials. Elsevier Applied Science Publishers Ltd, Barking, pp. 260.

Wu, J., Roth, C. B., and Low, P. F. (1988) Biological reduction of structural iron in sodium-nontronite. *Soil Science Society of America Journal* **52**, 295-296.

Yau, Y., Peacor, D. R., and McDowell, S. (1987) Smectite-to-illite reactions in Salton Sea shales: A transmission and analytical electron microscopy study. *Journal of Sedimentary Petrology* **57**, 335-342.

Young, R. A. (1995) The Rietveld method. Oxford University press, Oxford New York, pp.298.

Zachara, J. M., Fredrickson, J. K., Li, S. W., Kennedy, D. W., Smith, S. C., and Gassman, P. L. (1998) Bacterial reduction of crystalline Fe(III) oxides in single phase suspensions and subsurface materials. *American Mineralogist* **83**, 1426-1443.

Zeelmaekers, E., McCarty, D. K., and Mystkowski, K. (2007) SYBILLA. Chevron Energy Technology Company, Houston, Texas.

Zegeye, A., Fialips, C., White, M., Manning, D. A. C., and Gray, N. (2008) Refinement of kaolin and silica sand by microbial removal of iron impurities. *Geochimica et Cosmochimica Acta* **72**, A1072.

Zhang, G., Kim, J., Dong, H., and Sommer, A. J. (2007a) Microbial effects in promoting the smectite to illite reaction: Role of organic matter intercalated in the interlayer. *American Mineralogist* **92**, 1401-1410.

Zhang, G., Dong, H., Kim, J., and Eberl, D. D. (2007b) Microbial reduction of structural $Fe^{3+}$ in nontronite by a thermophilic bacterium and its role in promoting the smectite to illite reaction. *American Mineralogist* **92**, 1411-1419.

Zimmerley, S. R., Wilson, D. G., and Prater, J. D. (1958) Cycling leaching process employing iron oxidizing bacteria, *US Patent 2,829,964*, USA.

# 9 Appendix

Table 9.1: Water chemistry analysis of tap water used for sample preparation of the paper kaolins. Data source: Water works of Leipzig (KWL-Kommunale Wasserwerke Leipzig).

| Species | concentration [mg/L] | | |
|---|---|---|---|
| $Na^+$ | 28 | pH | 7.73 |
| $Mg^{2+}$ | 17 | σ | 610 µS/cm |
| $Ca^{2+}$ | 83,7 | hardness | 15.8 °dH * |
| $Fe^{2+/3+}$ | 0,02 | | |
| $Mn^{2+}$ | <0,005 | | |
| $F^-$ | 0,44 | | |
| $Cl^-$ | 43,3 | | |
| $NO^{3-}$ | 20,7 | | |
| $SO_4^{2-}$ | 189 | | |

* °dH: German degrees of hardness (Deutsche Grad Wasserhärte). 1 °dH = 17.848 mg/L $CaCO_3$.

Table 9.2a: Relative deviations between chemical composition, calculated from Rietveld analysis and measured by XRF (XRD-XRF), and between the adapted values and XRF (XRD-XRF adapted), and between the XRD adapted values and STA measurements (XRD-XRF-STA) of the kaolin sample LA540 and of the grain-size fractionated material.

| | | deviations [%] | | | | | | | | |
|---|---|---|---|---|---|---|---|---|---|---|
| LA540 | crosscheck | $SiO_2$ | $Al_2O_3$ | $Fe_2O_3$ | MgO | CaO | $Na_2O$ | $K_2O$ | $TiO_2$ | $P_2O_5$ |
| bulk | XRD-XRF | -0.45 | -2.58 | 1.37 | 0.62 | 0.19 | 0.08 | 0.00 | 0.42 | 0.34 |
| | XRD-XRF adapted | 0.61 | -0.87 | 1.39 | 0.64 | 0.04 | 0.08 | 0.12 | 0.00 | 0.00 |
| | XRD-XRF-STA | 0.61 | -0.87 | 1.39 | 0.64 | 0.04 | 0.08 | 0.12 | 0.00 | 0.00 |
| >20 µm | XRD-XRF | -1.77 | -3.74 | 2.04 | 0.85 | 0.19 | 0.03 | 1.33 | 0.58 | 0.48 |
| | XRD-XRF adapted | 0.00 | 0.01 | 2.06 | 0.87 | -0.02 | 0.03 | 0.00 | 0.00 | 0.01 |
| | XRD-XRF-STA | n.d. | n.d. | n.d. | n.d. | n.d. | n.d. | n.d. | n.d. | n.d. |
| 2-20 µm | XRD-XRF | 0.91 | -2.19 | 0.44 | 0.12 | 0.06 | 0.06 | 0.35 | 0.28 | 0.07 |
| | XRD-XRF adapted | 0.11 | -0.22 | 0.45 | 0.13 | 0.03 | 0.06 | 0.08 | 0.00 | 0.01 |
| | XRD-XRF-STA | 0.00 | -0.73 | 0.41 | 0.09 | 0.03 | 0.06 | 0.06 | 0.00 | 0.01 |
| 0.6-2 µm | XRD-XRF | -0.83 | -1.10 | 1.10 | 0.43 | 0.19 | 0.06 | -0.19 | 0.27 | 0.69 |
| | XRD-XRF adapted | 0.00 | -0.32 | 1.11 | 0.44 | -0.10 | 0.06 | 0.09 | 0.00 | 0.06 |
| | XRD-XRF-STA | 0.00 | -1.46 | 0.97 | 0.30 | -0.10 | 0.06 | 0.01 | 0.00 | 0.06 |
| 0.2-0.6 µm | XRD-XRF | 1.62 | -6.08 | 3.81 | 1.78 | 0.56 | 0.00 | 3.23 | -0.51 | 0.40 |
| | XRD-XRF adapted | 0.00 | 0.29 | 3.56 | 1.53 | 0.38 | 0.00 | -0.04 | 0.00 | 0.00 |
| | XRD-XRF-STA | 0.00 | 0.29 | 3.56 | 1.53 | 0.38 | 0.00 | -0.04 | 0.00 | 0.00 |
| <0.2 µm | XRD-XRF | 0.67 | -8.85 | 4.13 | 2.22 | 0.66 | 0.55 | 1.57 | -0.69 | -0.26 |
| | XRD-XRF adapted | 0.00 | 0.11 | 3.68 | 1.76 | 0.78 | 0.55 | -0.03 | 0.00 | 0.00 |
| | XRD-XRF-STA | -0.10 | -0.35 | 3.68 | 1.76 | 0.78 | 0.55 | -0.03 | 0.00 | 0.00 |

n.d.: not determined due to lack of sample

Table 9.2b: Relative deviations between chemical composition, calculated from Rietveld analysis and measured by XRF (XRD-XRF), and between the adapted values and XRF (XRD-XRF adapted), and between the XRD adapted values and STA measurements (XRD-XRF-STA) of the kaolin sample LA540 MO and of the grain-size fractionated material.

| | | deviations [%] | | | | | | | | |
|---|---|---|---|---|---|---|---|---|---|---|
| LA540 MO | crosscheck | $SiO_2$ | $Al_2O_3$ | $Fe_2O_3$ | MgO | CaO | $Na_2O$ | $K_2O$ | $TiO_2$ | $P_2O_5$ |
| bulk | XRD-XRF | 1.95 | -1.59 | 0.97 | 0.27 | 0.11 | 0.08 | 0.26 | 0.38 | 0.96 |
| | XRD-XRF adapted | 0.16 | -0.29 | 0.96 | 0.26 | -0.16 | 0.08 | -0.08 | 0.00 | 0.36 |
| | XRD-XRF-STA | -0.02 | -0.67 | 0.95 | 0.25 | -0.16 | 0.08 | -0.08 | 0.00 | 0.36 |
| >20 µm | XRD-XRF | 4.81 | -7.10 | 2.20 | 1.00 | 0.22 | 0.01 | 3.28 | 0.47 | 0.62 |
| | XRD-XRF adapted | 0.00 | -0.08 | 2.15 | 0.95 | -0.05 | 0.01 | 0.05 | 0.00 | 0.03 |
| | XRD-XRF-STA | 0.00 | -0.08 | 2.15 | 0.95 | -0.05 | 0.01 | 0.05 | 0.00 | 0.03 |
| 2-20 µm | XRD-XRF | 3.82 | -0.56 | 0.57 | 0.06 | 0.07 | 0.00 | 1.33 | -0.47 | 0.91 |
| | XRD-XRF adapted | 0.00 | -0.12 | 0.52 | 0.01 | -0.32 | 0.00 | 0.16 | 0.00 | 0.04 |
| | XRD-XRF-STA | 0.00 | -0.12 | 0.52 | 0.01 | -0.32 | 0.00 | 0.16 | 0.00 | 0.04 |
| 0.6-2 µm | XRD-XRF | 0.90 | -0.25 | 0.89 | 0.20 | 0.12 | 0.00 | 0.00 | 0.33 | 0.86 |
| | XRD-XRF adapted | 0.00 | -0.06 | 0.89 | 0.20 | -0.27 | 0.00 | 0.00 | 0.00 | 0.00 |
| | XRD-XRF-STA | 0.00 | -0.06 | 0.89 | 0.20 | -0.27 | 0.00 | 0.00 | 0.00 | 0.00 |
| 0.2-0.6 µm | XRD-XRF | -0.49 | -9.21 | 3.29 | 1.99 | 0.95 | 0.18 | 2.26 | 0.41 | 0.37 |
| | XRD-XRF adapted | 0.00 | -0.03 | 2.93 | 1.63 | 0.78 | 0.18 | -0.03 | 0.00 | 0.00 |
| | XRD-XRF-STA | 0.00 | -0.03 | 2.93 | 1.63 | 0.78 | 0.18 | -0.03 | 0.00 | 0.00 |
| <0.2 µm | XRD-XRF | -0.82 | -6.27 | 3.62 | 2.50 | 1.16 | 0.93 | -0.33 | -0.95 | 0.11 |
| | XRD-XRF adapted | 0.00 | -5.75 | 3.42 | 2.30 | 1.11 | 0.93 | 0.09 | 0.00 | 0.00 |
| | XRD-XRF-STA | 0.00 | -5.75 | 3.42 | 2.30 | 1.11 | 0.93 | 0.09 | 0.00 | 0.00 |

Table 9.2c: Relative deviations between chemical composition, calculated from Rietveld analysis and measured by XRF (XRD-XRF), and between the adapted values and XRF (XRD-XRF adapted), and between the XRD adapted values and STA measurements (XRD-XRF-STA) of the kaolin sample B4914 and of the grain-size fractionated material.

| | | deviations [%] | | | | | | | | |
|---|---|---|---|---|---|---|---|---|---|---|
| B4914 | crosscheck | $SiO_2$ | $Al_2O_3$ | $Fe_2O_3$ | MgO | CaO | $Na_2O$ | $K_2O$ | $TiO_2$ | $P_2O_5$ |
| bulk | XRD-XRF | -0.51 | -1.79 | 0.75 | 0.14 | 0.13 | 0.00 | 0.59 | 0.47 | 0.21 |
| | XRD-XRF adapted | -0.03 | -0.03 | 0.74 | 0.13 | 0.04 | 0.00 | 0.05 | 0.00 | 0.01 |
| | XRD-XRF-STA | 0.01 | -0.13 | 0.69 | 0.08 | 0.04 | 0.00 | 0.07 | 0.00 | 0.01 |
| >20 µm | XRD-XRF | -0.32 | -1.09 | 0.54 | -0.02 | 0.08 | 0.00 | 0.45 | 0.20 | 0.16 |
| | XRD-XRF adapted | 0.00 | 0.00 | 0.54 | -0.02 | 0.01 | 0.00 | 0.01 | 0.00 | 0.00 |
| | XRD-XRF-STA | 0.03 | -0.26 | 0.49 | -0.07 | 0.01 | 0.00 | 0.04 | 0.00 | 0.00 |
| 2-20 µm | XRD-XRF | 0.43 | -1.82 | 0.53 | -0.01 | 0.09 | 0.00 | 0.55 | 0.04 | 0.10 |
| | XRD-XRF adapted | 0.00 | 0.00 | 0.53 | -0.01 | 0.05 | 0.00 | 0.00 | 0.00 | 0.00 |
| | XRD-XRF-STA | 0.00 | -0.25 | 0.49 | -0.05 | 0.05 | 0.00 | 0.01 | 0.00 | 0.00 |
| 0.6-2 µm | XRD-XRF | -0.81 | 0.05 | 0.77 | 0.11 | 0.15 | 0.00 | -0.43 | -0.13 | 0.32 |
| | XRD-XRF adapted | 0.00 | 0.01 | 0.78 | 0.12 | 0.01 | 0.00 | -0.02 | 0.00 | 0.00 |
| | XRD-XRF-STA | 0.00 | -0.32 | 0.75 | 0.09 | 0.01 | 0.00 | 0.04 | 0.00 | 0.00 |
| 0.2-0.6 µm | XRD-XRF | -0.75 | -1.47 | 1.13 | 0.35 | 0.19 | 0.00 | 0.11 | 0.16 | 0.09 |
| | XRD-XRF adapted | 0.00 | 0.00 | 1.07 | 0.28 | 0.07 | 0.00 | -0.01 | 0.00 | 0.00 |
| | XRD-XRF-STA | 0.00 | -1.16 | 1.04 | 0.26 | 0.07 | 0.00 | 0.15 | 0.00 | 0.00 |
| <0.2 µm | XRD-XRF | -2.02 | -1.16 | 1.71 | 0.47 | 0.35 | 0.23 | -0.12 | 0.33 | 0.21 |
| | XRD-XRF adapted | 0.19 | -1.82 | 1.60 | 0.36 | 0.26 | 0.23 | -0.11 | 0.00 | 0.01 |
| | XRD-XRF-STA | n.d. | n.d. | n.d. | n.d. | n.d. | n.d. | n.d. | n.d. | n.d. |

n.d.: not determined due to lack of sample

Table 9.2d: Relative deviations between chemical composition, calculated from Rietveld analysis and measured by XRF (XRD-XRF), and between the adapted values and XRF (XRD-XRF adapted), and between the XRD adapted values and STA measurements (XRD-XRF-STA) of the kaolin sample B4914 MO and of the grain-size fractionated material.

| | | deviations [%] | | | | | | | | |
|---|---|---|---|---|---|---|---|---|---|---|
| B4914 MO | crosscheck | $SiO_2$ | $Al_2O_3$ | $Fe_2O_3$ | MgO | CaO | $Na_2O$ | $K_2O$ | $TiO_2$ | $P_2O_5$ |
| bulk | XRD-XRF | -0.11 | -1.56 | 0.66 | 0.16 | 0.08 | 0.00 | 0.03 | 0.47 | 0.05 |
| | XRD-XRF adapted | -0.01 | -0.03 | 0.71 | 0.21 | -0.03 | 0.00 | 0.00 | 0.00 | 0.00 |
| | XRD-XRF-STA | 0.00 | -0.09 | 0.65 | 0.15 | -0.03 | 0.00 | 0.01 | 0.00 | 0.00 |
| >20 µm | XRD-XRF | -0.99 | 1.38 | 0.47 | -0.06 | 0.07 | 0.00 | -0.99 | -0.07 | 0.12 |
| | XRD-XRF adapted | 0.01 | -0.04 | 0.47 | -0.06 | -0.02 | 0.00 | 0.01 | 0.00 | 0.00 |
| | XRD-XRF-STA | 0.00 | -0.09 | 0.43 | -0.10 | -0.02 | 0.00 | 0.00 | 0.00 | 0.00 |
| 2-20 µm | XRD-XRF | 0.90 | -2.89 | 0.54 | 0.03 | 0.05 | 0.00 | 1.00 | 0.19 | 0.17 |
| | XRD-XRF adapted | 0.00 | 0.00 | 0.52 | 0.01 | -0.03 | 0.00 | 0.00 | 0.00 | 0.00 |
| | XRD-XRF-STA | 0.00 | -0.04 | 0.44 | -0.07 | -0.03 | 0.00 | 0.04 | 0.00 | 0.00 |
| 0.6-2 µm | XRD-XRF | -0.27 | -0.70 | 0.69 | 0.13 | 0.07 | 0.00 | 0.23 | -0.37 | -0.23 |
| | XRD-XRF adapted | 0.00 | 0.00 | 0.67 | 0.10 | -0.04 | 0.00 | 0.00 | 0.00 | 0.00 |
| | XRD-XRF-STA | 0.00 | -0.03 | 0.63 | 0.07 | -0.04 | 0.00 | 0.00 | 0.00 | 0.00 |
| 0.2-0.6 µm | XRD-XRF | -0.76 | -1.34 | 1.01 | 0.37 | 0.12 | 0.00 | 0.08 | 0.15 | 0.13 |
| | XRD-XRF adapted | 0.00 | 0.00 | 0.96 | 0.31 | -0.05 | 0.00 | 0.00 | 0.00 | 0.00 |
| | XRD-XRF-STA | 0.01 | -0.30 | 0.92 | 0.28 | -0.05 | 0.00 | -0.05 | 0.00 | 0.00 |
| <0.2 µm | XRD-XRF | -1.11 | -2.38 | 1.04 | 0.42 | 0.58 | 1.17 | -0.35 | 0.34 | 0.29 |
| | XRD-XRF adapted | 0.17 | -0.67 | 0.95 | 0.33 | 0.45 | 1.17 | 0.02 | 0.00 | 0.00 |
| | XRD-XRF-STA | 0.17 | -0.67 | 0.95 | 0.33 | 0.45 | 1.17 | 0.02 | 0.00 | 0.00 |

Table 9.2e: Relative deviations between chemical composition, calculated from Rietveld analysis and measured by XRF (XRD-XRF), and between the adapted values and XRF (XRD-XRF adapted), and between the XRD adapted values and STA measurements (XRD-XRF-STA) of the kaolin sample B4915 and of the grain-size fractionated material.

| | | deviations [%] | | | | | | | | |
|---|---|---|---|---|---|---|---|---|---|---|
| B4915 | crosscheck | $SiO_2$ | $Al_2O_3$ | $Fe_2O_3$ | MgO | CaO | $Na_2O$ | $K_2O$ | $TiO_2$ | $P_2O_5$ |
| bulk | XRD-XRF | -0.17 | -1.86 | 0.75 | 0.23 | 0.11 | 0.07 | 0.24 | 0.49 | 0.15 |
| | XRD-XRF adapted | 0.07 | -0.03 | 0.73 | 0.21 | 0.04 | 0.07 | -0.04 | 0.00 | 0.00 |
| | XRD-XRF-STA | -0.12 | -0.09 | 0.74 | 0.22 | 0.04 | 0.07 | -0.01 | 0.00 | 0.00 |
| >20 µm | XRD-XRF | -0.24 | -1.49 | 0.58 | -0.03 | 0.08 | 0.00 | 0.58 | 0.42 | 0.08 |
| | XRD-XRF adapted | 0.00 | 0.00 | 0.58 | -0.03 | 0.04 | 0.00 | 0.00 | 0.00 | 0.00 |
| | XRD-XRF-STA | 0.00 | 0.00 | 0.58 | -0.03 | 0.04 | 0.00 | 0.00 | 0.00 | 0.00 |
| 2-20 µm | XRD-XRF | 0.05 | -1.67 | 0.59 | 0.01 | 0.09 | 0.00 | 0.72 | 0.29 | 0.07 |
| | XRD-XRF adapted | 0.00 | 0.00 | 0.58 | 0.00 | 0.06 | 0.00 | 0.04 | 0.00 | 0.00 |
| | XRD-XRF-STA | 0.00 | -0.01 | 0.54 | -0.05 | 0.06 | 0.00 | 0.03 | 0.00 | 0.00 |
| 0.6-2 µm | XRD-XRF | -0.76 | -0.22 | 0.93 | 0.14 | 0.15 | 0.00 | -0.43 | -0.12 | -0.19 |
| | XRD-XRF adapted | 0.00 | 0.00 | 0.92 | 0.12 | 0.01 | 0.00 | 0.00 | 0.00 | 0.00 |
| | XRD-XRF-STA | 0.00 | 0.24 | 0.90 | 0.11 | 0.01 | 0.00 | 0.00 | 0.00 | 0.00 |
| 0.2-0.6 µm | XRD-XRF | -0.39 | -1.65 | 1.09 | 0.20 | 0.18 | 0.00 | -0.08 | 0.38 | -0.24 |
| | XRD-XRF adapted | 0.00 | 0.00 | 1.04 | 0.15 | 0.06 | 0.00 | -0.01 | 0.00 | 0.00 |
| | XRD-XRF-STA | 0.00 | 0.10 | 1.00 | 0.11 | 0.06 | 0.00 | -0.02 | 0.00 | 0.00 |
| <0.2 µm | XRD-XRF | -1.93 | -5.03 | 1.87 | 0.81 | 0.63 | 0.67 | 2.12 | 0.69 | 0.20 |
| | XRD-XRF adapted | 1.74 | -0.36 | 1.64 | 0.58 | 0.54 | 0.67 | 0.00 | 0.00 | 0.00 |
| | XRD-XRF-STA | 0.10 | -1.85 | 1.61 | 0.54 | 0.54 | 0.67 | 0.18 | 0.00 | 0.00 |

Table 9.2f: Relative deviations between chemical composition, calculated from Rietveld analysis and measured by XRF (XRD-XRF), and between the adapted values and XRF (XRD-XRF adapted), and between the XRD adapted values and STA measurements (XRD-XRF-STA) of the kaolin sample B4915 MO and of the grain-size fractionated material.

| | | deviations [%] | | | | | | | | |
|---|---|---|---|---|---|---|---|---|---|---|
| B4915 MO | crosscheck | $SiO_2$ | $Al_2O_3$ | $Fe_2O_3$ | MgO | CaO | $Na_2O$ | $K_2O$ | $TiO_2$ | $P_2O_5$ |
| bulk | XRD-XRF | -0.23 | -1.69 | 0.74 | 0.24 | 0.07 | 0.07 | 0.16 | 0.49 | 0.15 |
| | XRD-XRF adapted | 0.00 | -0.04 | 0.73 | 0.23 | 0.00 | 0.07 | 0.00 | 0.00 | 0.00 |
| | XRD-XRF-STA | -0.12 | -0.09 | 0.74 | 0.22 | 0.04 | 0.07 | -0.01 | 0.00 | 0.00 |
| >20 µm | XRD-XRF | 0.25 | -2.30 | 0.55 | -0.03 | 0.07 | 0.00 | 0.99 | 0.38 | 0.08 |
| | XRD-XRF adapted | 0.00 | 0.01 | 0.55 | -0.03 | 0.04 | 0.00 | -0.01 | 0.00 | 0.00 |
| | XRD-XRF-STA | -0.01 | -0.17 | 0.46 | -0.12 | 0.04 | 0.00 | 0.03 | 0.00 | 0.00 |
| 2-20 µm | XRD-XRF | 0.34 | -2.14 | 0.60 | 0.00 | 0.06 | 0.00 | 0.67 | 0.38 | 0.08 |
| | XRD-XRF adapted | 0.00 | 0.00 | 0.60 | 0.00 | 0.02 | 0.00 | 0.00 | 0.00 | 0.00 |
| | XRD-XRF-STA | 0.01 | -0.01 | 0.55 | -0.05 | 0.02 | 0.00 | 0.00 | 0.00 | 0.00 |
| 0.6-2 µm | XRD-XRF | -1.02 | -0.59 | 0.93 | 0.14 | 0.10 | 0.00 | -0.13 | 0.28 | 0.07 |
| | XRD-XRF adapted | 0.00 | 0.00 | 0.93 | 0.14 | -0.02 | 0.00 | 0.00 | 0.00 | 0.00 |
| | XRD-XRF-STA | 0.00 | 0.19 | 0.89 | 0.10 | -0.02 | 0.00 | -0.03 | 0.00 | 0.00 |
| 0.2-0.6 µm | XRD-XRF | -0.19 | -1.59 | 1.21 | 0.28 | 0.14 | 0.00 | -0.54 | 0.43 | -0.20 |
| | XRD-XRF adapted | 0.04 | 0.00 | 1.15 | 0.22 | 0.04 | 0.00 | -0.02 | 0.00 | 0.00 |
| | XRD-XRF-STA | 0.00 | -0.09 | 1.16 | 0.23 | 0.04 | 0.00 | -0.01 | 0.00 | 0.00 |
| <0.2 µm | XRD-XRF | -1.05 | -5.32 | 1.44 | 0.62 | 0.36 | 1.22 | 2.22 | 0.31 | 0.17 |
| | XRD-XRF adapted | 0.00 | 0.02 | 1.19 | 0.37 | 0.28 | 1.22 | 0.00 | 0.00 | 0.00 |
| | XRD-XRF-STA | 0.15 | -0.66 | 1.16 | 0.33 | 0.28 | 1.22 | 0.11 | 0.00 | 0.00 |

Table 9.2g: Relative deviations between chemical composition, calculated from Rietveld analysis and measured by XRF (XRD-XRF), and between the adapted values and XRF (XRD-XRF adapted), and between the XRD adapted values and STA measurements (XRD-XRF-STA) of the kaolin sample B4915 K and of the grain-size fractionated material.

| | | deviations [%] | | | | | | | | |
|---|---|---|---|---|---|---|---|---|---|---|
| B4915 K | crosscheck | $SiO_2$ | $Al_2O_3$ | $Fe_2O_3$ | MgO | CaO | $Na_2O$ | $K_2O$ | $TiO_2$ | $P_2O_5$ |
| bulk | XRD-XRF | -0.40 | -1.83 | 0.75 | 0.25 | 0.07 | 0.08 | 0.41 | 0.48 | 0.19 |
| | XRD-XRF adapted | 0.01 | -0.04 | 0.72 | 0.22 | -0.02 | 0.08 | 0.02 | 0.00 | 0.00 |
| | XRD-XRF-STA | 0.01 | -0.04 | 0.72 | 0.22 | -0.02 | 0.08 | 0.02 | 0.00 | 0.00 |
| >20 µm | XRD-XRF | -0.42 | -2.10 | 0.87 | 0.12 | 0.08 | 0.00 | 0.68 | 0.52 | 0.23 |
| | XRD-XRF adapted | 0.00 | 0.00 | 0.87 | 0.11 | -0.02 | 0.00 | 0.00 | 0.00 | 0.00 |
| | XRD-XRF-STA | 0.00 | -0.08 | 0.85 | 0.09 | -0.02 | 0.00 | -0.01 | 0.00 | 0.00 |
| 2-20 µm | XRD-XRF | 0.37 | -2.20 | 0.60 | 0.01 | 0.06 | 0.00 | 0.69 | 0.37 | 0.08 |
| | XRD-XRF adapted | 0.00 | 0.00 | 0.60 | 0.01 | 0.03 | 0.00 | 0.00 | 0.00 | 0.00 |
| | XRD-XRF-STA | 0.00 | -0.12 | 0.56 | -0.03 | 0.03 | 0.00 | 0.06 | 0.00 | 0.00 |
| 0.6-2 µm | XRD-XRF | -0.63 | -1.41 | 0.87 | 0.16 | 0.10 | 0.00 | 0.18 | 0.47 | 0.26 |
| | XRD-XRF adapted | 0.00 | -0.01 | 0.85 | 0.14 | -0.02 | 0.00 | 0.01 | 0.00 | 0.00 |
| | XRD-XRF-STA | 0.00 | -0.01 | 0.85 | 0.14 | -0.02 | 0.00 | 0.01 | 0.00 | 0.00 |
| 0.2-0.6 µm | XRD-XRF | -2.21 | -0.60 | 1.10 | 0.27 | 0.13 | 0.00 | 0.37 | 0.55 | 0.15 |
| | XRD-XRF adapted | 0.00 | -0.11 | 0.99 | 0.16 | -0.02 | 0.00 | 0.00 | 0.00 | 0.01 |
| | XRD-XRF-STA | 0.00 | -0.26 | 0.95 | 0.12 | -0.02 | 0.00 | -0.02 | 0.00 | 0.01 |
| <0.2 µm | XRD-XRF | -2.55 | -3.31 | 1.38 | 0.54 | 0.43 | 1.00 | 1.14 | 0.59 | 0.74 |
| | XRD-XRF adapted | 0.00 | -0.04 | 1.22 | 0.38 | 0.10 | 1.00 | 0.00 | 0.00 | 0.00 |
| | XRD-XRF-STA | 0.00 | -0.61 | 1.19 | 0.35 | 0.10 | 1.00 | 0.12 | 0.00 | 0.00 |